COMBINING ROCK PHYSICS AND SEDIMENTOLOGY FOR SEISMIC RESERVOIR CHARACTERIZATION OF NORTH SEA TURBIDITE SYSTEMS

A DISSERTATION
SUBMITTED TO THE DEPARTMENT OF GEOPHYSICS
AND THE COMMITTEE ON GRADUATE STUDIES
OF STANFORD UNIVERSITY
IN PARTIAL FULFILLMENT OF THE REQUIREMENTS
FOR THE DEGREE OF
DOCTOR OF PHILOSOPHY

By
Per Åge Avseth
May, 2000

I certify that I have read this dissertation and that in my opinion it is fully adequate, in scope and quality, as a dissertation for the degree of Doctor of Philosophy.

_____

Gerald Mavko (Principal Adviser)

I certify that I have read this dissertation and that in my opinion it is fully adequate, in scope and quality, as a dissertation for the degree of Doctor of Philosophy.

_____

Amos Nur (Geophysics)

I certify that I have read this dissertation and that in my opinion it is fully adequate, in scope and quality, as a dissertation for the degree of Doctor of Philosophy.

_____

Jack Dvorkin (Geophysics)

I certify that I have read this dissertation and that in my opinion it is fully adequate, in scope and quality, as a dissertation for the degree of Doctor of Philosophy.

_____

Stephan Graham (Geologic and Environmental Science)

Approved for the University Commettee on Graduate Studies:

_____

Abstract

   With the dawn of a new century, the petroleum industry is increasing its focus on the exploration of reservoirs in deep-water clastic systems (specifically turbidite sands). These sedimentary environments represent major hydrocarbon targets in numerous areas of the world. Turbidite systems are often characterized by very complex sand distributions, and reservoir description based on conventional seismic and well-log stratigraphic analysis may be very uncertain in these depositional environments. There is a need to employ more quantitative seismic techniques to reveal reservoirs units in these complex systems from seismic amplitude data.

   In this study we focus on North Sea turbidite systems. Our goal is to improve the ability to use 3D seismic data to map reservoirs in these systems. A cross-disciplinary methodology for seismic reservoir characterization is presented that combines rock physics, sedimentology, and statistical techniques. We apply this methodology to two turbidite systems of Paleocene age located in the South Viking Graben of the North Sea.

   First, we investigate the relationship between sedimentary petrography and rock physics properties. Paleocene turbidite sands occur either with slight contact cementation, or as completely uncemented and friable, yielding very different seismic responses. Clay content and sorting also affect the seismic properties of these sands. Rock physics diagnostics can be used to quantify cement and clay volume, as well as degree of sorting.

   Next, we define seismic scale sedimentary units, which we refer to as *seismic lithofacies*. These facies represent populations of data that have characteristic geologic and seismic properties. Unconsolidated thick-bedded clean sands with water, plane-laminated thick-bedded sands with oil, and pure shales have very similar acoustic impedance values. However, the Vp/Vs ratio helps resolve these ambiguities. We establish a statistically representative training database by identifying seismic lithofacies from thin-sections, cores, and well-log data for a selected type-well. This procedure is guided by diagnostic rock physics modeling. Based on the training data, we perform

multivariate classification of data from other wells in the area. From the classification results we can create cumulative distribution functions (cdfs) of seismic properties for each facies. Pore fluid effect is accounted for by using the Biot-Gassmann theory.

We conduct AVO (amplitude versus offset) analysis to predict seismic lithofacies from seismic data. Based on the facies classification results, we assess uncertainties in AVO response related to the inherent natural variability of each seismic lithofacies using a Monte Carlo technique. AVO probability plots show that there are overlaps between different facies, but the most likely responses for each facies are definitely separated. Based on the Monte Carlo simulation, we also generate bivariate probability density functions (pdfs) of zero-offset reflectivity (R(0)) versus AVO gradient (G) for different facies combinations. By combining the R(0) and G values estimated from 2D and 3D seismic data with the bivariate pdfs estimated from well-logs, we use both quadratic discriminant analysis and Bayesian classification to predict lithofacies and pore fluids from seismic amplitudes.

We apply this methodology for seismic reservoir characterization of the Glitne and Grane turbidite fields. In the Glitne area, 3D AVO inversion results are translated into facies and pore fluid probability maps. These maps show that the Glitne turbidite system is a point-sourced submarine fan in which thick-bedded clean sands are present in the feeder-channel and in the lobe-channels, whereas interbedded sand-shale facies are found in interchannel and marginal areas of the system. Oil sands have highest probabilities in the central lobe-channel, and in parts of the feeder channel. We apply the same methodology to discriminate between volcanic tuffs, pelagic shales and turbidite reservoir sands along selected seismic lines in the Grane area.

Finally, we take advantage of the link established between sedimentology and rock physics to do facies-guided forward seismic modeling. We show how rock physics and seismic modeling can be used to guide the interpretation of reservoir geometries and architectural elements in turbidite systems. We study the Grane turbidite system and document significant variability in the seismic architecture within this system. These observations are important for assessing sandstone connectivity in the Grane area as well as in other geologically analogous systems.

Acknowledgments

When I first came to Stanford in 1994 to pursue a Masters of Science degree in Geophysics I was supposed to go back to Norway after 2 years. However, my advisor, Professor Gary Mavko, and Professor Amos Nur, convinced me to stay for a Ph.D. I feel very privileged and lucky that I got that opportunity, and my 6 years here at Stanford Rock Physics research group (4 years as a Ph.D. student) have been a fantastic and rewarding experience, both scientifically and socially.

First I would like to thank Gary Mavko for being a fantastic advisor; he has guided me along the path that led to where I am today, completing six chapters of this thesis, and one chapter of my life. With his open mind, he embraced my ideas of linking rock physics to sedimentology from the first day. His enthusiasm encouraged me, his constructive comments inspired me, and his approachable, laid-back attitude made me regard him not only as a professor, but also as a good friend.

Then I would like to thank my other defense committee members: Amos Nur, Jack Dvorkin, Steve Graham and Jef Caers (chairman). Special thanks to Jack for the great collaboration and for helping me write my very first publication. Moreover, I thank Amos for leading the SRB research group. In our research group he makes us all feel as a family, and he is truly a great "father". And then I would like to thank Margaret Muir. What would SRB be without her? In Europe, Margaret is a royal name. Whether it is a coincidence or not: She rules! With her tremendous administration of SRB, the success of the group is for granted.

I would like to thank Tapan Mukerji. I highly admire his "infinite" amount of knowledge. Whenever I encountered intricate problems in my research, he was able to solve them. And he would always dedicate time to explain and help. But if he once every now and then said "no", it just meant "yes, but you have to buy me a dinner at Pollo Rey".

Table of contents

List of figures

List of tables

Chapter 1

Introduction

"The future of 3-D seismic is going to be
a greater understanding of what we can get from the data.
...we are not fully utilizing the technology we have today."
Alistair Brown, 1999

1.1   Objective

The main objective of this thesis is to conduct seismic reservoir characterization of North Sea turbidite systems. This general objective contains several more specific goals: 1) To characterize hydrocarbon reservoirs from seismic data using the rock physics link between seismic and reservoir properties; 2) To link rock physics to sedimentary facies and geologic properties to be able to describe lithofacies and depositional environments from seismic data; and 3) To improve the understanding of seismic signatures in North Sea deep-water clastic depositional systems. The motivations for each of these problems are described below.

1.2   Background and motivation

1.2.1   Rock physics and seismic reservoir characterization

The petroleum industry is facing a future where new technologies, creativity and integration of different disciplines, are at the core of focus for higher exploration success rates and improved oil recovery. Techniques like 3D AVO-analysis, seismic monitoring (4D), and multi-component ocean bottom seismic (4C) all represent new geophysical tools that have become essential to the oil industry in pursuing the following goals: 1)

Detect the presence of hydrocarbon reservoirs (i.e., exploration); 2) Describe the shape, size and extent of reservoirs (i.e., reservoir delineation/appraisal); 3) Characterize the heterogeneities and transport properties of reservoirs and the connectivity between various reservoir compartments (i.e., reservoir characterization); and 4) Forecast the performance of a reservoir during production (i.e., reservoir monitoring/forecasting).

The recent development of 3D, 4D, and 4C seismic imaging, has given us a unique opportunity to conduct seismic reservoir characterization with improved certainty and in a more efficient way. Geometries have become easier to delineate, and seismic amplitude information, from which one can predict lithologies, estimate porosities, and detect hydrocarbons, has become more reliable.

However, the transformation from seismic to reservoir data is often based on interpretations or statistical correlations, without accounting for the physical link between seismic wave propagation and reservoir properties. There is a need to improve the physical understanding of seismic information before using it in reservoir characterization. Several authors have studied the seismic properties of rocks, establishing important relationships between seismic properties and reservoir parameters, such as porosity and clay content (e.g., Han, 1986; Marion, 1990; Klimentos, 1991; Yin, 1992), diagenesis (e.g., Jizba, 1991; Liu, 1994; Galmudi, 1998; Dvorkin and Nur, 1996; Anselmetti and Eberli, 1997), fractures (e.g., Chen, 1995; Haugen and Ursin, 1996; Ruger, 1996; Teng, 1998), lithology (e.g., Castagna et al, 1985; Blangy, 1992; Greenberg and Castagna, 1992), as well as pore fluids (e.g., Wang and Nur, 1990; Batzle and Wang, 1992, Liu, 1998). These existing rock physics theories and models can be applied to predict reservoir parameters from seismic data with greater success than just pure statistical conversions or interpretations of seismic amplitudes. Successful examples include dynamic reservoir characterization of 4D time-lapse data (e.g., Lumley et al, 1994; Landrø, 1999; Yuh et al., 1999; Sengupta, 2000), characterization of fractures in hydrocarbon reservoirs from 3D pre-stack seismic data (e.g., Teng, 1998; Lynn et al., 1995), detection of submarine gas hydrates from 2D shallow seismic data (e.g., Dahl and Ursin 1992; Ecker, 1998), and characterization of aquifers from ultra-shallow seismic data (e.g., Bachrach, 1998; Cardimona et al, 1998). These examples demonstrate that the rock physics link is essential for rigorously relating seismic data to reservoir properties.

Moreover, the physical link should be combined with statistics to account for uncertainties related to variability in the rock physics parameters (Mavko and Mukerji, 1998; Takahashi, 2000). Finally, there is a need to link rock physics to geologic parameters like facies and depositional environments. This link will ensure that the assumptions made are geologically valid, and that the results are geologically reliable.

1.2.2 Relating sedimentology, rock physics, and seismic properties

One of the fundamental aspects of this thesis is to establish a link between rock physics and sedimentology. More specifically, we want to relate lithofacies to rock physics properties. This will improve the ability of using seismic amplitude information for reservoir prediction and characterization in these systems, as facies have a major control on reservoir geometries and porosity distributions. Furthermore, facies occur in predictable patterns in terms of lateral and vertical distribution and can also be linked to sedimentary processes and depositional environments (Walker, 1984). Hence, facies represent an important parameter in seismic exploration and reservoir characterization.

Traditionally, seismic facies have been interpreted at a large scale from seismic traveltimes based on geometric patterns in the reflections. This has been a purely visual and qualitative methodology where pre-defined "seismic facies" have been interpreted from the seismic data (e.g., Mitchum et al., 1977, Weimer and Link, 1991). The first interpretation of depositional facies from 3-D seismic data using reflection amplitude information, was by Brown et al. (1981), who recognized river channels from amplitude maps. Their work was followed by other authors doing facies imaging from seismic amplitude maps, and most successfully in fluvial systems where channel facies have been easily recognized (e.g., Rijks and Jauffred, 1991; Brown, 1992; Enachescu, 1993; Ryseth et al., 1998). Some authors have studied the correlation between seismic amplitudes and lithology by seismic forward modeling (e.g., Varsek, 1985; Campbell, 1992; Zeng et al., 1996). Zeng et al. (1996) linked lithofacies to rock physics properties and conducted a facies guided seismic modeling study of a micro-tidal shore-zone depositional system. Furthermore, several authors have used seismic inversion to estimate lithology and

reservoir properties from pre-stack seismic data (e.g., Dahl and Ursin, 1992; Buland et al., 1996).

1.2.3 Seismic characterization of turbidite systems

The oil industry is increasingly focusing on the exploration of reservoirs in deep-water clastic systems (specifically turbidite sands), because these may include large volumes of unexplored hydrocarbon in several areas of the world (Pettingill, 1998). Today, submarine fans and turbidite systems represent major petroleum reservoirs in many sedimentary basins throughout the world. Of the 25 largest oil and gas fields in the United States, six occur in turbidite reservoirs (Weimer and Link, 1991). Submarine fans and turbidite reservoirs are responsible for 22% of petroleum production in the North Sea (Watson, 1984), 83% of production in the Campos Basin in offshore Brazil (Bacoccolli and Toffoli, 1988), and 90% of production in the Los Angeles Basin (Taylor, 1976).
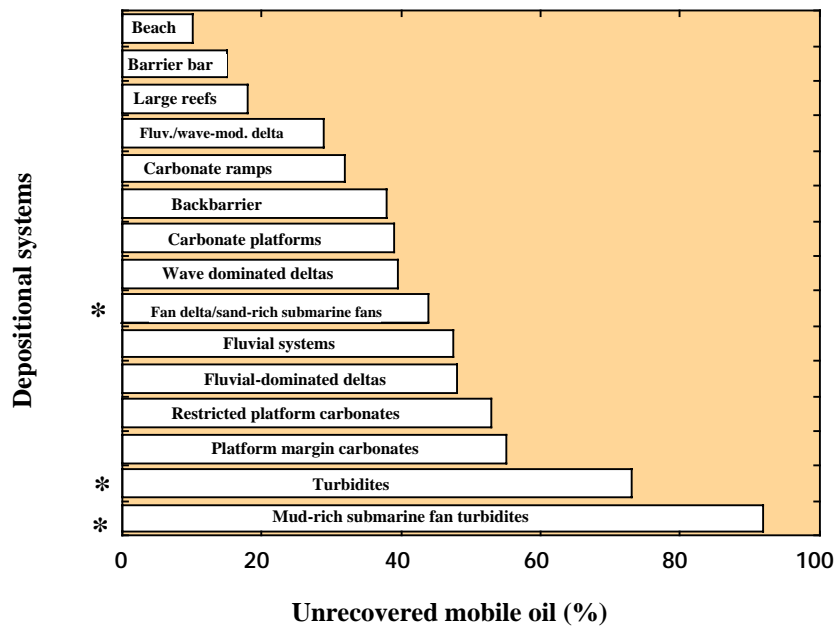
Figure 1.1: Unrecovered mobile oil as a function of depositional origin. Relatively simple, homogeneous reservoir systems (e.g., beach systems) are produced effectively, whereas much oil in highly compartmentalized systems (e.g., turbidites) is often left behind in conventional development. The latter reservoirs are particular targets of improved oil recovery, IOR (Tyler and Finley, 1991). (* = deep water clastic systems).

Deep-water clastic systems and associated turbidite reservoirs are often characterized by very complex sand distributions. As a result, reservoir description based on conventional seismic and well-log stratigraphic analysis may be very uncertain in these depositional environments (Tyler and Finley, 1991; Weimer et al., 2000). Figure 1.1 shows that reservoirs in turbidite systems have been produced very inefficiently during conventional development. More than 70% of the mobile oil is commonly left behind because of the heterogeneous nature of these reservoirs.

Because conventional seismic methods of interpreting and characterizing reservoirs from seismic are not very efficient in these complex systems, there is a need to employ more quantitative seismic techniques to reveal reservoirs units from 3-D seismic data. In this study we focus on turbidite systems, and our goal is to improve the ability of using seismic amplitude data to map reservoirs in these systems. This is especially important in the Tertiary fields of the North Sea where wells are sparse and the traps are subtle.

1.3   Approach

Our approach to solve the aforementioned problems, is to develop a cross-disciplinary methodology that combines well-log facies analysis, statistical rock physics, and seismic inversion. We apply this methodology to two turbidite systems of Tertiary age, located in the South Viking Graben in the North Sea. The reservoir sands represent the Heimdal Formation of late Paleocene age and include two oil fields of economic interest, the Glitne and the Grane fields. A map of the area and a description of the local and regional geology are given in Appendix A.

By linking lithofacies to rock properties, and then using statistical techniques to account for natural variability within different facies, and overlap between them, we obtain a probabilistic link between facies, rock properties, and seismic response. This link allows one to predict the most likely facies and conditional probabilities of their occurrence from seismic data. Furthermore, the link between rock physics and lithofacies allows for a facies-guided forward seismic modeling that can improve the interpretation of turbidite systems, their depositional geometries, and reservoir architecture.

This thesis consists of six chapters, including this introduction. The chapters are linked together and represent different stages in the presented methodology. Moreover, the chapters consider different scales. We start at the micro-scale, where a physical understanding of the rocks and pore fluids is obtained. Then we do rock physics and facies analysis of well-log data. Finally, we end at the seismic scale where prediction of reservoir properties is made. Figure 1.2 shows the different steps of the methodology in a flow-scheme.
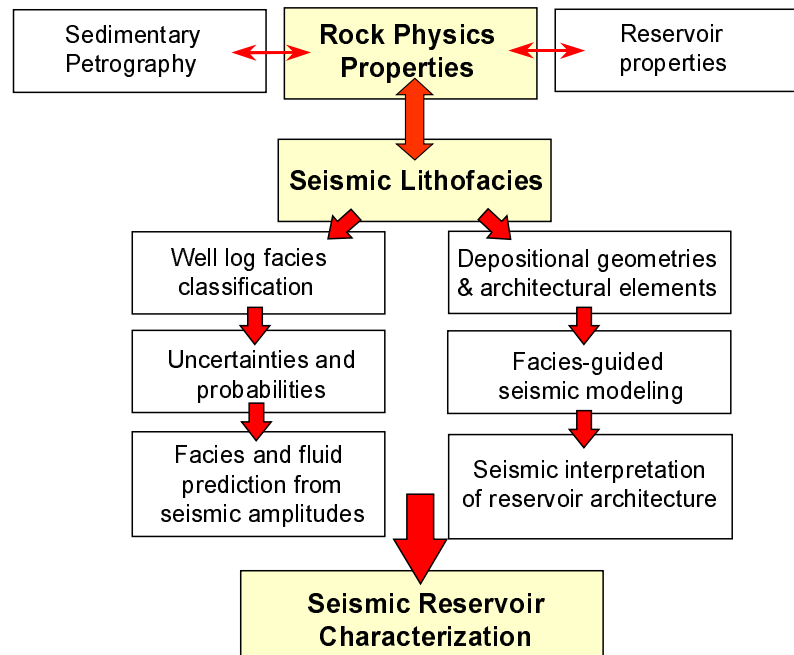
Figure 1.2: Flow-scheme showing the different steps of the thesis, and how they are linked together.

1.3.1   Rock physics diagnostics of lithology, rock texture, and diagenesis

In Chapter 2, we investigate the link between microscale sedimentary petrography and rock physics properties. This is done in order to understand the acoustic behavior of rocks, i.e., density and P-wave velocity, as a function of diagenesis, lithology, clay content, and sandstone texture. Well-log data are analyzed and compared with microstructure models in order to diagnose the rocks at the grainscale. Thin-sections and SEM images are used to confirm the diagnostics, where available. In general, the results

of this chapter are important to better understand the link between sedimentology and rock physics properties at a microscopic scale. Parts of Chapter 2 were done in collaboration with Jack Dvorkin at the Stanford Rock Physics Laboratory, and Johannes Rykkje at Norsk Hydro Research Center. This work was presented at the 68th Annual International SEG Convention in New Orleans (Avseth et al., 1998a), and has been submitted for publication in Geophysical Research Letters (Avseth et al., 2000a).

1.3.2 Lithofacies recognition and classification using statistical rock physics

Chapter 3 combines rock physics diagnostics and statistics to recognize different clusters of data, such as facies or lithologies with characteristic rock physics properties. These can be defined from cores or other direct sources of information, or they can be inferred from mathematical models that diagnose the type of rock based on well-log measurements, as described in Chapter 2. These clusters of data, or facies, represent the training data that are used in the classification of well data in several wells. we apply three different methods, including quadratic discriminant analysis, non-parametric pdf classification, and neural networks. The results of this chapter are important for the establishment of a probabilistic link between sedimentology and rock physics. Parts of Chapter 3 were presented at the 1999 IAMG annual meeting in Trondheim (Avseth et al., 1999a), and at the 1998 AAPG annual convention in Salt Lake City (Avseth, 1998). This chapter has furthermore been done in collaboration with Tapan Mukerji (Stanford Rock Physics Laboratory).

1.3.3 Seismic facies and pore-fluid mapping

Chapters 4 and 5 employ the probabilistic link between lithofacies and rock physics properties to predict facies from seismic amplitude data. We first create cumulative distribution functions (cdfs) of seismic properties, based on the well-log classification in Chapter 3. Pore fluid effects are taken into account using the Biot-Gassmann theory. From the facies and pore fluid cdfs, we generate probability density functions (pdfs) of seismic parameters including zero offset reflectivity and AVO (amplitude versus offset)

gradient. These parameters can be estimated from real seismic data (i.e., seismic inversion). By calibrating them to the well-log derived pdfs, we can predict the most likely lithofacies and pore fluids from the inversion results. Moreover, we can estimate conditional probability maps of the different facies.

In Chapter 4, we use this methodology to conduct seismic reservoir characterization of the Glitne field, where 3D AVO inversion results are translated into facies and pore fluid probability maps. This work was presented at the 68th annual international SEG convention in New Orleans (Avseth et al., 1998b), as well as at the 1998 AAPG international conference in Rio de Janeiro (Avseth et al., 1998c). This chapter, together with parts of Chapter 3, have been accepted for publication in Geophysics (Avseth et al., 2000b).

In Chapter 5, we apply the same methodology to discriminate between volcanic tuffs and reservoir sands along selected two-dimensional seismic lines. This chapter was presented at the 69th annual international SEG convention in Houston (Avseth et al., 1999b).

In general, the results of Chapters 4 and 5 can be used as input data for risk assessment and reservoir management, as well as for reservoir modeling and performance forecasting. We have collaborated with Tapan Mukerji (Stanford Rock Physics Laboratory), Arild Jørstad (Statoil), Tor Veggeland (Norsk Hydro) during the work done in Chapter 4, and with Tapan Mukerji and Jorun Aune Tyssekvam (Norsk Hydro) during the work done in Chapter 5.

1.3.4   Seismic interpretation guided by rock physics and seismic modeling

Chapter 6 takes advantage of the link between facies and rock physics to do facies guided forward seismic modeling. We show how rock physics and seismic modeling can be used to guide the interpretation of reservoir geometries and architectural elements in turbidite systems. We study the Grane turbidite system and document significant variability in the seismic architecture within this system. These observations are important in order to assess the sandstone connectivity in the Grane area as well as in other analog systems.

1.4   Available data

There is a comprehensive database available for this study, including thin-sections and cores, well-log data from twelve wells, common-depth-point (CDP) gathers from selected seismic lines, and a 3-D seismic cube covering one of the fields of interest. The thin-sections and cores are used to guide the facies identification from well-log data. The well-log data available for classification and generation of probability density functions (pdfs) includes P-wave velocity (Vp), density, and gamma ray for all the wells. In addition, we have S-wave velocity (Vs) and resistivity data (shallow and deep) from two of the wells. Helium porosity data are available from the cored zone in well #2. The pre-stack seismic data (i.e., CDP-gathers) both from the 2-D lines and the 3-D cube have been pre-processed for true amplitude recovery and AVO-analysis. The processing includes spherical divergence correction, pre-stack FK time migration, NMO moveout correction, Radon-transform multiple removal, and surface consistent offset balancing.

1.5   Future implications and visions

The work in this thesis will help the oil industry to do seismic reservoir characterization in a more physically and geologically reliable way. Several companies have already adapted the methodology of predicting facies from seismic amplitudes using statistical rock physics that is presented in this thesis (e.g., Walls et al., 1999; Bach et al., 2000).

Moreover, one can extend the work presented in this thesis, and make seismic reservoir characterization even more integrated and complete, taking into account other uncertainties than those related to rock physics properties and facies variability. This includes uncertainties related to thin-bed effects, tuning, and anisotropy, as well as uncertainties in overburden velocities.

Also, one can expand on the one-point uncertainty analysis and include spatial multi-point statistics when predicting lithofacies and pore fluids from seismic data (e.g., Damsleth and Omre, 1997). The same methodology can furthermore be applied in shallow applications, for aquifer characterization from remote sensing.

1.6   References

Anselmetti, F. S., and Eberli, G. P., 1997, Sonic velocity in carbonate sediments and rocks, *in* Palaz, I., and Marfurt, K.J., Eds., Carbonate Seismology: Society of Exploration Geophysicists, Tulsa, OK, 53-74.

Avseth, P., Dvorkin., J., Mavko, G., and Rykkje, J., 2000a (in prep.), Rock physics diagnostics of North Sea sands. Link between microstructure and seismic properties: Paper submitted for publication to Geophysics Research Letters.

Avseth, P., Mukerji, T., Mavko, G., and Veggeland, T., 2000b (in prep.), Seismic reservoir mapping from 3-D AVO in a North Sea turbidite system: Paper submitted and accepted for publication to Geophysics.

Avseth, P., Mukerji, T., Mavko, G., and Jørstad, A. K., 1999a, Seismic reservoir characterization constrained by well-log rock physics and facies classification: Proceedings of the 5th Ann. Conf. of the Int. Ass. for Math. Geol. (IAMG), 597-602.

Avseth, P., Mukerji, T., Mavko, G., and Tyssekvam, J. A., 1999b, Integrating seismic lithofacies prediction and depositional geometry analysis for reservoir delineation in a North Sea turbidite system: 69th Ann. Internat. Mtg., Soc. Expl. Geophys., Expanded Abstracts, 752-756.

Avseth, P., Dvorkin, J., Mavko, G., and Rykkje, J., 1998a, Diagnosing high-porosity sandstones for reservoir characterization using sonic and seismic data: 68th Ann. Internat. Mtg., Soc. Expl. Geophys., Expanded Abstracts, 1024-1027.

Avseth, P., Mukerji, T., Mavko, G., and Veggeland, T., 1998b, Statistical discrimination of lithofacies from pre-stack seismic data constrained by well-log rock physics. Application to a North Sea turbidite system: 68th Ann. Internat. Mtg., Soc. Expl. Geophys., Expanded Abstracts, 890-893.

Avseth, P., Mukerji, T. and Mavko, G., 1998c, Seismic lithofacies prediction using AVO-analysis; Application to a North Sea turbidite system: AAPG Internat. Mtg., Rio de Janeiro, Expanded Abstract, 390-391.

Avseth, P., 1998, Seismic lithofacies in North Sea deep-water clastic systems: AAPG Ann. Mtg., Salt Lake City, Expanded Abstract, A36.

Bacoccolli, G. E., and Toffoli, L.C., 1988, The role of turbidites in Brazil's offshore exploration – a review: Offshore Tech. Conf. Proc. 5659, 379-388.

Bach, T., Espersen, T. B., Pedersen, J. M., Hinkley, R., Pillet, W. R., and Rasmussen, K. B., 2000 (in prep.), Inversion of seismic AVO data: *in* Inverse Methods II, Lecture notes in Earth Sciences, Springer-Verlag.

Bachrach, R., 1998, High resolution shallow seismic subsurface characterization: Ph.D. thesis, Stanford University.

Batzle, M. L. and Wang, Z., 1992, Seismic properties of pore fluids: Geophysics, **57**, 1396-1408.

Blangy, J.P., 1992, Integrated seismic lithologic interpretation: The petrophysical basis: Ph.D. thesis, Stanford University.

Brown, A. R., Dahm, C. G., and Graeber, R. T., 1981, A stratigraphic case history using three-dimensional seismic data in the Gulf of Thailand: Geophysical Prospecting, **29**, 327-349.

Brown, A. R., 1992, Interpretation of three-dimensional seismic data: AAPG Memoir 42, 3d edition, 253p.

Buland, A., Landrø, M., Anderssen, M., and Dahl, T., 1996, AVO inversion of Troll Field data: Geophysics, **61**, 1589-1602.

Campbell, A. E., 1992, Seismic modeling of an Early Jurassic, drowned carbonate platform; Djebel Bou Dahar, High Atlas, Morocco: AAPG Bull., **76**, 1760-1777.

Castagna, J. P., Batzle, M. L., and Eastwood, R. L., 1985, Relationships between compressional-wave and shear-wave velocities in clastic silicate rocks: Geophysics, **50**, 571-581.

Cardimona, S. J., Clement, W. P., and Kadinsky-Cade, K., 1998, Seismic reflection and ground-penetrating radar imaging of a shallow aquifer: Geophysics, **63**, 1310-1317.

Chen, W., 1995, AVO in azimuthally anisotropic media: Fracture detection using P-wave data and a seismic study of naturally fractured tight gas reservoirs: Ph.D. thesis, Stanford University.

Damsleth, E., and Omre, H., 1997, Geostatistical approaches in reservoir evaluation: J. Petr. Tech., **49**, 498-501

Dahl, T., and Ursin, B., 1992, Non-linear AVO inversion for a stack of anelastic layers: Geophys. Prosp., **40**, 243-265.

Dvorkin, J., and Nur, A., 1996, Elasticity of High-Porosity Sandstones: Theory for two North Sea datasets, Geophysics, **61**, 1363-1370.

Ecker, K., 1998, Seismic characterization of gas hydrates: Ph.D. thesis, Stanford University.

Enachescu, M. E., 1993, Amplitude interpretation of three-dimensional reflection data: The Leading Edge, **12**, 678-685.

Galmudi, D., 1998, Pressure solution, porosity reduction, and transport in rocks: Ph.D. thesis, Stanford University.

Greenberg, M. L., and Castagna, J.P., 1992, Shear-wave velocity estimation in porous rocks: Theoretical formulation, preliminary verification and applications, Geophys. Prospect., **40**, 195-209.

Han, D.-H., 1986, Effects of porosity and clay content on acoustic properties of sandstones and unconsolidated sediments: Ph.D. thesis, Stanford University.

Haugen, G., and Ursin, B.,1996, AVO-A analysis of a vertically fractured reservoir underlying shale", 66th Ann. Int. Meet., Soc. Expl. Geophys., Expanded Abstracts, 1826-1829.

Jizba, D. L., 1991, Mechanical and acoustical properties of sandstones and shales: Ph.D. thesis, Stanford University.

Klimentos, T., 1991, The effects of porosity-permeability-clay content on the velocity of compressional waves: Geophysics, **56**, 1930-1939.

Landrø, M., Discrimination between pressure and fluid saturation changes from time lapse seismic data, 69th Ann. Int. Meet., Soc. Expl. Geophys., Expanded Abstracts, 1651-1654.

Liu, X., 1994, Nonlinear elasticity, seismic anisotropy, and petrophysical properties of reservoir rocks: Ph.D. thesis, Stanford University.

Liu, Y., 1998, Acoustic properties of reservoir fluids: Ph.D. thesis, Stanford University.

Lumley, D., Nur, A., Strandenes, S., Dvorkin, J., Packwood, J., 1994, Seismic monitoring of oil production; a feasibility study: 64th Ann. Int. Meet., Soc. Expl. Geophys., Expanded Abstracts, 319-322.

Lynn, H., Simon, M. K., Layman, M., Schneider, R., Bates, C. R., and Jones, M., 1995, Use of anisotropy in P-wave and S-wave data for fracture characterization in a naturally fractured gas reservoir: Leading Edge, Soc. Expl. Geophys., **14**, no. 8, 887-893.

Marion, D., 1990, Acoustical, mechanical and transport properties of sediments and granular materials: Ph.D. thesis, Stanford University.

Mavko, G., and Mukerji, T., 1998, A rock physics strategy for quantifying uncertainty in common hydrocarbon indicators: Geophysics, **63**, 1997-2008.

Mitchum, R. M., Jr., Vail, P. R., and Sangree, J. B., 1977, Stratigraphic interpretation of seismic reflection patterns in depositional sequences: *in* Payton, C. E., Ed., Seismic stratigraphy – application to hydrocarbon exploration: AAPG Mem., **26**, 117-133.

Pettingill, 1998, Turbidite giants – lessons from the world's 40 largest turbidite discoveries: EAGE/AAPG 3rd Research Symposium on Developing and Managing Turbidite Reservoirs, Almeria, Expanded Abstracts, A027.

Rijks, E. J. K., and Jauffred, J. C. E. M., 1991, Attribute extraction: An important application in any detailed 3-D interpretation study: The Leading Edge, **10**, 11-19.

Ruger, A., 1996, Variation of P-wave reflectivity with offset and azimuth in anisotropic media: 66th Ann. Int. Meet., Soc. Expl. Geophys., Expanded Abstract, 1810-1813.

Ryseth, A., Fjellbirkeland, H., Osmundsen, I.K., Skålnes, Å., and Zachariassen, E., 1998, High-resolution stratigraphy and seismic attribute mapping of a fluvial reservoir; Middle Jurassic Ness Formation, Oseberg Field: AAPG Bull., **82**, 1627-1651.

Sengupta, M., 2000, Integrating flow simulation and rock physics to characterize seismic time-lapse data: Ph.D. thesis, Stanford University.

Takahashi, I, 2000, Quantifying information and uncertainty of rock property estimation from seismic data: Ph.D. thesis, Stanford University.

Taylor, J.C., 1976, Geological appraisal of the petroleum potential of offshore Southern California; the borderland compared to onshore coastal basins: USGS Circ., **730**.

Teng, L., 1998, Seismic and rock-physics characterization of fractured reservoirs: Ph.D. thesis, Stanford University.

Tyler, N., and Finley, R. J., 1991, Architectural controls on the recovery of hydrocarbons from sandstone reservoirs: *in* Miall, A. D., and Tyler, N., Eds., Three-dimensional facies architecture of terrigenous clastic sediments and its implications for hydrocarbon discovery and recovery: Soc. Sed. Geol., 1-5.

Varsek, J. L., 1985, Lithology prediction and discrimination by amplitude offset modeling: Geophysics, **50**, 1377.

Walker, R., 1984, 1984, Facies Models, 2nd edition: Geol. Assn. Can.

Walls, J., Turhan Taner, M., Guidish, T., Taylor, G., Dumas, D., and Derzhi, N., 1999, North Sea reservoir characterization using rock physics, seismic attributes, and neural networks; a case history: 69th Int. Annual Meeting, Soc. Expl. Geophys., Expanded Abstracts, 1572-1575.

Wang, Z., and Nur, A., 1990, Wave velocities in hydrocarbon-saturated rocks; experimental results: Geophysics, **55**, 723-733.

Watson, M. P., 1984, Submarine fans in a developing extensional regime – their significance in the North Sea hydrocarbon province: AAPG Bulletin, **68**, p.538.

Weimer, P., and Link, M. H., 1991, Seismic facies and sedimentary processes of ancient submarine fans and turbidite systems: Springer-Verlag, New York.

Weimer, P., Slatt, R. M., Dromgoole, P., Bowman, M., and Leonard, A., 2000, Developing and managing turbidite reservoirs: Case histories and experiences: Results of the 1998 EAGE/AAPG Research Conference: AAPG Bulletin, **84**, 453-465.

Yin, H., 1992, Acoustic velocity and attenuation of rocks: Isotropy, intrinsic anisotropy, and stress-induced anisotropy: Ph.D. thesis, Stanford University.

Yuh, S. H., Nordaas, K., Gibson, R. L., Jr., and Datta-Gupta, A., 1999, A feasibility study of time-lapse seismic monitoring using stochastic reservoir models: 69th Ann. Int. Meet., Soc. Expl. Geophys., Expanded Abstracts, 1663-1666.

Zeng, H., Backus, M. M., Barrow, K. T., and Tyler, N., 1996, Facies mapping from three-dimensional seismic data: Potential and guidelines from a Tertiary sandstone-shale sequence model, Powderhorn Field, Calhoun County, Texas: AAPG Bulletin, **80**, 16-46.

Chapter 2

Rock physics properties of North Sea sedimentary rocks

2.1   Abstract

This chapter investigates the relationship between acoustic rock physics properties and different sedimentologic parameters, including grain texture, clay content, lithology, and diagenesis in North Sea sedimentary rocks. First, we analyze the effect of burial depth (diagenesis) on seismic properties. For a given lithology, porosity decreases with depth, causing velocity and density to increase. During shallow burial (0-2 km), porosity loss is mainly due to mechanical compaction. In this interval, velocity of sands tend to be lower than or similar to velocities of shales. Quartz cementation of sands initiates at ca. 2.0 km depth, within the Paleocene interval, and below this level sands have much higher velocity than shales.

The Paleocene interval represents the zone of our interest, and we study the relationship between rock physics and sedimentologic properties within this interval in more detail. We apply the technique of rock physics diagnostics (Dvorkin and Nur, 1996) to infer rock type and texture from velocity-porosity relations. Using such diagnostics, one can theoretically determine the amount of contact cement and non-cement pore-filling material. The result shows that the Paleocene turbidite sands occur either with slight contact cementation, or as completely uncemented and friable, yielding dramatically different seismic responses. These results are directly supported by thin-section observations and EDS (Energy Dispersive Spectroscopy) analysis. We also find that clay content and sorting affects the seismic properties of these turbidite sands, and

rock physics diagnostics can be used to quantify clay content and degree of sorting. For shales, we are able to quantify the silt content (i.e., small quartz grains). Finally, we apply rock diagnostics to discriminate other lithologies encountered within the Paleocene North Sea, including tuffaceous mudstone, limestone, and marl.
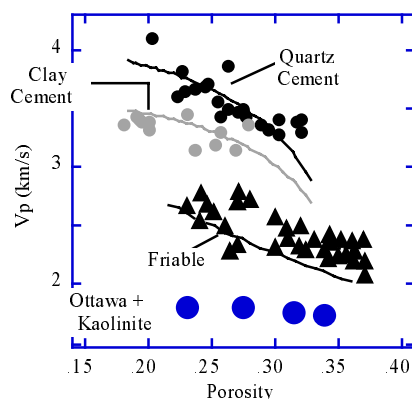
Figure 2.1: The elastic-wave velocity versus porosity for quartz- and clay-cemented North Sea sands, friable North Sea sands (the North Sea data and the models are discussed in Dvorkin and Nur, 1996), and hand-made Ottawa sand and kaolinite mixture (data from Yin et al., 1993). All data are for room-dry samples at 30 MPa differential pressure.

2.2   Introduction

The main goal of this chapter is to better understand the link between rock physics properties and sedimentologic reservoir properties such as clay content, sorting, texture, and diagenesis. Achieving this goal will improve the understanding and interpretation of seismic signatures. We examine how velocity-porosity relations are controlled by sedimentologic factors in North Sea rocks, focusing on turbidite sands and shales of Paleocene age. Relations between the acoustic rock properties and porosity allow one to infer porosity from seismic data, and these relations can also aid in pore-fluid detection. However, velocity-porosity relations may be complicated and we often observe a wide scatter of data points. Han (1986), Klimentos (1991), and Vernik and Nur (1992) explained this scatter in terms of clay content, fitting empirical models to sandstone data as a function of velocity, porosity, and clay content. In addition to clay content, diagenesis (i.e., cementation) is an important controlling factor in the relationship between porosity and velocity in sedimentary rocks. Jizba (1991) studied the effect of

cementation on rock physics properties of sandstones, Avseth and Mavko (1995) showed that the scatter observed in velocity-porosity data can be decomposed into depth-lines, while Dvorkin and Nur (1996) showed mathematically how cement could cause complexity in the velocity-porosity plane depending on cement location and mineral composition (Figure 2.1). Rock texture and lithology also greatly affect the observed scatter (e.g., Bryant and Raikes, 1995; Vernik, 1994; Anselmetti and Eberli, 1997).

We investigate the possibility of discriminating between these sedimentologic factors in the velocity-porosity plane for sedimentary rocks located in the Glitne and Grane turbiditic oil fields in the North Sea (see Appendix A). If we can make this distinction, then we can predict from seismic amplitude data, sedimentologic parameters other than porosity, such as lithology. One can also obtain more unique porosity predictions from seismic velocities, based on relationships that take into account local geology.

We first investigate the effect of depth of burial on the seismic properties of sands and shales, and how it affects the scatter in the velocity-porosity plane, using well-log data from different wells in two North Sea oil fields. We then apply the technique of rock physics diagnostics (Dvorkin and Nur, 1996) to well-log data from the Heimdal Formation sands, to study the effect of rock texture and cementation. This technique allows for quantification of various sedimentologic/diagenetic factors in terms of rock physics properties. It is applied by adjusting an effective-medium theoretical model curve to a trend in the velocity-porosity data, and then assuming that the microstructure is such as used in the model. By superimposing such model curves on cross-plots in the velocity-porosity plane, we can sort (*diagnose*) data into characteristic clusters.

Texture identification is crucial in the sands under examination, because the reservoir zone can produce drastically different seismic response depending on whether the sands are truly unconsolidated (friable) or have initial quartz cementation (i.e., poorly consolidated sandstones). Also, textural changes, if not properly identified, may be misinterpreted in seismic data as pore-fluid changes leading to serious reservoir characterization errors.

We expand on the texture identification and conduct rock physics diagnostics of other lithologies. Specifically, we study the effect of clay content in shaly sandstones, and how it alters existing clean sandstone models. Furthermore, we do rock physics diagnostics of

shales and show how one can quantify silt content from velocity and porosity. We also extend rock physics diagnostics to limestone, marls, and tuffaceous sediments. This extension of rock physics diagnostics to include other lithologies provides a tool for identification of lithofacies not represented in cored intervals (which usually only include sands) based on well-log measurements (i.e., sonic velocities and densities). This will aid in creating training data for later classification and prediction of seismic lithofacies (Chapters 3, 4, and 5).

2.3   The effect of depth of burial on the rock physics properties of sands and shales

2.3.1   Mechanical and chemical compaction and porosity reduction with depth

During burial, the acoustic properties of sedimentary rocks change dramatically due to diagenesis. Diagenesis represents the collective process that brings about change in sediments during burial and lithification, including mechanical, chemical and biological alterations (Boggs, 1987). Diagenetic processes change with burial depth, time (age), and/or temperature. The process most damaging to porosity and permeability during early burial is packing change and ductile grain deformation (Surdam et al., 1989). In the North Sea, this mechanical compaction dominates the diagenetic reduction of porosity during burial from 0 to 2.5-3 km (Ramm et al., 1992).

During progressive compaction of sandstone, the number of grain contacts and the area of contacts between grains increases. If the grains are spherically shaped and there are no ductile grains present, the intergranular volume of a sandstone may reduce from the initial very high values to about 26% (closest packing of spheres) (Graton et al., 1935). However, resistance to grain reorientation due to their angularity retards compaction. Sandstones with more ductile components, such as clay matrix, phyllitic rock fragments, and mica, undergo a more severe loss of porosity by mechanical compaction (Surdam et al., 1989).

Chemical compaction affects the porosity of rocks as well. In particular, quartz cementation is of great importance in quartz-rich sands, and drastically affects porosity,

permeability, and seismic properties. It may occur during shallow burial, associated with meteoric flow precipitation or diffusion (Bjørlykke, 1988; Dutton and Diggs, 1990), but is more common at deeper diagenetic levels associated with pressure solution. In quartz-rich sandstones, pressure solution and related quartz cementation is probably the process that is most important for porosity reduction during deep burial (Surdam et al., 1989). Sandstones in continuously subsiding sedimentary basins, such as in the North Sea and the Gulf Coast, are subject mainly to mechanical compaction and tend to have poorly developed quartz cement down to a depth of 2.5-3.0 km (Bjørlykke and Egeberg, 1993). Chemical compaction that occurs through pressure solution and quartz cementation will normally dominate porosity reduction below this depth level (Ramm and Bjørlykke, 1994). Lander and Walderhaug (1999) developed a numerical model of compaction and quartz cementation that provides a general method of porosity prediction in quartzose and ductile grain-rich sandstones in mature and frontier basins. They simulated compaction and cementation of North Sea Jurassic sediments from deposition to present depth of burial, and found that quartz cementation initiated at 2 km depth.

The presence of clay coating and abundant pore-filling clays in sandstones normally inhibits quartz cementation. Consequently, chemical compaction related to quartz cementation is most significant in clean sandstones. Quartz cementation is furthermore inhibited by the early migration of hydrocarbons, and/or overpressure (Dutton and Diggs, 1990).

Diagenesis of shales is restricted to mechanical compaction during shallow burial (at temperatures less than ~80 ^{0}C). The rate of shale compaction decreases with increase in burial (Magara, 1980). The rate of porosity decrease is rapid at shallow depths and slows at greater depth of burial. Eventually, pure shales tend to have a nearly constant porosity versus depth trend (Proshlyakov, 1960). This is because a stable clay fabric tends to develop in the early stages of burial, and remains unchanged during the subsequent burial history (Sintubin, 1994). Chemical proccesses in shales begin at an intermediate diagenetic level (80-140 ^{0}C), including the transformation of smectite to illite and liberation of organic acids from organic matter (Surdam et al., 1989).

2.3.2   Rock physics properties as a function of depth

Acoustic properties of rocks are greatly affected by both mechanical and chemical compaction. In general, for a given lithology, there will be an increase in seismic velocity with depth as porosity decreases and effective pressure increases. Effective pressure, that is approximately the difference between the overburden and pore pressure (Gangi, 1991; Gueguen and Palciauskas, 1994), normally increases with depth and causes the rock to mechanically compact. Another effect of increased effective pressure is the closing of microcracks and stiffening at grain contacts. This effect also contributes to the stiffening of a rock, without directly affecting the total porosity .
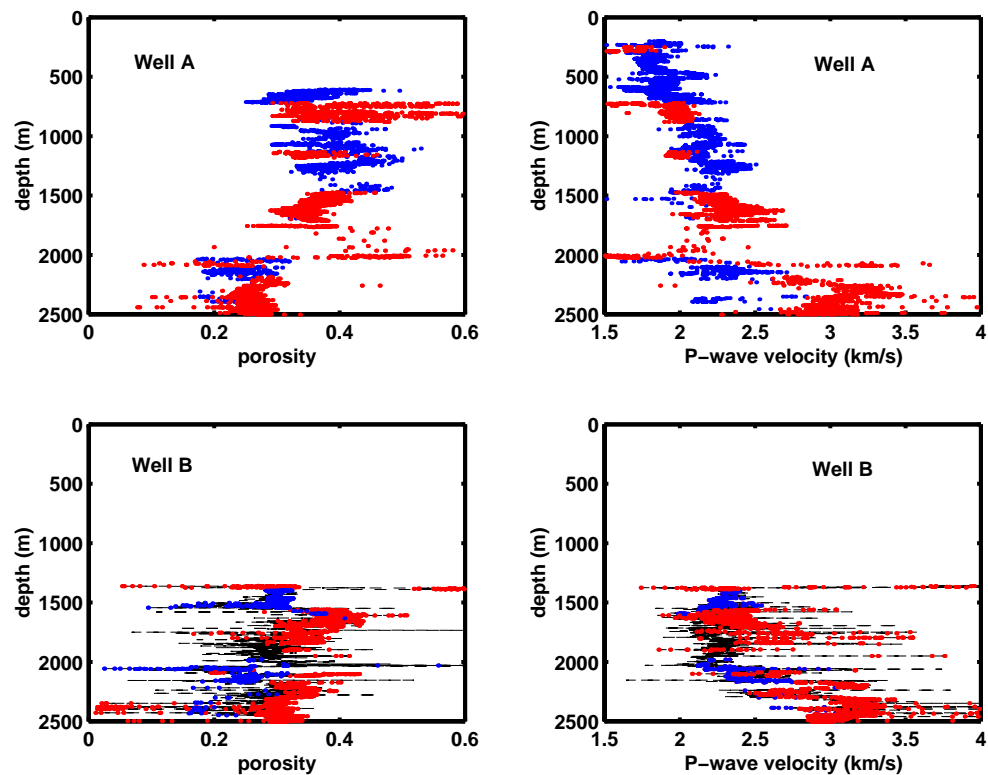
Figure 2.2: Porosity and P-wave velocity versus depth for two wells in the Glitne field, North Sea. Sandstone intervals are shown in red, shale in blue.

Figure 2.2 shows porosity and P-wave velocity data from two wells, Well A and Well B, located in the Glitne field in the South Viking Graben. Porosity is calculated from density logs. Clean sands and pure shales were interpreted based on completion log

observations and gamma ray values. The porosities of the sands and shales gradually decrease with depth. The P-wave velocity in shales also gradually increases with depth. In the sands, on the other hand, there is a pronounced jump in the velocity occurring at about 2000 m.
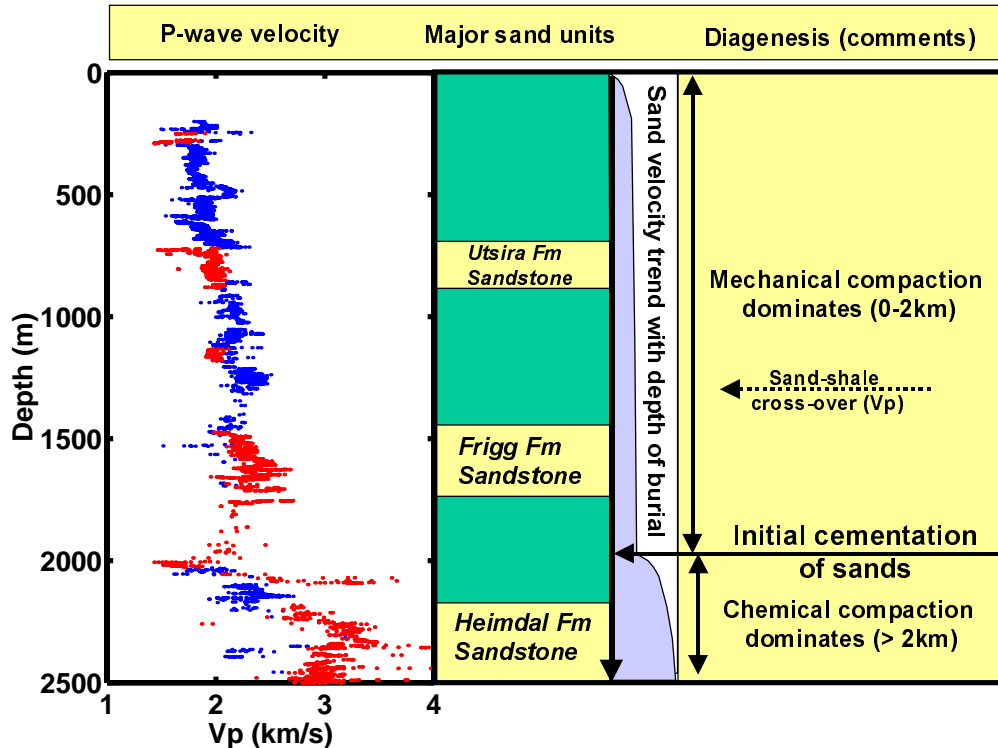
Figure 2.3: Sonic velocity versus depth for sands (red) and shales (blue) in a North Sea well (Well A) penetrating 2500 m of sediments, including three major sand units. The velocities in the Heimdal sands are much higher than in the Frigg and Utsira sands. Mechanical compaction alone cannot explain this sharp increase. It is likely that this increase is due to chemical compaction. This conclusion is confirmed in the rock physics diagnostics in section 2.5.

Figure 2.3 shows the sonic velocity versus depth trends for relatively clean sandstones (red) and relatively pure shales (blue). The data are from the interval between the sea floor and rocks of Paleocene age (Tertiary) in Well A. Three major sand units are identified, representing the Utsira Formation (at ca. 800 m depth), the Frigg Formation (at ca. 1600 m) and the Heimdal Formation (at ca. 2200 m). The Utsira sands have slightly lower velocities than the overlying shales, whereas the Frigg Formation has slightly higher velocities than the overlying shales. The Heimdal Formation sands have much higher velocities than the shales that cap them. This dramatic increase in velocity with depth for sands of the Heimdal Formation can not be explained by purely mechanical

compaction and corresponding porosity reduction with depth. Purely mechanical compaction would have resulted in a gradually increasing velocity, and a decreasing velocity gradient with depth, as observed in the shales. The jump in velocity observed in the Heimdal sands, however, can be explained by chemical compaction. These sands most likely have slight quartz cementation, which produces a velocity increase through a stiffening effect on the grain contacts. The onset of cementation is interpreted to occur at about 2 km depth. We assume that mechanical compaction dominates above 2 km, whereas quartz cementation dominates below this depth. This interpretation fits with the simulation results of Lander and Walderhaug (1999) mentioned in section 2.3.1. In section 2.5.1, we do thin-section and SEM analysis of the Heimdal Formation sands and confirm that some of the sands have slight quartz cementation.

Another interesting observation from the velocity versus depth trends, is the cross-over in velocity between sands and shales occurring at ca. 1400 m. Still, the overall velocity contrasts between sands and shales in the mechanical compaction zone (0-2 km) are relatively weak. We do not observe a strong contrast in velocity between sands and shales until the sands enter the chemical compaction zone. The transition from mechanical to chemical compaction therefore represents a very significant seismic boundary in the North Sea.

By cross-plotting velocity versus porosity for various sand and shale intervals at different depths, we can evaluate the progress of diagenesis and compaction of the rocks (Figure 2.4). We analyze velocity-porosity data for sand intervals and their overlying shales at four different depths, using data from Wells A and B. The sandstone intervals include the Utsira sands (called Sst 800 in Figure 2.4) where data range from 820-830 m (Well A), the Frigg sands (Sst 1500) from 1500-1600 m (Well A), a nameless sand interval (Sst 1800) from 1833-1843 m (Well B), and the Heimdal sands, including Sst 2200(a) (Well A) from 2172-2220 m, and Sst 2200(b) (Well B) from 2250-2350 m. The shale intervals include Shale 650 (Well A) ranging from 620-670 m, Shale 1400 (Well B) from 1400-1500 m, Shale 1800 (Well B) from 1805-1825 m, and Shale 2100 (Well B) spanning the interval from 2120-2150 m. The various sand intervals create separate data clusters in an enechelon pattern, with overlapping yet decreasing porosity values, but discrete jumps and great separation in velocity. These velocity jumps can be attributed to

the increasing depth, which causes an increase in effective pressure and stronger mechanical and chemical compaction, as discussed above. The individual sand clusters at given depths show relatively constant or slowly increasing velocities with decreasing porosities. According to rock physics diagnostics introduced below in section 2.4, this variation is related to deteriorating sorting and/or increased clay content in the sands.

The cross-plot in Figure 2.4 also shows the velocity-porosity "pathways" as we proceed from a relatively clean sand to pure shale. At shallow depths, the path is fairly flat, with not much of velocity contrast between sands and shales. With increasing depth, the contrast in velocity between sands and shales increases dramatically, mainly due to the quartz cementation of sands.
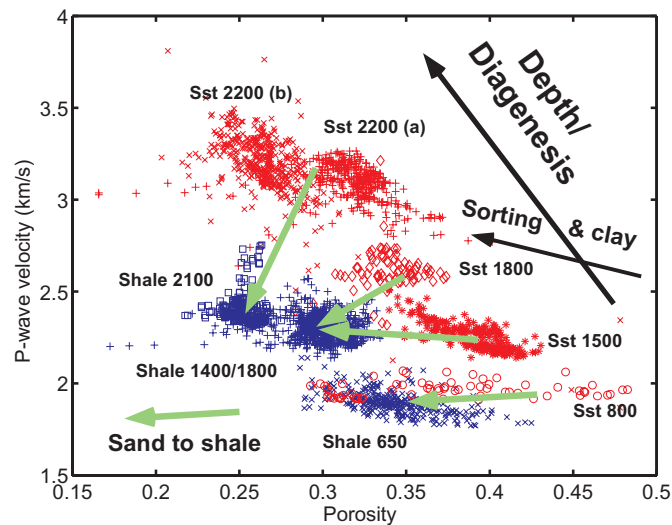
Figure 2.4: Velocity-porosity cross-plot for sands (red) and shales (blue) at different depth levels in the North Sea (data taken from Well A and Well B). The porosity ranges overlap between sand clusters at different depths, and between sands and shales. Velocity, however, shows a separation between sands at different levels. The velocity contrast between sands and shales is very weak for the shallow depth of burial, but increases with depth.

Figure 2.5 shows three of the sand and shale clusters. The paths assumed to represent increasing clay content from clean sands to pure shales, are superimposed. We observe overturned V-shape paths at all depth levels. At the shallowest level, the V-shaped path is highly compressed. The sands overlap with the shales probably because this sand cluster includes both clean and shaly sands, whereas the shales are both pure and sandy. The whole clay content spectrum is therefore represented in the data. With increasing depth,

the V-shape path is less compressed. This is consistent with Yin's (1992) laboratory observations, where he measured pressure dependent velocity and porosity in sand-shale mixtures. At the greatest depth, there is a large drop in velocity from the shaly sands to the pure shales. This drop is related to the effect of proceeding from grain supported to clay supported sediments under relatively high effective pressure (Marion, 1990). In the case under examination, the velocity difference is further amplified because the sands are slightly cemented.
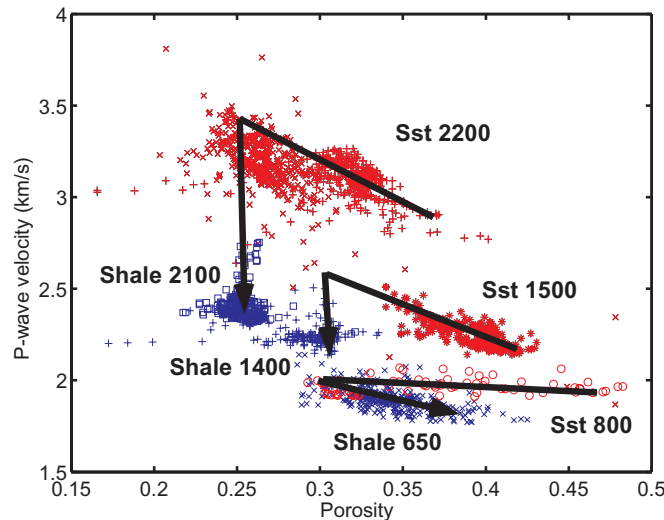
Figure 2.5: Velocity-porosity cross-plot for sands (red) and shales (blue) at different depth levels in the North Sea (data taken Well A and Well B), with superimposed paths that correspond to gradually increasing clay content, from clean sands (0% clay) to pure shales (100% clay).

2.4   Rock physics diagnostics — theory and models

Rock physics diagnostic was introduced by Dvorkin and Nur (1996) as a technique to infer rock microstructure from velocity-porosity relations. Such diagnostic is conducted by adjusting an effective-medium theoretical model curve to a trend in the data, assuming that the microstructure of the sediment is such as that used in the model.

2.4.1   Clean sands

Dvorkin and Nur (1996) introduced two theoretical models for high-porosity sands (see model curves in Figure 2.6). The *friable-sand model,* or the "unconsolidated line",

assumes that porosity reduces from the initial sand-pack value due to the deposition of the solid matter away from the grain contacts. The unconsolidated line is represented by the modified lower Hashin-Shtrikman (MLHS) model (see Appendix B; Hashin and Shtrikman, 1963; Dvorkin and Nur, 1996), and connects the critical porosity end-point ($\phi \approx 0.4$) and the pure mineral end-point ($\phi = 0$). The velocity near critical porosity is determined by the Hertz-Mindlin theory (Mindlin, 1949), whereas the mineral end-point is defined by the elastic moduli of the mineral, in our case quartz (K_{qz} = 36.8 GPa and G_{qz} = 44 GPa, where *K* and *G* are the bulk and shear moduli, respectively). The porosity reduction between these points will be a gradual stiffening of the rock, as smaller grains fill the pore-space between the larger grains. For a clean sandstone, this porosity reduction is caused by deteriorating sorting (depositional), grain crushing (mechanical compaction) and/or packing (depositional and compactional). This non-contact additional solid matter weakly affects the stiffness of the rock.

During burial of a sandstone, the rock is also likely to become cemented. This cement may be diagenetic quartz, calcite, albite, or other minerals. Cementation produces a strong stiffening effect, because it acts to weld grain contacts. The *contact-cement model* assumes that porosity reduces from the initial porosity of a sand pack due to the uniform deposition of cement layers on the surface of the grains. The contact cement dramatically increases the stiffness of the sand by reinforcing the grain contacts. In particular, the initial cementation effect will cause a large velocity increase during a small porosity decrease. The mathematical formulation of the contact-cement model is given in Appendix B.

We introduce another, *constant-cement* model, which assumes that sands of varying porosity all have the same amount of contact cement. Porosity variation within this group of sands is solely due to non-contact pore-filling material (e.g., deteriorating sorting). Mathematically, this model is a combination of the contact-cement model, where porosity reduces from the initial sand pack porosity to porosity, ϕ_b, due to contact cement deposition, and the friable-sand model where porosity reduces from ϕ_b due to the deposition of the solid phase away from the grain contacts (Figure 2.6). Considering a given reservoir, this is the most likely scenario, because the amount of cement is often

related to depth, whereas sorting is related to lateral variations in flow energy during sediment deposition. However, it is possible that cement has a local source, and therefore it may cause a considerable lateral variation in velocity.
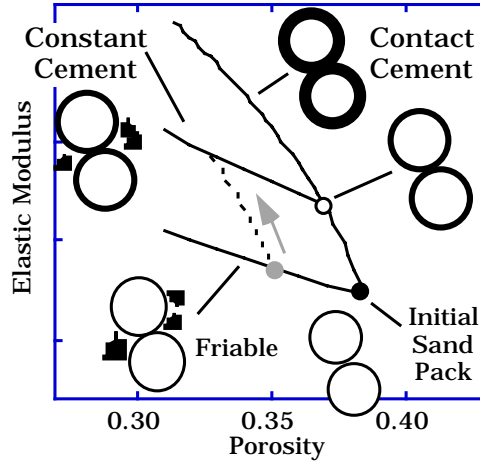
Figure 2.6: Schematic depiction of three effective-medium models for high-porosity sands in the elastic-modulus-porosity plane. The elastic modulus may be compressional, bulk, or shear.

To use the constant cement model, one must first adjust the initial-cement porosity, ϕ_b, that corresponds to the point shown as an open small circle in Figure 2.6. The dry-rock bulk and shear moduli at this porosity (K_b and G_b, respectively) are calculated from the contact-cement model (see equations in Appendix B). Equations for the dry-rock bulk (K_{dry}) and shear (G_{dry}) moduli at a smaller porosity, ϕ, are:

$$K_{dry} = (\frac{\phi / \phi_b}{K_b + 4G_b / 3} + \frac{1 - \phi / \phi_b}{K_s + 4G_b / 3})^{-1} - 4G_b / 3,$$

$$G_{dry} = (\frac{\phi / \phi_b}{G_b + z} + \frac{1 - \phi / \phi_b}{G_s + z})^{-1} - z, \; z = \frac{G_b}{6} \frac{9K_b + 8G_b}{K_b + 2G_b}.$$

(2-1)

Here, K_s and G_s are the bulk and shear moduli of the mineral phase, respectively. The effect of pore fluid can be accounted for by using Gassmann's (1951) equations. Notice

that it is possible to arrive at the constant-cement line by first moving along the friable-sand line and then adding contact cement to the rock (dashed line in Figure 2.6). This path would correspond to the onset of cementation following deposition, which represents the true geologic path.

2.4.2 Shaly sands

The constant cement fraction lines can also be applied to shaly sands. Instead of filling the pore space between larger grains with smaller quartz grains, we assume that clay particles represent the pore filling material. The clay minerals are likely located in the pore space between quartz grains and cement, completely surrounded by the quartz during the entire compaction process, leading to stiff effective mineral moduli (Figure 2.7). Hence, we assume the bulk (K) and shear (G) moduli of the zero-porosity composite mineral to be given by the Voigt average equations.:

$$K_{s\_eff} = f_{qz} \cdot K_{qz} + f_{clay} \cdot K_{clay} \ , \qquad (2\text{-}2)$$

and

$$G_{s\_eff} = f_{qz} \cdot G_{qz} + f_{clay} \cdot G_{clay} \ , \qquad (2\text{-}3)$$

where f_{qz} is the fraction of quartz and f_{clay} is the fraction of clay in the solid phase. K_{qz}, the bulk mineral modulus of quartz, equals 36.8 GPa, whereas G_{qz}, the shear mineral modulus of quartz, is 44 GPa. The mineral moduli of clays are highly variable. We assume the clays to be a smectite/illite mixture typical for North Sea Tertiary shales and inter-bedded mudstones (Dypvik, 1983; Pearson, 1990; Bjørlykke and Aagaard, 1992). Hence, we use the values calculated by Brevik (1996) based on a large data base of wireline logs from the North Sea: $K_{clay} = 17.5$ GPa and $G_{clay} = 7.5$ GPa.
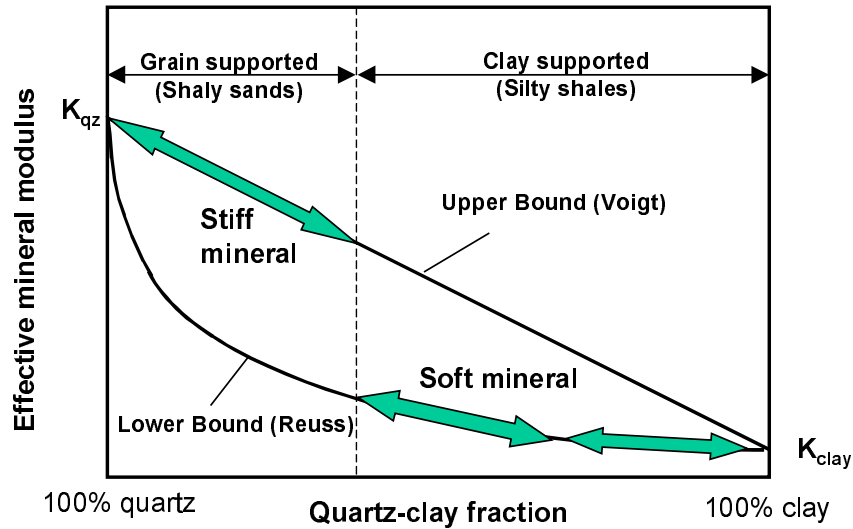
Figure 2.7: Schematic plot of effective compressional mineral modulus (i.e., end-point values at zero porosity) as a function of quartz-clay fraction. We assume that the effective compressional mineral modulus in shales is given by the Reuss lower bound ("soft mineral"), whereas in shaly sands it is given by the Voigt upper bound ("stiff mineral"). The same assumptions are made for the effective shear mineral modulus.

2.4.3   Shales

In general, shales are mixtures of clay-sized particles, consisting primarily of clay minerals, and silt particles, which are mostly quartz and feldspar. Krynine (1948) estimated the "average" shale to be about 50% silt, whereas Pettijohn (1975) and others suggested that shales average about 65% silt.

In shales, silt grains are suspended in the clay matrix. Furthermore, shales are normally not cemented at shallow to intermediate diagenetic levels (0-3.5 km). Therefore, shales can be easily modeled using the unconsolidated line. The depositional porosity (i.e., critical porosity) is very high (60-80%) due to the "card-stack" arrangements of clay platelets (Riecke and Chilingarian, 1974). We assume that all silt grains are quartz and that they are suspended in the clay matrix even at the zero-porosity end-member. This results in a soft effective mineral moduli (see Figure 2.7), which can be calculated using the Reuss average equations:

$$\frac{1}{K_{s\_eff}} = \frac{f_{qz}}{K_{qz}} + \frac{f_{clay}}{K_{clay}}, \qquad (2-4)$$

and

$$\frac{1}{G_{s\_eff}} = \frac{f_{qz}}{G_{qz}} + \frac{f_{clay}}{G_{clay}},$$ (2-5)

where the input parameters are the same as given for the shaly sands effective mineral moduli.

2.4.4 Carbonates

The porosity reduction processes in carbonate rocks are different from those described for sands and shales (e.g., Anselmetti and Eberli, 1997). Chemical diagenesis plays a much more important role in carbonates than it does for sands and shales at the depths of this study (~ 2 km).

Limestone has a mineral compressional modulus, K_s, of 76.8 GPa, and a mineral shear modulus, G_s, of 32 GPa (Mavko et al, 1998). Critical porosity can greatly vary, and it represents an uncertain parameter in the rock physics modeling of limestones. However, we assume that the limestone is granular at deposition with a critical porosity of 0.4, a typical value for granular media (e.g., Nur et al., 1998). We choose to apply both lower and upper modified Hashin-Shtrikman bounds, as we expect a broad range of porosity trends in this type of rock, representing both soft and stiff types of porosity.

Marls are shaly sediments in which particles of carbonate are suspended in the clay matrix (Shumann, 1989). Hence, this rock can be modeled in the same way as shales (eq. 2.4 and 2.5), where the mineral moduli are effective values calculated from the fractions of clay and calcite.

2.4.5 Tuffs and tuffaceous sediments

Tuffs are volcanic ash-fall and ash-flow deposits, and are abundant in the Tertiary interval of the North Sea subsurface. In both ash-fall and ash-flow deposits there is usually a mix between the tuff and siliciclastic sediments, referred to as tuffaceous sediments. The rock physics diagnostics of tuffaceous muds are represented by a modification of the shale diagnostics, where the mineral moduli are effective values from

the fractions of tuff and clay. However, the mineral moduli of tuff are very uncertain. We assume the same values as quartz, as tuffs normally contain high percentages of volcanic glass, which are again comprised of small crystals of mainly quartz and feldspar (Schumann, 1989). Hence, we expect tuffaceous muds to behave similar to silty or sandy shales in terms of seismic properties.

2.5   Rock physics diagnostics of North Sea turbidite systems

We apply the rock physics models above to diagnose rocks of Paleocene age in the North Sea. We use data from two wells, Well #1 and Well #2, located in two different oil fields in the Southern Viking Graben, North Sea. Well #1 is located in the Glitne field, the same field as Well A and Well B used in section 2.3. Well #2 is from the Grane field located about 100 km Northeast of the Glitne field (see map in figure A.1, Appendix A). The Paleocene interval is comprised of mostly pelagic/hemipelagic shales and turbidite sandstones, but volcanic tuffs, marls, and limestones are also present. The Paleocene sands encountered in both the Glitne and Grane areas are referred to as the Heimdal Formation, and hence represent the same stratigraphic level, yet separate turbidite systems.

2.5.1   Diagnosing clean sands

Diagnosing microstructure from well-log data

The gamma-ray and P-wave velocity log curves for the two wells under examination are shown in Figure 2.8. In Well #1, we observe a great variability in clay content causing a very heterogeneous pattern of intercalating sands and shales. Only a relatively thin (10 m) sand interval (gray bar in Figure 2.8a) is identified as a practically clay-free reservoir sand. In Well #2, unlike in Well #1, a thick oil-saturated sand interval (gray bar in Figure 2.8c) is marked by extremely low and constant (about 55 API) gamma-ray readings and high P-wave velocity (about 3 km/s). This sand layer is surrounded by shale packages whose gamma-ray and velocity strongly contrast those of the reservoir zone sand. Well #2 is slightly deviated (26 degrees), and the measured depth in this well therefore exceeds the true vertical depth. Consequently, the observed sand thickness in Well #2 is slightly

thicker than the true thickness. As mentioned, the clean sand zones in both wells represent the same stratigraphic unit, although located at different depths and in separate oil fields.

The velocity difference between the reservoir zones in the wells under examination is emphasized in Figure 2.9 where the P-wave velocity is plotted versus porosity. In the same porosity range, with similar gamma-ray count and close oil saturation, the velocity in Well #2 exceeds the velocity in Well #1 by about 500 m/s.
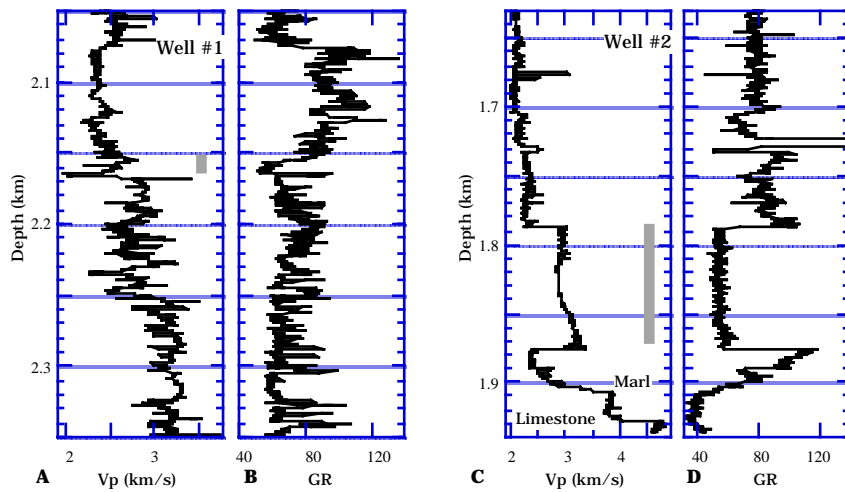
Figure 2.8: Gamma-ray and P-wave velocity curves for Well #1 and Well #2. The investigated clean sand intervals are marked by gray vertical bars.
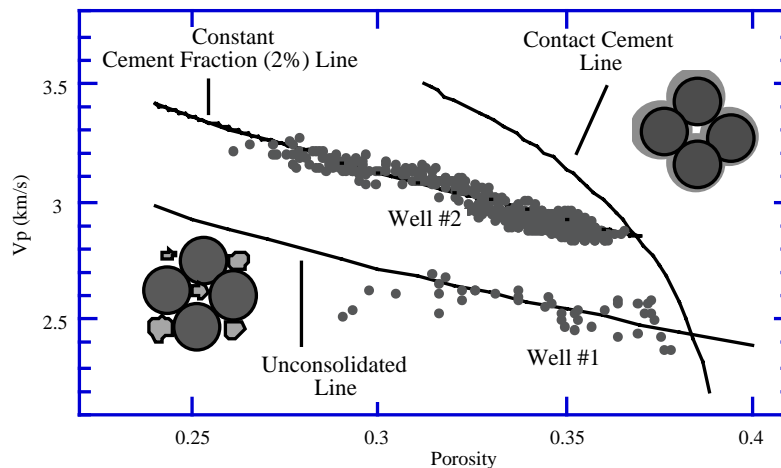
Figure 2.9: P-wave velocity versus porosity for the pay zones in Well #1 and Well #2 with model curves superimposed. Porosity is calculated from bulk density.

In order to understand the reason behind the observed velocity difference in the two wells, we superimpose the model lines on the velocity-porosity cross-plot in Figure 2.9. The three curves come from the contact cement, constant cement, and friable sand models. The solid is assumed to be pure quartz; the porosity of the initial sand pack is 39%, and the initial-cement porosity, ϕ_b, is 37% (the latter corresponds to contact cement occupying about 2% of the pore space of the initial sand pack).

The rock diagnostics shown in Figure 2.9 implies that the sands in Well #2 have little initial contact cementation. The porosity decrease from the initial-cement porosity is likely to be due to deteriorating sorting (smaller grains fall in the pore space between larger grains and have a large effect on the velocity). The reservoir zones sands in Well #1 appear to lack any contact cementation, with porosity reducing from the initial sand-pack porosity due to deteriorating sorting.

Mud filtrate invasion and saturation effects

Potentially, the trends observed in our cross-plots could be influenced by variation in pore fluid, as the thick-bedded, clean reservoir sand units identified in Well #1 and Well #2 are both saturated with oil. The shallow and deep resistivity logs available for Well #1 (Figure 2.10) indicate invasion of water (i.e., mud filtrate) in the shallow zone. The density logs from both Well #1 and Well #2 measure in the mud filtrate invaded zone as confirmed by calibration to the helium measurements (Figures 2.11 and 2.12). The density porosities are calculated using the following formula:

$$\phi = \frac{(2.65 - \rho_b)}{(2.65 - \rho_{fl})}, \tag{2-6}$$

where the mineral density is assumed to be 2.65 g/cm^3 (i.e., quartz), ρ_b is the density log value, and ρ_{fl} is the value we invert for in the calibration with the helium porosities, representing the density of the pore fluid. The density of oil in the area is approximately 0.8 g/cm^3, while mud-filtrate density is approximately 1.05 g/cm^3.
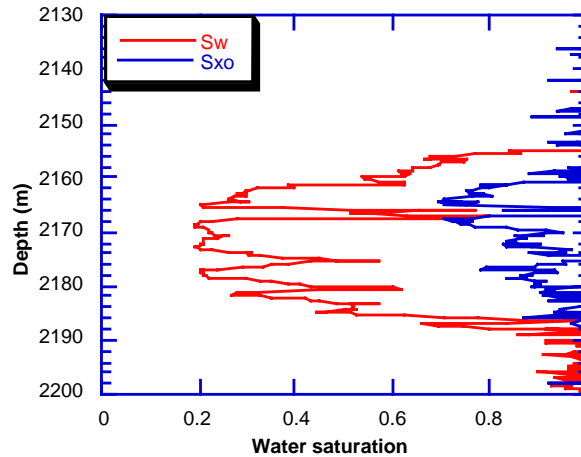
Figure 2.10: Saturation curves derived from resistivity logs in the reservoir zone of Well #2, indicating the effect of mud filtrate invasion. Sw is water-saturation in the reservoir. The oil-saturation of the reservoir equals 1-Sw. Sxo is the water-saturation in the invaded zone. The residual oil saturation in the invaded zone equals 1-Sxo. The shallow zone is saturated with 80-100% water (i.e., mud filtrate), whereas the reservoir itself has an oil saturation of 40-80%.

Helium porosity measurements are not available in the friable sand zone (2154-2165 m) in Well #1, because the unconsolidated nature of the sands did not allow for core sample acquisition. Helium porosity measurements are only available in the plane-laminated thick sand unit (2167-2184 m), residing just below the friable sand unit in Well #1. The density derived porosities match the helium porosities when we use a pore fluid density of 1.09 g/cm^3. The oil saturation and mud filtrate invasion effect is fairly constant throughout the reservoir zone in Well #1 (Figure 2.10), and we assume that the density log measures the mud filtrate invaded zone for the whole reservoir, even in the friable zone. For the reservoir zone in Well #2, the oil-water contact is located at 1845 m (measured depth; 1845 m measured depth equals 1765 m true vertical depth). However, throughout the whole reservoir, we get a perfect match between helium porosities and density porosity values using a pore fluid density of 1.05 g/cm^3, which indicates that also in the oil zone of this well the density log measures the invaded zone. We have no direct proof that the velocity logs measure the invaded zone for these wells, but the perfect match between the velocity-porosity data of the unconsolidated sand unit in Well #1 and the unconsolidated line in Figure 2.9 was obtained assuming mud filtrate as pore fluid. We therefore assume that the velocity log in Well #1 measures the same zone as the

density log, that is the mud filtrate invaded zone. We also assume that the velocity log in Well #2 measures the same zone as the density log, giving values representative of mud filtrate saturation.
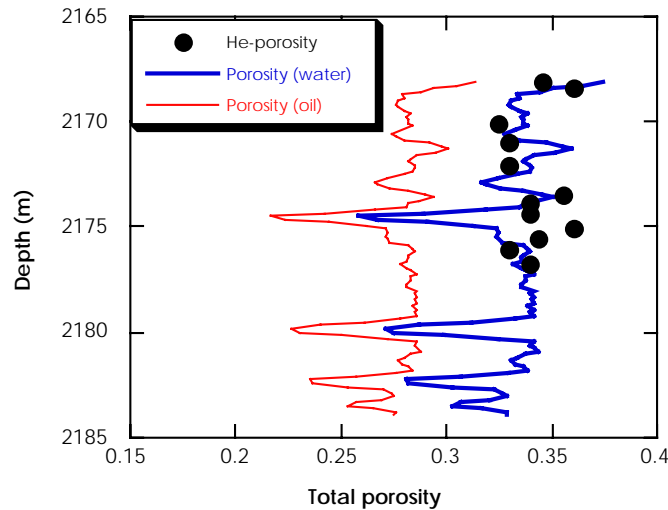
Figure 2.11: Porosity logs derived from the density log in oil zone of Well #1 (laminated sand interval, where helium porosity measurements are available). If we assume oil density of the pore-fluid (0.8 g/cm^3), the porosity log shows too low values compared to the helium porosity measurements. Assuming a pore fluid density 1.09 g/cm^3, the porosity log matches with the helium porosities. This proves that the formation is invaded by mud filtrate in the zone measured by the density tool.
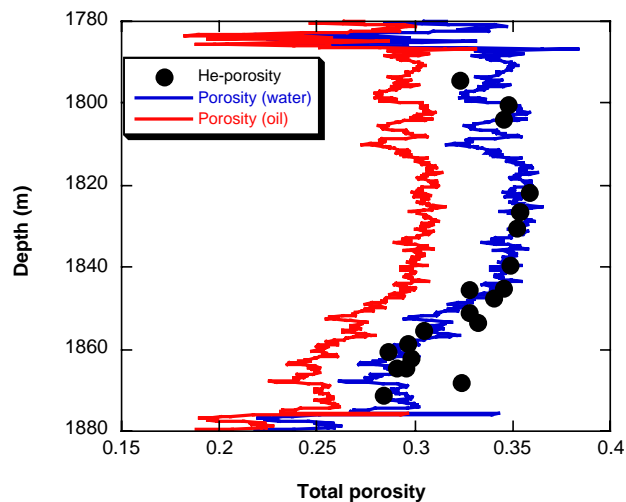
Figure 2.12: Porosity logs derived from the density log in the reservoir zone of Well #2. A pore fluid density of 1.05 g/cm^3 yields a perfect match between the density derived porosity and the helium porosities. This proves that the formation is invaded by mud filtrate in the zone measured by the density tool.

Implications for seismic response

To understand how the type of sand (unconsolidated versus cemented) affects the seismic response, we analyze the offset dependent reflectivity in CDP gathers at the well locations. This procedure is referred to as AVO (Amplitude Versus Offset) analysis and has been described in detail by Ostrander (1984), Shuey (1985) and Castagna (1993), among others. Part of the theory behind AVO is furthermore included in Chapter 4.
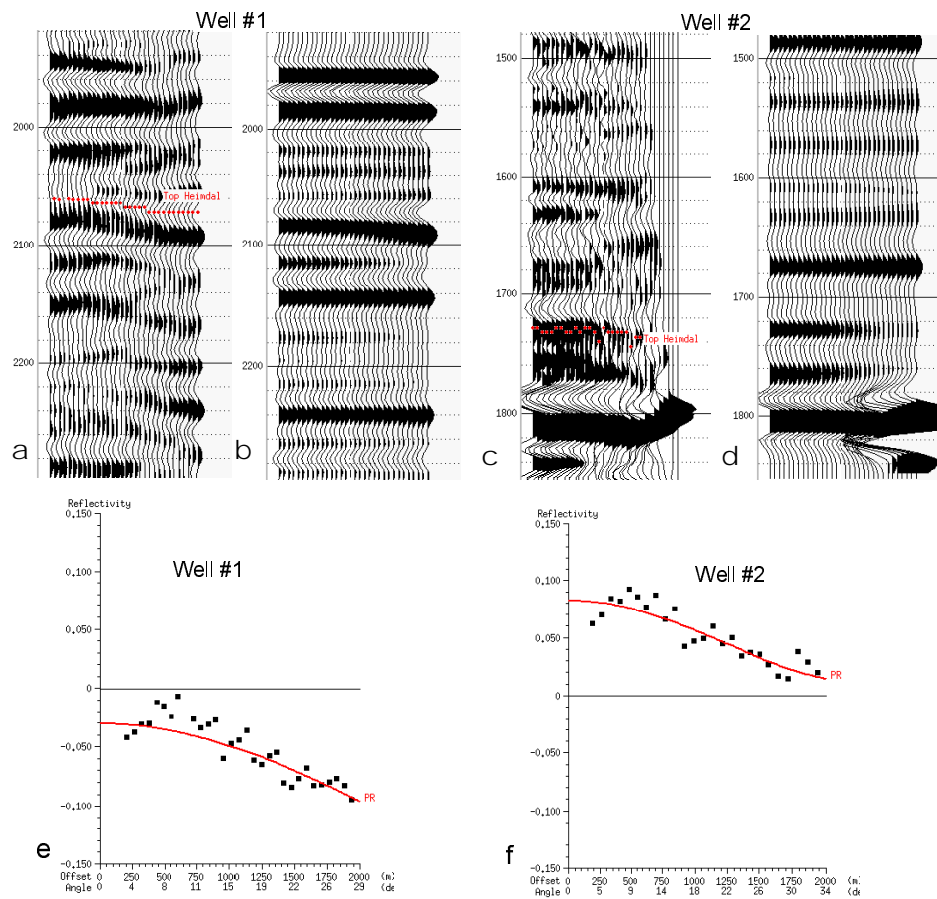
Figure 2.13: Top. Real (a and c) and synthetic (b and d) CDP gathers. In synthetic gathers, the AVO effect was modeled only at the target zones. Bottom. Real reflectivity versus offset and angle (symbols) and theoretical Zoeppritz lines

Figure 2.13a shows the real CDP gather at Well #1 where the picked horizon is at the top of the Heimdal Formation. Figure 2.13b shows a synthetic CDP gather for this well where the input parameters (Vp, Vs, and density) came from the well-log measurements. This synthetic gather was produced using a 30 Hz zero-phase Ricker wavelet. The

reflectivity is plotted versus offset (angle) in Figure 2.13e with the theoretical Zoeppritz line superimposed. The contrast in seismic properties at the shale-sand interface produces a relatively weak and negative zero-offset reflectivity that becomes increasingly negative with offset.

Contrary to Well #1, the top of the Heimdal Formation in Well #2 (which is capped by elastically similar shales) produces a strong positive reflector with reflectivity decreasing with increasing offset. The synthetic section shows a similar response (Figure 2.13d). For Well #2, the reflectivity is plotted versus offset (angle), together with the theoretical Zoeppritz line, in Figure 2.13f.

The observed significant difference in the seismic response between Well #1 and Well #2 is clearly due to the difference in sand texture (cemented versus friable). The fact that the synthetic response is very close to the real data in both wells means that we can rely on well-log-based rock diagnostics to predict seismic response.

Confirming the sandstone diagnostics from thin-section and SEM-analysis
Quartz cementation

Thin sections of samples from both reservoir zones are shown in Figure 2.14. The porosity of both samples is about 35%, and they are predominantly composed of quartz. No contact cementation is apparent in either of the images. The Well #1 image (on the left), unlike the image from Well #2 (on the right), shows clay coating (black) around quartz grains.
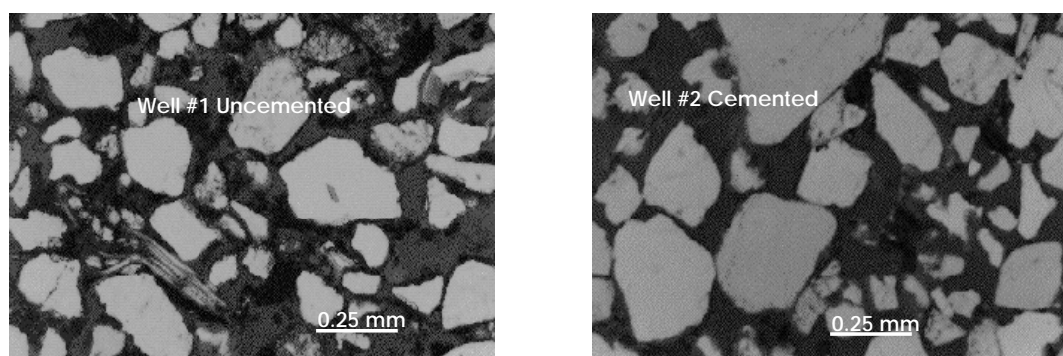
Figure 2.14: Thin sections of two selected samples from the reservoir zones of Well #1 (left), taken at 2154.0 m, and Well #2 (right), taken at 1800.25 m.

The presence of contact cement in Well #2 reveals itself in a SEM (Scanning Electronic Microscope) image in Figure 2.15. Not detectable in the back-scatter light, it shows as a dark rim around a light grain in cathodoluminescent light. Energy Dispersive Spectroscopy (EDS) analysis, an X-ray analysis method, shows that both the grain and cement are pure quartz (Figure 2.16). The hexagonal crystal shapes in the upper left corner in Figure 2.15 are also typical for overgrowth cementation. These shapes are observed throughout the reservoir zone in Well #2 (Figure 2.17). No cement rims or hexagonal crystal shapes have been found in the sand interval from Well #1.
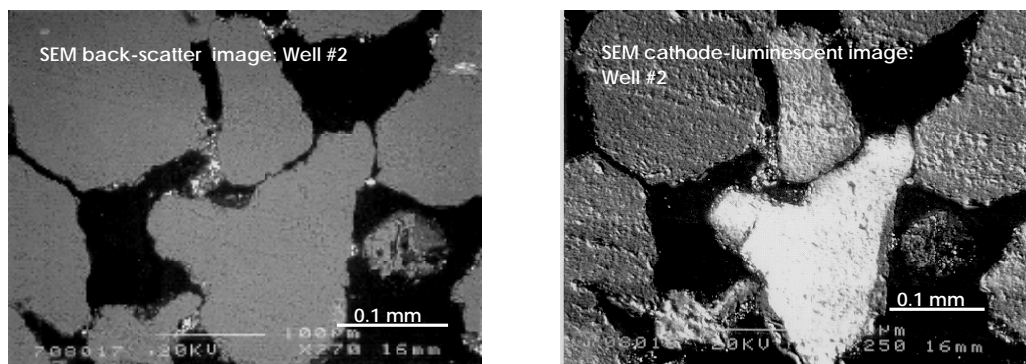
Figure 2.15: SEM images of a Well #2 sample (1800.25 m) in back scatter light (left) and cathodoluminescent light (right).
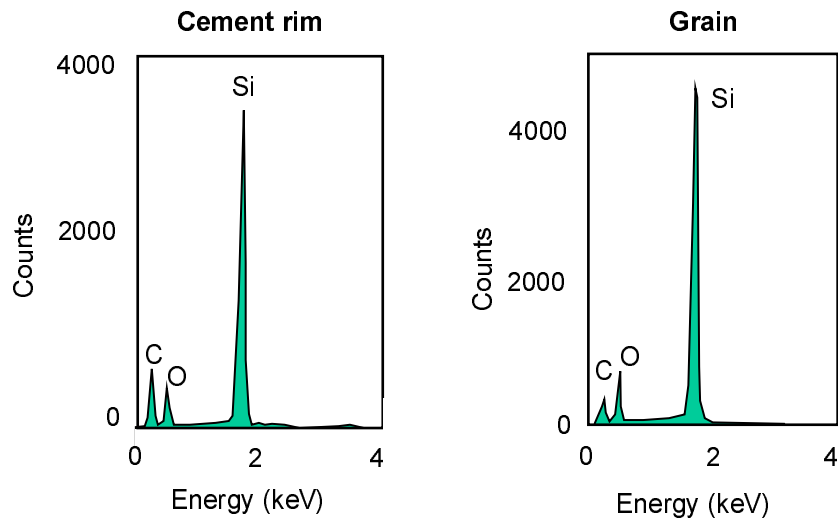
Figure 2.16: EDS spectrograms of cement rim (left) and grain (right) observed in the cathodoluminescent SEM image in Figure 2.15, confirming that both the grain and the cement is quartz, SiO_2. The carbon peak (C) is from the preparation of the sample.
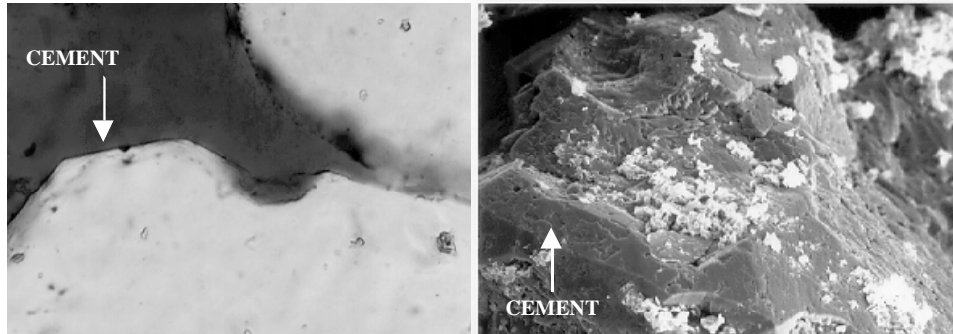
Figure 2.17: A thin section (left) and a SEM image (right) of grains with crystal cement shapes from different depths (1800.25 m and 1818.0 m, respectively) in the reservoir zone in Well #2.

EDS analysis of the clay coating (Figure 2.18) shows presence of pyrite (FeS) which is likely associated with organic matter (Johannes Rykkje, pers. comm.; Boggs, 1987). The high Si peak is related to interference between coating and the quartz grain. The peaks of Al, Si and K can reflect remnants of dissolved K-feldspar, or illitized kaolinite. Also we identify mineral signatures typical for mixed smectite/illite (Al, Si, and K, with traces of Mg and Cl). The clay and organic matter that coat the sand grains can explain why the sands in Well #1 are not cemented, as clay coating tends to inhibit quartz cementation.
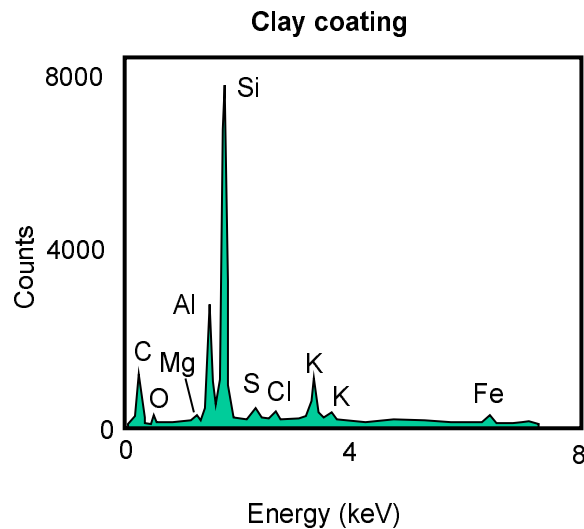
Figure 2.18: EDS spectrogram of clay coating observed in thin-section image in Figure 2.14 (Well #1), showing presence of pyrite (FeS), indicative of organic matter. The aluminum (Al), potassium (K) and magnesium (Mg), together with silicon (Si) and chlorine (Cl), are indicative of mixed smectite-illite clays and/or illitized kaolinite.

The thin-section analysis thus confirms the result of our mathematical rock diagnostics. Consistent with this conclusion is also the fact that the cores extracted from Well #1 are piles of loose sand, whereas those from Well #2 support external stress. This structural integrity of the samples from Well #2 is apparently due to the binding effect of contact quartz cement.

Sorting variation

According to the diagnostics, the clean sands in Figure 2.9 have decreasing porosity with deteriorating sorting. We do an extensive thin-section analysis throughout a sand-interval for Well #3, representing the same reservoir sands as in Well #2 (thin-sections prepared for sorting analysis were not available in Well #1 or Well #2). Figure 2.19 shows Vp and density-porosity in Well #3. We observe almost mirror-shaped patterns in the Vp and density-porosity logs. Thin-section analyses show that clay and cement content is consistently close to zero (Ramm et al, 1992), so the porosity and velocity changes in this sand unit should be attributed to rock texture and grain size variation, presumably due to sorting.
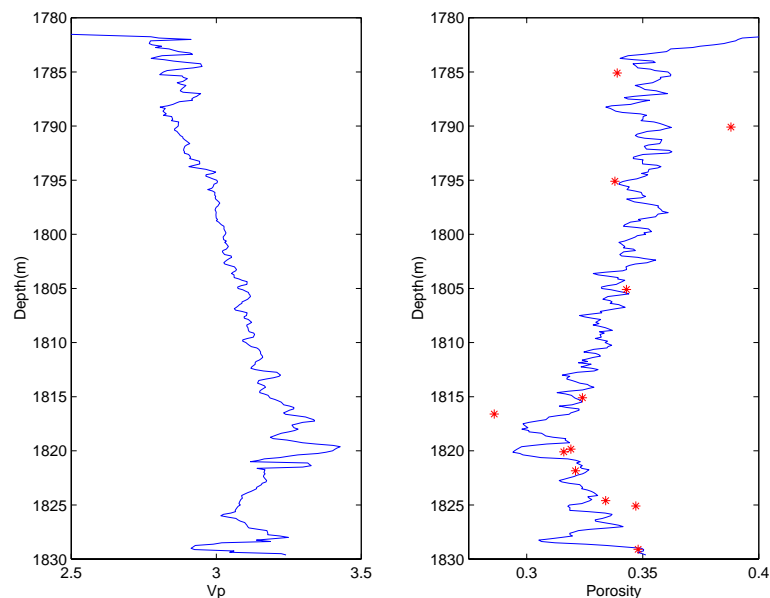
Figure 2.19: P-wave velocity and density-porosity versus depth in Well #3. Note how the porosity trend is almost a perfect mirror-shape of the velocity trend. Star symbols (*) represents helium porosities, at the locations where thin-sections are analyzed.
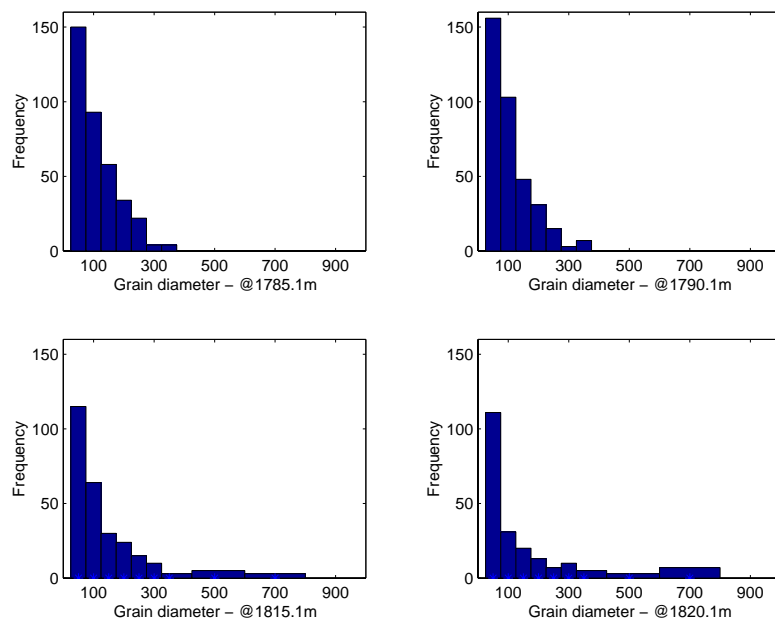
Figure 2.20: Histograms of grain size distribution from different depth locations throughout the sand unit in Well #3.
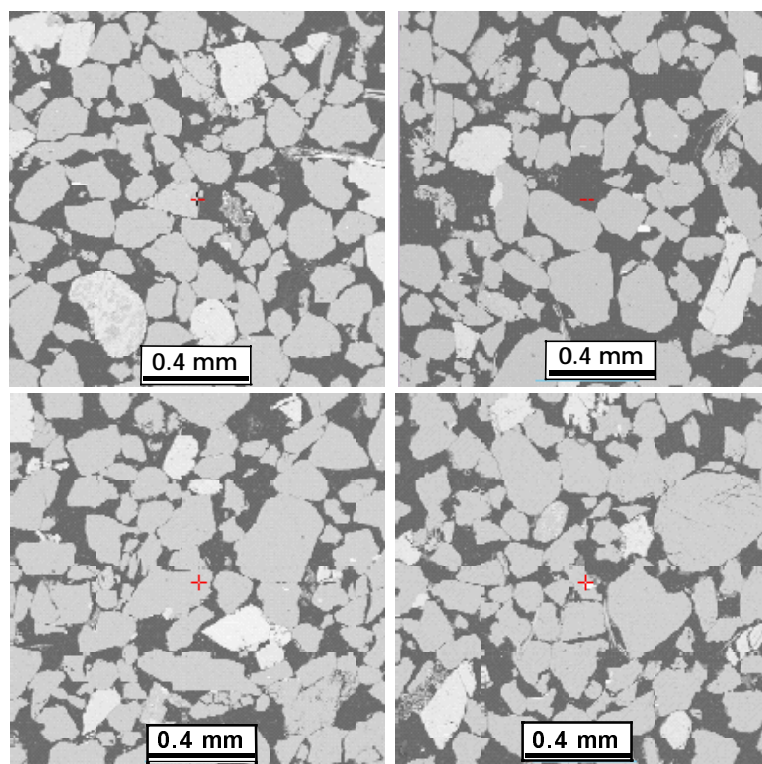
Figure 2.21: Thin-section images taken at depth 1785.1 m (upper left), 1890.1 m (upper right), 1815.1 m (lower left) and 1820.1 m (lower right) in Well #3.

We carry out quantitative grain-size analysis of twelve thin-sections, and Figure 2.20 shows the histograms of mean grain diameter within four of the thin-sections analyzed. We observe a marked change in the character. The two upper histograms (at 1785.1 and 1790.1 m) show a much smaller spread in grain size than the two lower histograms (at 1815.1 and 1820.1 m), where much larger grains are present. The corresponding thin-sections are shown in Figure 2.21. We can see that the two upper pictures have a more equally sized grain population whereas the two lower pictures show a larger variance in grain size, and indeed some larger grains. Furthermore, we observe that the porosity is lower and the grains more closely packed in the two lower pictures. Thus thin-section analysis confirms that the degree of sorting varies within the studied sand interval.

The grain size measurements were conducted using an image analysis computer program (Voyager). One source of error is that we have measured apparent grain diameters from two-dimensional images without accounting for the three-dimensional nature of the grains. However, for a given thin-section we assume that the grain size statistics (i.e. mean and standard deviation) are still representative. Another source of error is that two grains observed in contact may have been measured as one grain, causing erroneously large grain size measurements. A processing scheme comprising grain "erosion" (i.e., grains are reduced in size until all grain contacts disappear) before grain identification, and then the reverse process (i.e., grains are increased in size back to the original diameters) should take care of this problem, but the problem may still occur. The occurrence of some very large grains size values in the histograms in Figure 2.20 (> 700 μm), seems to reflect this problem. However, based on the good correlation between the shape of the histograms and the thin-section observations in Figure 2.21, we assume that the quantitative information is still valid. The next step is to study the relationship between derived sorting parameters from the quantitative thin-section analysis and rock physics properties from well-log (sonic velocities and density porosities) and core measurements (helium porosities). A good parameter of sorting (S) is defined by the standard deviation of grain size (σ) normalized to the mean grain size (M):

$$S = \sigma/M \tag{2-7}$$

When this value is relatively large, the sands are relatively poorly sorted, whereas when this value is relatively low the sands are relatively well sorted. Figure 2.22 shows how sorting affects velocity-porosity relations in the studied sand unit. There is a good correlation between Vp and density porosity at the depth locations where the thin-sections have been taken (upper left). Next, we observe a correlation between Vp and sorting (S), where velocity linearly increases when the sands become more poorly sorted. Sorting is also correlated to density porosity (lower left), and we observe a marked decrease in porosity as the sands become more poorly sorted. Helium porosities versus sorting show the same trend. Hence, the thin-section analysis confirms our hypothesis that the porosity decrease in the clean sands and sandstones of the Heimdal Formation is due to deteriorating sorting.
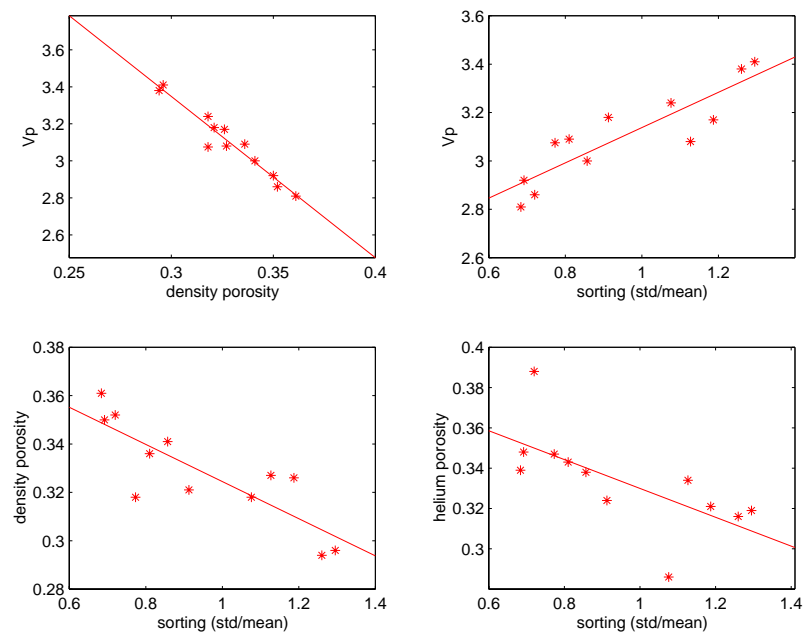
Figure 2.22: There is a very good correlation between velocity and porosity within the sand unit at the depths where thin-sections have been studied (upper left). The derived sorting factor shows a good correlation to Vp (upper right) and porosity (lower).

2.5.2   Diagnosing shaly sands and shales

Next, we do rock physics diagnostics of shaly sands and shales. The goal is to better understand the composition of the shales, in particular the silt (i.e., quartz) content. Direct information in terms of core or thin-sections are lacking in the Paleocene shaly intervals, which is why diagnostics are extra important for these rocks. Petrographic or mineralogical variations within the shales may cause internal seismic signatures, and it is important to understand the acoustic properties of shales and how we can distinguish these from other lithologies, in particular sands and sandstones.

Consider the data of the Sele Formation shales (see Appendix A for lithostratigraphic information), located at ca. 2100 m depth in Well #1 (Figure 2.8). This unit has been interpreted to be shales based on high gamma ray values, as well as mud-loggers cuttings observations. By plotting the velocity-porosity values of this unit together with the diagnostic shale model line, we find that there is a good correlation between the shale data and the shale line (Figure 2.23). However, the shales are plotting slightly above the model line. This probably reflect the fact that the shales are not 100% clay. The Sele Formation shales are, however, known to be very pure, with clay contents up to 80-90% (Alf Ryseth, pers. comm.). Consider another shaly interval in Well #1, this time the Lista Formation shales (Appendix A) located just above the Heimdal reservoir, at a depth of ca. 2140 m. These shales have slightly lower gamma ray values than the Sele Formation shales. The question that arises is whether or not this is due to higher silt content. The gamma ray log is known to be a good clay indicator in the Tertiary sequence in the North Sea. Still, the gamma ray values can vary with organic matter and K-feldspar, even if the clay content of the shale is not changing (Rider, 1986). Rock physics diagnostics, however, confirm that the Lista Formation shales are more silty than the Sele Formation shales. Using equations 2-4 and 2-5 we are able to quantify the silt content of the silty shales to be an average of 40%.

Now consider the zone below the reservoir sands in Well #1, ranging from ca. 2165-2200 m depth. This interval has core and thin-section information, just like the clean reservoir sands above. Thin-section analysis reveals two different lithofacies within this interval. The upper zone (2165-2180 m) is relatively clean sands, but with plane

lamination of clay. Figure 2.24 shows thin-section images from these sands. The grains are slightly smaller than the clean sands in Figure 2.14, and the intergranular pore space has higher clay content. The lower zone (2185-2200 m) are comprised of thin-bedded sands and shales. The thin-bedded sands shown in thin-section (Figure 2.24, right) are even more shaly and show even smaller grains and more pore-filling clay than the overlying thick-bedded zone (Figure 2.24, left). Figure 2.23 (right) shows the two zones of shaly sands, the plane-laminated shaly sands (diamonds) and thin-bedded sands-shales (crosses), cross-plotted in the velocity-porosity plane together with rock physics diagnostic models. The data points generally fall between the unconsolidated shaly sand line and the 2% cement fraction line. The unconsolidated shaly sand line is modeled assuming 20% clay in the matrix, and hence it has a lower effective mineral moduli than the unconsolidated clean sand line. The "flat" projection of the data trend from the contact cemented line to the uncemented shaly sand line, probably reflects that by increasing clay content the cement content gradually drops. However, the velocity stays fairly constant because of the pore filling effect of clay particles that counter-act the effect of decreasing cement volume.
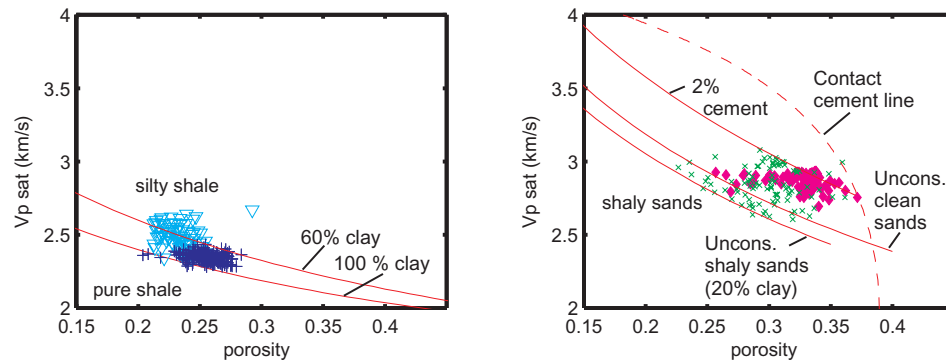
Figure 2.23: P-wave velocity versus porosity for shales and shaly sands superimposed on rock physics models. In the left plot we have included the unconsolidated shale line and silty shale line where the silt content is 40%. In the right plot, we have included the unconsolidated clean sand line, the 2% cement line, the contact cement line, and the unconsolidated shaly sand line where clay content is 20%.

The data are comprised of laminae or thin interbeds of shale, and the scatter in the Vp-porosity plane can be attributed to this interbedding. However, the laminae in the thick-bedded shaly sands are very thin (a few centimeters or millimeters) and are not

likely to be resolvable by the well-logs. The thin-bedded sand-shales, on the other hand, can have a significant scatter due to the binary lithology composition.
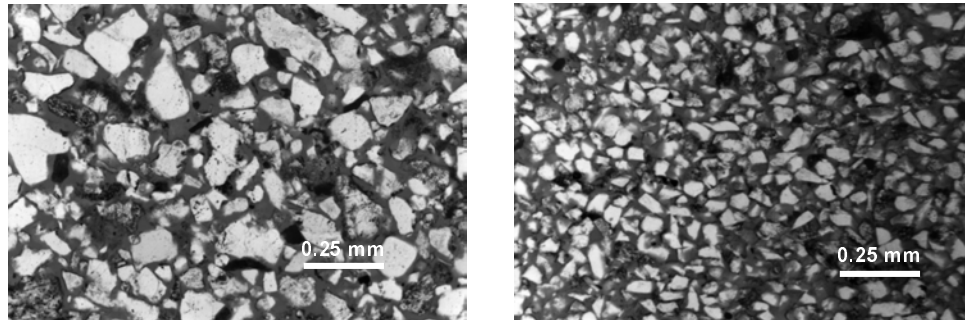
Figure 2.24: Thin-section images of the shaly sands encountered in Well #1. The left picture is taken from depth 2168 m, within a thick-bedded sand unit. Clay content in this shale is according to XRD analysis ca. 11% (Martinsen et al., 1995). The picture to the right is taken from depth 2183 m, within a thin sand bed of an interbedded sand-shale unit. The sand grains are smaller than in the thick-bedded unit to the left, and the clay content is 17%.

2.5.3 Diagnosing carbonates and tuff deposits

Carbonates and tuff deposits are commonly present within the Paleocene interval of the North Sea. In Well #2 we recognize a limestone bed at the base and marl deposits just above the base (i.e., Ekofisk Formation and Vaale Formation, respectively; see Appendix A for lithostratigraphic information). The lithology identification is based on cuttings (mud-loggers completion log), as well as geological interpretation of well-log data. The Balder Formation is located at 2050-2075 m depth in Well #1, and represents tuffaceous mudstones, also verified by cuttings. We analyze these lithologies in the velocity-porosity plane, and compare them with the rock physics diagnostic models (Figure 2.25) described in section 2.4.

For the tuffaceous mudstones, we change the effective mineral moduli until the modeled line creates a lower bound to the data. In this way we find the amount of tuff in the Balder Formation to be at least 20%.

For the limestones, we observe a large spread in the data, but they are nicely bounded between lower and upper modified Hashin-Shtrikman models. The wide range in the velocity-porosity values as well as the spread of the data, likely reflects local variations in diagenetic and depositional processes that have generated the limestones. The marl model

line was calculated by changing the shale line in terms of effective mineral moduli, to account for calcite content. We quantify the calcite content to be around 15% in these marls.
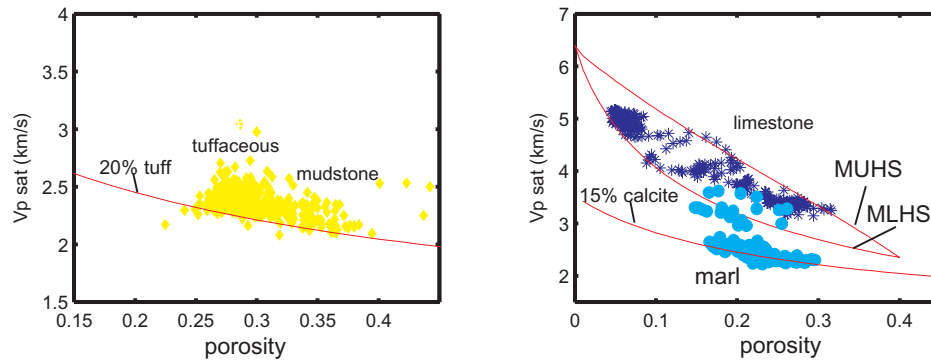
Figure 2.25: P-wave velocity versus porosity for different lithofacies superimposed on rock physics models. The tuff content of the modeled tuffaceous mudstone line is 20%, while the calcite content of the modeled marl line is 15%. (MUHS is the modified upper Hashin-Shtrikman model, while MLHS is the modified lower Hashin-Shtrikman model.)

2.6   Discussion

When rock physics is used in reservoir characterization, it is important to separate depth related changes and constant depth variations in seismic properties. Usually, hydrocarbon reservoirs are located within a small depth interval, with little depth dependent variations in the seismic properties. Depth related factors include mechanical and chemical compaction and related porosity reduction. However, variations in these may occur at a given depth level. In the North Sea case considered here, we observed that the transition from purely mechanical compaction to chemical compaction (i.e., quartz cementation) occurred within the Paleocene interval of interest. This diagenetic boundary is a very significant seismic horizon. As a consequence, sands are observed to change laterally from friable sands to cemented sandstones, giving completely different seismic signatures.

One question that arises is why we have quartz cementation in some of the Heimdal sands, whereas in other places the sands are friable, even though they represent the same

stratigraphic level. A possible explanation is that clean sands are quartz cemented at a critical depth level (approximately 2 km), while sands coated with clay have remained friable as quartz cementation has been inhibited by grain coating (Lander and Walderhaug, 1999). The quartz cementation could be related to pressure solution, although pressure solution is normally found to be important below 2.5-3 km depth in the North Sea (Ramm, 1992; Bjørlykke and Egeberg, 1993). An alternative explanation is that quartz cementation have occurred locally via diffusion or fluid flow from an adjacent source of silica (Martinsen et al., 1996). This source could be amorphous silica (biogenic silica, fossils and volcanic glass) present in either adjacent shales or volcanic tuffs. The solubility of silica is mainly controlled by grain size (specific surface area), temperature and pH. Amorphous silica particles usually have larger specific surface area than quartz grains and the solubility of amorphous silica is therefore higher than for quartz (Williams et al., 1985). After being transported through permeable media, the dissolved silica can reprecipitate as microcrystalline coatings around sand grains. Larger quartz overgrowths may also occur. Mathematical calculations by Berner (1980), however, show that very large volumes of pore water are needed to cement sands from external sources. Bjørlykke (1988) found that compactional drainage and fluid flow from shales and mudstones cannot be important sources of silica cement in thick sandstones (> 10 m), and that these sandstones are likely cemented mainly from internal sources. Hence, we believe that the external source of silica mentioned above can only explain the abundant quartz overgrowths seen at the very top and bottom of the sand in Well #2 (Martinsen, et al., 1996). It cannot explain the relatively constant cement volume (2%) observed within this sand unit, which is more than 50 m thick. Alternative internal sources of quartz cement (other than pressure solution) are biogenic silica, silica released by kaolinitization of feldspar, and dissolution of silt size quartz which is more soluble than coarser grained quartz (Füchtbauer, 1978).

Within the Paleocene interval, we have conducted detailed rock physics analysis, related seismic properties to sedimentary petrography, and used rock physics models to predict/diagnose petrographic changes from velocity-porosity relations. By separating velocity-porosity data into different clusters, with characteristic sedimentary features and rock physics properties, we can use these as training data in a classification procedure

(Chapter 3), and ultimately predict these various clusters from seismic data (Chapter 4). But why do we use physical models to diagnose the rocks? Why do we not just use thin-section and core information and correlate the various intervals with corresponding seismic properties, without taking into account the physical relations? First, thin-section and core data are not always available, especially in non-sand lithologies. Even in sandy intervals where such information is available, we will not automatically find out what petrographic factor will be most important seismically until we investigate the rock physics properties. The Heimdal sands are clearly a good example: The friable and cemented thick-bedded sands look very similar in core and thin-section, but small amounts of quartz cementation in some of the sands makes a big difference in seismic response. The rock physics diagnostics helped us distinguish between these two different rock types.

The rock physics diagnostics used in this chapter have two major pitfalls. The first is ambiguities in the velocity-porosity plane. A data point in this plane does not necessarily have a unique diagnostic result. For sands, there are ambiguities between clay content and sorting. Both these factors have similar paths in the velocity-porosity plane. There also seems to be ambiguities between different lithologies. Marls, tuffaceous muds, and silty shales show great overlaps. One way to solve the ambiguities would be to use shear wave information. In this chapter we have only used P-wave velocities. However, shear wave information is often not available. Furthermore, the rock physics models for shear wave velocity are known to show great discrepancy to real data (Dvorkin and Nur, 1996), indicating that the models as of today are not completely valid. One solution to this problem is to diagnose clusters of data using multivariate statistical methods as an alternative to physical rock diagnostics. Examples of this are shown in Chapter 3. The second factor that may cause the rock physics diagnostics to fail is the issue of resolution. The well-log data can show effective values of small scale heterogeneities, while the rock physics models used to diagnose the rocks in this chapter assume homogeneous rock types. This could be corrected for by using effective rock physics models that account for thin-bedded layering, e.g., the Backus average method (Backus, 1962; Mavko et al., 1998).

2.7 Conclusions

- The seismic properties of the studied North Sea sedimentary rocks are highly dependent on clay content, diagenesis, rock texture, lithology, and clay content.

- At shallow burial levels, North Sea shales tend to have higher velocities than sands, as shales suffer from more severe mechanical compaction. With depth and continued mechanical compaction, sandstones gradually acquire higher velocities than shales due to higher mineral moduli. A velocity "cross-over" occur within the Tertiary interval in the North Sea.

- At a certain depth, quartz cementation of sands initiate, and the velocity of sandstones becomes much higher than the velocity of shales or uncemented sands at the same depth. In the North Sea, this initial cementation may occur at a depth of about 2 km (or even 1.7 km as observed in the Grane area). Only a few percent of contact diagenetic cement strongly affect the elastic properties of sands resulting in a drastic difference between the seismic response of slightly cemented and friable reservoirs.

- Clay content, cement volume, degree of sorting, and lithology can be identified via rock physics diagnostics based on well-log data.

- Rock physics diagnostics are important to incorporate into seismic interpretation. If neglected, the seismic response related to sedimentary and diagenetic changes may be misinterpreted as fluid or porosity changes, which could result in the erroneous prediction of hydrocarbons.

- Rock physics diagnostics can be used as a tool to identify characteristic clusters of data (facies) that can serve as training data in classification procedures (see Chapter 3).

2.8   References

Anselmetti, F. S., and Eberli, G. P., 1997, Sonic velocity in carbonate sediments and rocks; *in* Palaz, I., and Marfurt, K.J., Eds., Carbonate Seismology: Soc. Expl. Geophys., Tulsa, 53-74.

Avseth, P., and Mavko, G., 1995, The influence of diagenesis on the acoustic properties of grain-supported siliciclastic sedimentary rocks: Annual Meeting, Stanford Rock Physics and Borehole Geophysics Project, **58**, Paper B1.

Backus, G. E., 1962, Long-wave elastic anisotropy produced by horizontal layering: J. Geophys. Res., **67**, 4427-4440.

Berner, R. A., 1980, Early diagenesis: A theoretical approach: Princeton series in geochemistry, Princeton Univ. Press.

Bjørlykke, K., 1988, Sandstone diagenesis in relation to preservation, destruction and creation of porosity: *in* Chilingarian, G. V., and Wolf, K. H., Eds., Diagenesis, I: Developments in Sedimentology, **41**, Elsevier, 555-587.

Bjørlykke, K., and Aagaard, P., 1992, Clay minerals in North Sea sandstones: *in* Houseknecht, D. W., Ed., Origin, diagenesis and petrophysics of clay minerals in sandstones: SEPM special publication, **47**, 65-80.

Bjørlykke, K. and Egeberg, 1993, Quartz cementation in sedimentary basins: AAPG Bull., **77**, 1538-1548.

Boggs, S., Jr., 1987, Principles of sedimentology and stratigraphy: Merrill Publishing Company.

Brevik, I., 1996, Inversion and analysis of Gassmann skeleton properties of shaly sandstones using wireline log data from the Norwegian North Sea: 66th Ann. Internat. Mtg., Soc. Expl. Geophys., Expanded Abstracts, 130-133.

Bryant, S., and Raikes, S., 1995, Prediction of elastic-wave velocities in sandstones using structural models: Geophysics, **60**, 437-446.

Castagna, J.P., 1993, AVO analysis – tutorial and review, *in* Castagna, J. P., and Backus, M., Eds., Offset Dependent Reflectivity – Theory and Practice of AVO analysis: Investigations in Geophysics, **8**, Soc. Expl. Geophys., 3-36.

Dutton, S. P., and Diggs, T. N., 1990, History of quartz cementation in the Lower Cretaceous Travis Peak Formation, East Texas: Journal of Sedimentary Petrology, **60**, 191-202.

Dvorkin, J., and Nur, A., 1996, Elasticity of High-Porosity Sandstones: Theory for Two North Sea Datasets, Geophysics, **61**, 1363-1370.

Dypvik, H., 1983, Clay mineral transformation in Tertiary and Mesozoic sediments from North Sea: AAPG Bull., **67**, 160-165.

Füchtbauer, H., 1978, Herkunft des Quartz Zements Abschätzung der Quartz Auflösung in Silt und Sandsteinen: Geol. Rundsch., **67**, 99-109.

Gangi, A. F., 1991, The effect of pore fluids and pressures on the seismic velocities in cracked and/or porous rocks: SEG Research Workshop on Lithology, Tech. Abstracts, 35-38.

Gassmann, F., 1951, Uber die Elastizität poröser Medien: Vier. der Natur. Gesellschaft in Zurich, **96**, 1-23.

Graton, L. C., and Fraser, H. J., 1935, Systematic packing of spheres with particular relation to porosity and permeability: AAPG Bull., **43**, 785-909.

Gueguen, Y., and Palciauskas, V., 1994, Introduction to the physics of rocks: Princeton Univ. Press.

Han, D., 1986, Effects of porosity and clay content on acoustic properties of sandstones and unconsolidated sediments: Ph.D.-thesis, Stanford University.

Hashin, Z., and Shtrikman, S., 1963, A variational approach to the elastic behavior of multiphase materials: J. Mech. Phys. Solids, **11**, 127-140.

Jizba, D., 1991, Mechanical and Acoustical Properties of Sandstones and Shales: Ph.D.-Thesis, Stanford University.

Klimentos, T., 1991, The effects of porosity-permeability-clay content on the velocity of compressional waves: Geophysics, **56**, 1930-1939.

Krynine, P. D., 1948, The megascopic study and field classification of sedimentary rocks: Journal of Geology, **56**, 130-165.

Lander, R. H., and Walderhaug, O., 1999, Predicting porosity through simulating sandstone compaction and quartz cementation: AAPG Bull., **83**, 433-449.

Magara, K., 1980, Comparison of porosity-depth relationships of shale and sandstone: J. Petr. Geol., **3**, 175-185.

Marion, D.,1990, Acoustical, mechanical and transport properties of sediments and granular materials: Ph.D.-Thesis, Stanford University.

Martinsen, O., Bloch, S., Holmefjord, I. B., Rykkje, J., and Torkildsen, G., 1995, Standard Core Description, Well [#1] (Our well numbering, because well name is confidential): Norsk Hydro internal report.

Martinsen, O., Holmefjord, I. B., Midtbø, R. E., Torkildsen, G., and Rykkje, J. M., 1996, Standard core description, Well [#2] (Our well numbering, because well name is confidential): Norsk Hydro internal report.

Mavko, G., Mukerji, T., and Dvorkin, J., 1998, The rock physics handbook: tools for seismic analysis in porous media: Cambridge University Press.

Mindlin, R. D., 1949, Compliance of elastic bodies in contact: J. Appl. Mech., **16**, 259-268.

Nur, A., Mavko, G., Dvorkin, J., and Galmudi, D., 1998, Critical porosity: A key to relating physical properties to porosity in rocks: The Leading Edge, **17**, 357-362.

Ostrander, W. J., 1984, Plane-wave reflection coefficients for gas sands at non-normal angles of incidence: Geophysics, **49**, 1637-1648.

Pearson, M. J., 1990, Clay mineral distribution and provenance in Mesozoic and Tertiary mudrocks of the Moray Firth and Northern North Sea: Clay Minerals, **25**, 519-541.

Pettijohn, F. J., 1975, Sedimentary rocks: Harper & Row, New York.

Proshlyakov, B. K., 1960, Reservoir properties of rocks as a function of their depth and lithology: Geol. Neft. Gaza, **12**, 24-29.

Ramm, M., Martinsen, O., Holmefjord, I., Johnsen, A., and Rykkje, J., 1992, Standard core description, Well [#3] (Our well numbering, because well name is confidential): Norsk Hydro internal report.

Ramm, M., 1992, Porosity depth trends in reservoir sandstones: theoretical models related to Jurassic sandstones offshore Norway: Marine and Petroleum Geology, **9**, 553-567.

Ramm, M., and Bjørlykke, K., 1994, Porosity/depth trends in reservoir sandstones: assessing the quantitative effects of varying pore-pressure, temperature history and mineralogy, Norwegian Shelf data: Clay minerals, **29**, 475-490.

Rider, M. H., 1986, The geological interpretation of well-logs: Whittles Publishing.

Riecke, H. H., III, and Chilingarian, G. V., 1974, Compaction of argillaceous sediments: Elsevier, New York.

Shuey, R. T., 1985, A simplification of the Zoeppritz equations: Geophysics, **50**, 609-614.

Shumann, W., 1989, Norsk steinhåndbok, Aschehoug.

Sintubin, M., 1994, Clay fabrics in relation to the burial history of shales: Sedimentology, **41**, 1161-1169.

Surdam, R. S., Dunn, T. L., MacGowan, D. B., and Heasler, H. P., 1989, Conceptual models for the prediction of porosity. Evolution with an example from the Frontier Sandstone, Bighorn Basin, Wyoming: *in* Coalson, E. B., Ed., Petrogenesis and petrophysics of selected sandstone reservoirs of the Rocky Mountain region: Rocky Mt. Assoc. Geol., 7-28.

Vernik, L., and Nur, A., 1992, Petrophysical classification of siliciclastics for lithology and porosity prediction from seismic velocities: AAPG Bull., **76**, 1295-1309.

Vernik, L., 1994, Predicting lithology and transport properties from acoustic velocities based on petrophysical classification of siliciclastics. Geophysics, **59**, 420-427.

Williams, L. A., Parks, G. A., and Crerar, D. A., 1985, Silica diagenesis, I. Solubility controls: J. Sed. Petr., **55**, 301-311.

Yin, H., 1992, Acoustic velocity and attenuation of rocks: Isotropy, intrinsic anisotropy, and stress-induced anisotropy: Ph.D. thesis, Stanford University.

Yin, H., Mavko, G., and Nur, A., 1993, Critical porosity; a physical boundary in poroelasticity: 34th U. S. symposium on Rock mechanics, *in* Haimson, B. C., ed., Rock mechanics in the 1990s, Oxford-New York, International Journal of Rock Mechanics and Mining Sciences & Geomechanics, Abstracts, **30**, 805-808.

Chapter 3

Seismic lithofacies identification and classification from well-logs using statistical rock physics

3.1 Abstract

In this chapter we first identify populations or clusters of data, referred to as *seismic lithofacies*, representing seismic scale sedimentary units with characteristic rock physics properties. Next, we use these clusters as training data in facies classification of well-log data from several wells. The goal is to establish a probabilistic link between rock physics properties and lithofacies to be used in the seismic reservoir characterization, predicting lithofacies from seismic data (Chapter 4). Seismic lithofacies can furthermore be used as building blocks in forward seismic modeling (Chapter 6).

For turbidite systems, we define six different facies groups (I-VI) based on clay content, grain size, and bedding configuration. The facies are primarily determined from well-logs (gamma ray, density, and sonic logs), but sub-facies of thick-bedded sandstones (Facies II) are defined by certain textural parameters (clay location, cementation, etc.), as well as sedimentary structures, which are determined from core and thin-section analyses. Rock physics diagnostics presented in Chapter 2 is also used to guide in the recognition of characteristic clusters of data. Rock physics analysis furthermore shows that unconsolidated thick-bedded clean sands and pure shales have very similar acoustic impedance distributions. However, the Vp/Vs-ratio helps resolve these ambiguities.

Having established a statistically representative training data base from a type-well, we perform multivariate classification of data from other wells in the area. We use different multivariate statistical methods and neural network for the classification, and compare the success-rates of the different methods. We find that the Mahalanobis quadratic discriminant analysis (MLDA), the probability density function classification (PDF), and the neural network (NN) classification all have a "success rate" of about 80%, when we use Vp and gamma ray logs together. Neural network does slightly better than MLDA, which again does slightly better than PDF. However, NN requires much more computational effort than MLDA and PDF. The advantage of PDF to MLDA is that it will easily reveal other types of lithofacies than in the training data, and/or erroneous log measurements.

We also study the ability of statistically separating the different lithofacies in the velocity-porosity plane. This becomes a feasibility study of the rock physics diagnostics presented in Chapter 2. The rock diagnostics can separate into characteristic clusters (i.e., facies), but sometimes there will be overlap between different populations, and there will be ambiguities in the diagnostic results. The success-rate of facies separation in terms of Vp and porosity is 81%, very close to the success rate when separating in terms of Vp and gamma ray. Vs-porosity gives a somewhat lower success rate (74.5%), while Vp, Vs, and porosity all together give a higher success rate (84%).

3.2   Introduction

Facies analysis and classification has been an important procedure among petroleum geologists for decades. A facies is defined as a rock unit with distinctive lithologic features, including composition, grain size, bedding characteristics, and sedimentary structures. Facies furthermore occur in predictable patterns in terms of lateral and vertical distribution and can also be linked to sedimentary processes and depositional environments. When Walther (1894) formulated what is today known as the *Walther's law of facies*, a new concept was introduced that had large impact on the way geologists analyzed the stratigraphic record. Walther stated: "It is a basic statement of far-reaching significance that only those facies and facies areas can be superimposed primarily which

can be observed beside each other at the present time." Careful application of Walther's law, suggests that in a vertical sequence, a conformable transition from one facies to another implies that the two facies can also be found laterally adjacent to each other (Middleton, 1973). Prograding and retrograding depositional systems can explain these facies associations. Hence, if we have Walther's law in mind, we can understand lateral stratigraphic relationships by analyzing vertical well-log sections.

By introducing seismic lithofacies that represent seismic scale sedimentary units, we try to improve our lateral facies prediction by we linking facies observed in vertical well-logs to seismic attribute maps. Facies have a major control on reservoir geometries and porosity distributions, so by relating lithofacies to rock physics properties one can improve the ability to use seismic amplitude information for reservoir prediction and characterization in these systems. Moreover, the seismic lithofacies classified from well-logs can serve as a calibration of statistical populations, each of which we can assume has stationarity in the seismic parameters. These can serve as constraints in the seismic reservoir characterization (Chapter 4).

The key requirement for the classification, irrespective of the specific method used, is to establish a good, statistically representative training database. This is done by selecting a type well with good quality logs, which are then subjected to careful petrophysical and geological analysis to define the principal seismic lithofacies categories. Core data, thin section descriptions, and estimates of fluid and well bore invasion effects are all used as aids in this process. Once we have a representative training data set, it can be used as inputs for the various classification techniques. In this way, we can integrate statistical prediction methods with geologic interpretation and rock physics analysis, and thus have a better control on the reservoir characterization results.

In this chapter we use well-log data from the Glitne turbidite field in the North Sea (see map in Figure A.1). A type well is selected (same as Well #1 in Chapter 2) from which the training data are defined. This well is used to classify other wells in the area. We show examples from three wells including the type well.

3.3 Seismic lithofacies in deep-water clastic systems

3.3.1 Seismic lithofacies definition and description

A seismic lithofacies is a seismic scale sedimentary unit which is characterized by its lithology (sand, silt, and clay), bedding configuration (massive, interbedded, or chaotic), petrography (grain size, clay location, and cementation) and seismic properties (P-wave velocity, S-wave velocity, and density). A descriptive facies scheme is suggested in order to objectively determine facies from well-logs, cores, and thin sections (Table 3.1 and Figure 3.1). Our scheme comprises six major facies (I-VI) that are geologically characterized by a specific grain size, clay content, and bedding configuration. Facies I represents gravels and conglomerates, Facies II are thick-bedded sandstones, Facies III are interbedded sands and shales, where the individual bed is below seismic resolution (i.e., thinner than approximately 10 m for 30 Hz seismic data in the Tertiary North Sea), Facies IV are shales with a significant silt content (i.e., more than approximately 30%), while Facies V are relatively pure shales. This scheme is general and aims to include all possible siliciclastic lithofacies that can be encountered in deep-water clastic systems.
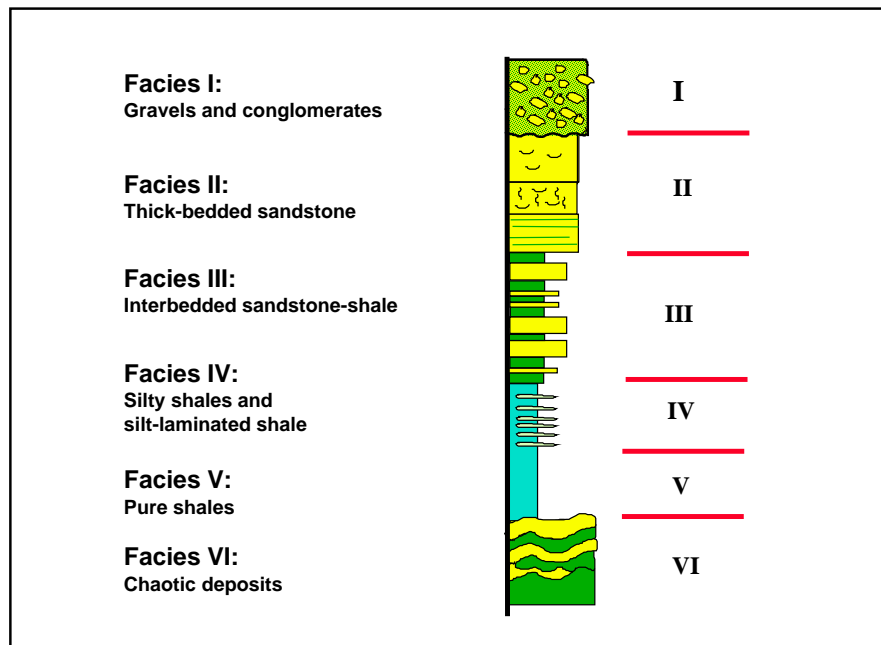
Figure 3.1: Seismic lithofacies in deep water clastic systems. Geologic description.

However, in the Glitne turbidite system studied in this chapter, we only recognize Facies II, III, IV, and V. Facies II-V represent a gradual transition from clean sandstone to pure shale, whereas sand-shale ratio can vary considerably for Facies I and VI. In the Grane turbidite system, studied in Chapters 5 and 6, we recognize other facies including tuff and carbonates, but these are not encountered within the target zone in the Glitne field.

Three sub-facies of Facies II are recognized and honor seismically important petrographic variations within the thick-bedded sand facies. These sub-facies are determined from core, thin-section and SEM analyses, and include cemented clean sands (Facies IIa), uncemented or friable clean sands (Facies IIb), and plane-laminated sands (Facies IIc). Thick-bedded shaly sands (Facies IId) are included as a possible facies to be encountered in deep-water clastic environments. These could be slurry-flow deposits as defined by Lowe et al. (1995), or sandy debris-flows as defined by Shanmugam et al. (1995). This type of facies, however, is not encountered in the area of study.

There is a gradual increase in clay content as we go from Facies IIa to IId, and the cleanest sandstones (IIa) are slightly cemented.

3.3.2 Facies associations in turbidite systems (classical submarine fans)

Our seismic lithofacies can be linked to depositional sub-environments and sedimentary processes within a deep-water clastic system. Walker (1978) suggested an idealistic depositional model that gives a simplified but good picture of how we expect sedimentary facies to be distributed in a "classical" submarine fan system (Figure 3.2). The upper fan is characterized by channel fill turbidite conglomerates, debris-flow, or slump deposits (Facies I and VI), but can also be characterized by starved shale units (Facies V). The turbidity currents on the upper fan are usually transported through a single deep channel depositing conglomerates and thick-bedded sands (Facies I and II). This feeder-channel is usually confined by stable levees. The levee and overbank deposits are more fine grained, thin-bedded turbidites (Facies III). In the mid-fan and lower fan areas, a lot of the coarse-grained material is transported radially via channels and is deposited as thick elongated sand sheets, or as sandy lobes that spread out at the end of

the channels. Fine-grained material is transported either along the channels and then laterally as overbank deposits. The sand-shale ratio is therefore high within the channels (Facies II) and in the proximal parts of the lobes, but relatively low in interchannel areas and in the more distal fan environments (Facies III and IV). Outside the fan system, there will be mainly deposition of hemipelagic and pelagic shales (Facies IV and V).
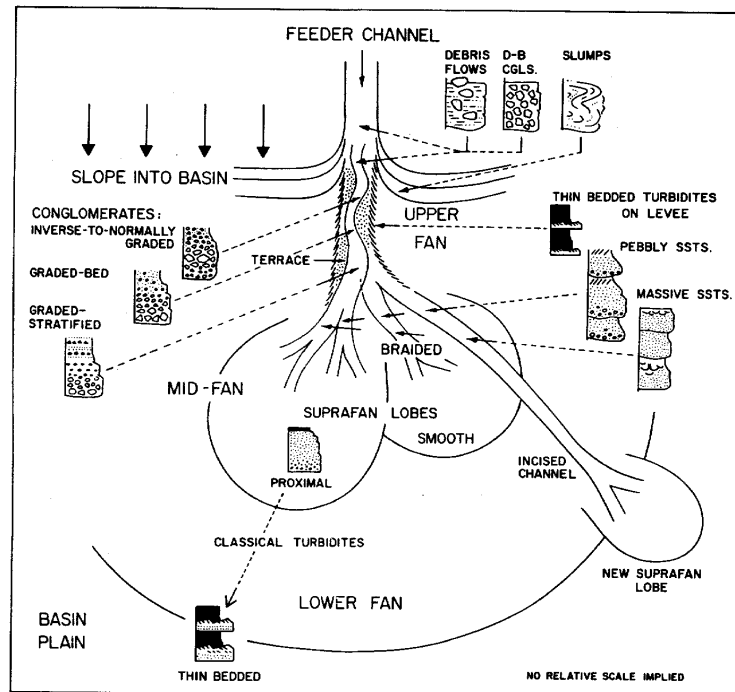
Figure 3.2: Walker's (1978) conceptual model for facies associations on a submarine fan.

Seismic Lithofacies Classification and Description		
Facies	*Geological description of facies and subfacies*	*GR log motif*
I **Gravels and conglome-rates**	Gravels, conglomerates, and pebbly sands. Sand-rich or mud-rich debris flow deposits.	Complex. Can be blocky if "clean".
II **Thick-bedded sandstone**	**IIa**: Very clean, well sorted, massive sandstones with small amounts of quartz overgrowths. Water-escape structures are common. Clay content less than 10%. **IIb**: Clean, massive sandstones with clay coatings. Water-escape structures are prominent. Pore-filling clay content slightly higher than in Facies II_a. (approximately 10-15 %). **IIc**: Plan-laminated sandstone. Higher pore-filling clay content (10-20%) and grain size in general smaller (fine to medium grained) than in Facies IIa and IIb. **IId**: Shaly sandstone (clay content between 20-40%).	Usually blocky and smooth. Bell and funnel shapes can occur. Low, but increasing GR values, from IIa.- IIc Intermediate in IId
III **Interbedded sandstone - shale**	Interbedded sand-shale couplets, where sand units are relatively thin-bedded compared to Facies II types of sand (i.e., below seismic resolution).	Serrated. Intermediate GR values
IV **Silty shales**	Silty shales and thin-laminated silt shale couplets. (In Rock Physics often referred to as "sandy" shales.)	Serrated High GR values
V **Pure shales**	Pure shales, often seen as thick, massive shale masses.	Serrated/smooth Very high GR values
VI **Chaotic deposits**	Syn-depositional deformation units, slide blocks, slump deposits, injection sands, shale diapirs, etc.	Serrated/complex

Table 3.1: Geological description of seismic lithofacies in North Sea deep-water clastic systems. (Clay contents, grain size, texture and sedimentary structures given for subfacies are from core observations in type-well).

3.4 Seismic lithofacies identification from a type-well

We select a type-well for identification of seismic lithofacies from well-log data (Figure 3.3; this is the same well as Well #1 in Chapter 2). Primarily, we have used the gamma ray log to determine the different facies, as it is a good clay indicator in the quartz-rich sediments of the North Sea. Facies II will usually show blocky log motifs and low gamma ray values. Fining upwards or coarsening upwards trends may occur, but are not typically recognized on gamma ray logs in deep water clastic systems, as clay content tends to be sorted equally from the fine grained sands and the coarse grained sands (Rider, 1986). Facies III will show a serrated log pattern, and the overall gamma ray values will be higher than for Facies II. However, individual sand beds within a Facies III unit may show gamma ray values as low as Facies II sands. Facies IV shows a less serrated pattern, but higher gamma ray values. Facies V can show serrated gamma ray values, but ideally it should be smooth, with very high gamma ray values. Facies I and VI will normally show a complex pattern, because of random arrangement of quartz and clays.
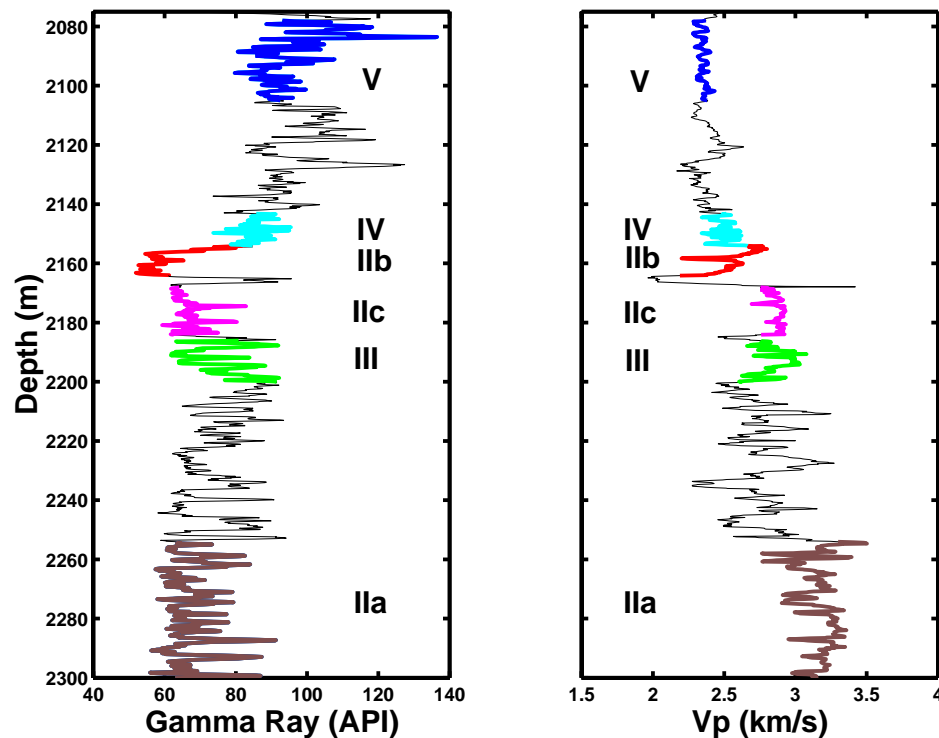
Figure 3.3: Lithofacies interpretation in type-well, representing training data for further classification.

Density and sonic logs have also been used to ensure that each facies occurs as significant clusters in terms of rock physics properties. Rock physics analysis can furthermore be used in a diagnostic way to determine lithofacies and to define training data when direct core and thin-section data are not available. The sub-facies IIb and IIc have been determined from core, thin-section, and SEM analyses (Figure 3.4), whereas IIa, representing a zone where no cores were taken, has been diagnosed as cemented thick-bedded sands using rock physics theory (Dvorkin and Nur, 1996). As confirmed in Chapter 2, the Heimdal Formation is comprised of both friable sands and cemented sandstones. Figure 3.5 shows the interval between 2252 – 2280 m in the type-well plotted in terms of velocity versus porosity, superimposed on the contact cement model, the constant cement fraction model (2 % quartz cement), and the unconsolidated line. We diagnose the zone as cemented sands (~2%). Also included in this plot is the zone defined as Facies IIb, which we know from core and thin-sections to be uncemented sands. These sands fit perfectly with the unconsolidated line. The cementation in Facies IIa is volumetrically not very significant, but in terms of elastic properties it has important impact. The seismic velocities and impedances are relatively high because of the stiffening effect of initial cementation (c.f., Chapter 2).
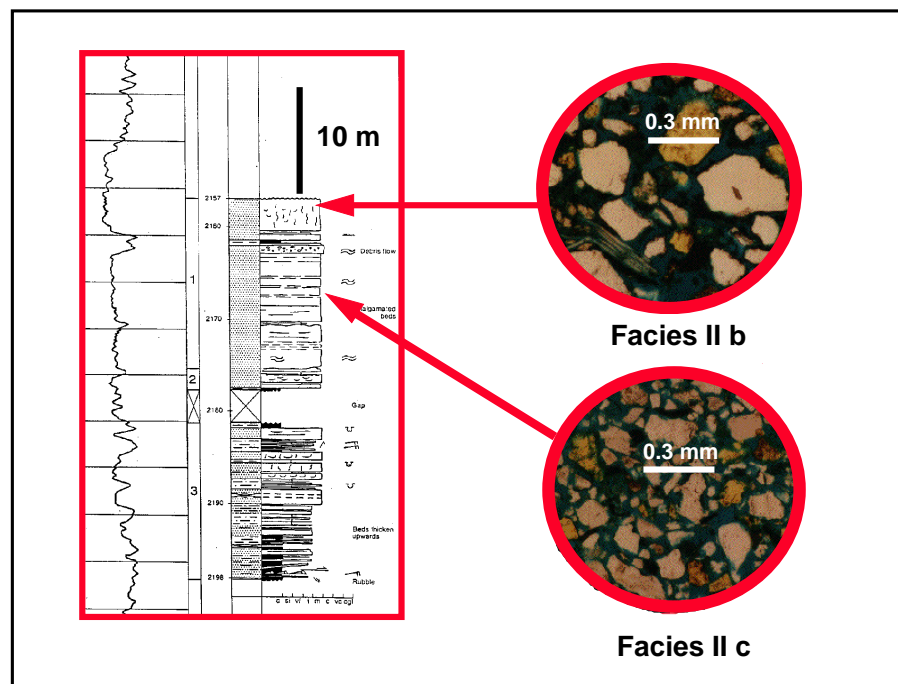
Figure 3.4: Sub-facies of Facies II are defined by petrographic differences determined from thin-sections and cores. (Core description is courtesy of Norsk Hydro).
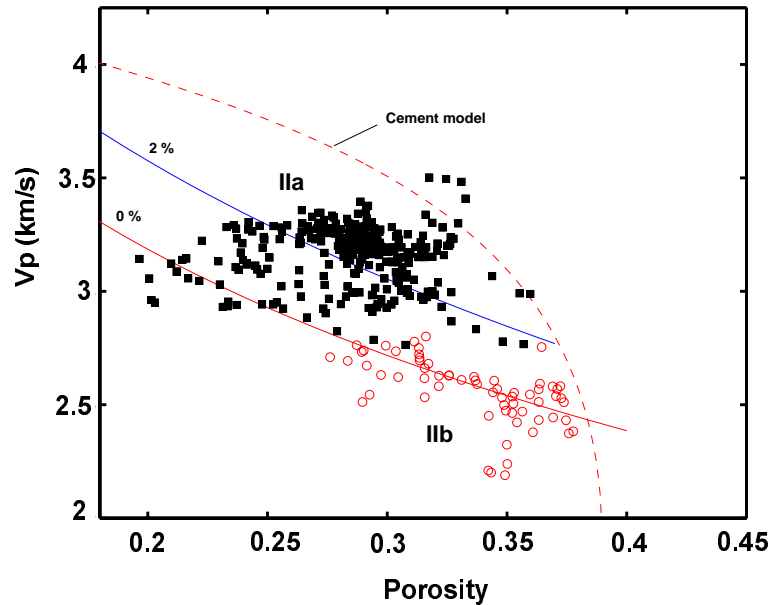
Figure 3.5: Rock physics diagnostics of two sandstone intervals in the type well, indicating an unconsolidated zone (Facies IIb, open circles) and a cemented zone (Facies IIa, filled squares). The unconsolidated sands have been confirmed by core observations (Figure 3.4). Presence of cemented Heimdal Formation sands has been confirmed in Chapter 2.

3.5 Rock physics analysis of seismic lithofacies

Figure 3.6 shows the different seismic lithofacies plotted as P-wave velocity versus gamma ray (left), and density versus gamma ray (right). We observe an overturned V-shape, and an ambiguity exists between Facies IIb and IV/V. Cemented sands (IIa) and laminated sands (IIc) as well as interbedded sand-shales have relatively high velocities. The sand-shale ambiguity is not observed in density versus gamma ray. Here we see a more linear trend where density increases with increasing gamma ray values (i.e., clay content) as we go from clean sands (Facies IIa and IIb) to silty shales (Facies IV). However, we observe that silty shales have higher densities than pure shales. The sand-shale ambiguity observed in terms of velocity is also observed in acoustic impedance, which is the multiplication of Vp and density (Figure 3.7; left). The overturned V-shape

we observe can be explained physically: for grain-supported sediments, increasing clay content tends to reduce porosity (i.e., increase density) and therefore stiffen the rock. However, for clay-supported sediments, porosity will increase with increasing clay content due to the intrinsic porosity of clay, and the rock framework will weaken. Hence, velocity will reach a peak when clay content is approximately 40%. This effect was described by Marion (1990) based on laboratory measurements of sand-shale mixtures. Zeng et al. (1996) also observed an ambiguity between clean sands and pure shales studying the acoustic impedance of Tertiary sediments in the Powderhorn Field, Texas.

The shear wave sonic log provides us with shear wave velocity (Vs). Figure 3.7 (right) shows the Vp/Vs ratio versus gamma ray value. Here we observe that Facies IIb can be distinguished from shales (Facies IV and V), as the Vp/Vs ratio increases with increasing shaliness. Higher Vp/Vs ratios in shales than sands are expected, since the shear strength in shales tends to be relatively weak compared to sands, due to the platy shapes of clay particles.

Potentially, the trends observed in our cross-plots could be influenced by variation in pore fluid, as the thick-bedded sand units identified as IIb and IIc are located within the oil zone. However, as discussed in Chapter 2, there are strong indications that there is invasion of mud filtrate in the shallow zone. Hence, we assume that the variations in seismic properties only reflect facies variations.
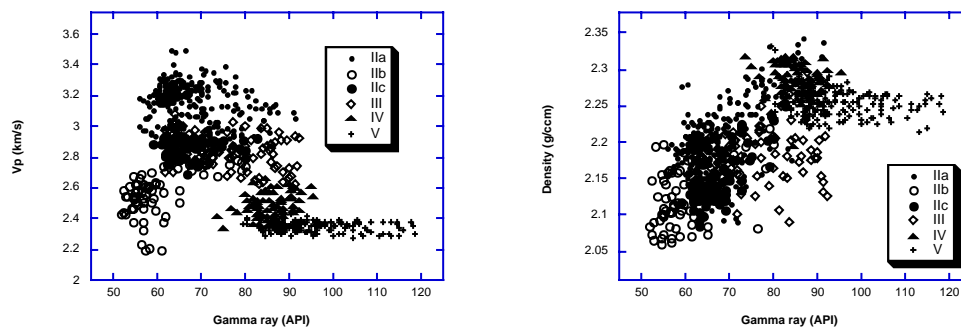
Figure 3.6: P-wave velocity versus gamma ray (left) and density versus gamma ray (right), for different seismic lithofacies in training data (i.e., Well #2). Note the ambiguity in P-wave velocity between Facies IIb and IV/V.
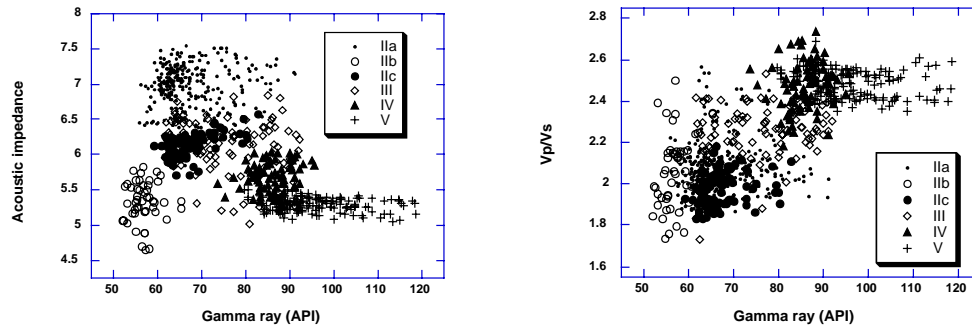
Figure 3.7: Acoustic impedance versus gamma ray (left) and Vp/Vs ratio versus gamma ray (right) in type-well.

3.6   Statistical classification of seismic lithofacies from well-logs

The log data from the type-well are used as training data for a multivariate statistical classification of seismic lithofacies in six other wells in the area. (Five of the wells are located in the Glitne field, including the type well. Two wells are located in a neighboring field, which penetrates Heimdal Formation sands at the same depth level.) In this section, the lithofacies numeric codes are as follows:

1 = Facies IIa   2 = Facies IIb   3 = Facies IIc

4 = Facies III   5 = Facies IV   6 = Facies V

Gamma ray, Vp, and density are the three parameters used in the classification. We primarily use gamma ray and Vp, as the density logs are found to be occasionally corrupted by washouts and rough borehole surfaces. However, porosity calculated from density is used in the training data validation together with velocity, since the density log in the type well has been corrected for washouts. Density logs in other wells are used complementarily during the classification, to double-check that the classification based on velocity and gamma ray is correct, and to help reveal the potential presence of non-siliciclastic lithologies (e.g., carbonates, volcanic ash-fall deposits, etc.). However, we did

not encounter non-siliciclastic facies in the wells used in the classification. Only the depth interval from 2100-2300 m was included in the analysis for each well, in order to avoid depth effects (i.e., pressure) when analyzing seismic properties.

3.6.1   Quadratic discriminant analysis

The first method we apply is based on simple quadratic discriminant analysis (Davis, 1986; Doveton, 1994). This method uses only the means and covariances of the training data. Samples are classified according to the minimum of the Mahalanobis distances to each cluster in the training data (Duda and Hart, 1973; Fukunaga, 1990). The Mahalanobis distance is defined as:

$$M^2 = \left(\mathbf{x} - \boldsymbol{\mu}_i\right)^T \Sigma^{-1} \left(\mathbf{x} - \boldsymbol{\mu}_i\right), \qquad\qquad (3\text{-}1)$$

where $\mathbf{x}$ is the sample vector, $\boldsymbol{\mu}_i$ are the vectors of means for the different categories or facies classes, and Σ is the training data covariance matrix. The Mahalanobis distance can be interpreted as the usual Euclidean distance scaled by the covariance.

Training data validation using Vp and gamma ray

Figure 3.8 shows the classification success rate in the type-well using the quadratic discriminant method. For this method we exclude one sample from the training data, and then classify that sample based on the remaining training data. This is referred to as the "jackknife" technique and is done successively for all samples in the training data. It is interesting to note how the combination of Vp and gamma ray improves our results in most cases. Using only gamma ray log, we observe poor results for Facies IIa, IIc, and III. Facies IIa can be hard to distinguish from Facies IIb, because the only difference is the quartz cementation. The Vp log easily distinguishes cemented sands from uncemented sands because of the increased stiffness related to initial cementation. In Facies IIc it is interesting to note that Vp as well as gamma ray alone do a poor job, whereas combined they do well in predicting Facies III. This is because Facies IIc, in terms of Vp overlaps with Facies III, and in terms of gamma ray it overlaps with Facies IIa and IIb. Overall, the

gamma ray log alone has an average success-rate of 45%, the Vp alone has a 60% success-rate whereas Vp and gamma ray together has an 82% success-rate.
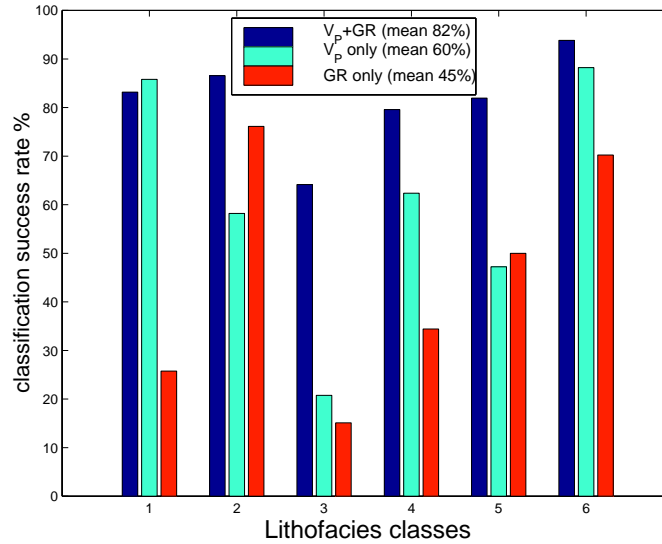
Figure 3.8: Minimum Mahalanobis distance classification success rate using only GR log, only Vp, and both GR and Vp.

Training data validation in the velocity-porosity plane

We apply the Mahalanobis distance method to calculate the success rate of discriminating between the different training facies in the velocity-porosity planes. First we calculate the success rate of separating the different facies using only Vp, then Vp and porosity, followed by Vs and porosity, and finally Vp, Vs, and porosity (Figure 3.9). The average success-rate for Vp-porosity is 81.0%, for Vs-porosity is 74.5%, and for Vp-Vs-porosity is 84.0%. This shows that we improve our ability to statistically distinguish lithofacies by introducing shear wave velocity, yet the improvement is moderate. Hence, the training data defined primarily based on clay content and rock texture, are distinguishable in the velocity-porosity plane. This manifests the feasibility of rock physics diagnostics as a technique to separate velocity-porosity data into clusters with characteristic lithology and texture, c.f. Chapter 2.
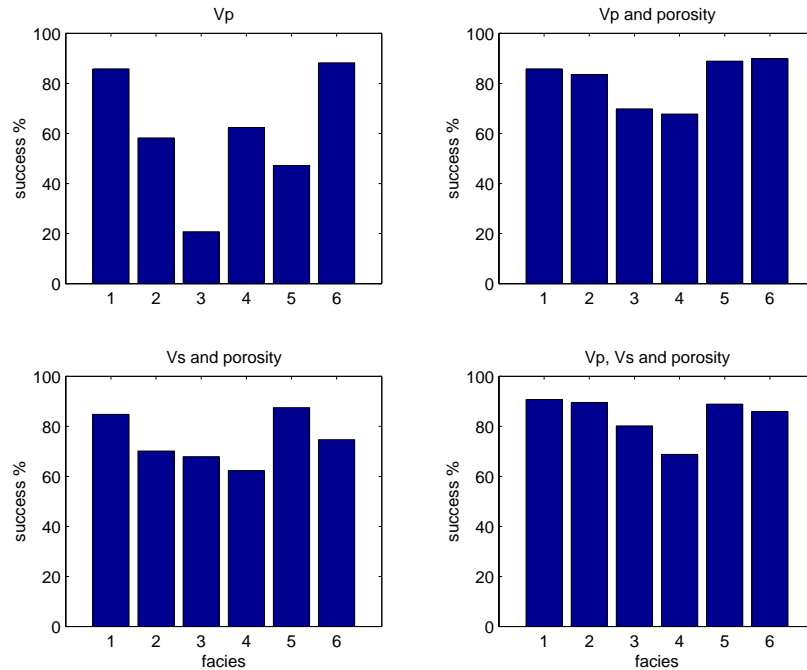
Figure 3.9: Classification success rates in terms of Vp, Vp-porosity, Vs-porosity and Vp-Vs-porosity for different facies.

3.6.2 Non-parametric PDF classification

An alternative way to classify well-logs in terms of lithofacies, is to use the complete probability distributions functions (pdf) of the log values, instead of using just their means and covariances. Figure 3.10 shows the estimated pdfs for Vp versus GR for the different facies in the type well. Values plotting outside any of the pdfs will not be classified, whereas samples that fall in an overlapping area, inside the pdfs of two or more facies, will be classified according to the facies that has the highest probability at that "location". This calibration pdf gives not only the most likely facies, but also the conditional probability of each facies given the observed Vp and gamma ray.
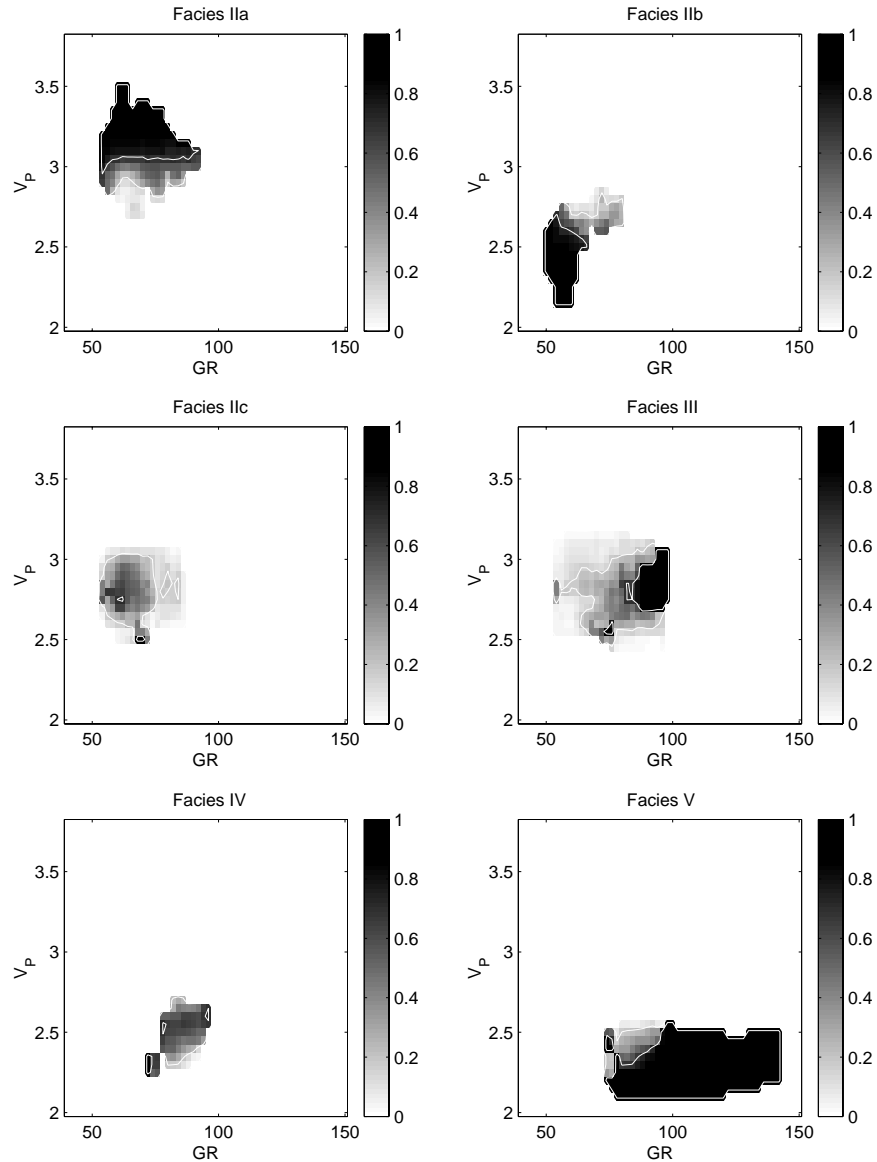
Figure 3.10: Pdf plots of Vp versus GR for different facies in type-well.

The raw histograms obtained from the training date are smoothed so as to get pdfs that capture the overall general trend without fitting the specific idiosyncrasies of the data. Over-smoothing on the other hand can give poor classification results. We determined the appropriate smoothing by dividing the whole training sample into two sets, one in-sample, for the PDF estimation, and another, out-of-sample, for validation. The smoothing that gave the best overall success rate with the validation data was selected.

3.6.3 Neural network classification

Neural networks represent yet another way to classify facies from well-logs. This approach can be useful when the discriminant surfaces are highly non-linear and are not well approximated by the simple quadratic discriminant analysis. Amongst others, Baldwin et al. (1989, 1990), and Rogers et al. (1992) used neural networks to classify porosity and density logs, and lithologies. Harris et al. (1993) trained networks to classify lithology from borehole imagery data. Other examples of various applications in geosciences, and a practical introduction to neural network theory, are given in Dowla and Rogers (1995).

While there are various kinds of neural networks, we use the popular multi-layer feed-forward architecture with weight adaption by back-propagation. There were six nodes in the hidden layer with a sigmoid transfer function. There are no hard and fast rules to pick the number of nodes to use, though there are some limiting analytical guidelines (e.g., Lin and Lee, 1996). In practice, the choice is made on the basis of trial and experiment, balancing between computation and training time, convergence, and network performance. For our lithofacies classification problem the input vector consisted of the Vp and gamma ray value from the log at each depth point. The desired output was a six element binary vector (corresponding to the six lithofacies classes) with a "1" at the position corresponding to the facies numeric code, and zero elsewhere. The weight update was done using conjugate gradient descent with momentum (Lin and Lee, 1996). Ordinary gradient descent can be slow if the learning constant parameter is small, and can oscillate too much if the parameter is set too large. Gradient descent with momentum helps to solve this problem by adding a fractional (<1) contribution from the previous time step to each weight change during the training session. The weight update scheme is implemented by:

$$\Delta w(t) = -\eta \nabla E(t) + \alpha \Delta w(t-1), \qquad (3\text{-}2)$$

where E is the error between the desired and actual network output, η is the learning parameter, α is the momentum parameter (<1), and Δw is the weight update. Figure 3.11

shows the decrease in the error as the network goes towards convergence in one training session.
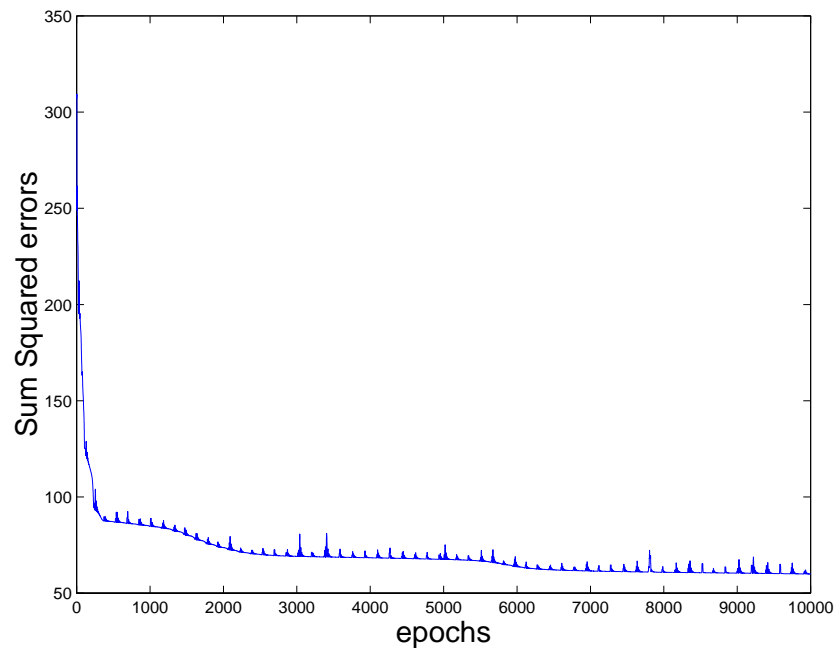
Figure 3.11: Neural network error plot.

3.6.4   Comparison of different methods

Figure 3.12 shows the classification results in the type-well (in the target zone: 2100-2300 m), using the different methods. The results are very similar, but some important differences occur. Note the thin dark blue stripe close to depth sample 600 in the pdf classification. This interval is actually classified as "zero", meaning no facies is recognized by the PDF method. Taking a look at the core section in Figure 3.4, we observe that this interval corresponds to a 1 m thick debris flow unit (Facies I), which is not represented in the training data.

Figures 3.13 and 3.14 shows the overall classification success rates of the different methods. In general, all the methods give about 80% success rate (Figure 3.13). Note that 80% success rate does not imply that the methods predict wrong facies in 20% of the well-log data. The training data was first identified at a "seismic" scale (units thicker than 10 m). Even though the statistical methods classify smoothed well-logs, some of the classified units come out at a scale smaller than the scale of the training data. This is a

drawback with the seismic lithofacies. If there is, for example, a 7 m sand unit located between two thick shale layers, it will be classified as a thick-bedded sand unit if the smoothed values are still closest to the values characteristic for thick-bedded sands. This does not really matter, because when cumulative density functions (cdfs) of seismic properties are derived from the classification results (see Chapter 4), we still use the well-log scale values. The upscaling from well-log scale to seismic scale happens later when probability density functions of seismic properties are calibrated to seismic inversion results. With this in mind, we observe that the NN method gives slightly better results than the two others. However, NN requires much more computation. PDF has a slightly lower success rate than MLDA, but we have already mentioned how the PDF was able to reveal a facies that was not included in the training data. Looking at each facies separately (Figure 3.14), we see that sometimes the MLDA method does best (Facies IIb and III), sometimes the PDF (Facies IIa and V) and sometimes the NN method (Facies IIc and IV). Nevertheless, the results are similar for each of the methods, regardless of facies. The exception is for laminated and interbedded facies types (IIc and III), where MLDA and PDF have "problems", respectively. Here the neural network seems to be more robust.

The neural network method can be tuned to give slightly different weights to the different facies. Figure 3.15 shows the classification success rate for three different networks. NN1 was trained with a training set biased towards Facies IIa. This causes poor performance for Facies III, but gives almost 100% success rate in classifying Facies IIa. The other two networks (NN2 and NN3) had more evenly biased training data, but had different initial weights. The similar results for both networks show that consistency can be achieved with proper selection of training data and network architecture.
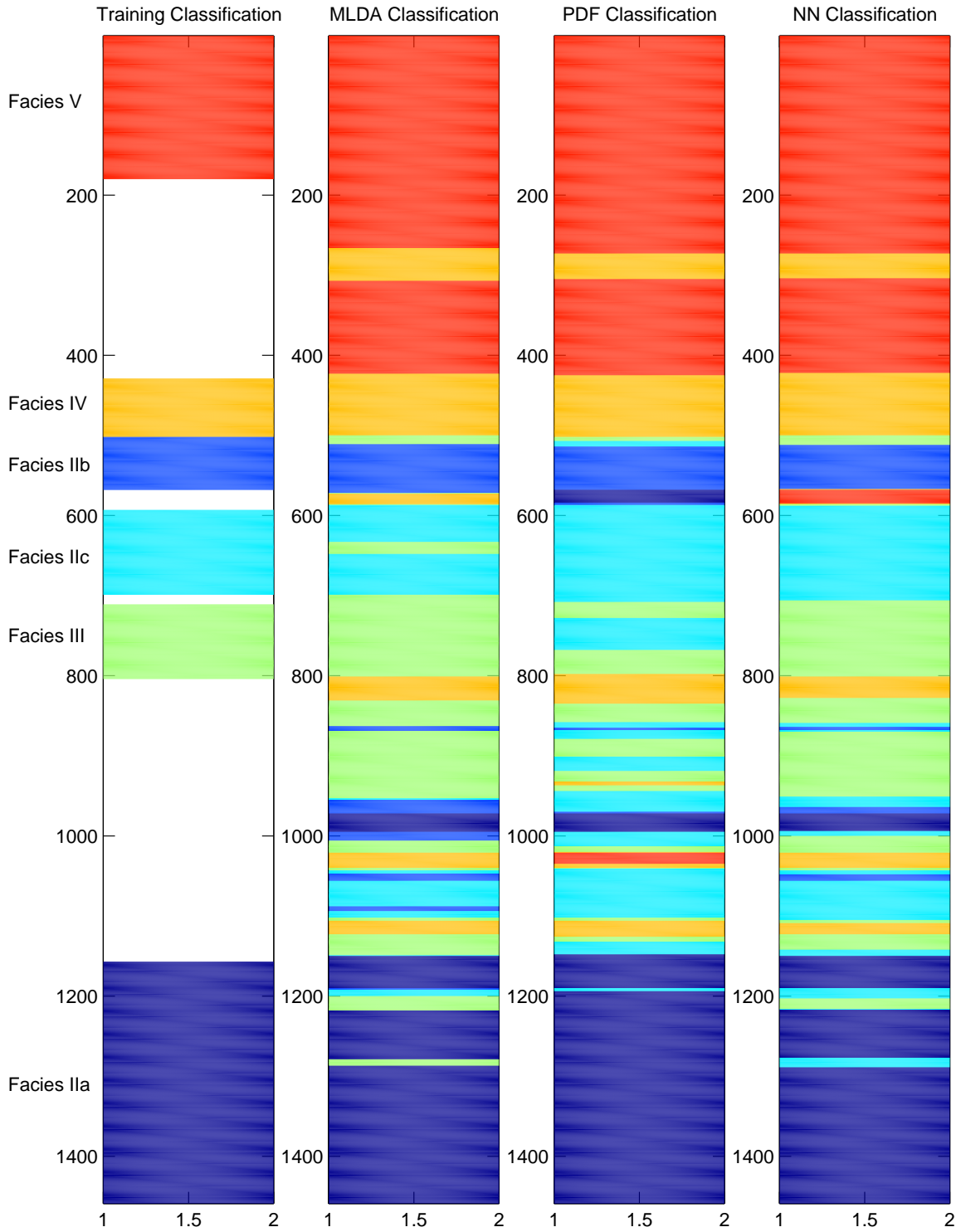
Figure 3.12: Comparing MLDA, PDF, and NN classification results in the type-well. The depth axis is annotated with sample number. Sample number 1 is located at about 2075m and sample number 1400 is located at approximately 2300m.
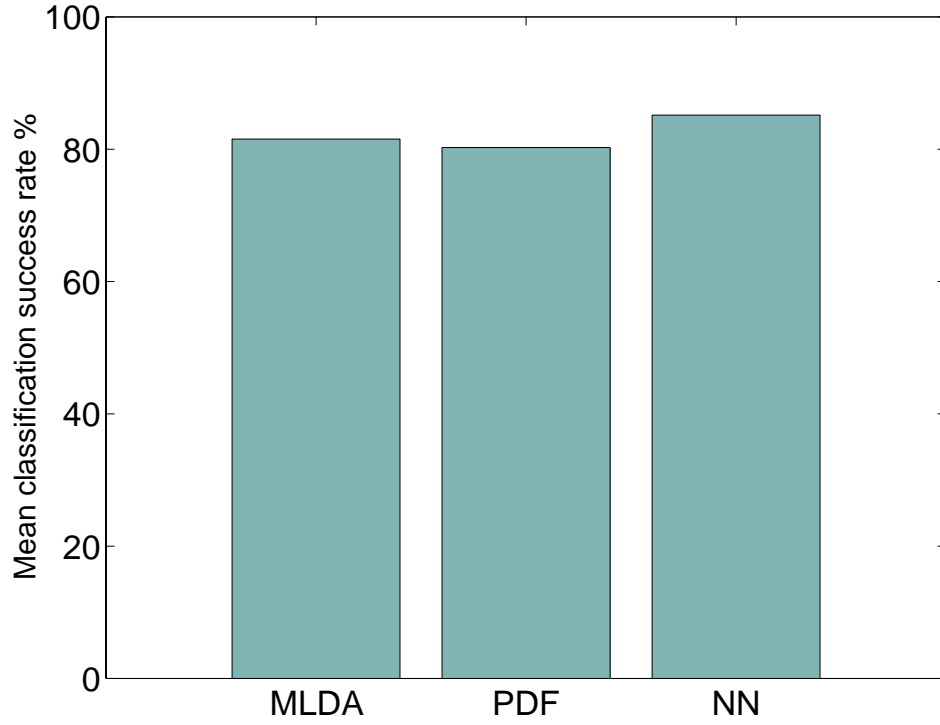
Figure 3.13: Mean classification success rate.
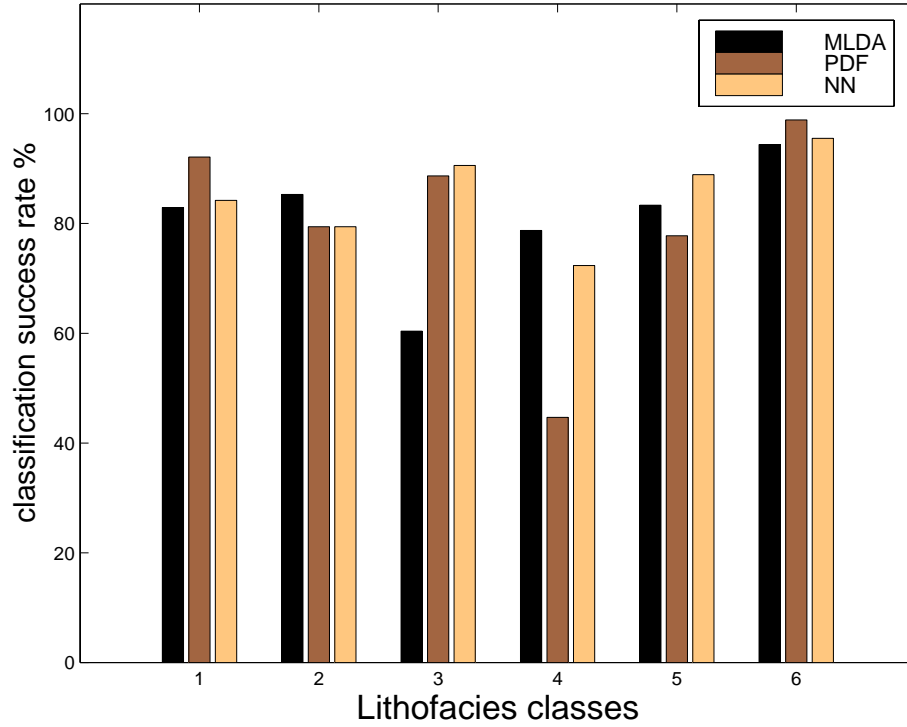
Figure 3.14: Classification success rate for different facies for the three different classification methods.
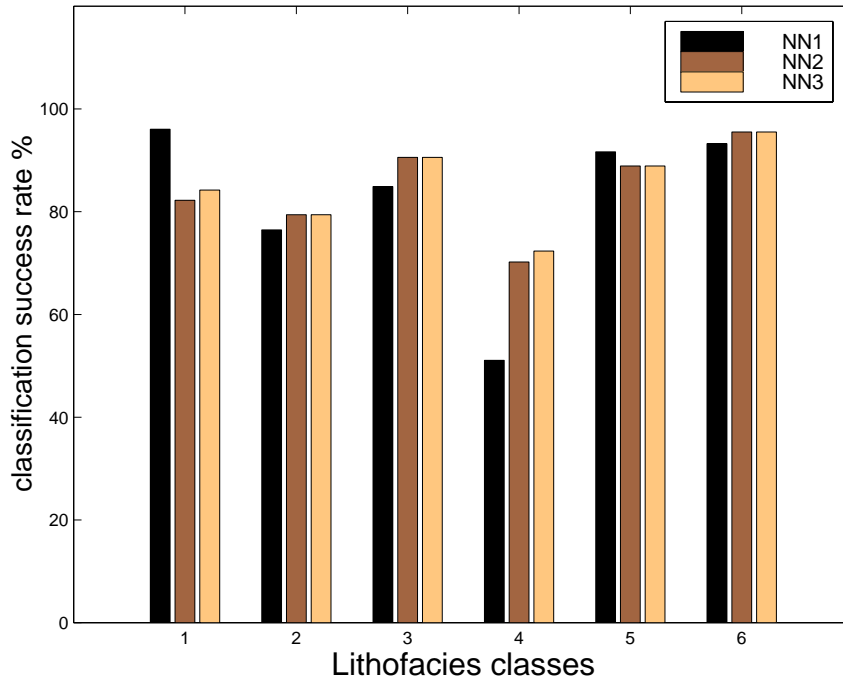
Figure 3.15: Classification success rate for neural network classifications with different weighting.

Now that we know that the classification of seismic lithofacies from well-logs works, we can go ahead and classify the six other wells. Care is taken to normalize the gamma ray values from other wells to that of the type well. We show examples from two wells, Well 3 and Well 6. Figure 3.16 shows the classification results in Well 3, and Figure 3.17 shows the classification results in Well 6.
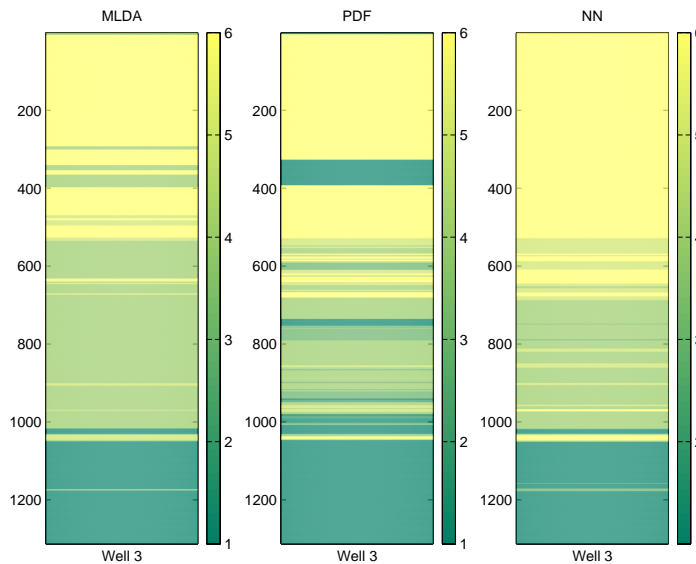
Figure 3.16: Classification results in Well 3, different methods.
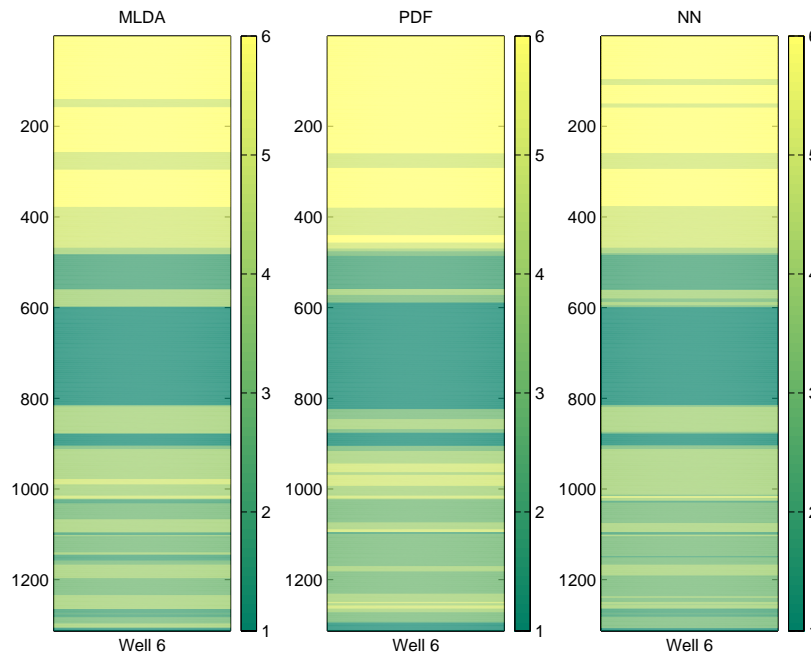
Figure 3.17: Classification results in Well 6, different methods.

3.6.5   Facies probabilities

So far we have only displayed the classification results in terms of most likely facies. However, one can also display probability plots of facies showing the conditional probability of each facies to be present at each depth location. Figure 3.18 shows the most likely facies juxtaposed with a contoured facies probability plot in the type-well. It is interesting to note that the intermediate zone, characterized by Facies IIc, III and IV (interbedded and laminated zones) have larger uncertainties in facies, i.e. lower facies-probabilities. Figure 3.19 and 3.20 show the facies probability plots for well 3 and 6. In Figure 3.19 we see a zone (just above depth point 400) which has zero probability for all six facies. This zone is unclassified, and it represents combinations of Vp and gamma ray values that were not encountered in the training pdfs from the type-well. This could be indicative of either erroneous measurement (e.g., due to bad hole conditions, etc.) or it could represent a lithofacies not included in the training data. As mentioned in section 3.6.2, we also observe a similar thin streak of zero probability above depth point 600 in the type-well (Figure 3.12), which is confirmed to represent a thin debris flow unit (see

core descriptions, figure 3.4). This lithofacies type occurs in rare instances in this area and was not included in the training data.
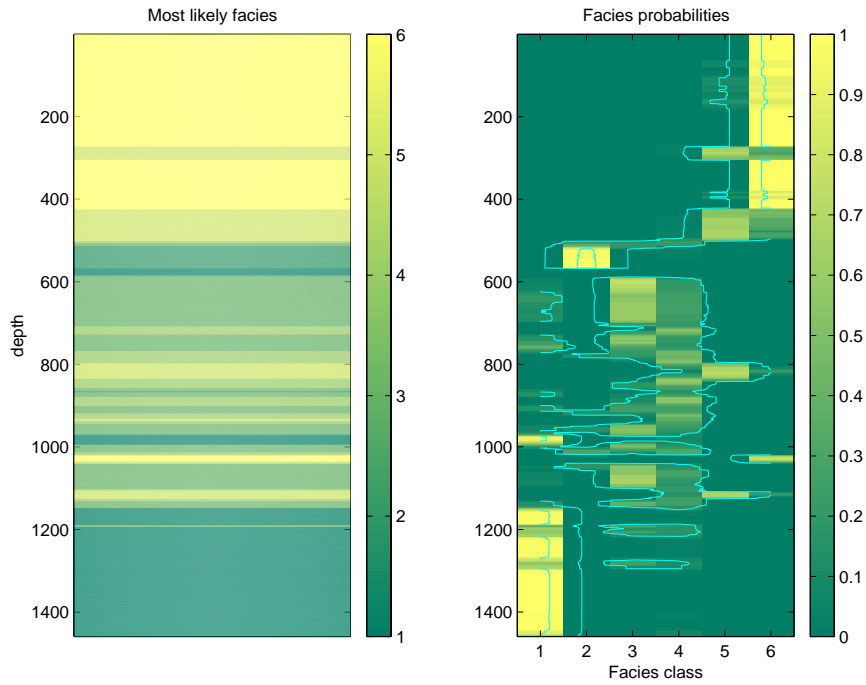
Figure 3.18: Most likely facies and facies probability in type-well
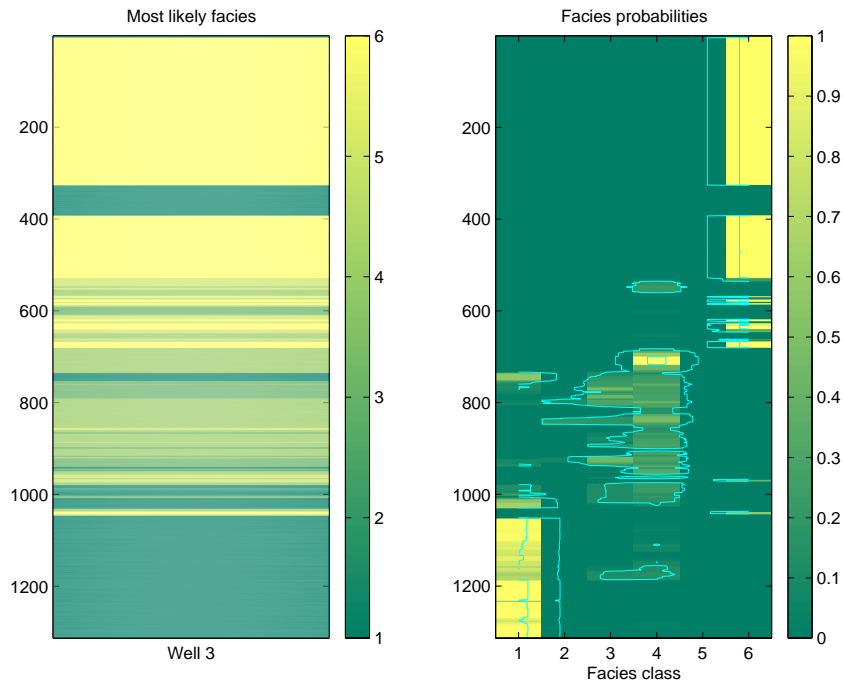
Figure 3.19: Most likely facies and facies probabilities in Well 3.
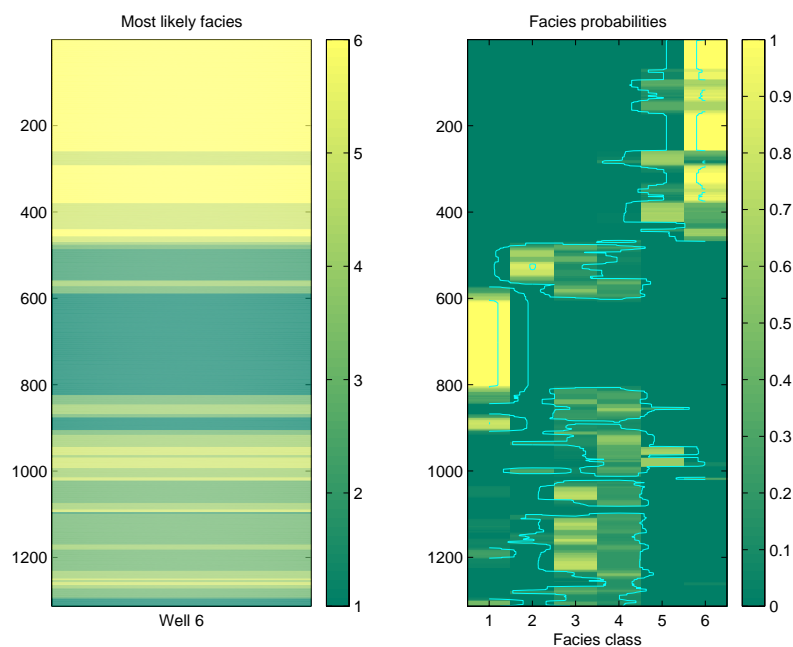
Figure 3.20: Most likely facies and facies probabilities in Well 6.

3.7   Discussion

In our seismic lithofacies scheme we have included the various siliciclastic sand and shale facies that are common in deep water clastic systems. In this way the facies scheme can be used in any deep-water clastic systems. (Other seismic lithofacies that are present in the North Sea Tertiary sequence, but were excluded from our scheme, include carbonate rocks and tuffaceous rocks. Carbonate cemented units can be present in North Sea turbidite sequences, and tuffaceous rocks are rather common in the volcanically active Paleocene period. These lithofacies are considered in Chapter 5, where data are from the Grane field.)   However, the seismic properties characteristic for our facies should not be used in any other area. Different mineralogical composition and diagenetic history will give different trends than discovered in this study. Other users of our scheme should link the facies to properties derived from well-logs and cores in their area.

The trends observed in our study, however, should be expected in other sedimentary basins with similar mineralogical composition and diagenetic history to the North Sea Tertiary sequences (i.e., poorly consolidated, quartz-rich sandstone sequences). In such cases, we expect ambiguities in velocity and acoustic impedance between sands and

shales. For instance, Zeng et al. (1996) discovered a clean sand - pure shale ambiguity in terms of acoustic impedance in Tertiary sediments in the Gulf of Mexico.

The seismic lithofacies defined in this study first of all create a probabilistic link between rock physics and sedimentology, to be used in the seismic reservoir characterization in Chapter 4. Secondly, they can serve as "building blocks" when doing seismic modeling in the area of study, and this is done in Chapter 6. In both cases, the use of seismic lithofacies becomes a predictive tool, as different seismic lithofacies will be associated with each other. Seismic lithofacies will therefore make it easier to interpret seismic amplitudes in terms of sedimentologic features in deep water clastic systems. Ultimately, the potential of seismic lithofacies in North Sea turbidite systems is improved reservoir characterization from 3-D seismic data, causing enhanced oil recovery in these type of reservoirs.

3.8   Conclusions

- Seismic lithofacies are seismic scale sedimentary units with characteristic rock physics properties. We have defined six different seismic lithofacies for turbidite systems. Geologically, these facies are defined by clay content, grain size, and bedding configuration. The potential benefits of seismic lithofacies are better understanding of seismic signatures and consequently improved reservoir characterization in these systems.

- Rock physics analysis of seismic lithofacies shows that thick-bedded sands can have the same acoustic impedance as a pure shale in North Sea deep-water clastic systems. The Vp/Vs ratio will resolve this ambiguity.

- In this chapter we have shown how to identify and classify seismic lithofacies from well-log data. A training well located in a North Sea turbidite system is used as a basis for classification of other wells in the area. We estimate not only the most likely facies but also the conditional probability of different facies at each depth. We compare different multivariate statistical methods and neural network schemes for the classification. The results show that the Mahalanobis quadratic discriminant analysis (MLDA), the probability density function classification (PDF), and the neural

network (NN) classification all have a success rate of about 80%, when Vp and gamma ray logs are used together. NN does slightly better than MLDA, which again does slightly better than PDF. However, NN requires much more computational effort than MLDA, and PDF. The advantage of PDF to MLDA is that it will easily reveal other types of lithofacies than in the training data, and/or erroneous log measurements.

- Seismic lithofacies classification creates a probabilistic link between rock physics properties and lithofacies to be used in seismic reservoir characterization, where lithofacies is predicted from seismic data (Chapter 4). Seismic lithofacies can furthermore be used as building blocks in forward seismic modeling (Chapter 6).

3.9   References

Baldwin, J. L., Bateman, A. R. M., and Wheatley, C. L., 1990, Applications of neural network to the problem of mineral identification from well-logs, Log Analyst, **3**, 279-293.

Baldwin, J. L., Otte, D. N., and Wheatley, C. L., 1989, Computer emulation of human mental process: Application of neural network simulations to problems in well-log interpretation, SPE paper 19619, 481-493.

Davis, J.C., Statistics and data analysis in geology: John Wiley & Sons, New York, NY.

Doveton, J. H., 1994, Geologic log analysis using computer methods, AAPG Computer Applications in Geology, No. 2, Am. Assoc. of Petr. Geol., Tulsa, Oklahoma.

Dowla, F. U., and Rogers, L. L., 1995, Solving problems in environmental engineering and geosciences with artificial neural networks, The MIT Press, Massachusetts.

Duda, R. O., and Hart, P. E., 1973, Pattern classification and scene analysis, John Wiley & Sons.

Dvorkin, J., and Nur, A., 1996, Elasticity of High-Porosity Sandstones: Theory for two North Sea dataset, Geophysics, **61**, 1363-1370.

Fukunaga, K., 1990, Introduction to statistical pattern recognition, 2nd ed., Academic Press.

Harris, D. A., Lewis, J. J. M., and Wallace, D. J., 1993, The identification of lithofacies types in geological imagery using neural networks, Conf. papers vol., EUROCAIPEP **93**, Aberdeen.

Lin, C-T, and Lee, C. S. G., 1996, Neural fuzzy systems, Prentice Hall, New Jersey.

Lowe, D., Hickson, T., and Guy, M., 1995, Slurry flows; an important class of sediment gravity flows with examples of slurry-flow deposits from the Lower Cretaceous of the North Sea: 1995 Annual Meeting, Geol. Soc. of Am., Abstracts with Programs, **27**, no. 6, 128-129.

Marion, D., 1990: Acoustical, mechanical and transport properties of sediments and granular materials. Ph.D.-thesis, Stanford University.

Middleton, G. V., 1973, Johannes Walther's Law of the correlation of facies. Geological Society of America Bulletin, **84**, 979-988.

Reading, H. G. and Richards, M., 1994: Turbidite systems in deep-water basin margins classified by grain size and feeder system; AAPG Bull., **78**, 792-822.

Rider, M. H, 1986, The geological interpretation of well-logs: Whittles Publishing.

Rogers, S. J., Fang, J. H., Karr, C. L., and Stanley, D. A., 1992, Determination of lithology from well-logs using a neural network, AAPG Bull., **76**, 731-739.

Shanmugam, G., Bloch, R., Mitchell, S., Beamish, G. W. J., Hodgkinson, R. J., Damuth, J. E., Staume, T., Syvertsen, S. E., Shields, K. E., 1995, Basin-floor fans in the North Sea; sequence stratigraphic models vs. sedimentary facies: AAPG Bull., **79**, 477-512.

Walker, R., 1978: Deep-water sandstone facies and ancient submarine fans: Models for exploration for stratigraphic traps; AAPG Bull., **62**, 932-966.

Walther, J., 1893-4, Einleitung in die Geologie als historische Wissenschaft: Verlag von Gustav Fisher, Jena, 3 vols.

Zeng, H., Backus, M. M., Barrow, K. T. and Tyler, N., 1996, Facies mapping from three-dimensional seismic data: Potential and guidelines from a Tertiary sandstone-shale sequence model, Powderhorn Field, Calhoun County, Texas: AAPG Bull., **80**, 16-46.

Chapter 4

Seismic reservoir mapping from 3D AVO in a North Sea turbidite system (The Glitne field)

4.1 Abstract

Reliably predicting lithologic and saturation heterogeneities is a key problem in reservoir characterization. The main goal of this chapter is to estimate uncertainties and map probabilities of occurrence of different lithofacies and pore fluids from seismic amplitudes in a North Sea turbidite system (The Glitne field). Based on the classification results in Chapter 3, we create cumulative distribution functions (cdfs) of seismic properties for each facies. Pore fluid variations are accounted for by applying the Biot-Gassmann theory. Then, we conduct AVO analysis to predict seismic lithofacies from seismic data. We analyze real CDP-gathers at several well locations, and successfully predict the seismic lithofacies indicated by the well-log data. This demonstrates the feasibility of AVO-analysis to predict seismic lithofacies. We assess uncertainties in AVO response related to the inherent natural variability of each seismic lithofacies using a Monte Carlo technique. AVO probability plots show that there are overlaps between different facies, but the most likely responses for each facies are nicely separated. Zero-offset reflectivity ($R(0)$) versus AVO-gradient (G) bivariate probability plots are created and calibrated to both 2D and 3D AVO inversion results. By combining the $R(0)$ and G values estimated from the seismic data with the bivariate probability density functions (pdfs) estimated from well-logs, we use both quadratic discriminant analysis and

Bayesian classification to predict lithofacies and pore fluids from the seismic amplitudes. The quadratic discriminant analysis is tested out on a synthetic seismic section, and the predicted facies match the "true" facies model very well, except in a zone where wavelet tuning occurs. For the 3D real data, the final results are spatial maps of the most likely facies and pore fluids, and their occurrence probabilities. These maps show that the studied turbidite system is a point-sourced sub-marine fan in which thick-bedded clean sands are present in the feeder-channel and in the lobe-channels, whereas interbedded sand-shale facies and shaly sands are found in interchannel and marginal areas of the system. Shales are located outside the margins of the turbidite fan. Oil is most likely present in the central lobe channel, and in parts of the feeder-channel.

4.2   Introduction

The development of 3D seismic imagery has given us a unique opportunity to predict reservoir geometries and properties with improved certainty, and in a more efficient way. Reservoir characterization increasingly relies on the information gained from 3D seismic data. In this study our goal is to improve our ability to use 3D seismic data to map reservoirs in North Sea turbidite fields, where wells are sparse and the traps are subtle.

Relating lithofacies to rock physics properties will improve the ability to use seismic amplitude information for reservoir prediction and characterization in these systems, as facies have a major control on reservoir geometries and porosity distributions. Facies furthermore occur in predictable patterns in terms of lateral and vertical distribution and can also be linked to sedimentary processes and depositional environments. Various workers have studied facies imaging from seismic amplitude maps, and have been most successful in fluvial systems where channel facies have been easily recognized (e.g., Brown et al., 1981; Rijks and Jauffred, 1991; Brown, 1992; Enachescu, 1993; Ryseth, et al., 1998). A methodology for facies mapping from seismic signatures (i.e., seismic pulse shape) using neural networks was first introduced by Neri (1997). Addy (1998) applied this methodology to a carbonate reef system. A few workers have studied the correlation between seismic amplitudes and lithology by seismic forward modeling (Varsek, 1985; Zeng et al., 1996). Zeng et al. (1996) linked lithofacies to rock physics properties and conducted a facies guided seismic modeling study of a micro-tidal shore-zone

depositional system. Furthermore, several workers have used seismic inversion to estimate lithology and reservoir properties from pre-stack seismic data (Lörtzer and Berkhout, 1992; Buland et al., 1996, Wrolstad, 1996, Hampson and Todorov, 1999).

We conduct seismic reservoir characterization constrained by the well-log rock physics and facies classification presented in Chapter 3, and apply it to the Glitne Field. The Glitne field is a turbidite system located in South Viking Graben, North Sea, whose reservoir sands represent the Heimdal Formation of Late Paleocene age and include an oil field of economic interest (Figure 4.1). By linking lithofacies to rock physics properties, using statistical techniques to account for natural variability within, and overlap between different facies, we obtain a probabilistic link between facies, rock properties, and seismic response. This allows us to predict the most likely lithofacies and conditional probabilities of facies from seismic data. The proposed methodology, including the steps presented in Chapter 2 and Chapter 3, ultimately improves the ability to delineate subtle traps and characterize reservoir units in complex depositional systems from seismic data.
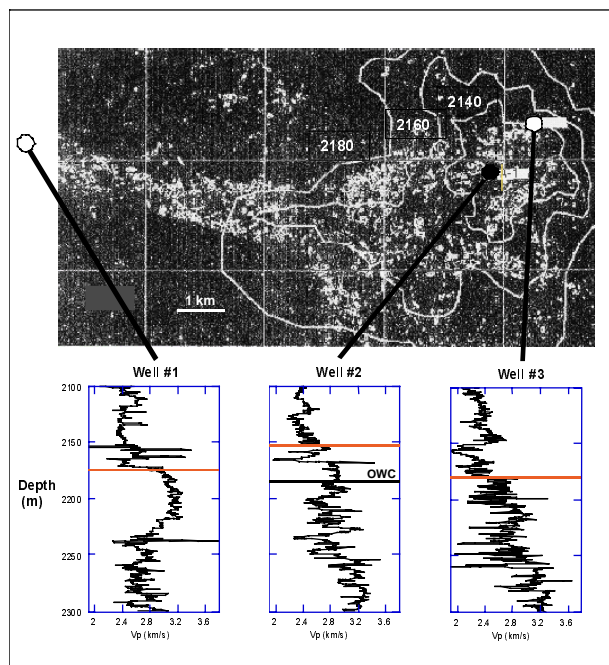
Figure 4.1: Seismic reflectivity map (above) of Top Heimdal Formation, corresponding to the orange lines in the well-logs (P-wave velocity) (below). The bright amplitudes reflect relatively strong positive stack responses. The three wells penetrate a submarine fan in the feeder channel (well #1), in a lobe-channel (well #2), and in the marginal area of the lobe (well #3). The Heimdal Formation dramatically changes character between the wells. Oil was encountered in well #2, and the area represents a commercial oil field, the Glitne Field. The contours in the seismic map are in two-way-traveltime (ms) and illustrate the structural topography of the lobe. (The reflectivity map is courtesy of Norsk Hydro).

4.3   Deterministic AVO analysis

4.3.1   AVO modeling and seismic detectability

Since the main goal of this chapter is to predict lithofacies from seismic data, we need to know whether it is possible to seismically discriminate the lithofacies defined in Chapter 3. If this is not the case, the lithofacies must be redefined. Because of the clean sand-pure shale ambiguity in acoustic impedance (Figure 3.7), there will also be an ambiguity in terms of zero-offset reflectivity, R(0). Hence, amplitude versus offset (AVO) analysis should be employed to detect seismic lithofacies from seismic data. The more linear trend in Vp/Vs ratio versus facies (Figure 3.7) should be recognized in terms of AVO response. It is well known that the Vp/Vs ratio has a strong impact on the offset-dependent reflectivity (e.g., Ostrander, 1984). In this section we therefore investigate the pre-stack seismic reflectivity, or AVO response, of the various seismic lithofacies.

AVO analysis is normally carried out in a deterministic way to predict lithology and fluids from seismic data (e.g., Smith and Gidlow (1987), Rutherford and Williams (1989), Hilterman (1990), Castagna and Smith (1994) and Castagna et al. (1996)). AVO seeks to extract rock parameters by analyzing seismic amplitude as a function of offset, or more correctly as a function of reflection angle. The reflection coefficient as a function of reflection angle is described by the complex Zoeppritz equations (Zoeppritz, 1919). For analysis of P-wave reflections, a well-known approximation is given by Aki and Richards (1980), assuming weak layer contrasts:

$$R(\theta_1) \approx \frac{1}{2}(1 - 4p^2 V_s^2)\frac{\Delta\rho}{\rho} + \frac{1}{2\cos^2\theta}\frac{\Delta V_P}{V_P} - 4p^2 V_S^2\frac{\Delta V_S}{V_S}, \qquad (4\text{-}1)$$

where:

$$p = \frac{\sin\theta_1}{V_{P1}} \qquad\qquad \theta = (\theta_1 + \theta_2)/2 \approx \theta_1$$

$$\Delta\rho = \rho_2 - \rho_1 \qquad\qquad \rho = (\rho_2 + \rho_1)/2$$

$$\Delta V_P = V_{P2} - V_{P1} \qquad\qquad V_P = (V_{P2} + V_{P1})/2$$

$$\Delta V_S = V_{S2} - V_{S1} \qquad\qquad V_S = (V_{S2} + V_{S1})/2$$

In the formulas above, p is the ray parameter, θ_1 is the angle of incidence, and θ_2 is the transmission angle. V_{P1} and V_{P2} are the P-wave velocities above and below a given interface, respectively. Similarly, V_{S1} and V_{S2} are the S-wave velocities, while ρ_1 and ρ_2 are densities above and below this interface.

Next, we do AVO modeling of the different facies defined in Chapter 3. Figure 4.2 shows the AVO curves for different half-space models, where facies IV is cap rock, and different facies are underlying. For each facies, the mean values of Vp, Vs and ρ, calculated from the training data in Chapter 3, are used as input in the modeling. We observe the clean sand-pure shale ambiguity (facies IIb and facies V) at near offsets, whereas clean sands and shales are distinguishable at far offsets.
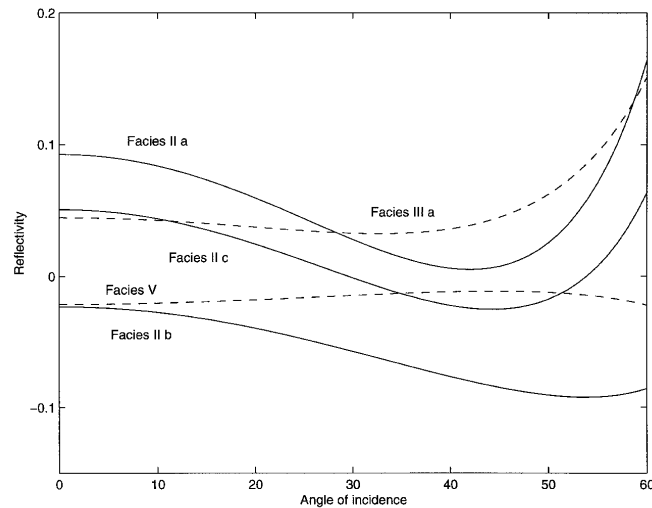
Figure 4.2: AVO curves for different half-space models (i.e. 2 layers - 1 interface). Facies IV is cap-rock. Input rock physics properties represents mean values for each facies.

4.3.2   AVO-analysis at the well locations

In this section, we assess the feasibility of the AVO method to discriminate lithofacies from real seismic data, by analyzing CDP (common-depth-point) gathers at well locations in a deterministic way. Figure 4.3 shows the real and synthetic CDP gathers at the three well locations in Figure 4.1, and the corresponding picked amplitudes at the Top Heimdal

horizon superimposed on exact Zoeppritz calculated reflectivity curves derived from the well-log data.
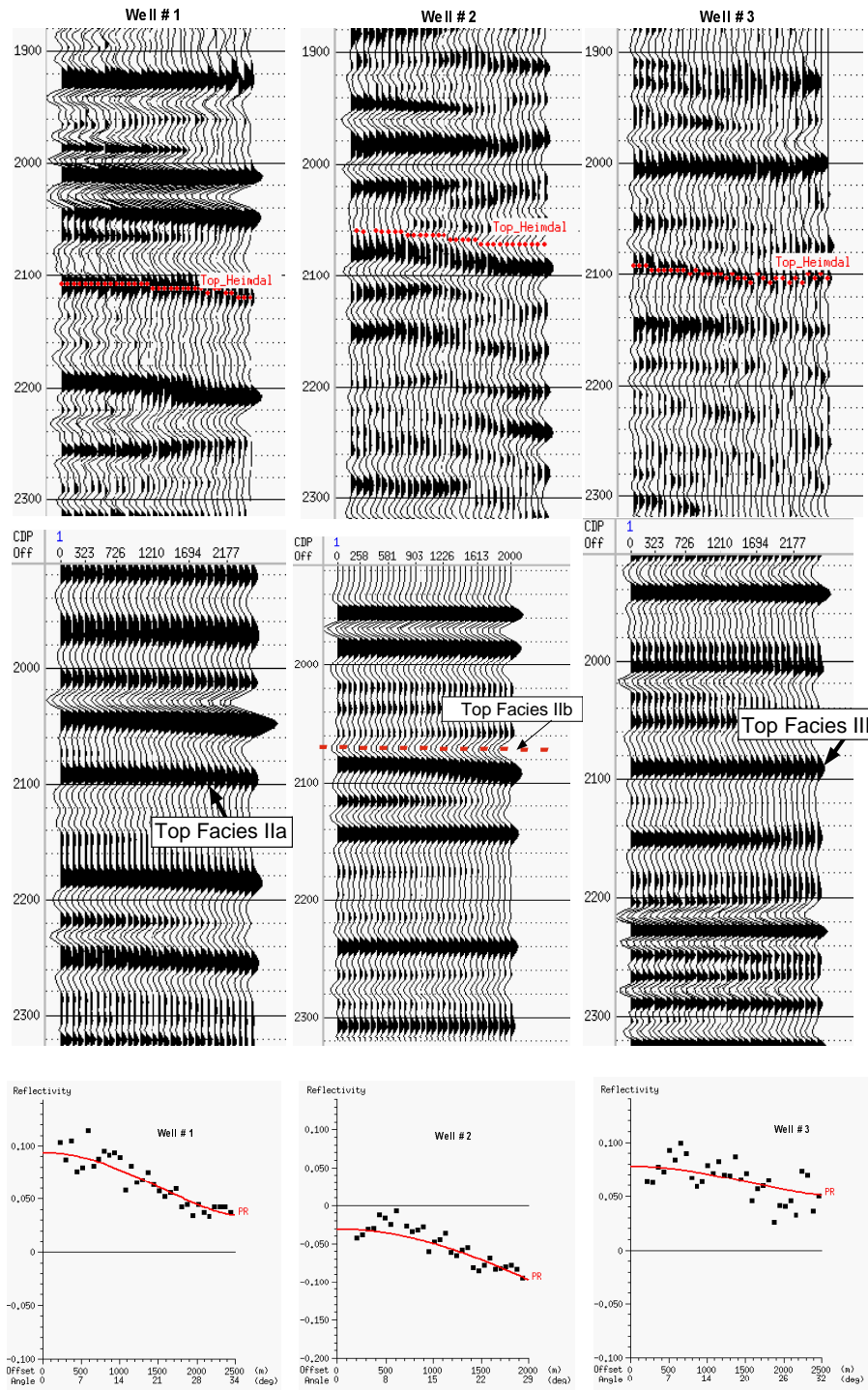
Figure 4.3: Real CDP-gathers (upper), synthetic CDP-gathers (middle) and AVO curves for wells # 1-3 (lower).

In well #2, the type well, the Top Heimdal sands are unconsolidated, represent oil-saturated sands, and are capped by silty shales. According to the saturation curves derived from deep resistivity measurements, the oil saturation in the reservoir varies from 20-80%, with an average of about 60% (see Figure 2.9). Because the sonic and density logs are assumed to measure in the mud filtrate invaded zone (0-10% oil), we do fluid-substitution to calculate the seismic properties of the reservoir using the Biot-Gassmann theory (Gassmann, 1951; Mavko et al., 1998) assuming a uniform saturation model. Before we do the fluid substitution, we need to know the acoustic properties of the oil and the mud-filtrate. These are calculated from Batzle and Wang's relations (Batzle and Wang, 1992). Input parameters for this calculation are as follows:

Oil GOR:	64 l/l
Oil gravity:	32 API
Oil density:	0.78 g/cm^3
Mud filtrate density:	1.09 g/ cm^3
Pore pressure at reservoir level:	20 MPa
Temperature at reservoir level:	77.2 ^{0}C

The corresponding AVO response shows a negative zero offset reflectivity and a negative AVO gradient.

In well #1, we have a water-saturated cemented sand below a silty shale. The corresponding AVO response in this well shows a strong positive zero-offset reflectivity and a relatively strong negative gradient. In lack of shear wave measurements in this well, we used a facies dependent Vp/Vs ratio derived from the training facies in well #2 (Figure 3.7) to calculate shear wave velocities. The vertical facies variation was determined by facies classification as described in Chapter 3.

Finally, in well #3 we observe a strong positive zero-offset reflectivity and a moderate negative gradient, corresponding to interbedded sand-shale facies capped by silty shales.

Also in this well shear wave information is not available, and a facies dependent Vp/Vs ratio is used to calculate the shear wave velocities.

Hence, we observe three distinct AVO responses in the three different wells. We conclude that the seismic lithofacies as well as the pore fluids control the AVO signature within our turbidite system. These results demonstrate the feasibility of AVO as a tool to predict lithofacies from seismic data in our case.

4.4   Creating non-parametric facies and pore fluid pdfs

Figure 4.4 depicts the classification results in wells # 1-3. We observe that the feeder channel sands in well #1 (2172-2220m) are mainly classified as cemented clean sands (facies IIa), whereas the lobe channel sands in well #2 (2155-2165m) are classified as uncemented sands (facies IIb). Furthermore, we observe that the Top Heimdal is represented by interbedded shales/sands in the lobe margin area where well #3 is located (2180-2240m). As confirmed in the deterministic AVO analysis in Figure 4.3, this dramatic variability in the lateral facies distribution going from a relatively proximal feeder-channel environment to a relatively distal lobe and lobe margin environment, has great impact on the seismic signatures in this turbidite system.
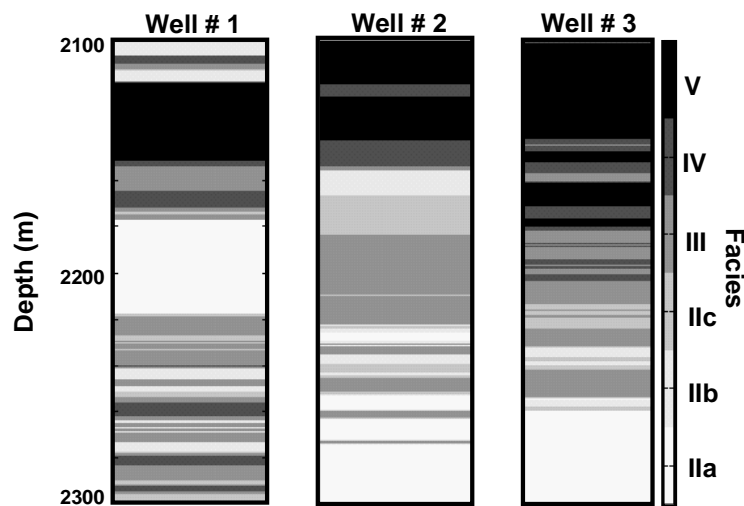
Figure 4.4: Seismic lithofacies classification results in the three wells shown in Figure 4.1. The channel sands in well #1(2172-2220m) are classified as cemented (IIa), while the marginal lobe facies encountered in well #3 (2180-2240m) are identified as interbedded sands-shales (III). Well #2 is the type-well and the reservoir facies comprise facies IIb at the top (2155-2165m) and facies IIc beneath (2166-2183m)

To correlate and describe the reservoir between the wells is an impossible task without using seismic data, and the goal is therefore to predict from seismic amplitudes the character of the reservoir in the interwell areas. In this section we generate probability density functions (pdfs) of seismic parameters based on the well classification, and these pdfs will then be used to create facies maps from seismic data.
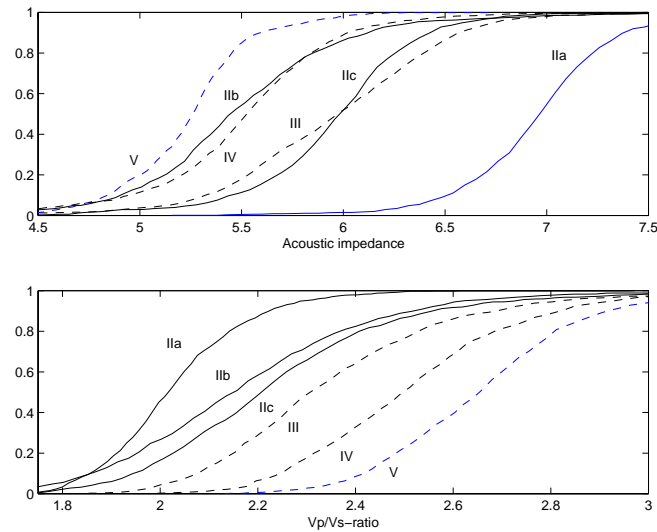
Figure 4.5: Cumulative distribution functions (cdfs) of acoustic impedance and Vp/Vs ratio for each of the brine saturated facies. We observe a much better discrimination in Vp/Vs ratio than in acoustic impedance.
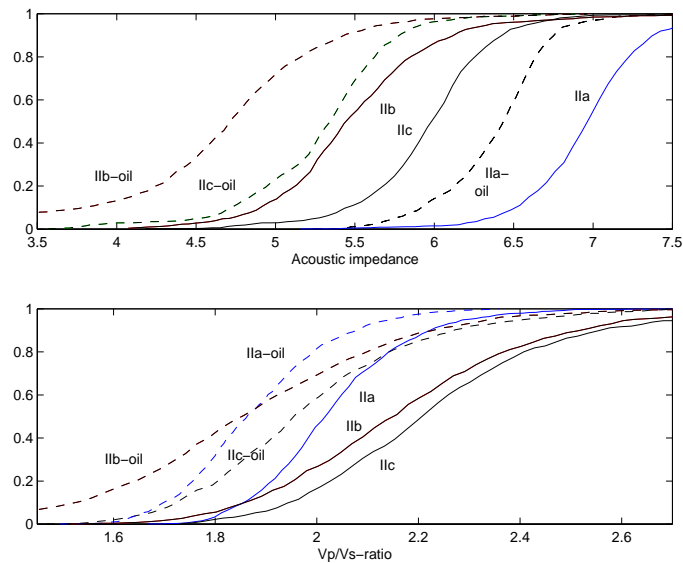
Figure 4.6: Cumulative distribution functions (cdfs) of acoustic impedance and Vp/Vs ratio for oil versus brine saturation in the sandy facies. We observe a much better discrimination in Vp/Vs ratio than in acoustic impedance.

Based on the facies classification, we first extract cumulative density functions of seismic properties for each of the lithofacies, and for oil-saturated sand facies (Figures 4.5 and 4.6). The oil-saturated cdfs were calculated from the water-saturated cdfs using the Biot-Gassmann theory (Gassmann, 1951; Mavko et al., 1998). As for the training data, we observe a much better discrimination in Vp/Vs ratio than in acoustic impedance in terms of lithofacies. The cdfs in Figure 4.6 show that Vp/Vs ratio also better discriminates pore fluids than acoustic impedance. Hence, as suggested in section 4.3, amplitude versus offset (AVO) analysis must be employed to predict lithofacies from seismic data. For analysis of P-wave reflections, the approximation given by Aki and Richards (1980; equation 4-1), can be further approximated (Shuey, 1985):

$$R(\theta) \approx R_0 + G \cdot \sin^2 \theta + F(\tan^2 \theta - \sin^2 \theta), \qquad (4\text{-}2)$$

where

$$R_0 = \frac{1}{2}\left(\frac{\Delta V_P}{V_P} + \frac{\Delta \rho}{\rho}\right),$$

$$G = \frac{1}{2}\frac{\Delta V_P}{V_P} - 2\frac{V_S^2}{V_P^2}\left(\frac{\Delta \rho}{\rho} + 2\frac{\Delta V_S}{V_S}\right),$$

and

$$F = \frac{1}{2}\frac{\Delta V_P}{V_P}.$$

This form can be interpreted in terms of different angular ranges, where R(0) is the normal incidence reflection coefficient, G describes the variation at intermediate offsets and is often referred to as the AVO gradient, whereas F dominates the far offsets, near critical angle. In this study we only need to consider the two first terms, valid for angles less than 30 degrees (Shuey, 1985):

$$R(\theta) \approx R(0) + G \cdot \sin^2 \theta, \qquad (4\text{-}3)$$

The zero offset reflectivity, R(0), is controlled by the contrast in acoustic impedance across an interface. The gradient, G, is more complex in terms of rock properties, but from the expression given above we see that the contrast in Vp/Vs ratio as well as the contrasts in Vp and density affect the gradient. The importance of the Vp/Vs ratio (or equivalently the Poisson's ratio) on the offset dependent reflectivity was shown by Ostrander (1984).

Based on the cdfs of velocities and density, we create probability density functions (pdfs) of AVO response for different lithofacies combinations, and assess uncertainties in seismic signatures related to the natural variability within each facies. Figure 4.7 shows examples of AVO pdfs for facies IIa and IIb with and without oil, capped by a silty shale (facies IV), which is the most common cap-rock observed above the Heimdal Formation in the area of study. The plots have been generated from the Monte Carlo simulated seismic properties drawn randomly from the two lithofacies cdfs, one for the cap rock and one for the underlying facies. First we simulated Vp and then Vs followed by density. We made sure the simulation honored the correlation between the three parameters. The corresponding reflectivity simulations are calculated using equation 4-3.
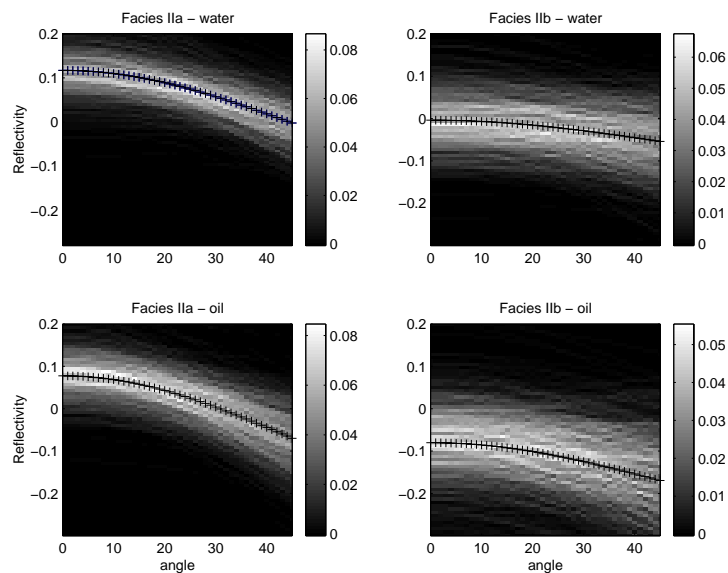
Figure 4.7: AVO pdfs for facies IIa and IIb with brine and oil, assuming facies IV as cap-rock. There are relatively large uncertainties in AVO response related to the variability within each facies, and there are overlaps between different facies, and pore fluid scenarios. However, the most likely AVO responses are distinct for each facies and pore fluid scenario. The superimposed black ticked lines are the deterministic AVO responses calculated from the median values of the cdfs. Equation 4-3 is used to calculate these pdfs. The results from this equation start deviate away from the exact Zoeppritz solution beyond 30 degrees.

Next, we generate bivariate probability density functions (pdfs) of zero-offset reflectivity (R0) versus the AVO gradient (G) (Figure 4.8). Also here we assume facies IV to be cap-rock. The center or peak of each contour plot represents the most likely set of R(0) and G for each facies. These pdfs show how R(0) and G can vary for a given facies combination, and that different facies combinations can have overlaps. However, the most likely set of R(0) and G is a unique characteristic of a given facies combination. For instance, a cemented sand (facies IIa) with brine will likely have a relatively large positive R(0) and a relatively large negative G, whereas an oil saturated cemented sand will more likely have a smaller positive R(0) and larger negative gradient. However, there is a great overlap between the water saturated and oil saturated sands, and oil sands can potentially show larger R(0) and smaller negative G values than water sands. There is also overlap between different types of sands. Another interesting observation is that even a shale-shale interface can cause a significant seismic response. In general, these pdfs create a probabilistic link between facies and seismic properties that can be used to predict the most likely facies and the conditional probability of a given facies, from seismic data.
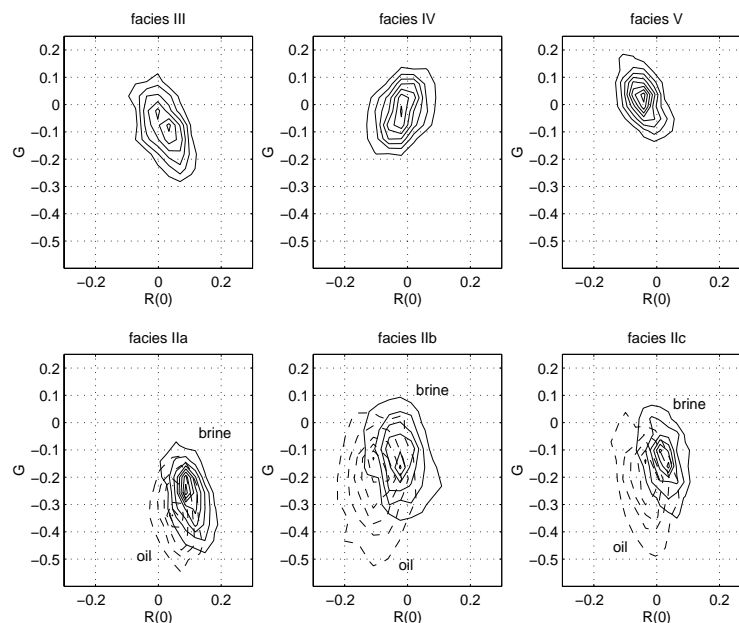
Figure 4.8: Bivariate distribution of the different seismic lithofacies in R(0)-G plane, assuming facies IV as cap-rock. The center of each contour plot represents the most likely set of R(0) and G for each facies.
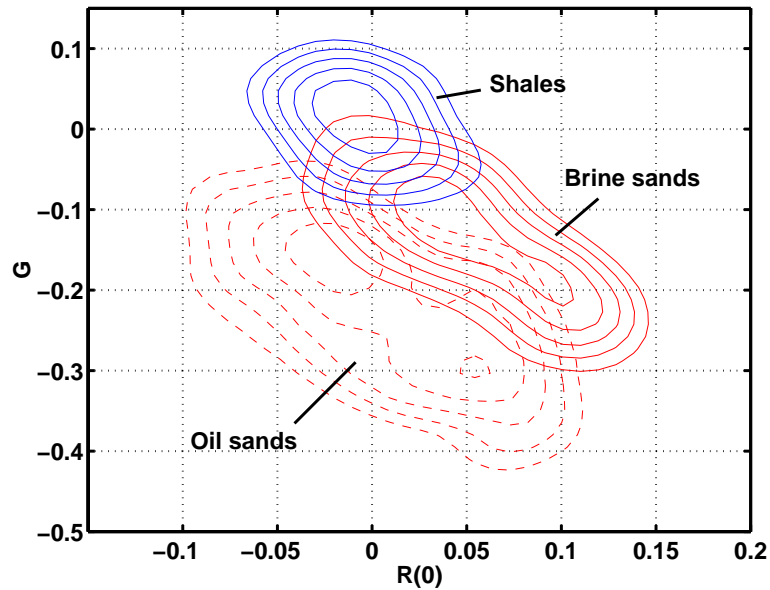
Figure 4.9: AVO-pdfs for main facies groups: oil sands, brine sands and shales. Only the isoprobability contours of 50 % and larger are included for each group. The R(0) and G pdfs nicely separates the three facies groups, but there are significant overlaps.

To better assess important trends in terms of the R(0)-G bivariate plots, we lump all oil sands together into one group, all brine sands in another and all shaly facies in a third one, and plot them together in the same cross-plot (Figure 4.9). Only the isoprobability contours of 50% and larger are included. In spite of significant overlaps, there is a fairly good separation between shales and sands, and between oil sands and brine sands. From these plots we observe that both R(0) and G are needed to discriminate facies and pore fluids in our case.

4.5   Characterizing facies and pore fluids from seismic data using probabilistic AVO analysis

Having explored the great facies variability and associated uncertainties in seismic properties, we realize that one must integrate the physical understanding of seismic signatures with statistical methods in order to predict reservoir characteristics from the seismic data.

In this section we use our AVO-pdfs to predict lithofacies and pore fluids from 2D and 3D pre-stack seismic data. We first conduct a realistic seismic forward modeling along a 2D cross section intersecting the type-well, and predict most likely lithofacies and

pore fluids along the top reservoir horizon from the synthetic data. This becomes a feasibility study on how well the methodology works, because the input earth model is known. Then we use the same technique to predict facies and pore fluids from the real 2D seismic section intersecting the well. Finally, we characterize facies and pore fluids, and map their occurrence probability, over the whole field using 3D AVO inversion results.

4.5.1   2D synthetic seismic modeling and test of methodology

Forward seismic modeling

We create a 2D earth model based on the facies information from the type well (well #2) combined with stratigraphic information from seismic interpretation of the 2D seismic line intersecting the type well (Figure 4.10). This model is a simplification of the real case. However, it is a realistic model that honors vertical facies variations observed in the type well, and takes into account the interpreted lateral extent and geometry of the observed facies.

In Figure 4.10, the seismic section is zero phase, peak frequency is 30 Hz, and a black peak in the wiggle display represents a positive stacked amplitude. The seismic horizons included in the figure correspond to major lithostratigraphic boundaries (see lithostratigraphic column, appendix A, Figure A-3). Top Balder is regarded the top of the Paleocene interval, and represents the boundary between overlying Eocene shales and Balder Formation tuff deposits. The thickness of Balder Formation is approximately a wavelength, so the trough beneath the peak horizon of top Balder, coincides with base Balder Formation/top Sele Formation. A subtle peak horizon is found at the base of Sele Formation and top of Lista Formation. Sele Formation has been recognized mainly as facies V (e.g., 2100-2140m in well #2), whereas Lista Formation has mainly been recognized as facies IV (e.g., 2143-2154m in well #2), according to the classification in Chapter 3 (see also Figure 4.4). The acoustic contrast between these different shales creates a recognizable seismic boundary. Top Heimdal is the interface of main interest, representing the top of the reservoir. This horizon changes character laterally, and a polarity change is observed in the stack section.
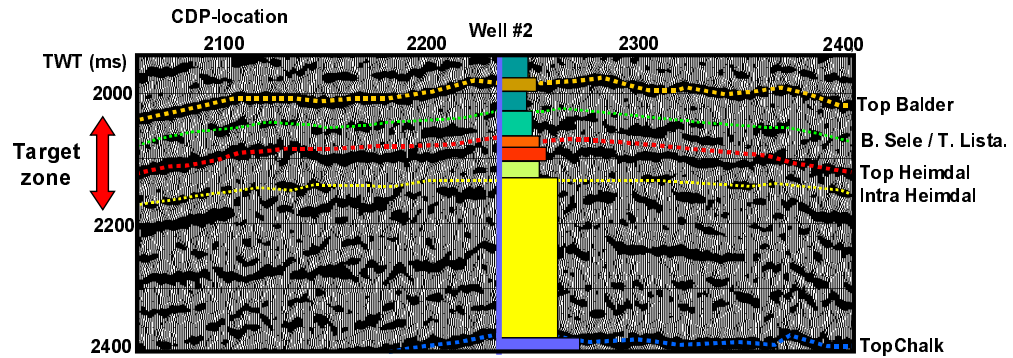
Figure 4.10: Seismic stack section intersecting the type-well (well #2), and superimposed facies observation at well location (From top to base: facies V = olive green, tuff = brown, facies IV = green, facies IIb-oil = orange, facies IIc-oil = red, facies III = light green, facies IIa-brine = yellow, Chalk = blue). Seismic interpretation combined with well-log facies and rock physics analysis constrains the synthetic seismic modeling.

We assume that this lateral variation reflects changes in the reservoir rock properties. We interpret the 2D cross-section to laterally transect from oil filled lobe sands at the well location, into marginal facies (facies III) in both directions. Marginal facies are observed conformably underlying the lobe sands, and these are believed to correlate with the marginal facies laterally from the lobe sands. This interpretation is guided by observations made in the seismic amplitude map in Figure 4.1, and the fact that facies III represents the top of the reservoir in well #3. Also, the general conceptual model of turbidite systems (Walker, 1978) in Figure 3.2, and application of Walther's law (Middleton, 1973; Chapter 3) support this interpretation. The resulting earth model is depicted in Figure 4.11.
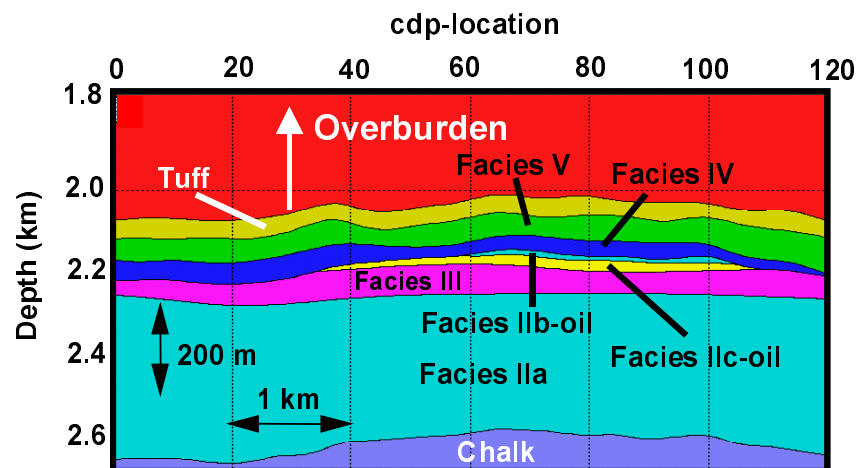
Figure 4.11: The geological model used as input for the seismic modeling. Elastic properties are given in Table 4.1. Note that this figure is not to scale. The lateral extension is 6 km and the vertical/lateral ratio is about 1/6.

Layer	Vp [m/s]	Vs [m/s]	Density [g/cc]	Vp/Vs	AI [m/s*g/cc]
0-150m water zone	1500	0	1	•	1500
Overburden (sand and shale)	1850-2390	450-950	1.8-2.2	4-2.5	3300-5260
Tuff (Balder Fm)	2600	1200	2.3	2.17	5980
Facies V (Sele Fm)	2300	950	2.25	2.42	5175
Facies IV (Lista Fm)	2400	1000	2.25	2.4	5400
Facies IIb-oil (Heimdal Fm)	2440	1300	2.02	1.88	4930
Facies IIc-oil (Heimdal Fm)	2630	1400	2.06	1.88	5420
Facies III (Heimdal Fm)	2750	1200	2.2	2.3	6050
Facies IIa (Heimdal Fm)	3100	1600	2.15	1.94	6650
Chalk (Ekofisk Fm)	3500	1700	2.3	1.94	8050

Table 4.1: Rock properties for each facies or layer in the earth model.

Facies and rock physics properties that build up the model are listed in the attached Table 4.1. Seismic forward modeling is conducted using a commercial 2D dynamic ray tracing package (NORSAR/NUCLEUS), assuming elastic and isotropic conditions. The seismic pulse used is a zero phase Ricker wavelet with 30 Hz center frequency. The modeling creates synthetic pre-stack seismic gathers along the section. Only primary reflectors are included, and the offset-dependent reflectivity is calculated using the Zoeppritz equations (Zoeppritz, 1919) at each interface. These gathers are stacked at limited ranges to create a near-stack, a far-stack and a full-stack seismic section corresponding to our earth model.
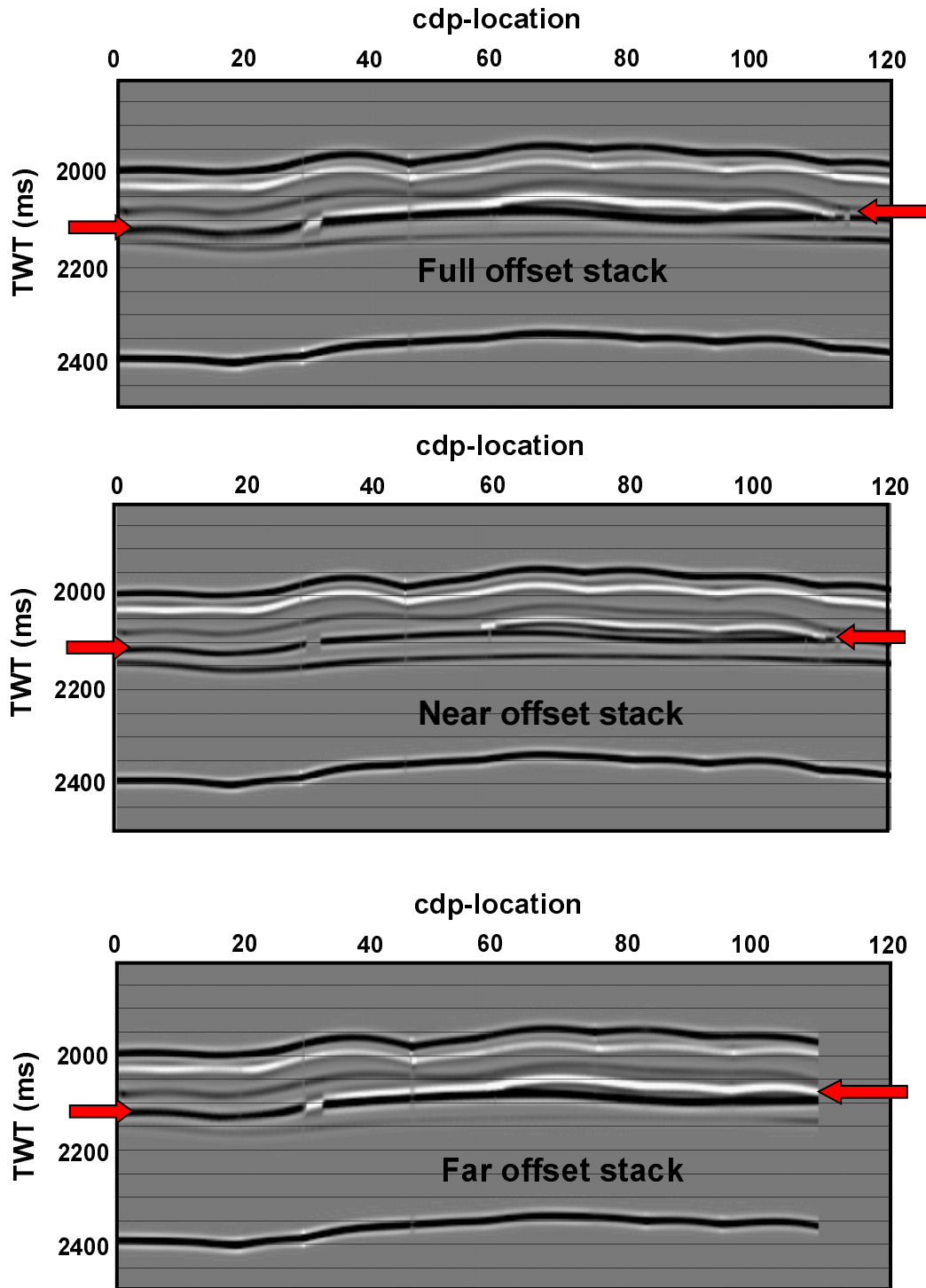
Figure 4.12: Synthetic seismic modeling results, including a full offset stack section (upper), a near offset stack (middle) and a far offset stack (lower). The data are zero-phase, and peak frequency is 30 Hz. White amplitudes represent negative reflectivity. Arrows on the sides indicate the top Heimdal horizon. Note the much brighter white amplitude on the far-offset stack section compared to the near offset stack section at the top Heimdal horizon (CDP range 35-110). Also note the phase change, and positive reflectivity along this horizon in the CDP range 0-35. The CDP spacing is 50m.

The results from the forward seismic modeling are shown in Figure 4.12. Comparing the synthetic full-stack section with the real stack section, we observe a good fit. This shows that the earth model can explain the seismic signatures observed in the real data. Considering the Top Heimdal horizon, we clearly observe a phase-shift as we go from marginal facies to the lobe on the full-stack. Correspondingly, we observe a bright spot on the far-stack with large negative amplitudes at the Top Heimdal level, while the near-stack shows a much weaker seismic response at this level.

AVO inversion and facies prediction from synthetic seismic data

The next step is to use the offset-dependent reflectivity information in the synthetic seismograms to see if we are able to predict the correct facies present immediately beneath the top Heimdal horizon. We extract R(0) and G along this horizon using AVO inversion based on generalized least-squares as available in a commercial AVO package (AVO Hampson & Russell). A common procedure to calculate R(0) and G from pre-stack seismic data is described below (e.g., Smith and Gidlow, 1987; Hampson and Russell, 1995).

For a given NMO-corrected CDP gather, R(t,x), it is assumed that for each time sample, t, the reflectivity data can be expressed as Shuey's formula (equation 4-3):

$$R(t, x) = R(t,0) + G(t)\sin^2 \theta(t, x), \qquad (4\text{-}4)$$

where $\theta(t,x)$ is the incident angle corresponding to the data sample recorded at (t,x). The relationship between offset(x) and angle(θ) is given by:

$$\sin \theta(t, x) = \frac{x}{\left(t_0^{\,2} + \dfrac{x^2}{V_{RMS}^{\,2}} \right)^{1/2}} \frac{V_{INT}}{V_{RMS}^{\,2}}, \qquad (4\text{-}5)$$

where V_{INT} is the interval velocity and V_{RMS} is the average root-mean-square velocity, as calculated from an input velocity profile (e.g., obtained from sonic log).

For any given value of zero-offset time, t_0, assume that R is measured at N offsets (x_i, i=1,N). Hence, we can rewrite the defining equation for this time as:

$$
\begin{bmatrix} R(x_1) \\ R(x_2) \\ . \\ . \\ . \\ R(x_N) \end{bmatrix} = \begin{bmatrix} 1 & \sin^2\theta(t,x_1) \\ 1 & \sin^2\theta(t,x_2) \\ . & . \\ . & . \\ . & . \\ 1 & \sin^2\theta(t,x_N) \end{bmatrix} \begin{bmatrix} R(t,0) \\ G(t) \end{bmatrix}
\tag{4-6}
$$

This matrix equation is in the form of **B**=**AC** and represents N equations in two unknowns. The least-squares solution to this equation is the so-called "normal equation":

$$
C = (A^T A)^{-1}(A^T B)
\tag{4-7}
$$

By solving the "normal equation", we obtain R(0) and G:

$$
R(0) = \frac{\sum_{i=1}^{N}\sin^2\theta(t,x_i) * \sum_{i=1}^{N}R(x_i)\sin^2\theta(t,x_i) - \sum_{i=1}^{N}\sin^4\theta(t,x_i) * \sum_{i=1}^{N}R(x_i)}{\left(\sum_{i=1}^{N}\sin^2\theta(t,x_i)\right)^2 - N*\sum_{i=1}^{N}\sin^4\theta(t,x_i)}
\tag{4-8}
$$

$$
G = \frac{\sum_{i=1}^{N}\sin^2\theta(t,x_i) * \sum_{i=1}^{N}R(x_i) - N*\sum_{i=1}^{N}R(x_i)\sin^2\theta(t,x_i)}{\left(\sum_{i=1}^{N}\sin^2\theta(t,x_i)\right)^2 - N*\sum_{i=1}^{N}\sin^4\theta(t,x_i)}
\tag{4-9}
$$

Combining the inverted AVO parameters, R(0) and G, with the bivariate probability distributions in Figure 4.8, we are able to predict the most likely seismic lithofacies present below the Top Heimdal horizon in the synthetic seismic section. The results are shown in Figure 4.13.

The lithofacies are indicated both in terms of a graph and as a color display. For computational reasons, the facies are given integer numbers 1 through 9, according to the following scheme:

1 = Facies IIa with oil   **4 = Facies IIa with brine**   **7 = Facies III**

2 = Facies IIb with oil   **5 = Facies IIb with brine**   **8 = Facies IV**

3 = Facies IIc with oil   **6 = Facies IIc with brine**   **9 = Facies V**

For convenience, the sandy facies with oil (1 through 3) are red colored, the sandy facies with brine (4 through 6) are yellow colored, whereas the shaly facies (7 through 9) are green colored.

In Figure 4.13, we have superimposed the true R(0) and G values calculated from Table 4.1, with the predicted (inverted) R(0) and G, respectively. There is a relatively nice fit between true and predicted R(0), whereas true and inverted G show larger discrepancy. The largest discrepancy in R(0) occurs where facies IIc is the true answer (CDP 36-60). However, facies IIc is relatively thin (~10m) and pinches out laterally. Hence the discrepancy can be related to tuning effects. The total thickness of the Heimdal Formation reservoir sands encountered in well #2, is about 35 meters. This is approximately half a wavelength, and at this location the sands are therefore seismically resolvable. Accordingly, we expect no major tuning other places along the line than at the pinch-out of facies IIc. Nevertheless, G shows relatively large discrepancy several places along the section. This could be due to focusing/defocusing of energy as some of the overlying horizons are rather curved, and this could have caused the non-hyperbolic moveouts that were observed locally. (The synthetic section used for the inversion has not been pre-stack migrated). The largest discrepancy in G, however, occurs in the pinch-out zone of facies IIc where we observe tuning of R(0). Consequently, this zone also has substantial error in terms of predicted facies. Shales of type IV and brine saturated sands

of type IIc are predicted where the true answer is oil saturated sands of type IIc. Elsewhere, the predicted most likely lithofacies underlying top Heimdal horizon, match very well with the true facies given in the earth model.
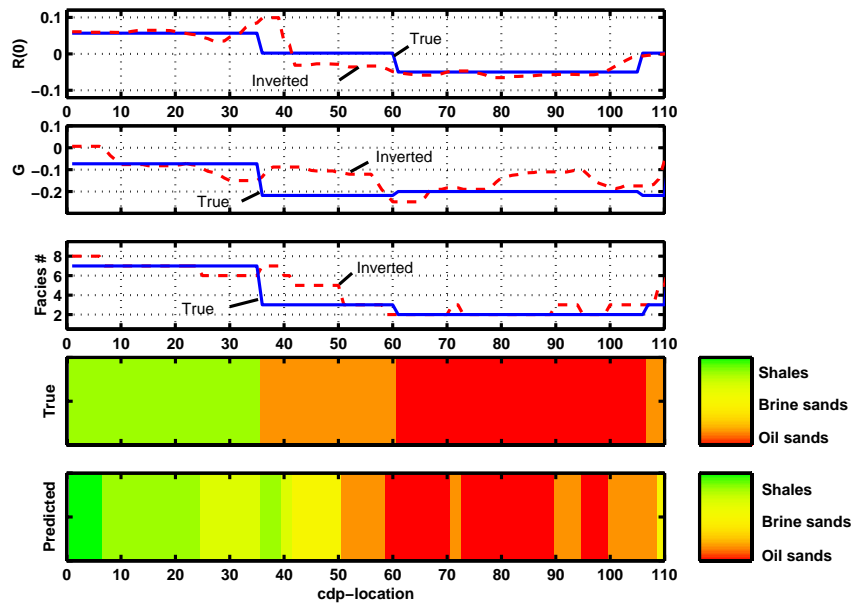
Figure 4.13: Seismic lithofacies prediction based on AVO-inversion along the top Heimdal horizon in the synthetic seismic section in Figure 4.12.

4.5.2 Facies and pore fluid prediction from real 2D seismic section

Now, we want to use the AVO-pdfs in Figure 4.8 to predict facies and pore fluids from a real 2D seismic section. We select the same 2D line as the one we derived our earth model from in the synthetic case (i.e., the seismic line intersecting the type well, well #2). Thus, if our earth model is more or less correct, we should expect the predicted reservoir rocks to be similar in the synthetic and the real cases. The assumption of a consistent cap-rock of facies IV is reasonable as the Lista Formation which overlies the Heimdal Formation reservoir rocks is normally represented by hemipelagic, silty shales (c.f., classification results in Figure 4.4).

Figure 4.14 shows the real 2D seismic stack section (wiggle-trace display, zero-phase wavelet, 30 Hz peak frequency) intersecting the type-well, the same line as shown in Figure 4.10. Figure 4.15 shows the extracted R(0) and G along the picked Top Heimdal horizon, and the predicted most likely seismic lithofacies present below the horizon. We

predict mainly oil sands of type IIb and IIc within the interval where the Top Heimdal horizon has a negative R(0). This is very similar to what is suggested in the earth model in Figure 4.11, though the sub-facies of sands are not always the same. Bear in mind that our oil facies pdfs represent 100% oil-saturation, whereas the true oil-saturation in the reservoir is varying between 0.2-0.8 (see Figure 2.9). This can have an effect on the prediction of sand type (IIb versus IIc).

In the area where the earth model has shaly sands or interbedded sand-shales (facies III), the prediction shows a more heterogeneous character. We observe both shaly sands (facies III) and thick-bedded, cemented sands (facies IIa) with oil. This indicates that there is likely another lobe-channel intersected by the real 2D line, that we did not include in the synthetic modeling. An alternative explanation is that this local oil-saturated sand is a result of tuning effects or noise in the data, as discussed for the synthetic case. A third explanation is lateral facies variations in the Lista Formation above the reservoir, obstructing our assumption of a cap-rock consisting of only facies IV. These issues are further discussed in section 4.5.
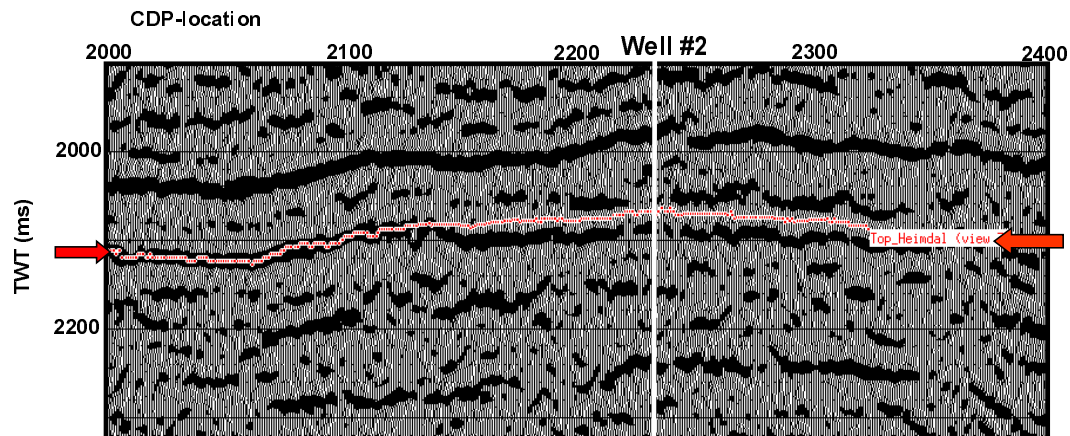
Figure 4.14: Seismic section intersecting the lobe of the submarine fan. The picked horizon and the arrows on the side indicate the top of the Heimdal sands. There is a marked phase-shift along the top Heimdal horizon. CDP-spacing is 18m.
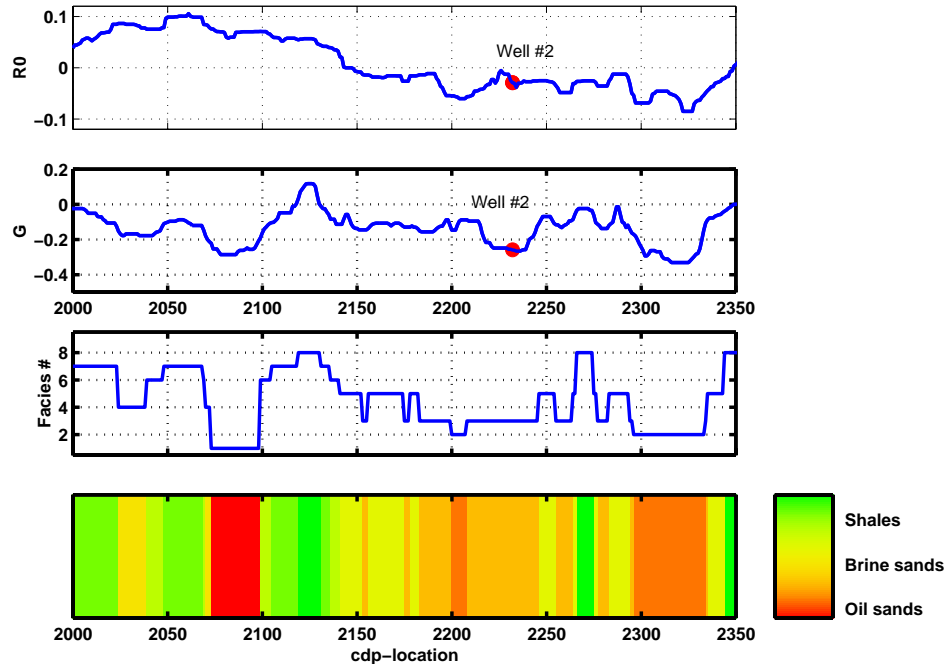
Figure 4.15: AVO inversion results and seismic lithofacies prediction along the 2D
seismic line intersecting well #2 (Figure 4.14).

4.5.3   Facies and pore fluid prediction and probability maps from 3D AVO data

The next step is to expand on our results from the 2D seismic line and perform facies
and pore fluid prediction from 3D seismic data. 3D AVO inversion is done on the
turbidite system using the same commercial inversion software that was used for the 2D
line (AVO Hampson & Russell). Again, we focus only on the horizon representing the
top of the system (top Heimdal). Figure 4.16 shows the three dimensional topography (in
two-way-traveltime) of this seismic horizon, where the geometries of the feeder-channel
and the lobe structure are outlined. The inversion gives us R(0) and G over the whole
area, along this horizon slice. Figure 4.17 shows the R(0) (left) and the gradient G (right).
These plots allow us to predict the most likely seismic lithofacies under this horizon. This
is done by combining the R(0) and G inverted from the seismic with the R(0)–G bivariate
pdfs derived from well-log data. Before we can do this, however, the inverted parameters
must be calibrated to the well-log values.
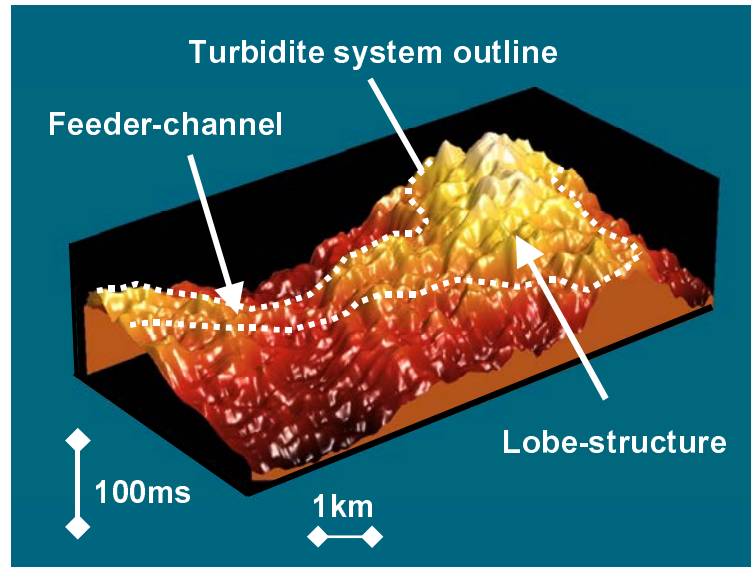
Figure 4.16: 3D seismic topography of top Heimdal horizon (traveltime). The depositional geometry of a feeder-channel and fan lobe is outlined (compare to Figure 4.1).
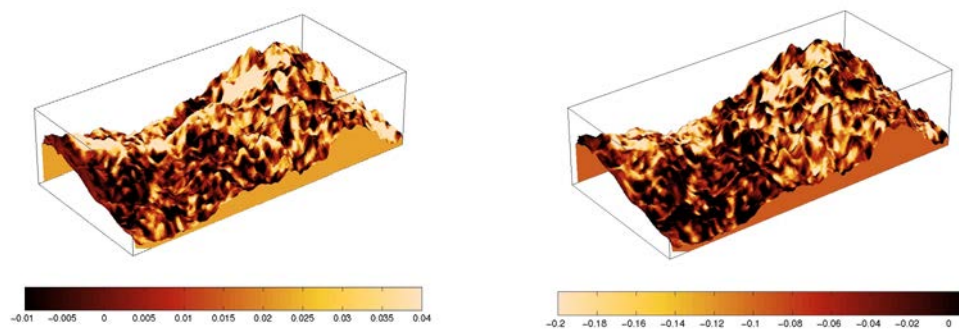
Figure 4.17: Zero-offset reflectivity, R(0) (left) and AVO gradient, G (right) along top Heimdal horizon.

Figure 4.18 shows the comparison between the well-log derived R(0) and G values and the R(0) and G from the AVO inversion. The upper left subplot shows the global training data from the well-logs. In the upper right subplot are the raw unscaled R(0) and G values derived from the least-squares AVO inversion. We calibrate the inverted R(0) and G at well #3. In this well we observe facies III beneath the top Heimdal horizon. We first calculate the mean uncalibrated R(0) and G from a small area around the well (approximately 200m x 200m). Then we calibrate these values to the mean values of R(0) and G of facies III calculated from the well-log data. The calibrated seismic data are shown in the lower right subplot.

The smaller scatter in R(0) and G in the seismic data compared to the well-log data is expected because of the scale difference. We assume that the well-log-derived pdfs still can be used to predict facies and pore fluids from the seismic data. This assumption implies that all the facies present beneath the top Heimdal horizon are also present in the global well-log training data. In order to compare the well-log R(0) and G with the calibrated R(0) and G from the seismic, we superimpose the estimated well-log pdf (lower left subplot in Figure 4.18) with the seismic data. The calibrated values match the well-log pdf very nicely.
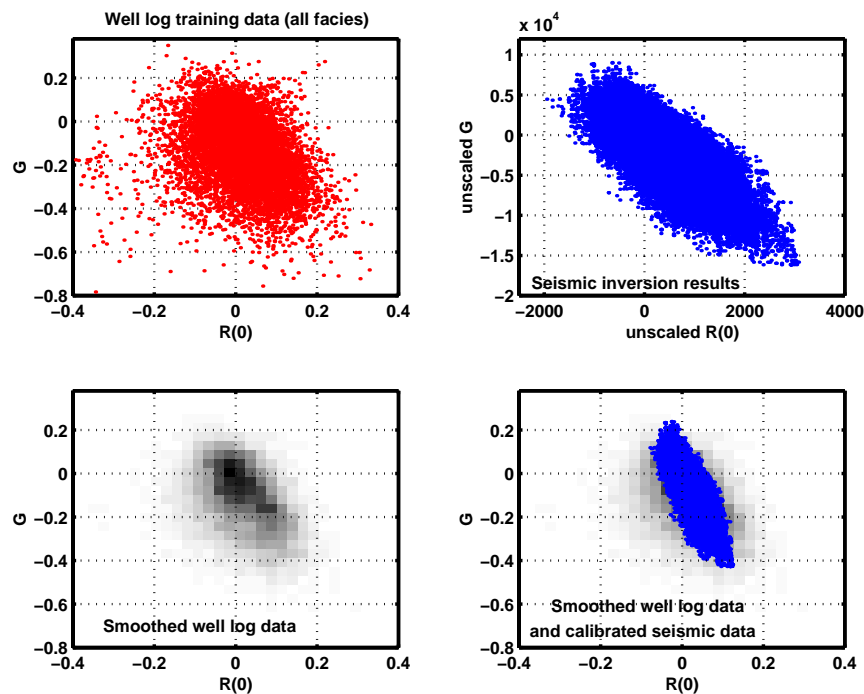
Figure 4.18: Comparing the global training data of R(0) and G derived from well-log data (upper left; Monte Carlo simulated values) to 3D AVO inversion results (upper right). The calibrated AVO parameters show a smaller range than the well-log data, but the scatter match nicely with the distribution of the well-log pdf (lower left and right). The dark colored two-dimensional bins in the lower left subplot represent relatively large frequencies of data points within a bin.

The next step is to use the well-log derived AVO pdfs to predict facies and pore fluids from the seismic data. To get a general picture of the reservoir, we first separate only between oil versus brine, and sands versus shales. Hence, we group similar facies together. Facies IIa with oil, IIb with oil and IIc with oil are lumped into a facies group referred to as oil sands. Similarly, we have created a brine sands group. Facies III, IV and

V have been lumped into a facies group of shales. First, we apply the Mahalanobis distance method to calculate the most likely facies group and pore fluid. The results are shown in Figure 4.19 (left: 3D topography; right: map-view). We predict oil-saturated sands in the lobe area where the lobe is structurally highest. The rest of the lobe area is most likely water-saturated according to the prediction. Furthermore, we predict oil-filled sands in the upper feeder-channel. Outside the submarine fan, mainly shale is predicted to be the most likely facies. The exception is an area just north of the feeder-channel where oil and brine sands are predicted. If this prediction is correct, it could imply the presence of some overbank sands.

The overall prediction is reasonable in terms of facies and pore fluid distribution. The sands are mainly predicted in the channel and lobe areas whereas oil is predicted in the structurally highest areas of the sand deposits.
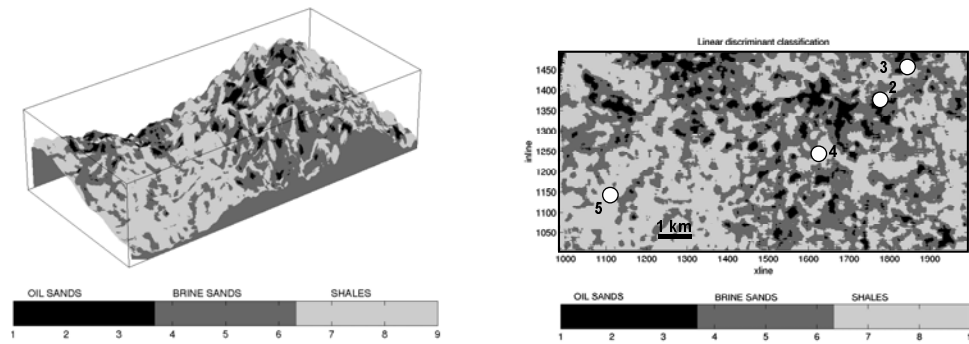
Figure 4.19: Lithofacies prediction beneath a seismic horizon with 3D topography (left) and in map-view (right).

The next step is to use non-parametric pdfs (i.e., PDF classification) to calculate the conditional posterior probabilities of the various facies groups and pore fluids. Figure 4.20 shows two map views of the top Heimdal horizon calculated from the well-log derived pdfs, one with the non-parametric facies classification results and one with the estimated probability of oil sands given the observed R(0) and G:

$$P\{oil|R(0),G\}. \qquad (4\text{-}10)$$

The map to the left shows the most likely facies and pore fluid. The results are very similar to the results from the quadratic discriminant method (see Figure 4.19). The oil sands are predicted mainly in the feeder-channel and in the central part of the lobe. The map to the right shows the probability of oil sands, and in accordance to the most likely facies map, we recognize relatively high probabilities in the central lobe, in the upper feeder-channel and in the possible splay deposits north of the feeder-channel. Outside the turbidite system, there are very low probabilities of oil sands.
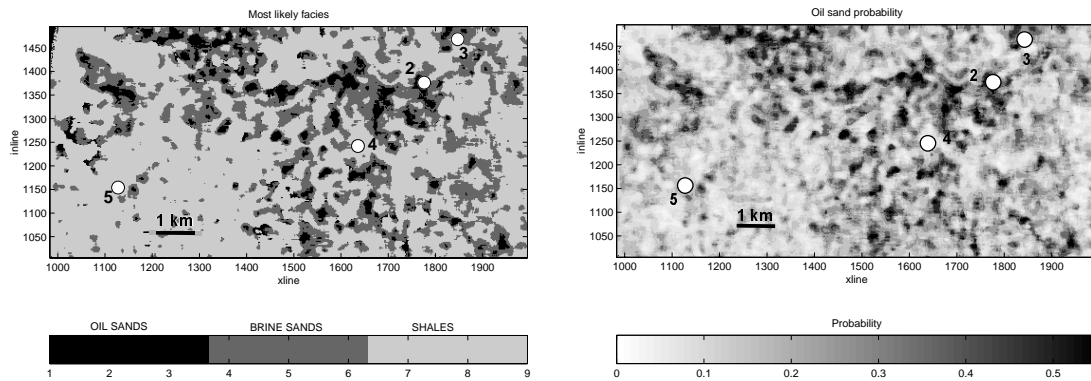
Figure 4.20: (Left) Most likely facies derived from pdfs; (Right) Oil sand probability.

Figure 4.21 shows probability of oil sands (upper left), brine sands (upper right), brine and oil sands together (lower left), and shales (lower right). The high probabilities of oil and brine sands together (sand probability map) nicely depict the depositional pattern of a submarine fan. Also note that there are relatively high probabilities of brine sands even where the most likely sands were predicted to be oil sands. This stems from the fact that brine sands and oil sands have a large overlap in terms of R(0) and G (see Figure 4.9). The low probabilities of shales in the lower right map depict the depositional pattern of a submarine fan as shales are found outside the margins of the system and in inter-channel areas of the lobe complex.
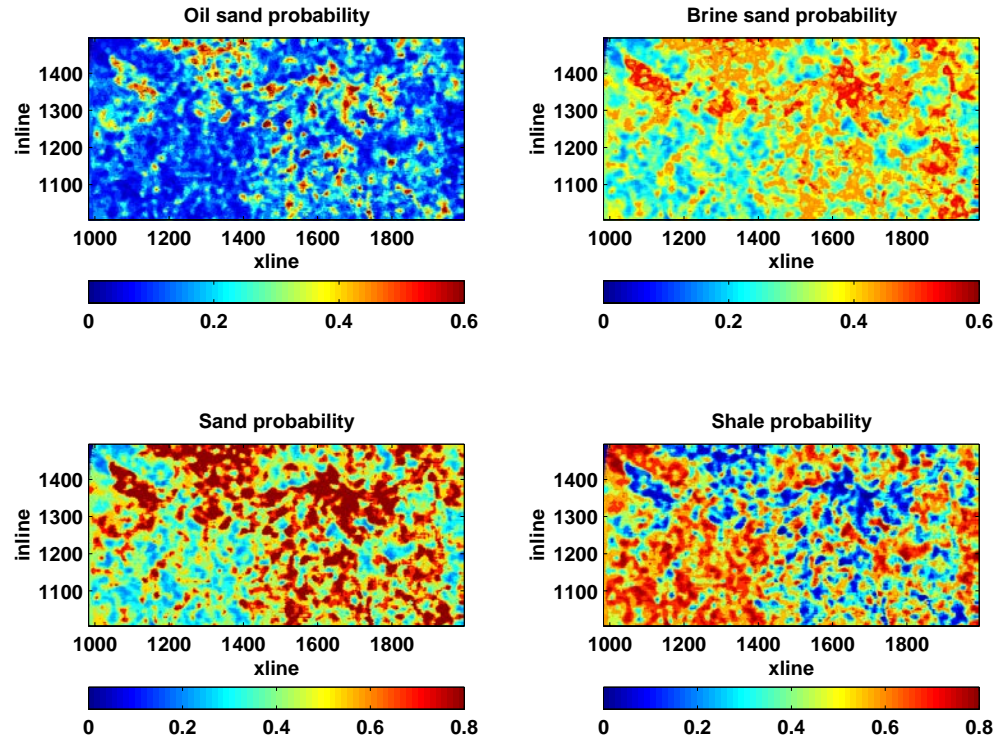
Figure 4.21: Probability maps of different grouped lithofacies.

We want to analyze more detailed probability maps of individual facies to gain a better sedimentologic understanding of the studied turbidite system. Figure 4.22 shows probability maps of the different facies. Because there are nine facies including oil saturated facies, probabilities larger than 0.11 indicate more likely occurrence than just by random chance. The upper three subplots show the three different subfacies of sand saturated with oil. We observe relatively high probabilities of facies IIa with oil predominantly in the upper feeder-channel and on the lobe structure, while faces IIb with oil has relatively low probabilities over the whole system. Facies IIc with oil has relatively high probabilities in scattered areas of the lobe area. Facies IIa with brine shows a very similar probability map as the same facies with oil, with relatively high probabilities in the feeder-channel and proximal parts of the lobe. This could be explained by the fact that facies IIa is a stiff rock type resulting in a large overlap between the pdfs of oil and brine (Figure 4.8). Facies IIb with brine shows relatively large probabilities in the southern lobe area, north of the feeder-channel and in a small area just south of the feeder-channel. The two last occurrence probabilities could reflect overbank or splay sands from the feeder-channel. Facies IIc is found to have relatively high probabilities

over a large area including the feeder-channel, lobe-structure and an area north of the feeder-channel. Facies III shows relatively large probabilities along the feeder-channel and in the distal portions of the lobe. This is in accordance with conceptual models that inter-bedded sands-shales and shaly sands occur in marginal areas of a turbidite system, either as levee deposits associated with channels, or in distal portions of the lobe (see Walker's conceptual model, Figure 3.2). Finally, both facies IV and V, show high probabilities outside the turbidite system.
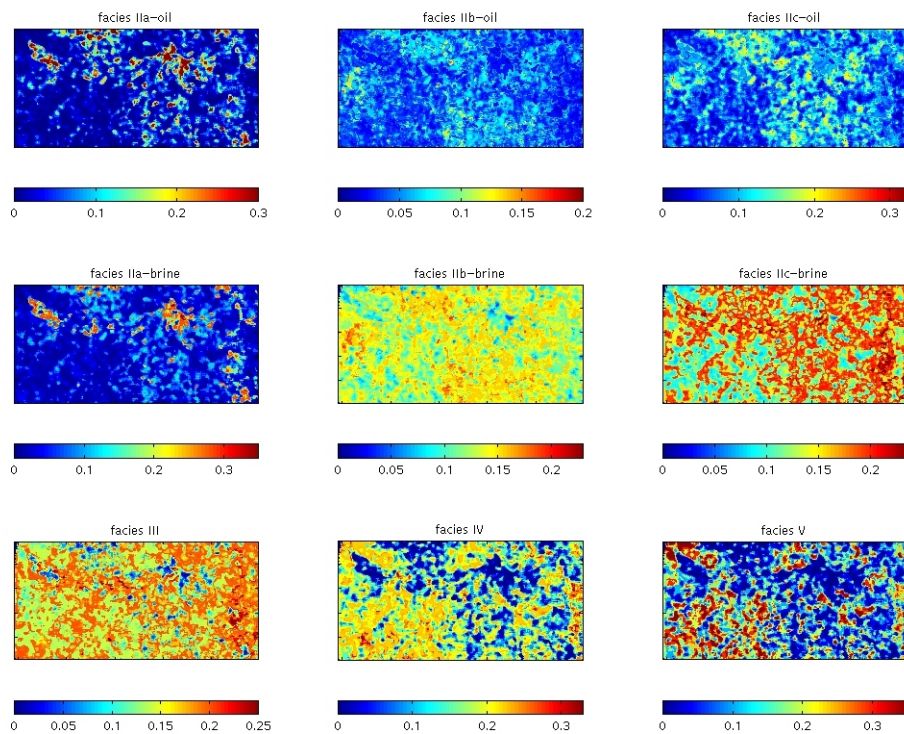
Figure 4.22: Estimated probability maps of the various facies defined in this study.

4.5.4   Blind test at well locations

Four wells penetrate the turbidite system inside the area of seismic inversion (see Figures 4.19 and 4.20). The calibration was done over an area around well #3, with the mean value of facies III. The exact R(0) and G values estimated at well #3 are also classified into the correct facies III (see Table 4.2). Based on the calibration at well #3, the three other wells were blind-tested in terms of facies and pore fluids. The results are

listed in Table 4.2. Starting from the left, well #5 encountered only shales at the target level, and the most likely lithofacies according to the seismic prediction is shale. Well #4 is located within lobe sands, but mostly brine saturated (the oil column is about 10m out of a total approximately 45m of reservoir sands). In contrast, the most likely facies is facies III, interbedded sand-shales. However, the total probability of thick-bedded sands (oil and brine) is 0.54, which is higher than the probability of shaly facies (0.46). Well #2 (the type well) located structurally higher on the lobe, encountered 35 meters of oil sands. We predict most likely brine sands, but the well is just on the fringe of an area of predicted most likely oil sands.

WELL	FACIES (well-log observation)	P{Sand} (only thick-bedded)			P{Shale} (includes inter-bedded sand-shales)	Facies correct ?	Fluid correct ?
		P{oil}	P{Brine}	P{Total}			
2	Thick-bedded oil sands (II)	0.25	0.44	0.69	0.31	Yes	No
3	Interbedded sand-shale (III)	0.1	0.31	0.41	0.59	Yes	-
4	Thick-bedded brine sands (II) (Thin oil cap)	0.16	0.38	0.54	0.46	Yes	Yes
5	Silty shale (IV)	0.09	0.23	0.32	0.68	Yes	-

Table 4.2: Blind test results at well locations. (P{x} indicates the probability of x to occur at a given well location). Shales occur only as brine-saturated, hence we include the dash symbol in the fluid prediction column for well #3 and well #5.

4.6   Discussion

We have shown how we can use statistical rock physics to translate 3D AVO inversion results into lithofacies and pore fluid probability maps. In our case we have successfully mapped the most likely distribution of good quality reservoir sands in a North Sea turbidite system and estimated the probability of finding oil within these sands. These maps are ultimate products in the process of geologically characterizing reservoirs from seismic data. They can be used as inputs for various decision and risk analyses during exploration and development, or as constraints for reservoir modeling and flow simulation during production and reservoir forecasting.

Although we have obtained a successful characterization of the turbidite system, it is important to be aware of certain limitations of the methodology proposed in this study. Firstly, we only used Vp and gamma ray to do the multivariate classification of facies from well-logs. More logs could have been used in this procedure, and it would especially be better to include other logs such as density and shear-wave velocity (Vs). Since the ultimate goal is to predict facies and pore fluids from seismic data, it is important that the training data clusters (i.e., training facies) express unique sets of rock physics properties. However, Vs was not acquired in most of the wells in the area, and we wanted to have comparable results from all the wells. Density logs were found to be corrupted by washouts in certain zones, predominantly in shaly intervals. The zones of corrupted density logs were identified by abnormally low density values for shales (less than 2.0 g/cm^3) combined with increased bore hole radius as measured by the caliper logs. The type-well also suffered from washouts, but in this well the density log was corrected for this effect. The test-classification of the training data using Vp, Vs, and porosity calculated from density logs gave very similar success rates to using only Vp and gamma ray (see Chapter 3.6). Thus, in our case, using only Vp and gamma ray during the classification is sufficient. In our calculation of acoustic impedance and Vp/Vs cdfs, we excluded data from zones where the density log was corrupted and wells where Vs was not available, respectively.

Another important factor to be considered in our methodology is that all the facies in the training data are at a well-log scale, whereas the prediction is at the seismic scale.

This issue could be handled by creating physically upscaled pdfs from the well-logs using effective medium theory, especially for the interbedded sand-shale sequences (facies III). An upscaling of thin-bedded sequences using effective medium theory (e.g., Backus, 1962) is needed if the intercalating layers have strong contrasts in the elastic properties. However, the interbedded sands-shales in the studied turbidite system are comprised of thin-bedded sands that have weak contrasts in seismic properties compared to the intercalating shales (c.f., small range in Vp within the facies III cluster in Figure 3.6). In core observations made of facies III in well #2, the thin-bedded sands seemed to have a relatively high clay content, while the thin-bedded shales seemed to have a relatively high quartz content (i.e., silt). From Marion's (1992) study of sand-shale mixtures, we know that shaly sands and silty/sandy shales can have similar elastic properties. We therefore do not expect the thin-bed scale effect on rock physics properties to be important for facies III, nor for the more thick-bedded facies observed in this turbidite system.

Another aspect of scale that can cause problems to AVO-analysis is tuning effects. Interference between the top and the base of individual layers that are near the seismic resolution limit can cause amplitude anomalies that are not related to rock physics properties. The effect of tuning on AVO has been demonstrated by Bakke and Ursin (1998) and Don (1998), among others. The AVO inversions employed in this study assume no tuning. As a result the parameter estimates can be wrong in areas where tuning occurs. Consequently, classification and prediction of facies and pore fluids can also be wrong. This was manifested in the synthetic modeling and prediction case (section 4.4.1). The training pdfs could be recreated to include the uncertainties caused by tuning.

The AVO inversion procedure itself is also a source of error. We use a linear approximation of the Zoeppritz equations in our calculation of R(0) and G. This approximation is known to be accurate for angles of incidences up to approximately 30 degrees (Shuey, 1985). The data inverted in our case are not exceeding this range, so the approximation is valid. The linear AVO inversion is furthermore sensitive to uncharacteristic amplitudes caused by noise (including multiples) or processing and acquisition effects. A few outlying values present in the pre-stack amplitudes are enough to cause erroneous estimates of R(0) and G. The 3D AVO inversion software used in this study, as opposed to the 2D AVO inversion software, applies a robust estimation

technique (Walden, 1991) to limit the damage of outlying amplitudes. Another potential problem during a sample-by-sample based AVO inversion are errors in the moveout correction (Spratt, 1987). Ursin and Ekren (1994) presented a method for analyzing AVO effects in the offset domain using time windows. This technique reduces moveout errors and creates improved estimates of AVO parameters.

Cap-rock anisotropy and other overburden effects could also influence the AVO-analysis. We have neglected the effect of anisotropy in this study. In particular, some of the shales may be transverse isotropic. Blangy (1994) showed how transverse isotropy of shaly cap-rocks could drastically influence the AVO response of a reservoir. Moreover, focusing and defocusing of wave energy caused by lateral velocity variations in the overburden can affect the AVO inversion results at a given target level. We suspect this to play a role in the Glitne area, based on overburden observations of shale deformation at ca. 1 km depth. The rugged traveltime map in Figure 4.14 can reflect lateral velocity fluctuations related to the shale deformation. If overburden variation is statistically homogeneous over the area, however, the calibration of the inverted R(0) and G with the well data partly accounts for this uncertainty. Local overburden effects on the other hand (e.g. major faults, shale diapirs, gas pockets etc.), can cause non-linear moveouts and abrupt changes in the offset dependent reflectivity. In this case, the straight-line approximation of Shuey (1985) breaks down, and the estimation of R(0) and G will be meaningless. Chiburis (1993) showed how normalizing a target horizon to an overlying reference horizon could reduce the effect of local velocity variations in the overburden on AVO analysis.

The pick of seismic horizon also represents an uncertainty. We do not know for sure if the seismic interpretation of the top Heimdal horizon in our 3D case is correct everywhere. If the horizon is incorrectly picked, the estimated AVO data we use are not representative of our reservoir. As we have observed in the 2D cross-section intersecting well #2, polarity reversals occur along the top Heimdal horizon. Picking these can be a very difficult task. In fact the 3D interpretation of the top Heimdal horizon, conducted prior to this study, was made based on the belief that the Heimdal sands always have much higher impedance than overlying shales, resulting in a consistent positive reflector. This study shows that this is not the case, as variation in sand texture has a dramatic

impact on the seismic response. However, it was an impossible task to double-check the 3D interpretation at every CDP gather prior to the 3D inversion. Therefore, the predictions from the 3D data can be affected by a subjectively picked horizon that not necessarily coincides with the true top reservoir horizon. In particular, some of the unconsolidated sands saturated with oil, seen on the 2D data as negative stack amplitudes (Figures 4.14 and 4.15), are not detected in the 3D case (Figure 4.22).

Another important issue is whether the well-log training data are representative of the statistics of the entire reservoir. The well-log pdfs are calculated from vertically stacked facies, whereas the predicted facies are located laterally beside each other. Based on Walther's law of facies, we believe that the different facies observed vertically to each other in the wells are also present laterally over the large area where 3D seismic inversion is done. However, there may be facies observed in the wells that are not present beneath the top Heimdal horizon. The opposite could also occur, namely, that there are facies we have not observed in the wells present beneath the top Heimdal horizon.

Moreover, it is important to note that in the lithofacies prediction from AVO parameters we assume the cap-rock to be facies IV (silty shale), which is not necessarily true everywhere. Nonetheless, well-log observations indicate that the top Heimdal is consistently capped by a silty shale, so the assumption is reasonable. Other cap-rocks could be included in the prediction, but this could on the other hand cause more ambiguities in the results. We are, however, including the variability within silty shales in the calculations of the pdfs.

Finally, regarding the spatial distribution of facies, one future expansion on this study would be to include spatial statistics in the facies prediction (e.g., Tjelmeland and Omre, 1996). This technique would imply a better control on the lateral facies transitions during the prediction, but requires *a priori* information about the lateral correlations. The latter is difficult to gain with the sparse well control in many North Sea turbidite fields.

With all these potential limitations and uncertainties that have not been considered, we still feel that the contribution of including the uncertainties related to variability in facies and rock physics properties strengthens the validity of reservoir characterization from 3D seismic data. Also, by linking the rock physics properties and seismic signatures to sedimentary facies, we can determine if our results are geologically plausible. In a

complete assessment of the uncertainties of reservoir characterization from seismic data, however, stochastic models of all the other factors mentioned above should be included.

The blind testing of wells (Table 4.2) represents a means of validating our methodology. The correct facies were predicted in all the wells, whereas pore fluid was incorrect in one well. The match between seismic predictions and well-log observations is not perfect, but that is not expected. Boreholes are "needle pin points" into the underground, whereas seismic data contains information from a relatively large area given by the Fresnel zone size. This is the reason why we calibrated the seismic data from an area around well #3. In addition, high frequency random noise is present in the well-log data, which makes the comparison between seismic and well-log data even more difficult. Nevertheless, the blind test results indicate that our methodology is reliable.

4.7   Conclusions

- We have presented a strategy to predict reservoir characteristics from seismic data. Based on the facies classification in Chapter 3 we have created non-parametric pdfs of seismic parameters. These have been used to characterize seismic lithofacies and pore fluids from seismic amplitude data.

- In the studied North Sea turbidite system, we find that different lithofacies can have similar acoustic impedance values. However, the Vp/Vs-ratio resolves these ambiguities. Hence, the set of AVO parameters R(0) and G will be characteristic for any of the defined facies, yet with some degree of overlap. R(0) contains information about the acoustic impedance while G contains additional information about the Vp/Vs ratio. Consequently, AVO analysis must be employed to predict lithofacies and pore-fluids from seismic data in this case.

- By combining AVO parameters estimated from seismic inversion with bivariate pdfs estimated from well-logs, we use Bayesian classification to predict lithofacies and pore fluids. The final results are spatial maps of the most likely facies and pore fluids, and their occurrence probabilities.

- We find that the system is a point-source sub-marine fan in which thick-bedded sands are indicated in the feeder-channel and in the lobe-channels, while

interbedded sand-shale facies and shaly sands in inter-channel and marginal areas of the system. Furthermore, we predict presence of oil both in the structurally highest part of the lobe and in parts of the feeder-channel.

- In general, our methodology provides a strategy to generate facies probability maps from 3D seismic data that can be used as input for well-log planning and risk analysis in hydrocarbon exploration and reservoir development. Such maps can also serve as constraints in reservoir simulation and production forecasting.

4.8   References

Addy, S., 1998, Seismic facies map using neural networks; an example from Sligo limestone in Lavaca County, Texas: 1998 Ann. Conv., Am. Assoc. Petr. Geol., Exp. Abstracts, Expanded Abstracts, A9.

Aki, K., and Richards, P. G., 1980, Quantitative seismology – theory and methods: W. H. Freeman and Co., San Francisco.

Backus, G. E., 1962, Long-wave elastic anisotropy produced by horizontal layering: J. Geophys. Res., **67**, 4427-4440.

Bakke, N., and Ursin, B., 1998, Thin-bed AVO effects: Geophysical Prospecting, **46**, 571-587.

Batzle, M., and Wang, Z., 1992, Seismic properties of pore fluids: Geophysics, **57**, 1396-1408.

Blangy, J. P., 1994, AVO in transversely isotropic media – An overview: Geophysics, **59**, 775-781.

Brown, A. R., Dahm, C. G., and Graebner, R. T., 1981, A stratigraphic case history using three-dimensional seismic data in the Gulf of Thailand: Geophysical Prospecting, **29**, 327-349.

Brown, A. R., 1992, Interpretation of three-dimensional seismic data: AAPG Memoir 42, 3d edition, 253p.

Buland, A., Landrø, M., Anderssen, M., and Dahl, T., 1996, AVO inversion of Troll Field data: Geophysics, **61**, 1589-1602.

Castagna, J. P., and Smith, S. W., 1994, Comparison of AVO indicators: A modeling study: Geophysics, **59**, 1849-1855.

Castagna, J. G., Swan, H. W., Foster, D. J., 1998, Framework for AVO gradient and intercept interpretation: Geophysics, **63**, 948-956.

Chiburis, E. F., 1993, AVO applications in Saudi Arabia, *in* Castagna, J. P., and Backus, M., Eds., Offset-dependent reflectivity: Theory and practice of AVO analysis: Soc. Expl. Geophys., Tulsa.

Don, W., 1998, AVO detectability against tuning and stretching artifacts: 68th Ann. Internat. Mtg., Soc. Expl. Geophys., Expanded Abstracts, 236-239.

Enachescu, M. E., 1993, Amplitude interpretation of three-dimensional reflection data: The Leading Edge, **12**, 678-685.

Gassmann, F., 1951, Über die elastizität poröser medien: Vierteljahrsschr. Naturforsch. Ges. Zürich, **96**, 1-23.

Hampson, D., and Russell, B., 1995, AVO UNIX Software: Hampson-Russell Software Services Ltd., Calgary.

Hampson, D. and Todorov, T., 1999, AVO lithology prediction using multiple seismic attributes: 69th Ann. Internat. Mtg., Soc. Expl. Geophys., Expanded Abstracts, 756-759.

Hilterman, F., 1990, Is AVO the seismic signature of lithology? A case history of Ship Shoal - South Addition: The Leading Edge, June 1990, 15-22.

Lörtzer, G. J. M., and Berkhout, A. J., 1992, An integrated approach to lithologic inversion; Part 1, Theory: Geophysics, **57**, 233-244.

Marion, D., 1992, Compressional velocity and porosity in sand-clay mixtures: Geophysics, **57**, 554-563.

Mavko, G., Mukerji, T., and Dvorkin J., 1998, The rock physics handbook. Tools for seismic analysis in porous media, Cambridge University Press, Cambridge, 329 pp.

Middleton, G. V., 1973, Johannes Walther's Law of the correlation of facies: Geological Society of America Bulletin, **84**, 979-988.

Neri, P., 1997, Revolutionary software for seismic analysis: World Oil, **218**, 90-93.

Ostrander, W. J., 1984, Plane-wave reflection coefficients for gas sands at non-normal angles of incidence: Geophysics, **49**, 1637-1648.

Rijks, E. J. K., and Jauffred, J. C. E. M., 1991, Attribute extraction: An important application in any detailed 3-D interpretation study: The Leading Edge, **10**, 11-19.

Rutherford, S. R., and Williams, R. H., 1989, Amplitude-versus-offset variations in gas sands: Geophysics, **54**, 68-688.

Ryseth, A., Fjellbirkeland, H., Osmundsen, I. K., Skålnes, Å., and Zachariassen, E., 1998, High-resolution stratigraphy and seismic attribute mapping of a fluvial reservoir; Middle Jurassic Ness Formation, Oseberg Field: AAPG Bull., **82**, 1627-1651.

Shuey, R. T., 1985, A simplification of the Zoeppritz equations: Geophysics, **50**, 609-614.

Smith, G. C., and Gidlow, P. M., 1987, Weighted stacking for rock property estimation and detection of gas: Geophysical Prospecting, **35**, 993-1014.

Spratt, S., 1987, Effect of normal moveout errors on amplitude: 57th Internat. Mtg., Soc. Expl. Geophys., Expanded Abstracts, 634-637.

Ursin, B., and Ekren, B., 1994, Robust AVO analysis: Geophysics, **60**, 317-326.

Varsek, J. L., 1985, Lithology prediction and discrimination by amplitude offset modeling: Geophysics, **50**, p.1377.

Walden, A. T., 1991, Making AVO sections more robust: Geophys. Prosp., **40**, 483-512.

Wrolstad, K., 1996, Clastic reservoir description from pre- and post-stack seismic data: American Association of Petroleum Geologists 1996 annual convention, San Diego, CA, United States.

Zeng, H., Backus, M. M., Barrow, K. T. and Tyler, N., 1996, Facies mapping from three-dimensional seismic data: Potential and guidelines from a Tertiary sandstone-shale sequence model, Powderhorn Field, Calhoun County, Texas: AAPG Bulletin, **80**, 16-46.

Zoeppritz, K., 1919, Erdbebenwellen VIIIB, Ueber Reflexion and Durchgang seismischer Wellen durch Unstetigkeitsflaechen: Goettinger Nachrichten, **I**, 66-84.

Chapter 5

Probabilistic AVO analysis and seismic lithofacies prediction in the Grane oil field

5.1   Abstract

In this chapter we delineate reservoir sands in the Grane oil field, North Sea, by combining lithofacies prediction from pre-stack seismic amplitudes and quantitative analysis of seismic scale depositional geometries. This field, developed in late Paleocene turbidites, has been problematic because of complex sand distribution and non-reservoir seismic anomalies. Two of the three most recent exploration wells did not encounter reservoir sands. In this chapter, the goal is to improve our ability to forecast reservoir sands from seismic data in this and similar turbidite fields in the North Sea.

We apply the same methodology as for the Glitne Field in Chapters 3 and 4. First we recognize and classify different lithofacies from well-log data, including sandstone, shale, marl, limestone, and tuff. As for the Glitne field, the Vp/Vs ratio, together with impedance, discriminate lithology better than does impedance alone. Hence, we conduct statistical AVO analysis to predict seismic lithofacies from seismic data. We derive probability density functions (pdfs) for each of the facies in terms of zero offset reflectivity (R(0)) and AVO gradient (G). R(0) and G from inversion of real seismic data are used to predict the most likely facies distribution along selected 2D seismic lines.

In this chapter we also analyze and quantify the seismic scale depositional geometries in the area. Where reservoir sands have been identified from seismic interpretation, there is a good correlation between reservoir sand thickness and a thicker, better defined Late

Paleocene seismic interval. We take advantage of this correlation and predict thickness of reservoir sands given the upper Paleocene interval thickness. These results are integrated with the sand predictions from the AVO inversion. A blind test is conducted on a well drilled at a location where post-stack seismic amplitudes indicate reservoir sands, but where only shales, tuffs, and some carbonates were encountered. Our lithofacies prediction results indicate that the most likely facies at that well location in terms of AVO response is volcanic tuff, whereas the geometry analysis indicate only the local presence of a thin sand unit around the well. We conclude that the seismic anomaly around the well is caused by an intra-upper Paleocene tuff unit, and this unit likely explains the local thickening of the upper Paleocene interval.
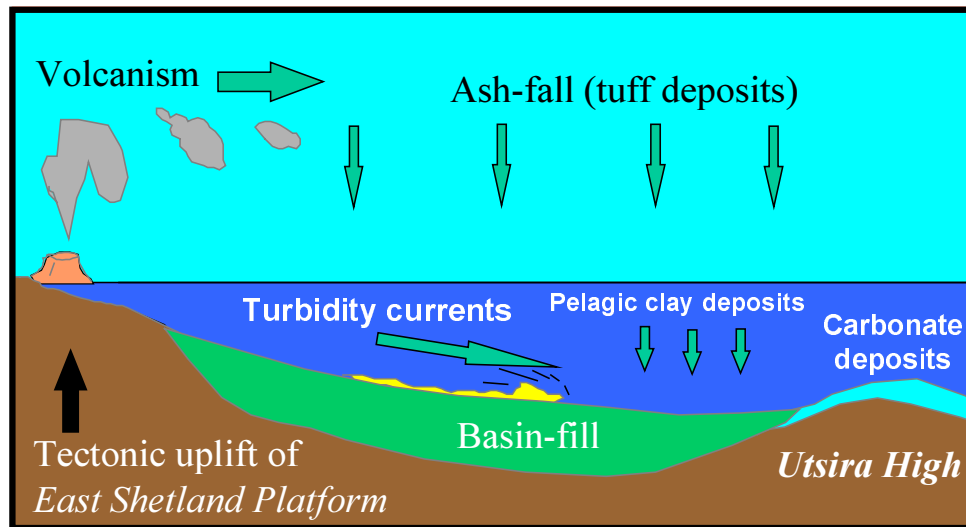
Figure 5.1: Structural setting and sedimentary processes in the South Viking Graben during the Paleocene, causing a great mix in lithologies in the Grane area, near the Utsira High.

5.2   Introduction

The sands of interest represent the Paleocene Heimdal Formation, and the area of study is the Grane oil field located on the eastern margin of the South Viking Graben (see Appendix A, Figures A.1 and A.2). This area is more complex than the Glitne in terms of lithology variation, as both carbonates and volcanic ash-fall deposits are relatively abundant within the studied Paleocene interval. This is related to the particular setting and the local basin topography during deposition. The Grane field is located on the eastern

flank of the South Viking Graben, near the Utsira High. The Utsira High had abundant limestone and marl deposition during Late Cretaceous and early Paleocene, as siliciclastic sedimentation rates were low. The complete Heimdal sequence is relatively thin (less than 100 m), and was deposited in the late Paleocene. During deposition of the sands, the limestones, marls, and shales were eroded and redeposited locally. During the Paleocene there were also repeated episodes of volcanic eruptions and ash-flow deposition, associated with the opening of the Norwegian Sea. Hence, the relatively thin Paleocene interval in the Grane area comprises a great mix of lithologies (Figure 5.1).

Figure 5.2 depicts a 3D visualization of the reservoir as delineated by conventional seismic interpretation, bounded by the Top Heimdal and Base Heimdal horizons. The figure includes the seismic horizon grids of the Top Chalk horizon and the overlying Base Balder Formation, which define the upper Paleocene target interval. The figure also shows five different wells, only three of which penetrate reservoir sands (#1, 2, and 3). Wells #4 and 5 were drilled aiming for possible satellite sands that could contain additional amounts of hydrocarbons. However, neither of these wells encountered reservoir sands. In this study we show how we can integrate seismic amplitude analysis with quantitative studies of seismic depositional geometries, to better delineate the extent of the reservoir, identify possible nearby satellite reservoirs, and reveal potential pit-fall anomalies caused by volcanic tuff or other non-reservoir rock types. For these purposes, we focus on three different 2D seismic lines intersecting well #1, well #3, and well #4, see map in Figure 5.3.
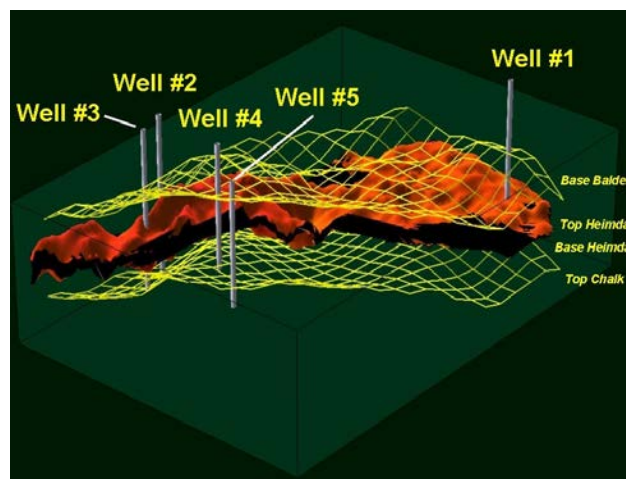
Figure 5.2: 3D-map (travel time) of the turbiditic oil field.
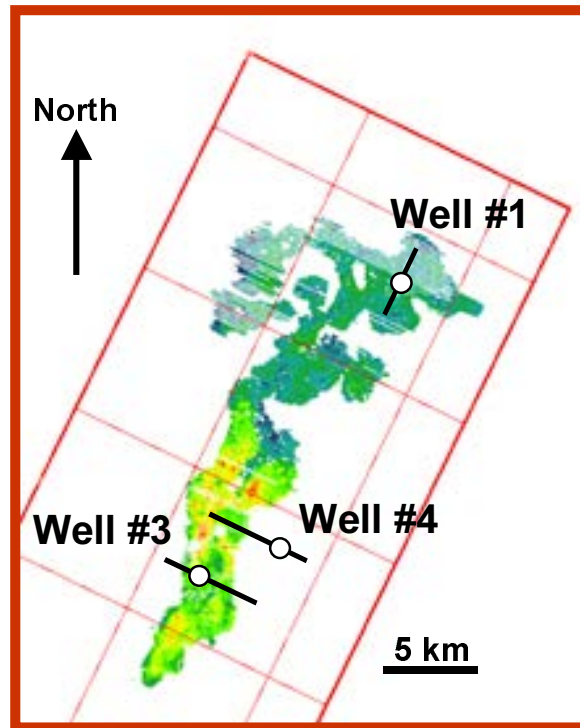
Figure 5.3: Map of the Grane oil field. The reservoir extent is based on conventional seismic interpretation. The 2D seismic lines considered in this chapter are indicated as black lines, and they intersect well #1 (brine sands), well #3 (oil sands), and well #4 (volcanic tuff), respectively.

5.3   Facies analysis

5.3.1   Facies identification and lithostratigraphic analysis in type well

In the first part of this chapter, we want to predict lithofacies from seismic amplitudes using the methodology introduced in Chapters 3 and 4. The first thing we must do is identify seismic scale sedimentary units with characteristic rock physics properties (i.e., seismic lithofacies). In the Grane field we identify the following lithofacies that can occur at seismic scale: cemented clean sandstone (i.e., Facies IIa), unconsolidated clean sands (IIb), silty shale (IV), pure shale (V), tuff, marl, and limestone. All these facies are identified in well #1 (see Figure 5.4), based on core observations available for the entire zone (Ramm et al., 1992).
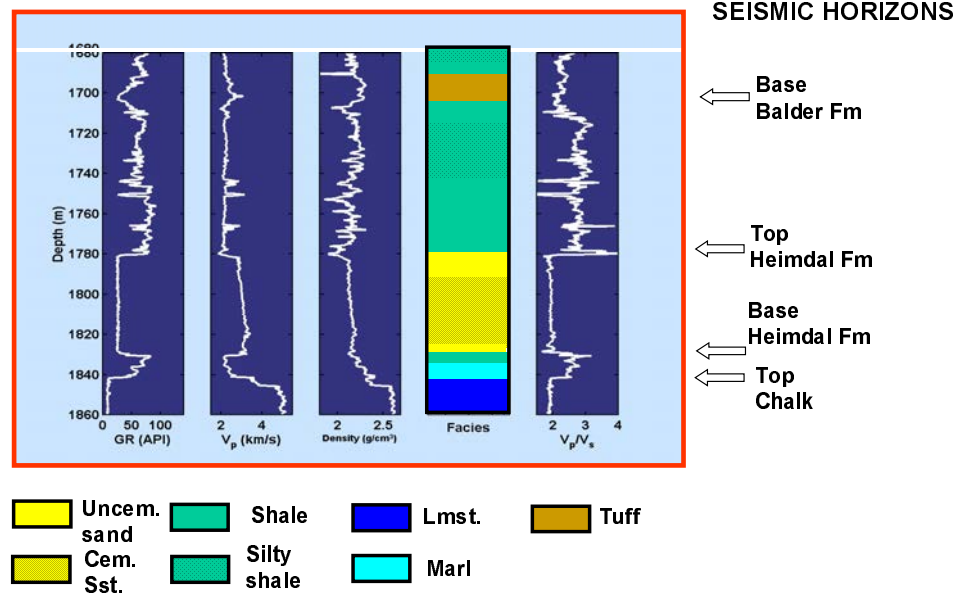
Figure 5.4: Various log data and facies in well #1, the type well. Facies observations are from cores. Key seismic horizons are notified.

The reservoir sands in well #1, representing the Heimdal Formation, are water-saturated. Rock physics diagnostics (see Chapter 2) confirm that most of the reservoir is slightly cemented with quartz (approximately 2%), but the upper 10 m is found to be uncemented.

Most of the shales in well #1 represent the Lista Formation, except a thin zone of Sele Formation shales located between 1710-1720 m. Some of the Lista Formation shales in well #1 show the presence of silt laminas. This is within a zone (1720-1755 m) where the gamma ray log shows relatively low values compared to the rest of the Lista Formation shales. This interval also has an abundance of ash layers. Nevertheless, we identify this zone as a silty shale.

The Balder Formation, representing the top of the Paleocene interval, consists mainly of volcanic tuff or tuffaceous turbidite deposits. A relatively low gamma ray, high P-wave velocity, and high density is characteristic for the Balder Formation.

The Ekofisk Formation is of Cretaceous age and represents the base of the target interval. It consists of chalk deposits (limestones) which are easily identified by a very large P-wave velocity and density, and very low gamma ray. The lower Paleocene Vaale

Formation directly overlies the Ekofisk Formation, and consists of marl deposits. These are mixed deposits of limestone and shale.
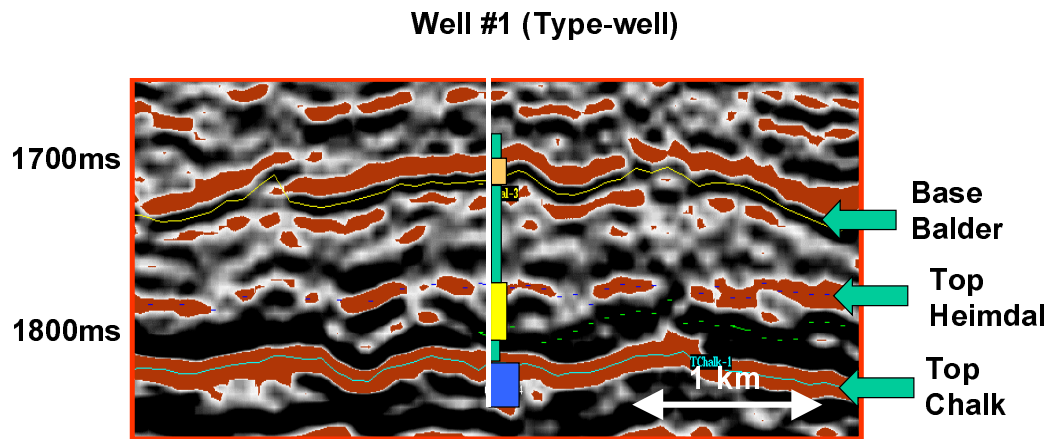
Well #1 (Type-well)

Figure 5.5: Seismic stack section intersecting well #1. Important seismic reflectors include Base Balder, Top Heimdal, and Top Chalk. The lithofacies column in the type-well is superimposed for comparison.

Figure 5.5 shows the seismic signatures (zero-phase wavelet, peak frequency 30 Hz) along a 2D post-stack section intersecting well #1. Here, we observe important seismic horizons that correspond with lithostratigraphic and facies boundaries. The Balder Formation shows a prominent red reflector, indicating a positive stack response. The Balder Formation is about a wavelength thick, and the black response below coincides with the base of the tuffaceous unit. The reservoir sands (Heimdal Formation) are also identified in Figure 5.4. The top reflector is prominent, but has an incoherent character. A black reflector that undulates in shape, just beneath the Top Heimdal reflector represents the base of the reservoir. We also observe some subtle internal reflectors within the reservoir. The Base Heimdal horizon interferes with the sidelobe of the peak wavelet representing Top Chalk, which is the most prominent seismic reflector in the area. It shows a very strong positive reflectivity.

5.3.2   Facies classification using quadratic discriminant analysis

Well #1 is used as a type-well for a multivariate statistical classification of seismic lithofacies in other wells. The gamma ray, density, and P-wave velocity logs are used as training data (Figure 5.4). The classification is done using a simple quadratic discriminant

analysis. Samples are classified according to the minimum Mahalanobis distance (c.f., equation 3-1).
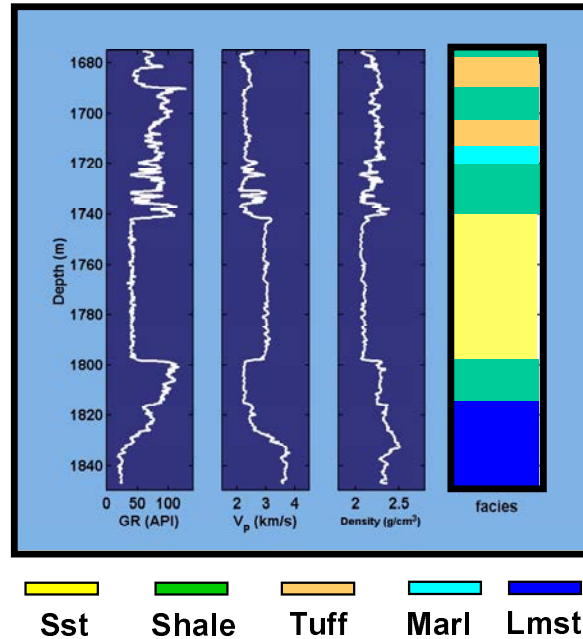
Figure 5.6: Classification results in well #3.

Figures 5.6 and 5.7 show the classification results in well #3 and #4, respectively. Well #3 penetrates reservoir sands, whereas well #4 does not. The sands in well #3 are oil-saturated, but matching density-derived porosities with helium porosity data (see Chapter 2.5) indicates an invasion of mud filtrate. The sands are classified as uncemented. However, the velocities are higher than for uncemented sands as predicted by rock physics diagnostics. One problem with separating between cemented and uncemented sands in this area, is that cementation content is not a discrete 0% or 2%, but varies. In the Grane area we do not observe completely uncemented sands, and the separation between cemented and uncemented sands by the Mahalanobis distance probably occurs at some threshold cement content between 0-2%. In the seismic prediction carried out in section 5.7, we therefore decide to lump cemented and uncemented sands together. We also lump silty shales and pure shales together, as their properties are found to be very similar in this area. Nevertheless, in the uncertainty analysis in section 5.5 we create cdfs and statistical AVO plots for both cemented and uncemented sands, and for silty and pure shales, to simulate possible seismic signatures occurring because of changes in these sedimentary characteristics.

Figure 5.7 shows the classification results for well #4. No sands are identified in the target zone. The Balder Formation tuff is identified at around 1680 m, whereas marl

deposits are identified at about 1770 m, probably representing Vaale Formation deposits. We identify a zone of tuff facies in the target zone between (1725-1735 m.), embedded in shaly facies. Core data from the well confirms the presence of tuff at this level (Figure 5.8).

The classification results give sharp boundaries between facies. However, if we look at the gamma ray and velocity logs, we see a somewhat gradual trend from the shales to the tuff. This reflects another problem with the classification: It will recognize threshold values, and gradual transitions between different facies will not be honored. Nevertheless, we do observe a P-wave velocity "jump" right above the zone where the Tuff is indicated. The Vp/Vs ratio is juxtaposed, and the tuff zone shows a relative decrease compared to the embedding shales.
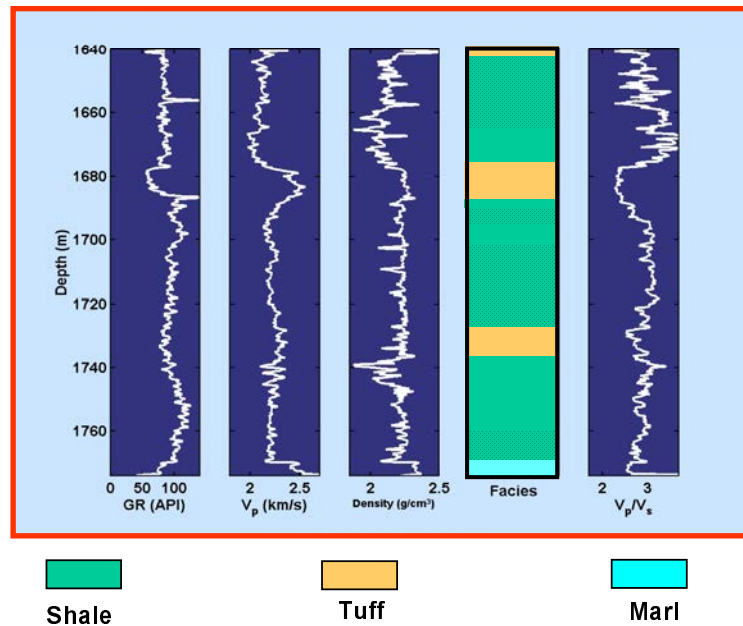
Figure 5.7: Facies classification results of well #4. The well was drilled on a seismic anomaly at a depth of 1722 m (see Figure 5.13), but no sand was encountered. Note the tuff unit identified by the classification, near the depth of this anomaly.

The intra-Paleocene tuff unit is of great interest, because it could explain the observed seismic anomaly interpreted to represent oil sands. The well that was drilled through the seismic anomaly, however, encountered no reservoir sands. In the next sections, we investigate the possibility of tuff to be responsible for the observed seismic anomaly, and we will use our seismic lithofacies prediction methodology to see if we are able to distinguish these tuffs from oil sands.
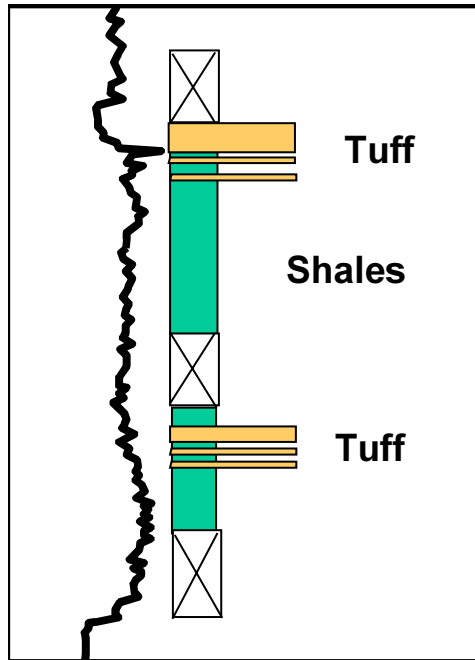
Figure 5.8: Core observations in well #4, compared to gamma ray log in the well. The depth range of the gamma ray log is 1660-1780 m.

5.4   Rock physics analysis

Rock physics analysis shows that the different classified facies have characteristic seismic properties, but there are overlaps between the various facies. Figure 5.9 shows the P-wave velocity plotted versus density. In the V-shape trend shales, marls, and tuffs have relatively low velocities and high densities, oil sands and brine sands have relatively low to intermediate velocities but low densities, and limestones (chalks) have very high velocities and densities. Note that the oil sands and brine sands have great overlaps. The oil is relatively heavy in the Grane field (18 API), and the seismic properties do not change as much as from brine saturated to oil saturated. The variability within the sand cluster is much larger than the change related to pore fluids. This shows that the rock texture of the sands in the area is seismically more important than pore fluids. In Chapter 2, we showed that the variability in these sands is due to sorting and cementation. The clay content in these sands is consistently very low.

.
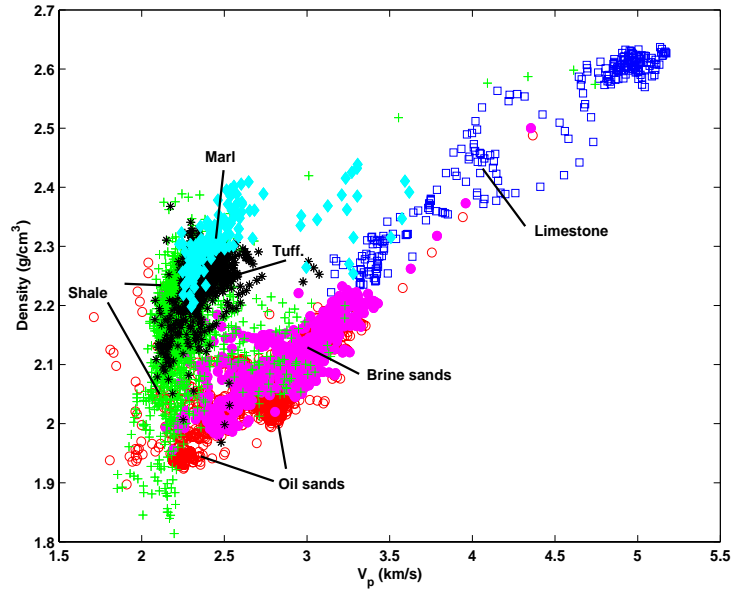
Figure 5.9: P-wave velocity versus density for different lithofacies.

Figure 5.10 shows acoustic impedance versus Vp/Vs ratio for the various facies. Here we observe that there is great overlap between the different lithofacies in terms of acoustic impedance, whereas the Vp/Vs ratio is a much better facies discriminator. The exception is the limestones. The limestones are easily distinguished in terms of acoustic impedance, whereas the Vp/Vs ratios are similar to those of sands (Vp/Vs ~ 2).
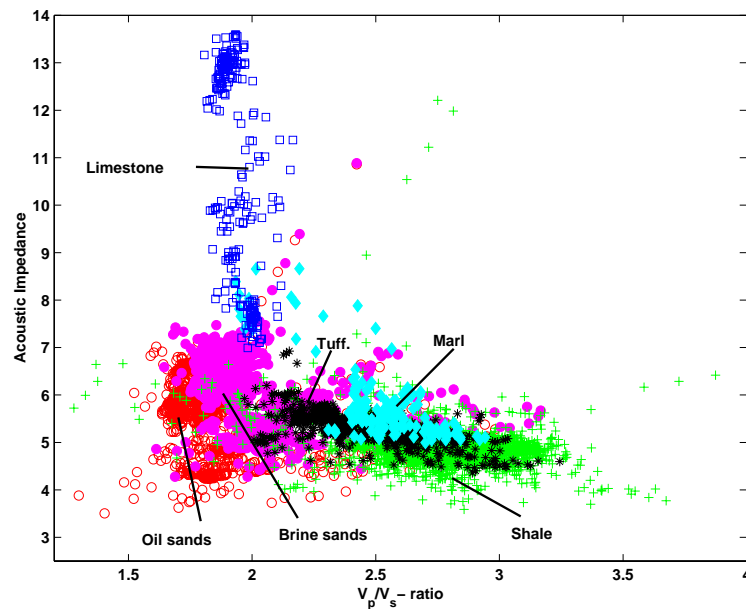
Figure 5.10: Acoustic impedance versus Vp/Vs ratio for different lithofacies.

The observations in Figure 5.10 indicate that AVO analysis must be conducted to predict lithofacies from seismic data. This is the same conclusion we made in the Glitne field in Chapter 4. The offset dependent reflectivity is strongly affected by both layer contrasts in acoustic impedance and Vp/Vs ratio.

5.5 Deterministic AVO-analysis

We first conduct deterministic AVO analysis in well #3, to study the offset dependent reflectivity of the oil sands in the area. We then do similar studies in well #4, to see if the tuffs encountered in this well yield a characteristic AVO response.

5.5.1 AVO-response of oil sand (well #3)

Figure 5.11 shows a seismic near-offset stack section intersecting well #3. This well encountered a thick reservoir sand saturated with oil. The oil-water contact is located at 1765 m. There is a prominent positive near-offset stack response at the top of the reservoir.
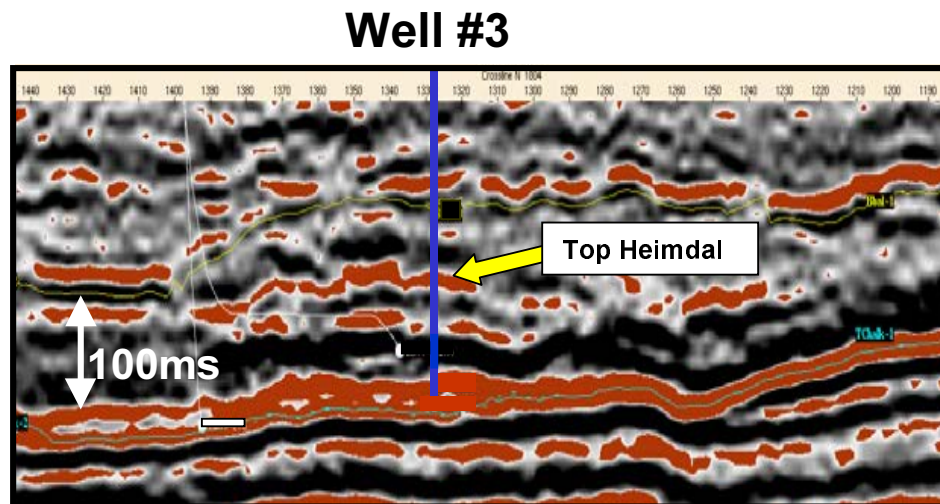
Well #3

Figure 5.11: Seismic stack section intersecting well #3. This well encountered a thick reservoir sand with oil saturation (top reflector is indicated by arrow). The internal positive reflector beneath the top is related to rock texture change, and this is discussed further in Chapter 6. CDP spacing is 25 m.

Figure 5.12 shows the real CDP gather and the modeled synthetic CDP gather at the well location. The synthetic gather is created based on the well-log properties in Figure 5.6. Shear wave information was not available in this well, but we used the Vp/Vs ratio

in well #1 to calculate Vs in this well. Because of the mud filtrate invasion effect, fluid substitution using the Biot-Gassmann theory (Mavko et al., 1998) is done to calculate the properties of the sands saturated with oil. The resulting synthetic CDP gather shows very similar response to the real gather. Moreover, the picked amplitude of the top reservoir shows a phase shift occurring at the same offset for the real and the synthetic case, when normalized at zero-offset reflectivity.

Figure 5.12: AVO analysis at well #3. There is an excellent match between the real and the synthetic gathers. The top of the oil-saturated sands shows a prominent zero offset reflectivity and a strong negative AVO gradient, resulting in a phase shift at approximately 1500 m offset.

5.5.2   AVO-response of volcanic tuff layer (well #4)

Figure 5.13 shows a seismic stack section intersecting well #4. Note the prominent seismic reflector around the well location. This anomaly was interpreted as potential reservoir sands before drilling well #4. The main reservoir sands of the Grane field can be observed as a significant seismic reflector around CDP location 1350. The stack response of reservoir sands will vary as a function of the sand texture, and because of phase shifts (see Figure 5.11) the stack response of the sands can be very weak. Variation in amplitude can also be related to tuning effects or diffractions related to an uneven top of the reservoir.
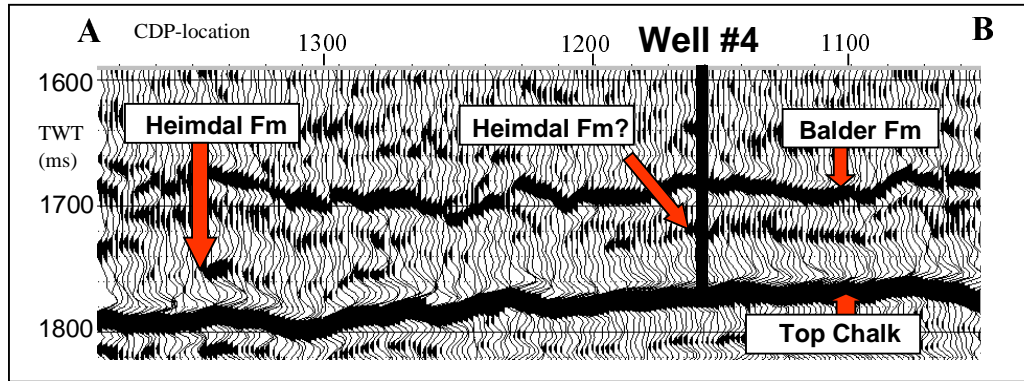
Figure 5.13: Seismic section intersecting well #4 (for scale and location see map in Figure 5.3).

Figure 5.14 shows the real and the synthetic CDP gather in well #4. The well-log data in Figure 5.7 are used as inputs for the AVO modeling. Note that shear wave velocity is available in this well. There is a good match between the real AVO response and the synthetic one. The AVO modeling confirms that the tuff unit gives a significant seismic reflector that is also recognized in the real data. The tuff unit shows a prominent zero-offset reflectivity that decreases with offset.

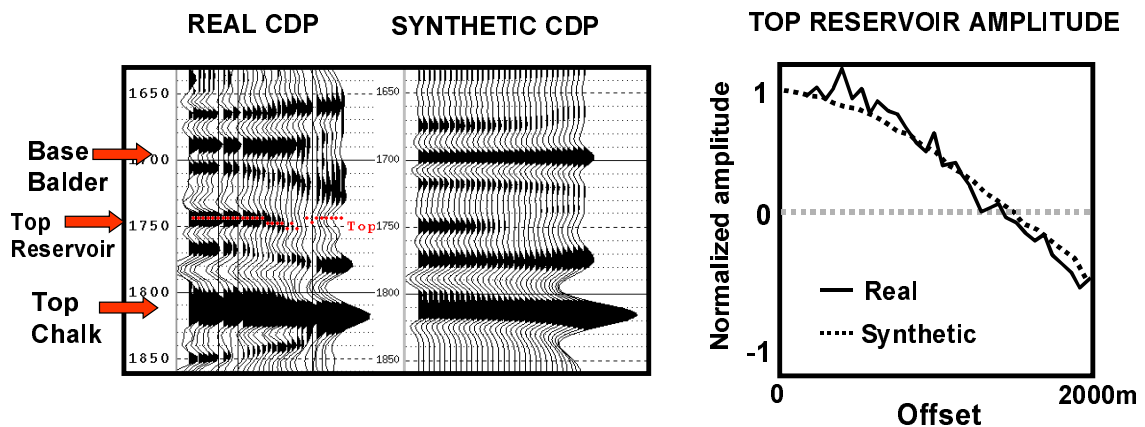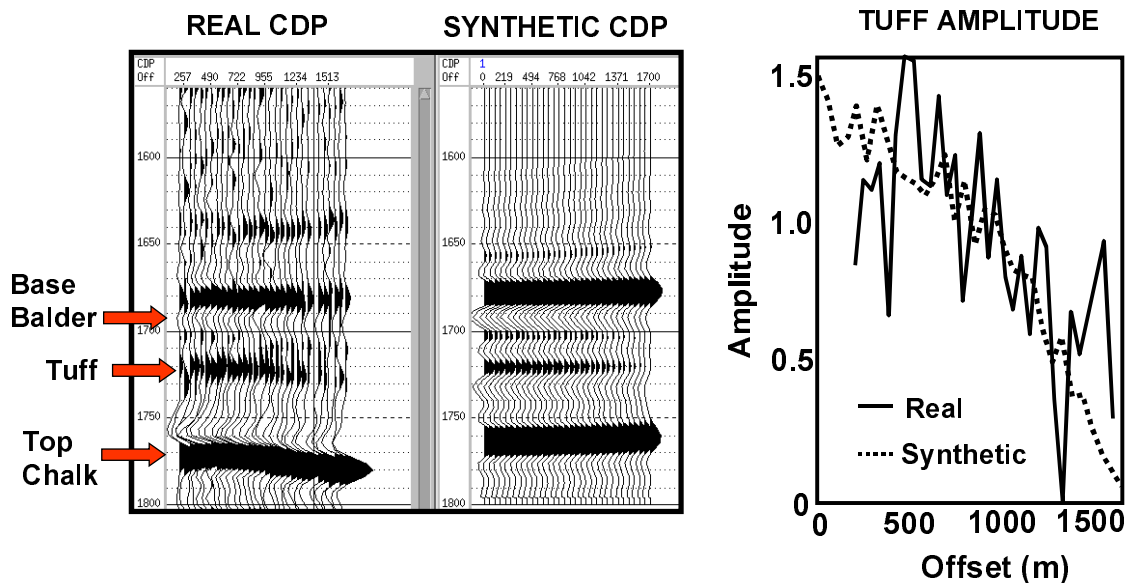

Figure 5.14: AVO analysis in well #4. There is a good match between the real and the synthetic gathers. The top of the tuff unit shows a prominent zero offset reflectivity and a negative AVO gradient, resulting in a weak far-offset reflectivity.

5.6   Probabilistic AVO and uncertainty assessment

To assess uncertainty related to facies variability within each facies, we generate cumulative distribution functions (cdfs) for each facies population. Figure 5.15a shows that tuff and marl have similar acoustic impedance distributions to oil-saturated, unconsolidated sands (IIb). The ambiguity between tuff, marl, and oil sands, is resolved by the Vp/Vs ratio, as marl and tuff have higher Vp/Vs ratios than the oil sands (Figure 5.15b).
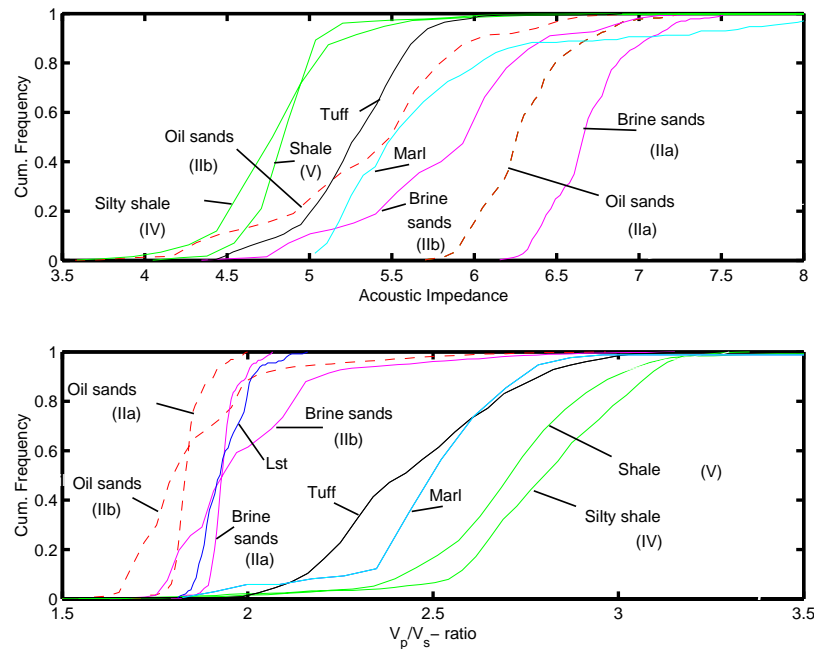
Figures 5.15: Cdfs of acoustic impedance (upper) and Vp/Vs ratio (lower) for the different facies populations. The Vp/Vs ratio better discriminates sandy facies from tuff, marl, and shaly facies.

The cdfs are the basis for the generation of the AVO probability density functions (pdfs). We do Monte Carlo simulation of the seismic properties from the cdfs, and calculate corresponding realizations of reflectivity versus offset, using Shuey's approximation of the Zoeppritz' equations (Shuey, 1985):

$$R(\theta) = R(0) + G \cdot \sin^2 \theta. \tag{5-1}$$

Here R(0) is zero offset reflectivity given by the impedance contrast across an interface whereas G is the AVO gradient and is strongly affected by the contrast in Vp/Vs ratio across an interface (see Chapter 4.3). The uncertainties in the properties of the cap-rock, as well as of the reservoir zone, are included in the simulations (Figure 5.16). Note that

tuff located under Facies V (pure shale) produces a significant R(0) and a negative AVO gradient. Shale-shale interfaces can also give some R(0) response.
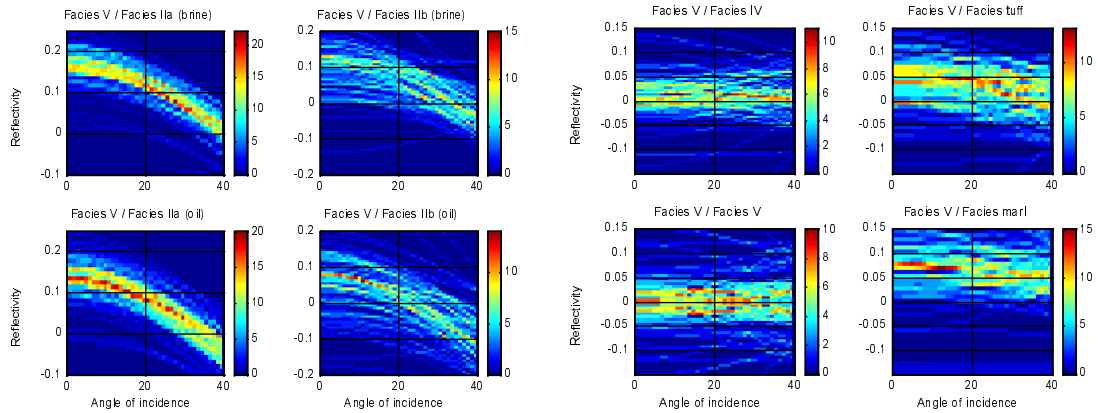
Figure 5.16: Examples of AVO-frequency plots for different half-space models. The natural variability of rock properties within each facies causes a spread in the AVO response. In these plots, AVO curves have been binned together into a 2D histogram of R(0) versus angle of incidence, and the highest density of AVO curves is indicated in red color. These plots therefore correspond to the probability distribution of AVO responses for the various facies combinations.

To better assess the overlaps between the AVO responses of different facies, we create bivariate pdfs of R(0) and G for the different facies combinations (Figure 5.17). As in the Glitne field, we assume shale as cap-rock. These pdfs create the probabilistic link between lithofacies and seismic properties, and they will be used in section 5.7 to predict lithofacies from seismic data.
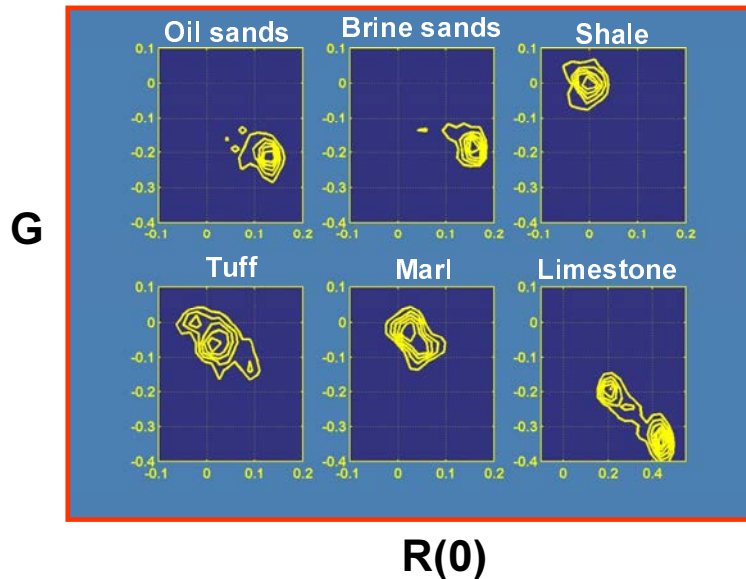
Figure 5.17: Bivariate pdfs of R(0) and G for different facies. We assume shale as cap-rock.

We observe that the various facies have different locations in terms of R(0) and G. Oil sands and brine sands have relatively large R(0) and G values, and there is great overlap between the two. Hence, this plot indicates that oil and brine sands can hardly be discriminated from seismic data. Shales have very low R(0) and G values centering around 0, because the cap-rock is also shale. Tuffs and marls have intermediate R(0) and G values. Finally, limestone has very large R(0) and G values, and is easily separated from the other facies.
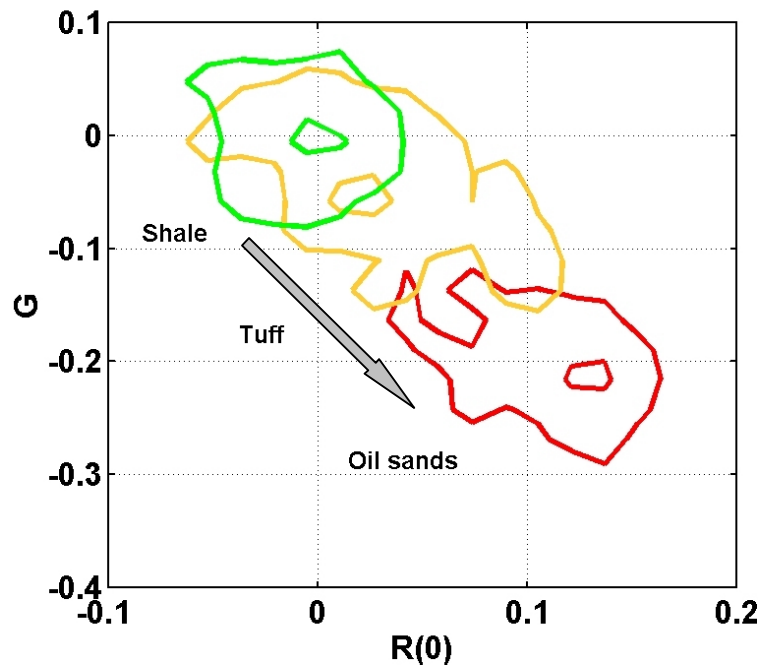
Figure 5.18: 50% (outer) and 90% (inner) isoprobability contours of shale, tuff, and oil sands. This figure illustrates the potential pitfall of tuff in the assessment of seismic amplitudes. The tuff data are located between shales and oil sands. Hence, a tuff data-point can easily be mistaken for an oil sand, if we ignore tuffs and only try to distinguish sands and shales.

Let us focus again on the seismic anomaly around well #4. Figure 5.18 illustrates the potential ambiguity between tuffs and oil sands. Intermediate positive R(0) and negative G of tuff could give similar stack responses to the strong positive R(0) and large negative G of oil sands. However, statistical AVO analysis should be able to distinguish the two, if both facies are included in the training data. Even statistical AVO would fail if tuff was not included as a facies in the training data. A tuff data point in Figure 5.18 could then be easily classified as oil sands.

5.7 Seismic lithofacies prediction

The next step is to apply the bivariate AVO pdfs to predict seismic lithofacies from pre-stack seismic data. We select two seismic lines from which we extract R(0) and G along the Top Heimdal horizon. This is accomplished using commercial AVO inversion software (AVO Hampson & Russell). The inverted R(0) and G values from the seismic data are calibrated to the well-log data and classified according to our bivariate pdfs of R(0) and G. One of the selected lines is the line intersecting well #3 (Figure 5.11). For this line the goal is to delineate the extent of the reservoir sands laterally, and see if the results correspond well with the extent determined from the conventional seismic interpretation. The other selected line is the line intersecting well #4 (Figure 5.13). For this line, the goal is to do a blind-test of the well. We would like to determine if we are able to predict the presence of volcanic tuff based upon a calibration within the main reservoir sands. Another issue is whether there are any local sands outside the main reservoir along this same line.
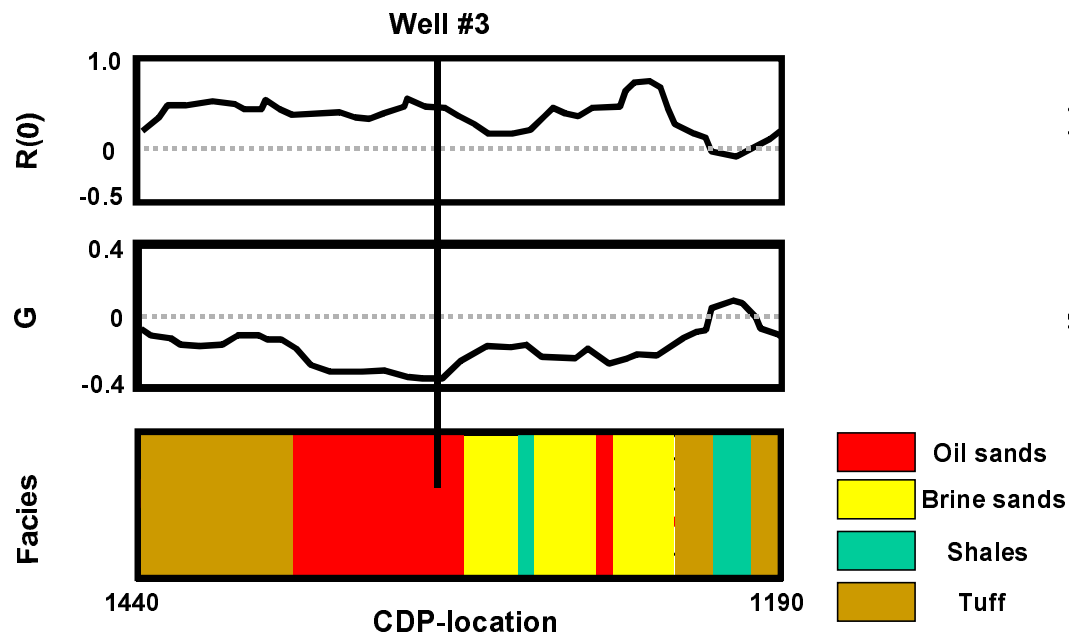
Figure 5.19: Seismic lithofacies prediction along Top Heimdal horizon in line intersecting well #3. We predict both oil and brine sands within the reservoir. The extent of the reservoir sands coincides well with the extent determined from the conventional seismic interpretation. Note that we predict volcanic tuff as well as shales outside the reservoir.

5.7.1 Reservoir delineation along seismic line intersecting well #3

Figure 5.19 shows the calibrated R(0) and G values along the Top Heimdal horizon in the line intersecting well #3, where oil sands were encountered. The AVO pdfs in Figure 5.17 are used to predict the most likely facies underlying this horizon. We predict both oil and brine saturated sands along the horizon. The total extent of the reservoir sands coincides nicely with the extent determined from conventional seismic interpretation (Figure 5.1).
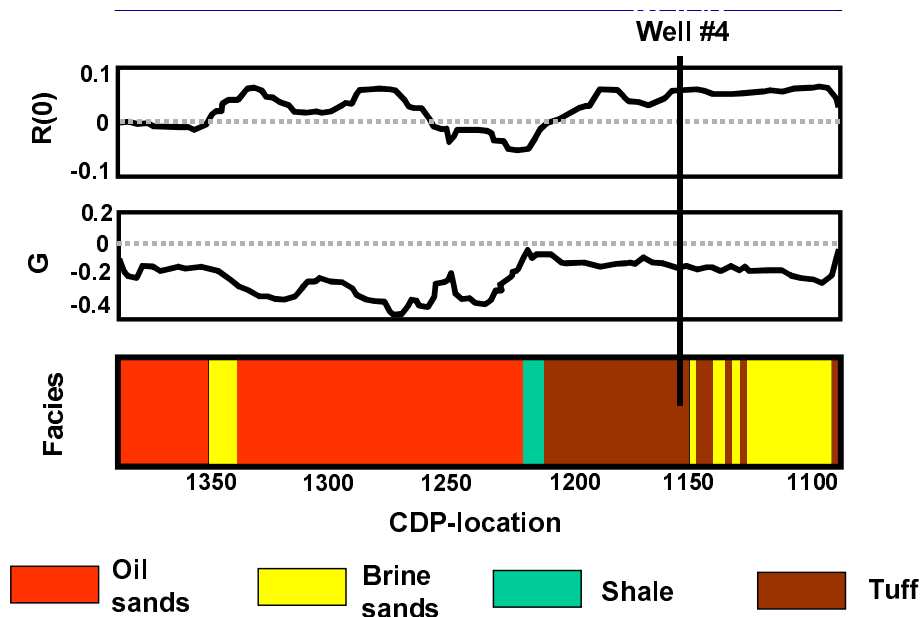
Figure 5.20: Seismic travel-time (TWT), R(0) and G along the Top Heimdal horizon extended to the anomaly around well #4. Lowermost, the most likely facies/pore-fluid predicted under the seismic horizon, assuming shale as cap-rock. We predict tuff at well #4.

5.7.2 Blind test of well #4

Next, we conduct a blind test on the seismic anomaly around well #4, and predict seismic lithofacies along the Top Heimdal horizon. For each location along a horizon, we obtain R(0) and G from inversion of pre-stack seismic data. These values are calibrated inside the main reservoir sands of the Grane field. We calibrate the average of unscaled R(0) and G values from a range of CDPs inside the reservoir (as defined by the map in Figure 5.3) with the mean values of R(0) and G for oil-saturated sandstone facies as defined by the training-data. Figure 5.20 includes the calibrated R(0) and G as well as the

predicted most likely lithofacies along this line. We confirm the oil-filled sands of the main reservoir (CDP 1225-1375). At well #4 we predict the most likely tuff facies to be present beneath the seismic anomaly seen in Figure 5.13. This matches the core observations and well-log classification results. A local water-saturated sand body is predicted just east of the well.

5.8   Quantitative depositional geometry analysis

Finally, we analyze depositional geometries. There is a correlation between travel-time thickness of reservoir sands (tt) and of the upper Paleocene interval (TT). We explain this by a simple conceptual geologic model (Figure 5.21).
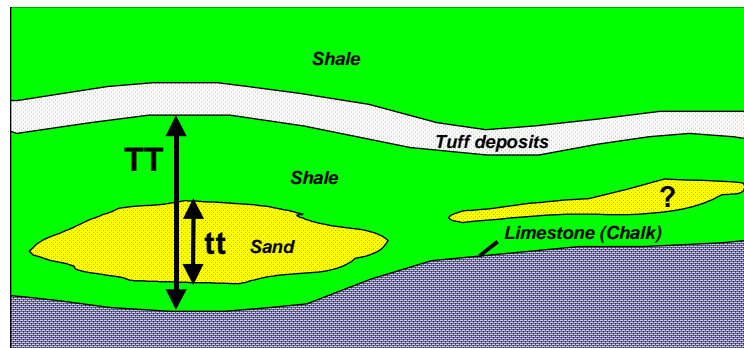
Figure 5.21: Geologic model showing how reservoir thickness and interval thickness are related.

The sands are embedded in upper Paleocene shales overlying lower Paleocene limestones and marls. An extensive tuff unit (i.e., Balder Formation) draped the upper Paleocene shales. Assuming that the shales are uniform in thickness, the interval thickness of the upper Paleocene should mimic the thickness of the reservoir. This assumption is verified in certain zones of the reservoir, based on the travel-time thickness derived from seismic interpretation. Figure 5.22 shows a map of the main reservoir and the various zones corresponding to the cross-plots in Figure 5.23.
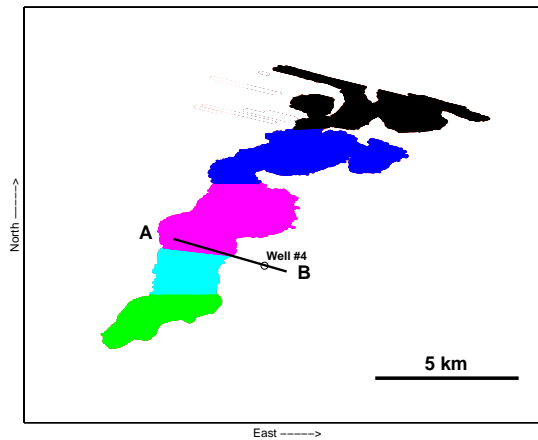
Figure 5.22: Reservoir map and scale. The different colored zones correspond to the zonal correlation plots in Figure 5.23. Line A-B depicts the intersection of the seismic line in Figure 5.13.
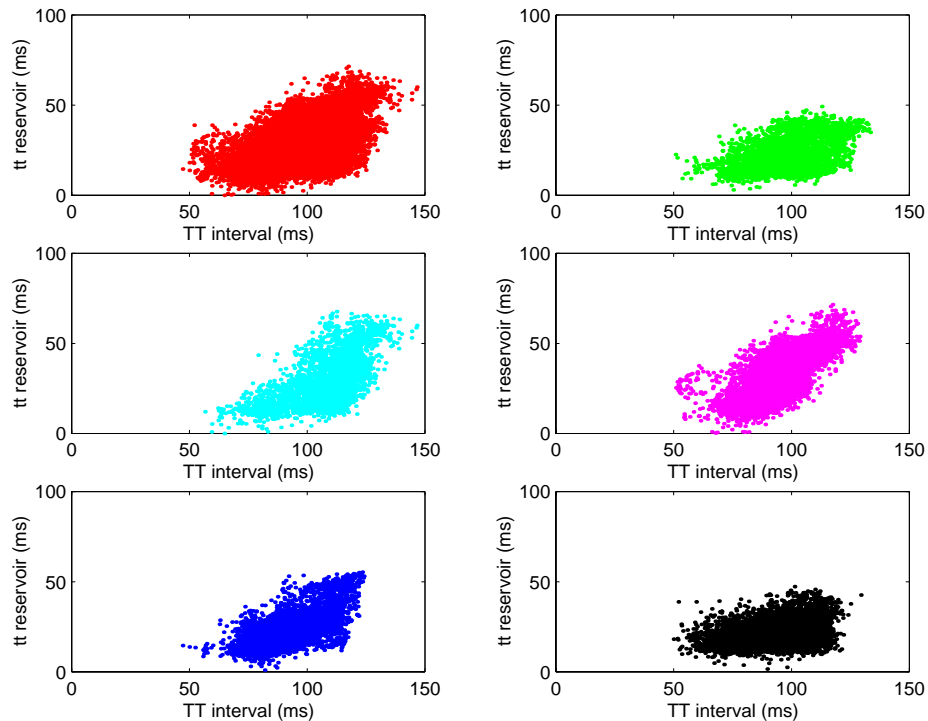
Figure 5.23: Cross-plots of upper Paleocene interval travel-time thickness (TT) and reservoir sand travel-time thickness (tt). The upper left represents the entire interpreted oil field in Figure 5.22. The rest corresponds to the different zones depicted in the same Figure.

We observe varying degree of correlation, and the best is found in the central part of the field. The sands are known to have suffered syn-depositional deformation and post-depositional remobilization (Martinsen et al., 1998), which would distort the correlations.

Other reasons for poor correlation include local erosion, differential compaction, and variation in depositional thickness of the shales. For these reasons, there are limitations in applying these correlations to predict reservoir sand thickness outside the interpreted turbidite system. Nonetheless, we use the correlations to predict the thickness of sand along the seismic line in Figure 5.13. The linear regression prediction and 1σ error are shown in Figure 5.24. The vertical axis begins at a seismic resolution which is ca. 15 ms (wavelength is ca. 60 ms) to clarify whether there are seismic scale sands that can explain the observed seismic anomaly. We predict only a very thin, local sand at seismic scale right around the well. This supports our lithofacies predictions that there are tuff deposits around the well, and these caused the seismic anomaly that was interpreted as sands before drilling. The tuff deposits could also explain the local thickening of the upper Paleocene interval around the well.
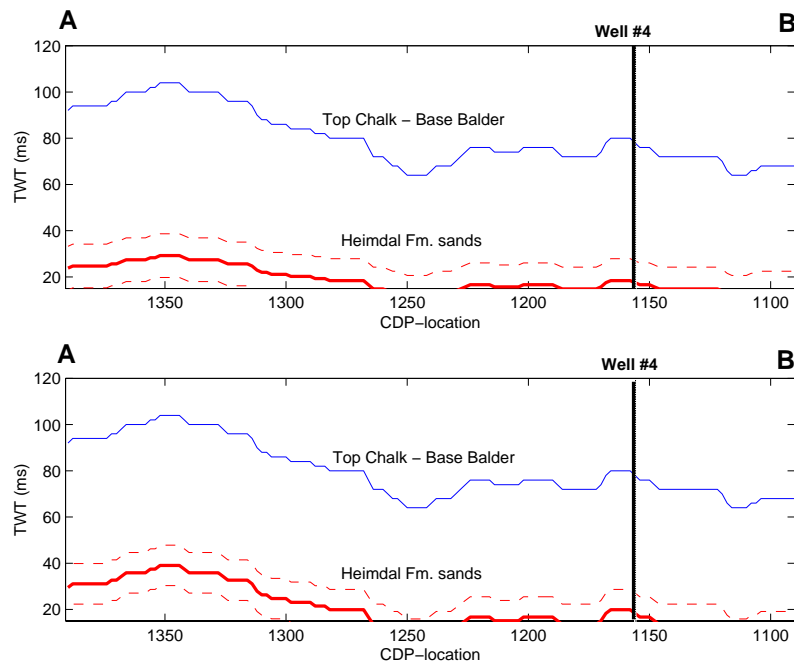
Figure 5.24: Reservoir sand travel-time thickness prediction based on linear regression of the trend representing the whole area (upper) and the central zone that has better correlation (lower). The dashed lines are standard deviations (1 from the linear regression lines.

5.9 Conclusions

- Volcanic tuff deposits or marls can cause seismic anomalies in North Sea Tertiary systems, and these lithofacies represent potential pit-falls in hydrocarbon exploration.
- Probabilistic AVO analysis can be applied to seismically discriminate sands from other lithofacies.
- Integration of seismic reservoir prediction based on amplitude information, and prediction based on quantitative analysis of depositional geometries, provides for a more reliable assessment of reservoir potential. Such a cross-disciplinary integration of geophysical and geological information is recommended for improved risk analysis and more successful drilling in complex turbidite systems.

5.10 References

Avseth, P., Mukerji, T., Mavko, G., and Veggeland, T., 1998., Statistical discrimination of lithofacies from pre-stack seismic data constrained by well-log rock physics: Application to a North Sea Turbidite System; SEG International Exposition and 68th Annual Meeting, New Orleans 1998.

Fukunaga, K., 1990: Introduction to statistical pattern recognition, 2nd ed., Academic Press.

Martinsen, O. J., Indrevær, G., Dreyer, T., Mangerud, G., Ryseth, A., and Søyseth, L., 1998: Slumping, sliding and basin floor physiography: Controls on turbidite deposition and fan geometries in the Paleocene Grane Field area, Block 25/11, Norwegian North Sea: AAPG Annual Convention, Extended Abstracts, A435.

Mavko, G., Mukerji, T., and Dvorkin J., 1998, The rock physics handbook: Cambridge University Press, Cambridge.

Ramm, M., Martinsen, O. J., Holmefjord, I., Johnsen, A., and Rykkje, J., 1992, Standard Core Description Well [#1] (Our well numbering, because well identification is confidential): Norsk Hydro internal technical report.

Shuey, R. T., 1985, A simplification of the Zoeppritz equations: Geophysics, **50**, 609-614.

Chapter 6

Seismic interpretation of reservoir architecture guided by rock physics and seismic modeling (Examples from the Grane area)

6.1   Abstract

In this chapter we show how rock physics and seismic modeling can be used to guide the interpretation of reservoir architecture in turbidite systems, with examples from the Grane area, North Sea. First, we document different seismic geometries and interpret these based on conceptual geologic models. Then we investigate seismic signatures in terms of rock physics properties. Rock physics analysis enhances our understanding of seismic signatures, and is included in the seismic interpretation process. The link between rock physics properties and seismic scale lithofacies established in Chapter 3, enables us to compare the qualitative interpretation of seismic geometries, with a quantitative analysis of seismic amplitudes. The amplitude analysis is done by a facies-guided seismic modeling, which confirms or guides the seismic interpretation of reservoir geometries and architectural elements.

This study documents important variability in the reservoir architecture in the Grane area in the North Sea. The northern Grane comprises a distinct feeder-channel which divides into distributaries that fed radial shaped lobes. The seismic signatures in the feeder-channel reveal acoustically transparent channel-deposits confined by reflective overbank fines. Rock physics analysis and seismic modeling indicates that the channel

sands are clean and unconsolidated, whereas the overbank deposits are interbedded sands-shales. In the lobe complex we observe disrupted, oblique reflectors indicating lateral migration of lobe-sands, as well as separated mound-shaped lobes due to lobe-switching. Well-log information from the lobe area indicates that these are thick-bedded, cemented sands. However, we suspect that distal portions of the depositional lobes are more heterogeneous, and that there was mud in the system during deposition. Moreover, no deformation is observed in the northern Grane. We expect moderate vertical and limited horizontal connectivity for the channel deposits, but the opposite for the depositional lobe sands.

The southern Grane shows completely different seismic architecture. Here, no distinct feeder-channel or overbank deposits are observed. However, the lobe sands are channelized and elongated, confined within structural features that existed during deposition (Martinsen et al., 1998). We observe internal seismic reflectors indicating lateral migration as well as vertical aggradation and channel-stacking. Seismic signatures also indicate erosion and channel cuttings at the base. Hence, the system in the south should be characterized by very good vertical and horizontal connectivities. Locally, however, internal reflectors indicate faulting and syn-depositional deformation, and geometries can be partly explained by tectonic rejuvenation and remobilization of sands (Martinsen et al., 1998). These factors likely degrade the reservoir connectivity. Rock physics analysis and seismic modeling indicate that the internal reflectors in the south Grane area are caused by changes in sandstone texture, most likely sorting.

In general, the combination of rock physics and facies analysis to guide seismic interpretation and modeling of geometries and amplitudes, improves our understanding of the reservoir architecture and connectivity in the Grane area. The results are valuable for reservoir modeling, flow simulation, and production forecasting in this and similar turbidite systems.

6.2   Introduction

Conventional seismic interpretation of hydrocarbon reservoirs seeks to map seismic scale sedimentary geometries, including structural and stratigraphic traps. The goal is to

determine reservoir location, size, and shape. This is a qualitative methodology that can be quite subjective. However, it requires good knowledge and experience in how seismic signatures relate to geologic factors. An experienced geologist can extract valuable information out of the geometries seen in seismic data, but more information can be gained, quantitatively, from seismic amplitudes. The amplitude information can be extracted in two ways, either as rock physics properties calculated from inversion of real amplitudes, or by modeling of rock properties into synthetic seismic amplitudes that are compared to real amplitudes. The amplitude information not only helps delineate subtle geometries, but adds another dimension to the geometries and can help the seismic interpreter to better understand the seismic signatures in an area. This is especially the case for 3D seismic data. There have been several studies where seismic amplitudes have been used to guide the delineation of reservoir geometries (e.g., Brown, 1992; Ryseth et al., 1998). Still, the amplitude information has, surprisingly enough, been underutilized in seismic exploration in the oil industry (Brown, 1999). The aforementioned procedures are rarely integrated with seismic interpretation. Both seismic modeling and inversion can be rather computer intensive and time consuming and are normally conducted by geophysicists at a stage after seismic interpretation.

We show that even simple 2D seismic modeling can add essential information and guide the conventional geometry-based seismic interpretation. By linking lithofacies to rock physics properties, we have provided a "common language" for geologists and geophysicists that can be used as building blocks during seismic modeling. Based on the facies we can build so-called architectural elements. These are defined by facies, scale, and geometry, and were first introduced by Miall (1985) as a way to describe different depositional units and geometries in fluvial systems. The reservoir quality will not only be dependent on the reservoir properties of the individual facies, but also on how these facies are positioned in relation to each other, forming various architectural elements. The arrangement of facies and architectural elements defines the vertical and lateral connectivity of a reservoir, which again controls the reservoir performance during production.
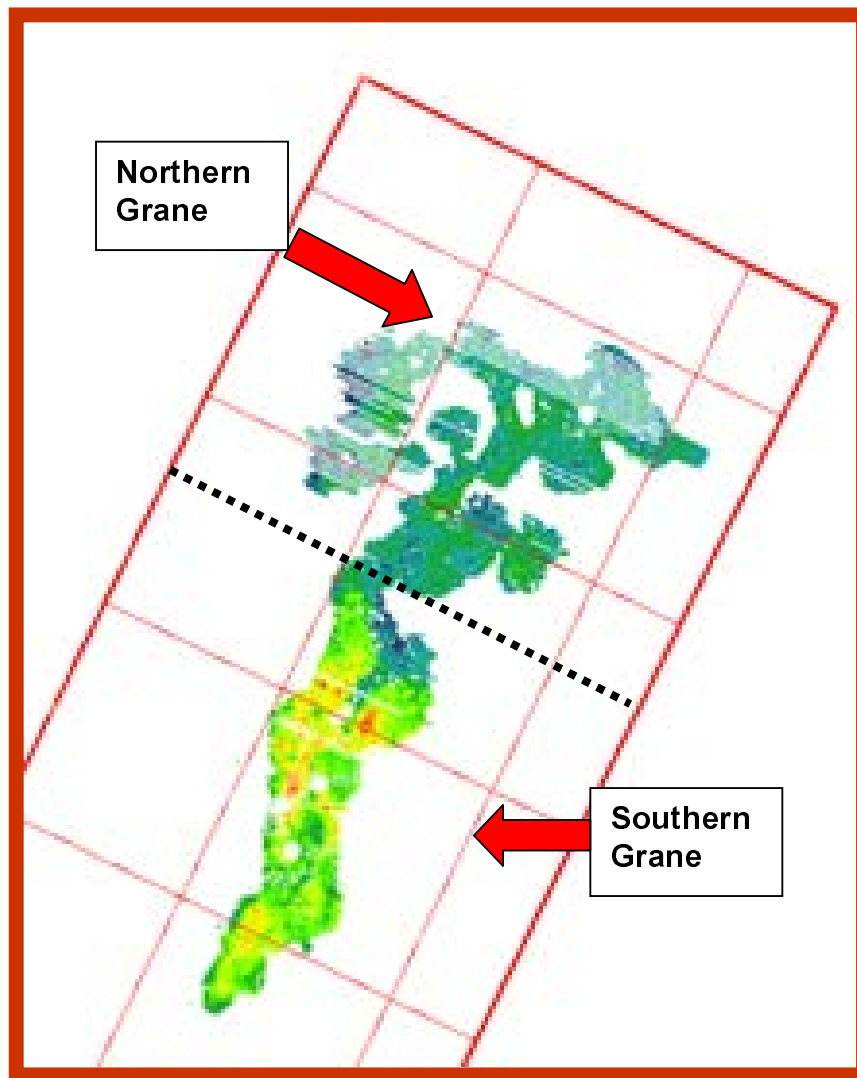
Figure 6.1: Outline of the Grane turbidite field based on conventional seismic interpretation. The field shows a different character in the north than in the south. In the north we observe what appears to be feeder channels and associated depositional lobes, whereas in the south we observe a sausage-shaped extensive channel complex. The Grane oil field is limited to the southern Grane, as most of the northern Grane is below the oil-water contact.

We show examples from the Grane turbidite system in the North Sea. Figure 6.1 shows a map of the Grane area, which is based on conventional seismic interpretation conducted by Norsk Hydro. We can clearly observe channel and lobe features in the northern part of the Grane area, whereas the southern part of the system shows a more elongated sausage shape. These features were documented and explained by Martinsen et

al. (1998), who related the differences to structural setting (i.e., geomorphic paleobathymetry), tectonic influence, and post-depositional remobilization of sands. We study seismic signatures along selected seismic lines intersecting the Grane turbidite system. The first step is to document the variability in seismic geometries and the character of reflectivity. Based on these observations, architectural elements are defined and interpreted in terms of depositional sub-environments and processes. The next step is to investigate the seismic amplitudes (in terms of rock physics properties). The link between rock physics properties and facies allow us to conduct facies-guided seismic modeling. In this way, we can validate our interpretations and potentially improve our understanding of the reservoir architecture in the Grane turbidite system.

6.3 Architectural elements in turbidite systems

6.3.1 Description of architectural elements in turbidite systems

Architectural elements are lithosomes characterized by geometry, facies composition, and scale (Miall, 1985). Architectural element analysis is a useful descriptive means to characterize depositional units, show the interconnectivity and lateral continuity of sand bodies, and interpret these in terms of causal sedimentary processes (Clark and Pickering, 1996). Architectural element analysis was first applied to fluvial systems (e.g., Allen, 1982; Miall, 1985). Several authors subsequently have studied architectural elements in turbidite systems, including Mutti and Normark (1987), Ghosh and Lowe (1993), Reading and Richards (1994), and Pickering et al. (1995).

In this chapter we will concentrate on seismic scale architectural elements, and hence we find the classification scheme of Reading and Richards (1994) most useful. They classified turbidite systems into 12 different categories depending on dominant grain size (gravel-rich, sand-rich, mud/sand-rich, and mud-rich) and type of feeder-system (point-source submarine fans, multiple-source submarine ramps, and linear-source slope aprons). They then described the expected reservoir architecture for the different classes. Table 6.1 includes the reservoir architectural elements they defined for sand-rich and mud/sand rich systems. These are the grain-sizes that are typical in North Sea turbidite systems. The

table shows that the reservoir architecture of both channel and lobes will be different depending on the dominant grain size. In sand-rich systems, channels will be braided since no stable channel axis with confining levees will develop, due to the lack of clay. The lobes will have a channelized nature, where lateral and vertical stacking of different lobes will occur. The channels will furthermore be more erosional in nature (Clark and Pickering, 1996). In systems where mud is available during deposition, stable levees can develop, and a single channel axis will be laterally confined within these overbank deposits. Successive lobe elements are generated during periodic avulsion of updip distributary channels, and they tend to separate into individual, radial, mound-shaped units. Well developed and persistent channel-overbank systems result in discrete, unconnected linear distributary channels and depositional lobes (Mutti and Normark, 1987). Increasing sand content within the fan results in decreasing overbank stability, increasing channel switching, and greater potential for lobe connectivity (Reading and Richards, 1994).
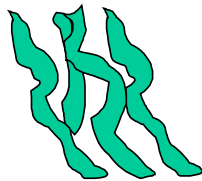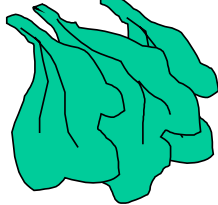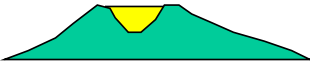
System type	Channels	Lobes
Sand-rich systems	Braided channels	Channelized lobes
Mud/Sand-rich systems	Channel- overbank complex	Depositional lobes

Table 6.1: Seismic scale reservoir architectural elements of deep-water depositional systems (modified from Reading and Richards, 1994).

6.3.2 Relating lithofacies to architectural elements

Because architectural elements are composed of lithofacies, we can assign facies (defined in Chapter 3) to the various elements in Table 6.1. Reading and Richards (1994) provide sand-shale bedding profiles and sand-shale ratios for these elements. Moreover, the facies distribution within a submarine channel-overbank complex has been described in detail by Clark and Pickering (1996). Walker (1978) provided a detailed facies analysis of classical submarine lobes, equivalent of Reading and Richards' depositional lobes in mud/sand-rich systems.

Starting with the channel-overbank complex, the channel is generally filled with thick-bedded, massive turbidite sands (Facies II), whereas the overbanks are usually characterized by thin-bedded sands-shales and shaly deposits (Facies III). Conglomerates and sedimentary breccias (Facies I) may be present in the channel axis in mud/sand-rich systems, but less likely in sand-rich systems. Overbank deposits tend to be poorly developed in sand-rich systems, hence we do not expect an abundance of Facies III in these systems. Depositional lobes are comprised of thick-bedded sands (Facies II) in the proximal area (i.e., lobe-channels), and more shaly and inter-bedded deposits (Facies III) in distal and lateral margins of the lobes. In sand-rich, channelized lobes we expect thick-bedded sands (Facies II) throughout the lobe area, with sharp transitions to surrounding shales (Facies IV and V). Of course, these are simplified conceptual models. The real architectural elements can be much more complex in character (e.g., Clark and Pickering, 1996). Nevertheless, for the purpose of discriminating heterogeneities at a seismic scale, the facies associations described above should be adequate.

Having built a model of a given reservoir architecture in terms of geometries and facies, the architectural elements themselves can be parameterized by rock physics properties. This allows for a seismic modeling of the given reservoir architecture, to confirm the seismic interpretation. In section 6.4 we do this for the Grane turbidite system.

6.3.3   Architectural elements and reservoir connectivity

The stacking architecture of channel and lobe sands is controlled by the interaction between lateral and vertical amalgamation processes operating during deposition. The resulting stacking architecture is critical to the interconnectivity of individual elements.

In a channel-overbank complex with well developed overbank deposits, the lateral continuity is much smaller than in a channel with poorly developed overbank facies. In the latter, the lack of levees allows frequent channel avulsion, resulting in high lateral continuity of the channel sands. Depositional lobes will have larger lateral but less vertical connectivity than the associated feeder-channel. Channelized lobes in sand-rich systems will have very good lateral and vertical connectivities.

6.4   Seismic interpretation and modeling of reservoir architecture

In this section, we interpret the seismic scale reservoir architecture in the Grane area. First we document seismic geometries in terms of architectural elements as defined in Table 6.1. Other geologic features like erosion, internal bedding, faulting, and deformation are also documented. We then use the facies described in Chapter 3 as building blocks in seismic modeling studies of the observed geometries to confirm and guide the seismic interpretation of the reservoir architecture. Ultimately, we seek to document the sandstone connectivity from seismic in different parts of the Grane area. We divide the Grane field in two, northern Grane and southern Grane, based on the observations made by Martinsen et al. (1998). They found that the northern system is characterized by radial shaped depositional lobes, while the southern system seems to be more confined and elongated in shape.

6.4.1   Northern Grane channel-overbank complex

<u>Seismic observations</u>

From the map in Figure 6.1, we observe feeder-channel and lobe features in the northern part of the Grane area. Figure 6.2 shows a seismic line (amplitude display, approximately 35 Hz peak frequency) striking northeast-southwest, intersecting what

appears to be a feeder-channel. Red amplitude indicates relatively strong positive reflectivity, whereas blue is relatively strong negative reflectivity. We observe a strong zero-offset reflectivity across the channel-complex, except for a relatively transparent center of the channel. We interpret these observations as a confined channel sand with more shaly overbank deposits on the sides.
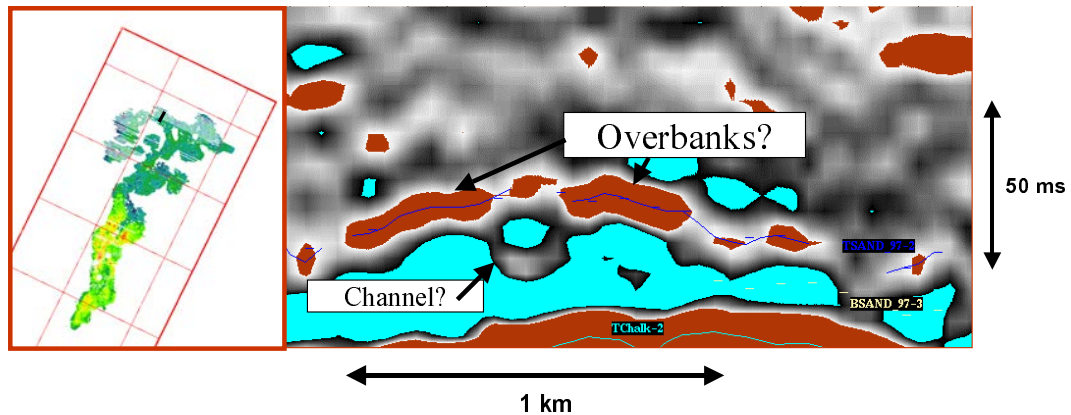
Figure 6.2: A seismic line intersecting what appears to be a channel-overbank complex in the northern Grane area. (Red is positive amplitude, while blue is negative amplitude).

A very similar channel-overbank feature is observed just west of the Grane area, outside the mapped extension of the Grane sands. Figure 6.3 shows a stacked section where we observe a clear, but low amplitude channel feature, and bright, positive amplitude overbank deposits.
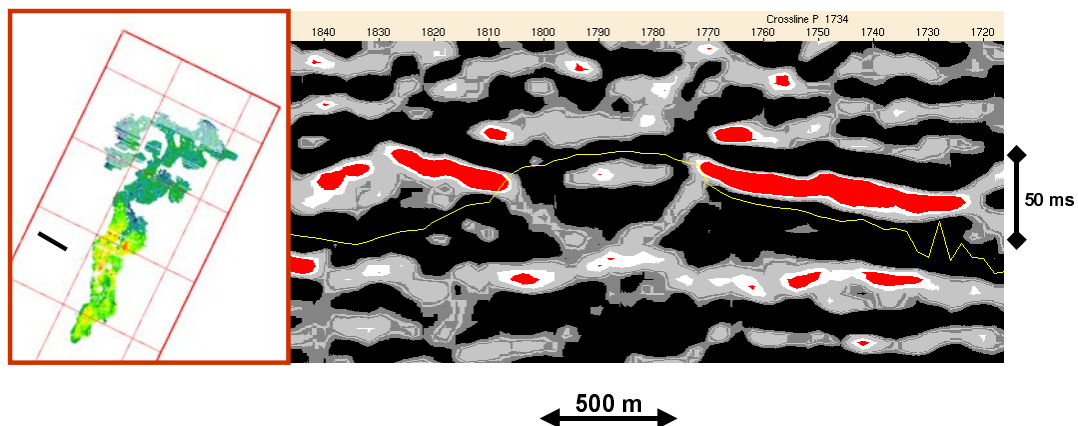
Figure 6.3: Channel-overbank complex west of Grane. (Red is relatively strong positive amplitude, whereas black represents zero or negative amplitudes).
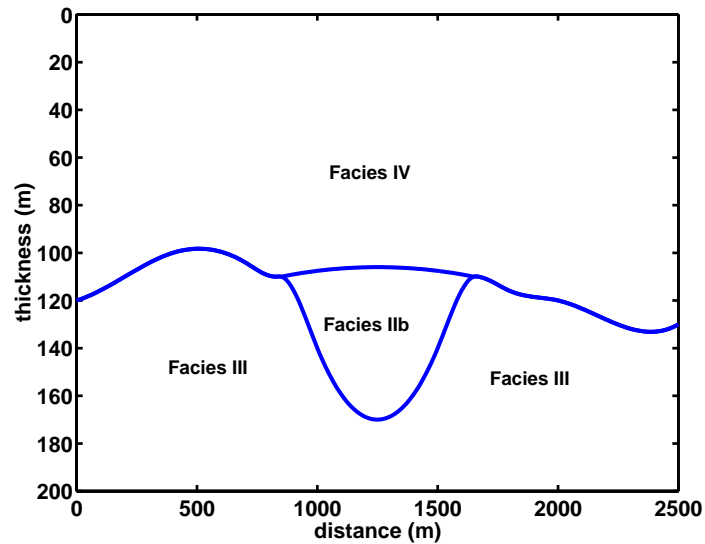
Figure 6.4: Seismic interpretation of seismic geometries observed in Figures 6.2 and 6.3. We interpret the bright-spots to be overbank deposits, whereas the dim-spot between is believed to be a channel axis. This interpretation is input into the seismic modeling in Figure 6.5.

Seismic modeling

Based on the interpretations above, we can create simple input geologic models for seismic modeling. These models are realistic arrangements of lithofacies and their geometries. Figure 6.4 shows the facies and architecture model interpreted from the seismic observations in Figures 6.2 and 6.3. The overbank deposits, corresponding to the bright amplitudes in the seismic, are interpreted to represent interbedded sands-shales (Facies III). The confined channel features observed in the middle, corresponding to the dim-spots in the seismic, are believed to be unconsolidated sands (Facies IIb), causing weak zero-offset and post-stack reflectors (c.f., Chapters 2 and 4). Finally, we assume that this channel-overbank system has been draped by shale (Facies IV). The dimensions of the modeled channel is approximately 500 m (width) by 70 m (thickness). The velocity and density models are shown in Figure 6.5, and are based on characteristic values for each facies (see Chapter 3).

We carry out forward seismic modeling of this channel-overbank complex (Figure 6.5). The synthetic seismic is produced using zero-offset convolution modeling, and the

wavelet is zero-phase with 35 Hz peak frequency. The seismic response we observe is very similar to what we observe in the real seismic data (Figures 6.2 and 6.3). The overbanks are characterized by bright positive amplitudes, whereas the channel axis is relatively dim. These results support our interpretations of channel-overbank architecture elements.
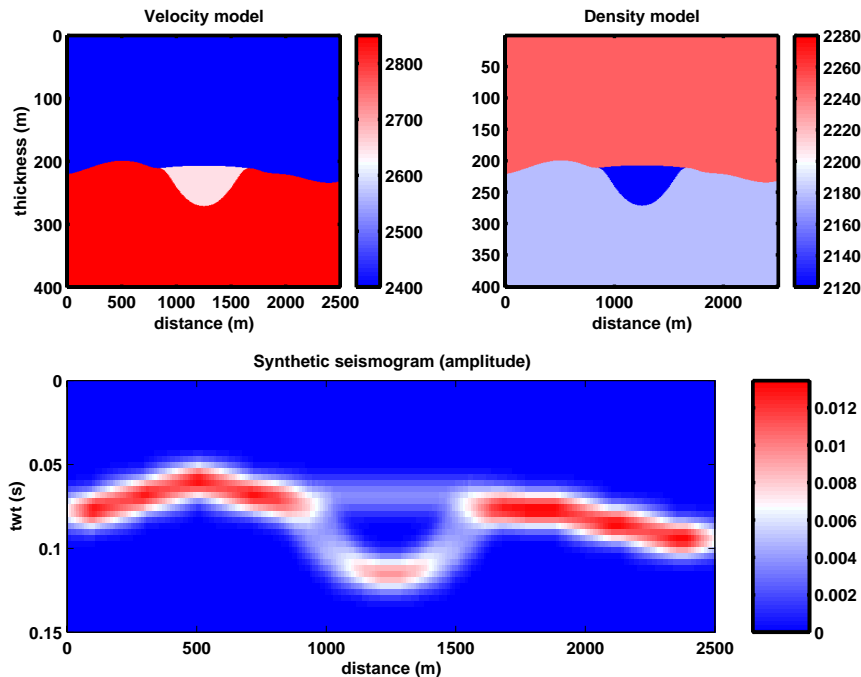
Figure 6.5: Facies guided seismic modeling of channel-overbank complex. Velocity and density models are depicted in the upper two subplots, and the resulting zero-offset seismic section is shown below.

6.4.2   Northern Grane depositional lobes

Seismic observations

Figure 6.6 shows a seismic line (near offset stack section) intersecting one of the lobes seen in the seismic map included in the same figure. This intersection is just east of the channel-overbank complex in Figure 6.2. Here we observe several segmented high-impedance reflectors, some of which are dipping to the south, partially overlapping each other. We interpret these as a lobe-complex that has gradually shifted to the south.
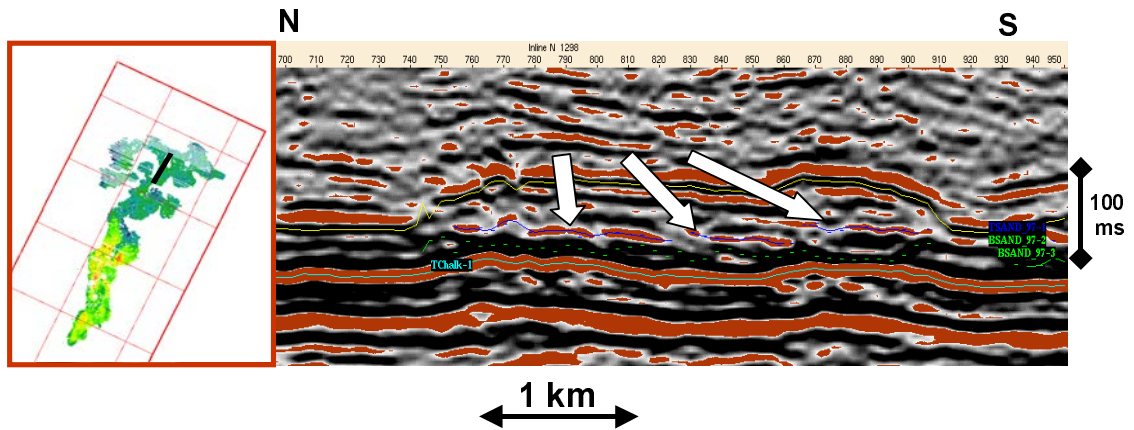
Figure 6.6: Seismic section intersecting the lobe system in the northern Grane. Note the oblique overlapping reflectors from left to right (north to south). This is interpreted as separate lobes laterally stacked besides each other (indicated by white arrows).

Figure 6.7 shows a seismic line intersecting the northern Grane lobe system more distally than in Figure 6.6. According to the map, this section intersects several individual lobes. In the seismic section we observe strong reflectors at the target level depicting more extensive features than in Figure 6.6. They also seem to be more mound-shaped. At least three individual segments of high reflectivity are observed, and these are partly overlapping each other. These are probably different lobes deposited at different times due to lobe-switching. From the seismic it looks as though the lobes are not connected to each other.
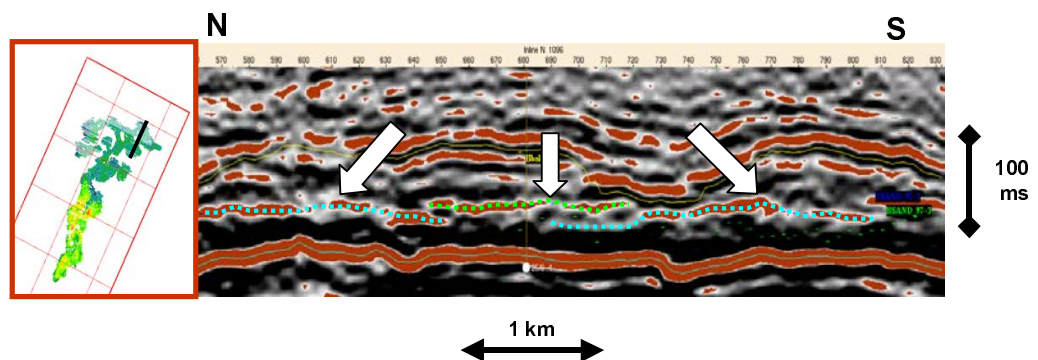
Figure 6.7: Seismic section intersecting the depositional lobes in the northern Grane. The top Heimdal reflector is segmented, and there seems to be 3 different lobes stacking beside each other. The middle lobe (green dotted line) seems to overlap the two lateral lobes (light blue dotted lines).

Seismic modeling

We want to see if we can reproduce the high-reflectivity seismic response of the interpreted lobe sands in Figures 6.6 and 6.7. We make a very simple geologic model, consisting of two separate lobes partly overlapping each other, but still disconnected and encased in shales (Figure 6.8). The sands are assumed to be cemented (Facies IIa). Well #1 in Chapter 5 penetrates one of the lobes in Figure 6.7, and the sands were found to represent Facies IIa. These are high impedance sands that can explain the bright reflectivity of the lobe features observed in Figures 6.6 and 6.7.
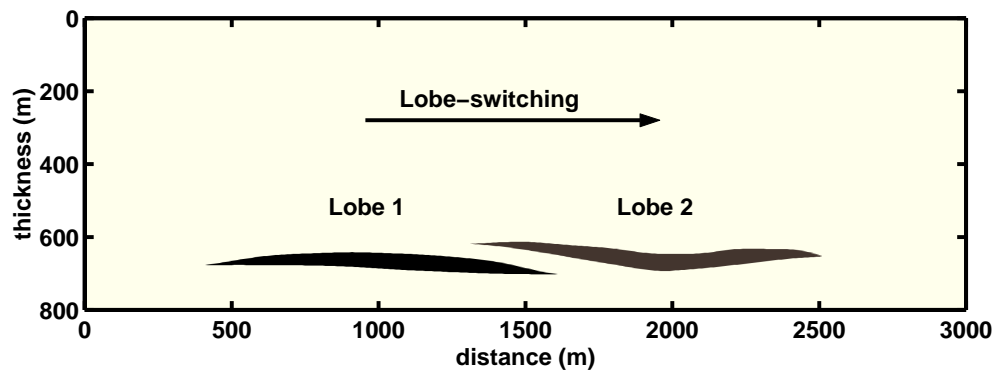
Figure 6.8: Simplified model of lobe-switching in the northern Grane area. The model assumes that the sands are encased in shales and that there is no connectivity between the sands. The sands are approximately 50 m thick, and the vertical separation in the overlapping area is also about 50 m.
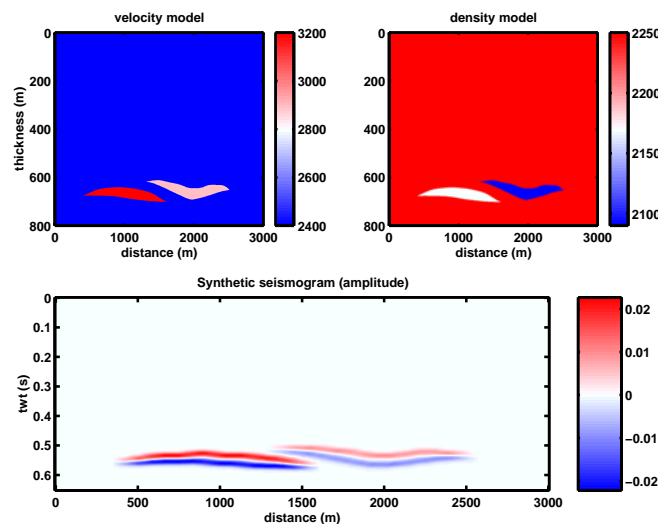
Figure 6.9: Synthetic seismic modeling of the two lobes in Figure 6.8. The two sands have slightly different properties related to texture change, but are both Facies IIa and hence produce a bright amplitude due to the contrast with the surrounding shales. Note that the sands are observed as separate features in the 35 Hz seismogram.

Figure 6.9 shows the synthetic modeling results of the depositional lobes in Figure 6.8. As in the real data, we observe a positive bright amplitude at the top of the lobe sands. The base of the sands show a negative amplitude. The two lobes are distinguished in the 35 Hz seismic section. This resembles the observations in the real data, where the different lobe-reflectors are separated. This may indicate that the lobes are disconnected.

6.4.3   Southern Grane channelized lobes

Seismic observations

Figure 6.10 shows a crossline that intersects the southern Grane lobe system from west to east. Here we observe lateral stacking of channels from the seismic data. Separate segments of strong reflectivity show a depositional pattern, where the channel-axis has shifted towards east. The segments are overlapping, causing internal reflectors. Hence, there must be acoustic contrasts between separate channels. From the well-log information in the southern Grane (see Chapter 5), the sands appear very homogeneous with no intercalations of shales. This means that the internal reflectors are caused by changes in sandstone texture. As shown in Chapter 2, sand texture (sorting and/or cementation) can be seismically significant in the Grane area.
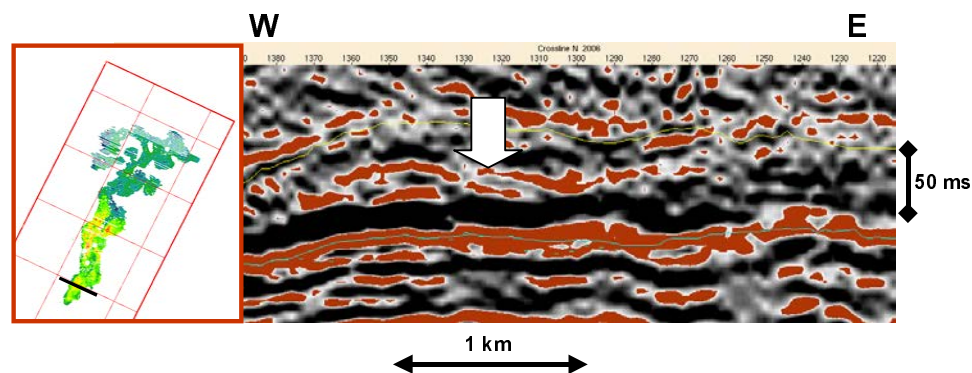

Figure 6.10: Seismic section intersecting the southern Grane fan. We observe seismic signatures of vertical and lateral stacking of separate channelized depositional units.

Figure 6.11 shows a north-south striking inline. Here we also observe a lateral offset stacking architecture, where segments to the south are partly overlying segments to the north. The eastward lateral stacking, perpendicular to the axis of deposition, probably reflects tectonic uplift in the west. Similar lateral stacking of channelized sands to the east have been observed in lower Eocene Balder sands and Frigg sands, as well (Timbrell, 1993). The lateral migration from north to south is probably due to progradation of the lobe system from north to south, depositing younger sands to the south. This is in accordance with biostratigraphic information from wells in the area (Martinsen et al., 1998).
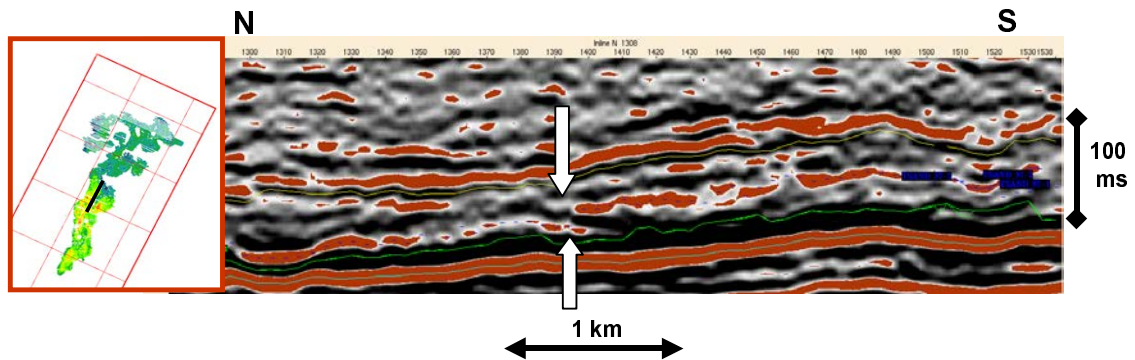
Figure 6.11: Seismic section striking north-south across the southern Grane system. The figure depicts at least two separate depositional units overlapping each other (at the arrows), the southmost on top of the one to the north. This indicates progradation and younger sediments to the south, which is in accordance with the biostratigraphic information at well locations.

Figure 6.12 shows a seismic line intersecting the southern Grane further north than Figure 6.11. Here we do not observe lateral stacking, but there is a very clear internal reflector that mimics the topography of the underlying reflector (Top Chalk). We interpret the internal horizon to reflect an abrupt textural change within the sands. Hence, we suggest a vertical aggradation of sands, where sands of different episodes and with different texture have amalgamated. In Figure 6.12, the basin topography may have confined the channelized lobe so much that lateral channel migration, as observed in Figure 6.10, was prevented. Still, the complete reservoir unit along this seismic line has a relatively large lateral extent, as well as substantial thickness.
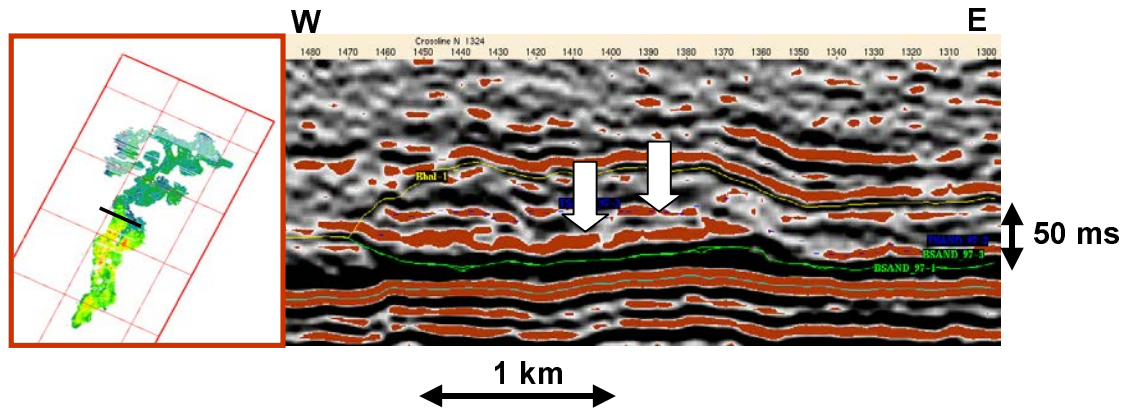
Figure 6.12: Seismic section showing strong positive top sand and internal sand reflectors (arrows), indicating vertical stacking/overlap of different sand units.

Furthermore, we observe local erosion in the southern Grane system. Figure 6.13 shows a seismic cross section where we observe channel cutting at the base of the reservoir, characterized by a negative zero-offset reflector (black trough response), as we go from sands to underlying shales.
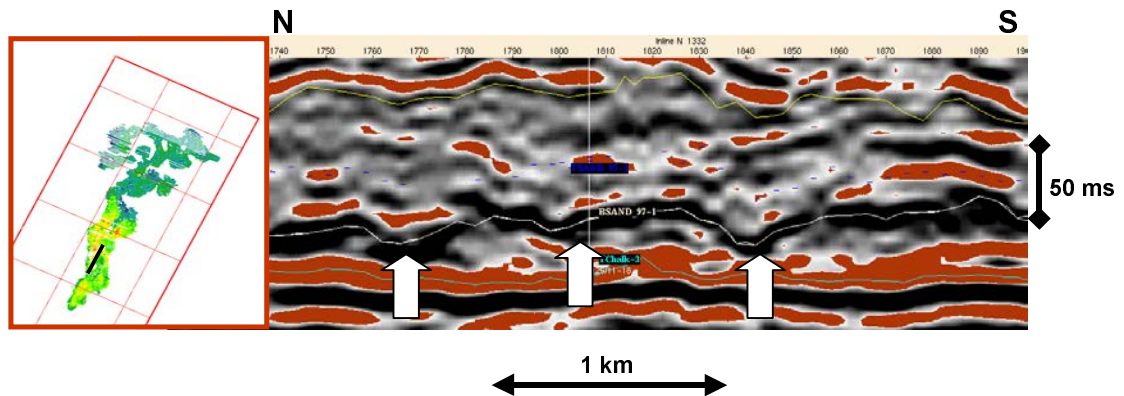
Figure 6.13: Seismic section showing signs of erosion at the base of the channelized southern Grane system (arrows).

Some of the irregular patterns we observe in Figure 6.13 may be due to syn- or post-depositional deformation. Post-depositional deformation is clearly visible in Figure 6.14. Here we observe small faults that compartmentalize the reservoir sands.
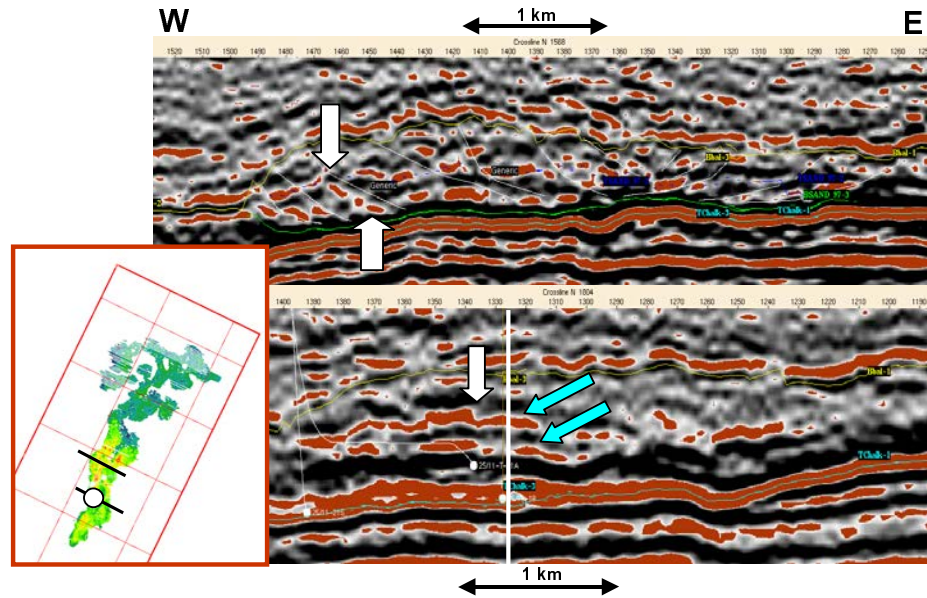
Figure 6.14: Seismic cross sections showing evidence of faulting and deformation in the southern Grane system (white arrows). Also note that there are two strong positive reflectors in the lower section, one top sand and one internal sand horizon (blue arrows). These are recognized in terms of changes in rock properties in the well penetrating the sands in the middle of this section (see Figure 6.15).

Rock physics analysis and seismic modeling of internal reflectors

In the southern Grane system, we have observed several occurrences of internal reflectors. All these internal reflectors seem to be depositional in nature, like the channelized cross bedding observed in Figure 6.10. We have already mentioned that the internal reflectors can be related to sandstone texture. From the well-log observations in the southern Grane (e.g., well #2 and well #3 in Chapter 5), we observe only thick, massive sands. However, the velocity logs indicate that there are significant velocity variations within the reservoir sands.

Figure 6.15 shows the rock properties of a well (well #3, Chapter 5) that penetrates the seismic section in Figure 6.14 (lower section). Within the reservoir sands, we see that the velocity increases and porosity decreases at the base. These changes in the rock physics properties correspond to the internal seismic reflector in Figure 6.14. By analyzing the reservoir zone in the velocity-porosity plane (Figure 6.15), we can use rock physics models to diagnose the sand texture (see Chapter 2). We find that the lower zone is more poorly sorted than the upper zone, and the zones likely represent separate

depositional units. The cement content is found to be constant on both sides of the internal textural boundary, approximately 2%, and therefore the internal reflector should not be related to cementation.
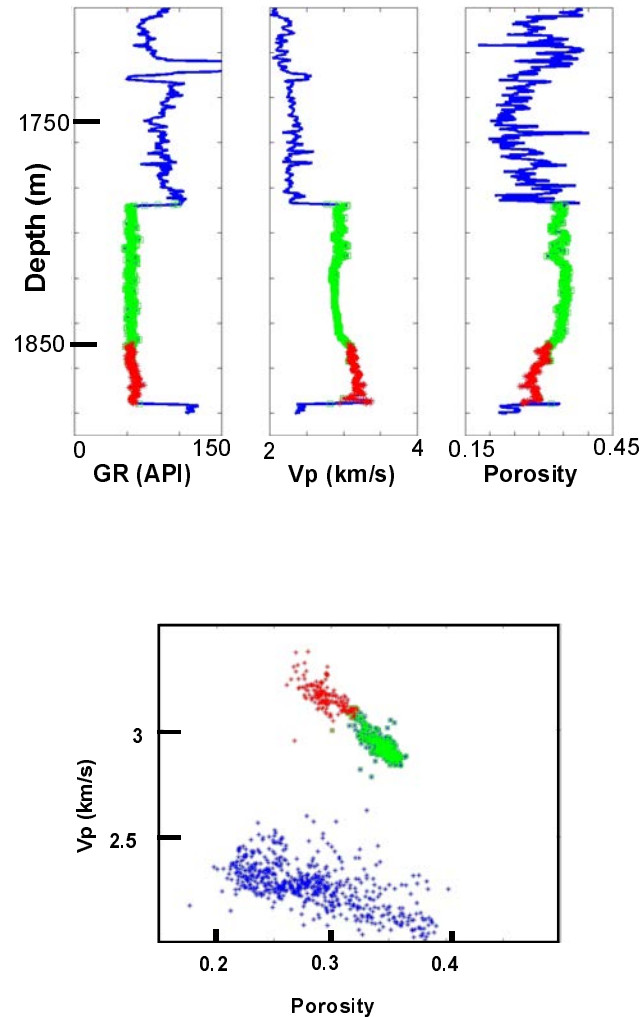
Figure 6.15: Gamma ray, Vp, and porosity in well #2 (location, see Figure 5.2). Cross plot of Vp versus porosity is shown to the right. The lower zone of the reservoir sands has higher velocities and lower porosities than the upper zone. This textural change is related to sorting/packing (c.f., Chapter 2), and explains the internal reflector observed in the seismic section in Figure 6.19.

The next step is to do seismic modeling to confirm that the abundant internal reflectors observed in the southern Grane system are related to contrasts in sandstone texture as observed in the well-logs. Figure 6.16 shows a geologic model of amalgamated channels sands with both vertical and lateral stacking patterns. We feed this model with

characteristic rock physics properties for each of the sands and the shales. For the different sand units, we assume a different texture. The lower unit is assumed to have a porosity of 29%, the intermediate unit 32%, and the upper unit 35%. The velocities are picked from the velocity-porosity relations in Figure 6.15. The densities are inverted from the porosities assuming brine saturation and quartz matrix (equation 2.6). Figure 6.17 shows the parameterized models.
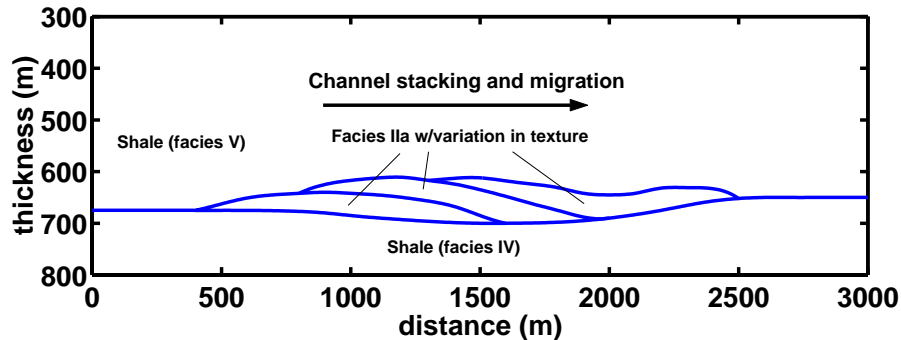
Figure 6.16: Geologic model showing lateral migration/stacking of channel sands.
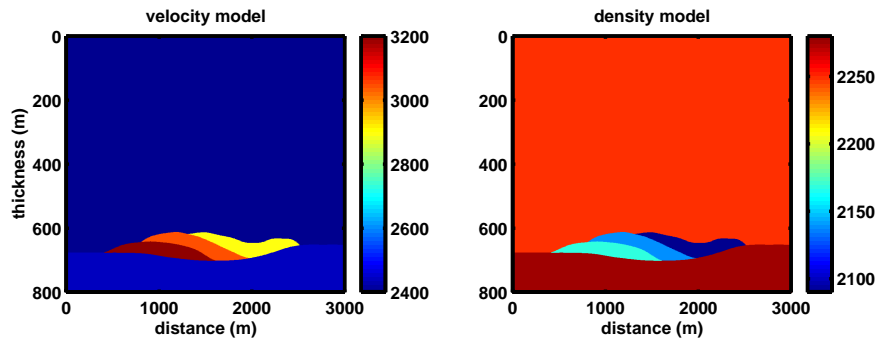
Figure 6.17: Velocity and density models of a laterally stacked channel-complex.

We make two synthetic seismic models of this case, one with 35 Hz and one with 50 Hz wavelets (Figure 6.18). In both cases we can observe the internal seismic reflectors occurring at the sand-sand interfaces. This shows that the internal reflectors in the real seismic sections can be caused by changes in sandstone texture. In addition, Figure 6.18 shows that the erosive nature of the channelized sands in the southern Grane system, into underlying shales, is easily recognized as a prominent negative reflector (compare with Figure 6.13).
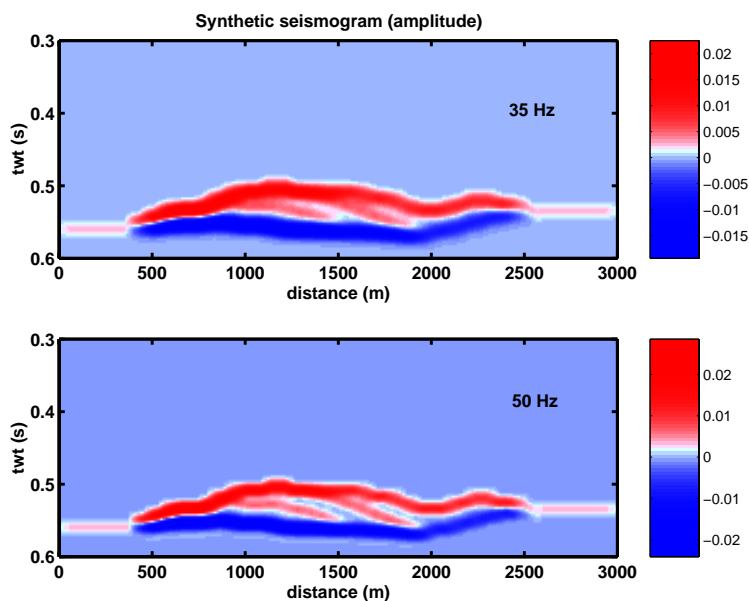
Figure 6.18: Synthetic seismic sections, one with a 35 Hz wavelet (upper) and one with a 50 Hz wavelet (lower). The results show that internal reflectors can occur due to sandstone texture in the studied turbidite system, even at 35 Hz. The top sand reflector is in general a strong positive amplitude, whereas the erosive base causes a strong negative amplitude.

6.5 Discussion

We have documented important differences in the seismic architecture in different parts of the Grane area. The information about the reservoir architecture and how it changes spatially have important implications for the assessment of reservoir connectivity and performance in the Grane field. The Grane oil field is in fact limited to the southern Grane system, and the features observed in the northern Grane are not of great importance to the hydrocarbon production of the Grane field. However, the observations made here can be valuable for other similar turbidite fields.

The reservoir characteristics of the Grane field are summarized in Table 6.2. The northern Grane system is characterized as an unconfined system with classical radial shaped depositional lobes (Martinsen et al., 1998). The observation of a channel-overbank complex, representing the feeder-channel to the northern Grane system, indicates that there may have been clay in the system during deposition. This is further supported by the observation of lobe-switching, instead of channelized lobes as in the south. Hence, the

northern system fits into the class of mud/sand-rich systems according to the scheme of Reading and Richards (1994). However, in the well penetrating the northern Grane lobe system (well #1 in Chapter 5), we only observe a thick and homogeneous sand unit. This well may be located in the center of a lobe channel, which would explain the thick massive sand (c.f., Reading and Richards, 1994). More heterogeneous facies may be located in more distal parts of the depositional lobes as well as in the overbank areas of the observed channel-overbank complex. Furthermore, we observe no deformation or signs of erosion in the northern Grane system.

The southern Grane system is a confined system with elongated channelized lobes (Martinsen et al., 1998). Extensive lateral and vertical channel stacking and migration is observed. There are no signs of overbank fines, but obvious signs of channel erosion (channel scours). Internal reflectors mainly arise from textural changes in the sands (sorting and/or packing). There are also proofs of syn-depositional deformation and faulting. The southern Grane system fits into the sand-rich system as defined by Reading and Richards (1994).

Basin topography can affect the stacking pattern of individual architectural elements, and can modify elements such as those described by Reading and Richards (1994). One important issue in the Grane area is whether the differences in architecture between northern and southern Grane are controlled by grain size, basin topography, or both. It is evident that the basin topography had a strong effect on the contrasting sandstone architecture in the south compared to the north (Martinsen et al., 1998). Based on observations in this study, we suggest that there is a relationship between basin topography and grain-size differences that cause the differences in sandstone architecture. The observation of stable overbank regions is the strongest evidence that mud was available during deposition in the northern Grane area. However, overbank deposits may have been formed by relatively poorly sorted, fine grained sands, in the absence of clays.

Corresponding to the dramatic changes in reservoir architecture from the north to the south, there should also be a drastic change in the sandstone connectivity. We expect much lower reservoir connectivity in the north than in the south. The depositional lobes in the north may have moderately good connectivity laterally, but we expect restricted connection between individual lobes. In the feeder-channel, we expect moderate vertical

connectivity, whereas the lateral connectivity across the channel-levee complex is probably poor. Along the channel axis, however, we expect good lateral connectivity. The channelized lobes in the south are likely to have very good connectivity in all directions. The connectivity may be reduced, however, in areas where faulting and deformation has been severe.

	Northern Grane	**Southern Grane**
Basin topography	Unconfined	Confined
Depositional geometry	Radial shaped	Elongated "sausage" shaped
Architectural elements	Channel-overbank complex and depositional lobes	Channelized lobes
Facies and grain size	Facies IIa, IIb and III(?) Presence of clays?	Facies IIa w/ sorting change No clay
Sedimentary processes	Lobe-switching Overbank deposition of fines/clays? No erosion	Channel-stacking Lateral migration/avulsion Erosion
Deformation	No signs of deformation	Faults Syn-depositional deformation
Lateral continuity	Moderate - Good	Good - Very good
Vertical connectivity	Moderate (?)	Good

Table 6.2: Seismic observations and interpretations in the Grane system. Comparing important differences in reservoir geologic characteristics between the northern and southern Grane systems.

All the observations made here are made at the seismic scale. There may be reservoir heterogeneities at a finer scale that we have not observed, and these can have important effects on the reservoir connectivity. Nevertheless, well-log information from several wells in the southern Grane area indicates that the reservoir sands are very homogeneous, and we do not expect the presence of more heterogeneous depositional units. As discussed above, this may be different in the northern Grane system if there was mud in the system during deposition. We have too little well control in the northern Grane to confirm this speculation.

In this chapter, we have only looked at zero-offset reflectivities. As shown in Chapter 5, pre-stack data and AVO analysis is required to discriminate between certain facies in the Grane area. However, including offset dependent reflectivity in seismic modeling requires much more time and computer effort, and one of the goals in this chapter was to do quick and easy modeling of geometries during interpretation. In areas where ambiguities are suspected, more detailed AVO analysis should be conducted (c.f., Chapter 5). One potential ambiguity in the observations made in this chapter is the identification of sands as channel fills. Based on the dim-spots, we interpreted these as unconsolidated sands. However, the dim-spots could also be explained by shales filling in the channels. This ambiguity could be resolved by AVO analysis of the dim-spots. Another ambiguity that may have occurred concerns the bright reflectors being interpreted as Facies III in the overbank areas, whereas the bright amplitudes in the lobe areas have been interpreted as cemented sands (Facies IIa). Because both these facies would create bright zero-offset amplitudes when capped by shales, AVO analysis could be used to differentiate these facies, as we did in the Glitne field (Chapter 4).

Some internal reflectors in the southern Grane area could be related to the oil-water contact (located at 1845 m depth in the well in Figure 6.15). However, all the internal reflectors we observed show depositional or deformational patterns. We observe no flat spots that are likely associated with an oil-water interface. The oil in the Grane area is relatively thick (18 API), and is not prone to cause any significant seismic reflector.

The top of the Heimdal sands in the Grane area is often irregular because of the channelized nature of the unit, syn-depositional deformation and faulting, as well as the reported sand injections into the overlying shales (Martinsen et al., 1998). Thus, the

seismic reflector representing the top of the reservoir may locally show a disrupted character. In these areas we should be careful in comparing simple convolutional seismic models with the real amplitudes. Nevertheless, we have shown that by conducting simple facies-guided seismic modeling of various reservoir architecture elements, we have managed to reproduce and explain many of the observations made in the real seismic data in the Grane area. In general, the lesson to be learned from this chapter is that rock physics and amplitude analysis can guide the interpretation of reservoir geometries. Finally, facies-guided seismic modeling should be an integral part of seismic interpretation in the oil industry.

6.6   Conclusions

- Rock physics and seismic modeling can be used to guide and/or confirm the interpretation of seismic geometries and reservoir architecture. Seismic lithofacies with characteristic rock physics properties can be related to architectural elements and serve as building blocks in seismic modeling.

- We employ facies-guided seismic modeling to infer reservoir architecture from the seismic signatures in the Grane Field. We observe various seismic scale architectural elements, including a channel-overbank complex and depositional lobes in the northern Grane, and channelized lobes in the southern Grane.

- Internal reflectors in the southern Grane are caused by abrupt transitions in sand texture between different depositional units that are vertically and laterally stacked and amalgamated.

- The documentation of the great variability in sandstone architecture in the Grane area is of essential value for reservoir management in this and similar turbidite fields.

6.6 References

Allen, J. R. L., 1982, Sedimentary structures, their character and physical basis: Developments in sedimentology **30** (parts I and II), Amsterdam, Elsevier.

Brown, A. R., 1992, Interpretation of three-dimensional seismic data: AAPG Memoir **42**, 3d edition, 253p.

Brown, A. R., 1999, A new dimension: AAPG Explorer, Special Issue, A Century, p. 80.

Clark, J. D., and Pickering, K. T., 1996, Architectural elements and growth patterns of submarine channels: Application to hydrocarbon exploration: AAPG Bull., **80**, 194-221.

Ghosh, B., and Lowe, D. R., 1993, The architecture of deep-water channel complexes, Cretaceous Venado sandstone member, Sacramento Valley, California; *in* Graham, S. A., and Lowe, D. R., Eds., Advances in sedimentary geology of the Great Valley Group, Sacramento Valley, California: SEPM field trip guidebook, 51-65.

Martinsen, O. J, Indrevær, G., Dreyer, T., Mangerud, G., Ryseth, A., and Søyseth, L., 1998, Slumping, sliding and basin floor physiography: Controls on turbidite deposition and fan geometries in the Paleocene Grane Field area, Block 25/11, Norwegian Sea: 1998 AAPG Annual Convention, Extended Abstracts, vol. **2**, A435.

Miall, A. D., 1985, Architectural element analysis: A new method of facies analysis applied to fluvial deposits: Earth Science Reviews, **22**, 261-308.

Mutti, E., and Normark, W.R., 1987, Comparing examples of modern and ancient turbidite systems: problems and concepts, *in* Weimer, P., and Link, M. H., Eds., Seismic facies and sedimentary processes of submarine fans and turbidite systems: New York, Springer-Verlag, 75-106.

Pickering, K. T., Clark, J. D., Ricci Lucchi, F., Smith, R. D., Hiscott, R. N., and Kenyon, N. H., 1995, Architectural element analysis of turbidite systems, and selected topical problems for sand-prone deep-water systems, *in* Pickering, K. T., Hiscott, R. N., Kenyon, N. H., Ricci Lucchi, F., and Smith, R. D., Eds., Atlas of deep-water environments: Architectural style in turbidite systems: London, Chapman and Hall, 1-10.

Reading, H. G., and Richards, M., 1994, Turbidite systems in deep-water basin margins classified by grain size and feeder system: AAPG Bull., **78**, 792-822.

Ryseth, A., Fjellbirkeland, H., Osmundsen, I.K., Skålnes, Å., and Zachariassen, E., 1998, High-resolution stratigraphy and seismic attribute mapping of a fluvial reservoir; Middle Jurassic Ness Formation, Oseberg Field: AAPG Bull., **82**, 1627-1651.

Timbrell, G., 1993, Sandstone architecture of the Balder Formation depositional system, UK quadrant 9 and adjacent areas, *in* Parker, J. R., Ed., Petroleum geology of northwest Europe: Proceedings of the 4th conference: London, The Geophysical Society, 107-121.

Walker, R., 1978, Deep-water sandstone facies and ancient submarine fans: Models for exploration for stratigraphic traps: AAPG Bulletin, **62**, 932-966.

Appendix A

Geologic setting and stratigraphy

A.1 Regional map of the North Sea and field locations

The studied deep-sea depositional systems are located in the South Viking Graben, North Sea (Figure A.1), and includes two oil fields of economic interest, the Glitne Field and the Grane Field. The reservoir sands in both these fields represents the Heimdal Formation of Paleocene age (Figure A.2).
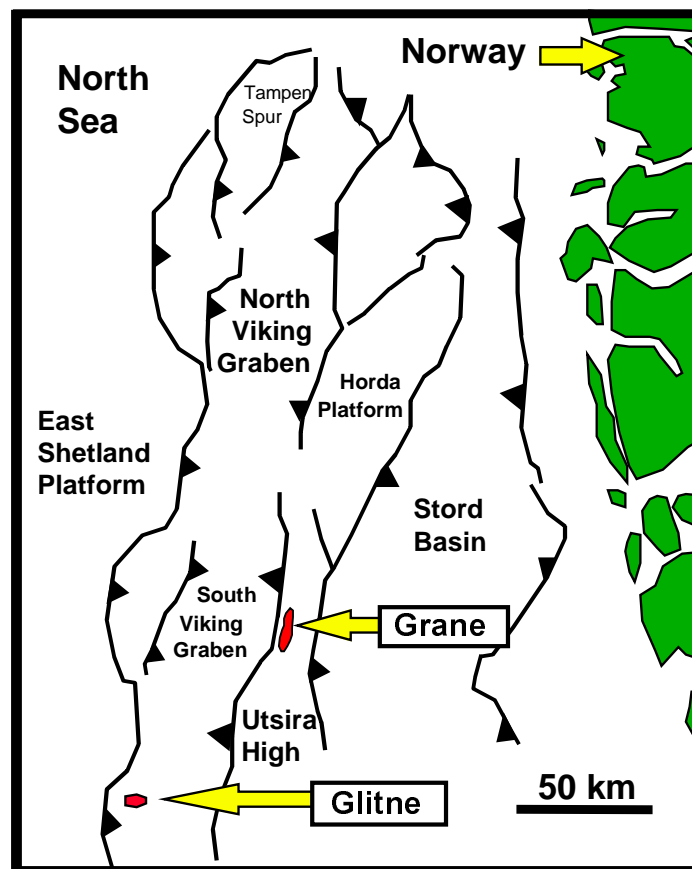

Figure A.1: North Sea structural map (major Jurassic faults) and location of studied deep-sea depositional systems, including the Glitne and the Grane oil fields.

A.2   Geologic setting

During the Early Tertiary, uplift of the Scottish mainland, associated with the opening of the North Atlantic, resulted in the influx of vast quantities of siliciclastic sediments into the North Sea (Glennie, 1990). There was also an uplift of the North Sea basin, possibly as part of the peripheral bulge associated with the formation of a new plate margin. Due to the uplift in west, there was in general an eastward progradation of the sediments (Figure 2).
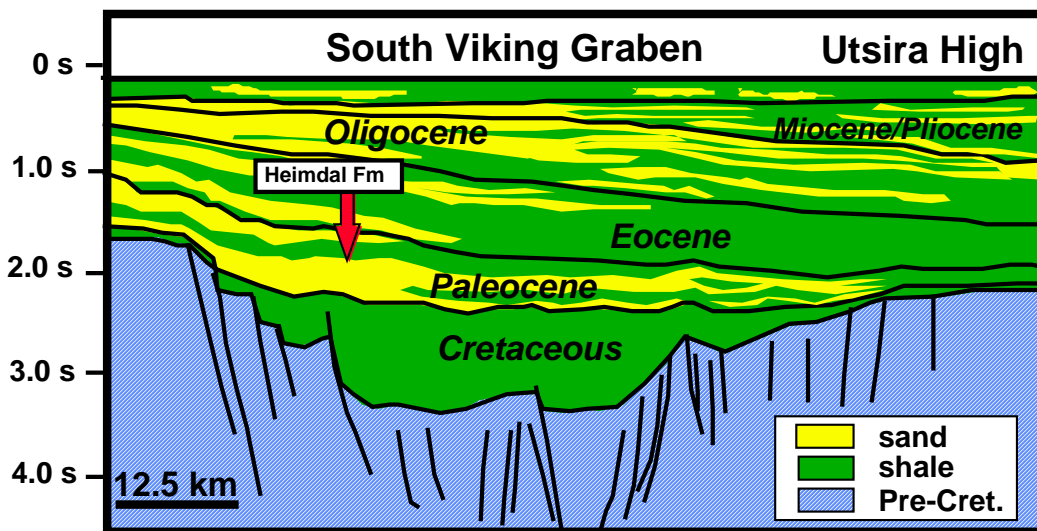

Figure A.2: Geologic cross-section of the North Sea. The studied deep-sea system is of Paleocene age and represents the Heimdal Formation (The figure is adapted from confidential Norsk Hydro internal report).

The induced shallowing of the North Sea basin, combined with an increased sediment supply, resulted in a filling to sea-level of much of the northwestern basin margin. At the end of the Paleocene, uplift ceased and most of the North Sea subsided again, with associated drowning of the prograding shoreline units and a return to deep-water shale deposition (Bertram and Milton, 1989). Moreover, at the end of Paleocene the general trend in sedimentation was disrupted by a period of volcanism related to the opening of the Norwegian Sea, and subsidence led to an Early Eocene transgression and marine muds covered the tuffaceous layers.

A.3 Lithostratigraphy

Table A.1 includes the Paleocene lithostratigraphic units of interest in this study. The target formation is the Heimdal Formation, and is normally embedded by Lista Formation shales. The listed lithologies are the predominant constitutes of the different formations. However, each formation can show lateral variation in lithology.

Age	Formation	Lithology
Early Eocene - Late Paleocene	Balder Formation	Volcanic ash-fall deposits (tuffaceous sediments)
Late Paleocene	Sele Formation	Shale
Late Paleocene	Lista Formation	Shales and silt-laminated shales
Late Paleocene	**Heimdal Formation**	Sandstone
Mid - Late Paleocene	Lista Formation	Shales and silt-laminated shales
Early Paleocene	Vaale Formation	Marl deposits and shales
Early Paleocene	Ekofisk Formation	Limestone (Chalk deposits)

Table A.1: Paleocene lithostratigraphy in the North Sea, Southern Viking Graben (after Isaksen and Tonstad, 1989).

Starting from the top, the Balder Formation is in general very tuff-rich, but shales and turbidite sands can occur within this unit. The Sele Formation is in general a very clay-rich shale, but silt content can vary, and intercalation of tuffaceous and carbonate units

can be present. Turbidite sands can also occur within the Sele Formation, and these are referred to as the Hermod Formation sands. The Lista Formation is also predominantly shaly, but silt-laminated units, tuffs and carbonate units can be present. The Heimdal Formation is encased by the Lista Formation, and therefore the reservoir sands of the Glitne and Grane area are normally capped by shales. The Heimdal Formation has been renamed since this study started and is now referred to as the Heimdal Group, but in this study we have chosen to use the former classification. Below the Lista and Heimdal Formations, we find the Vaale and Ekofisk Formations of Early Paleocene age. These units normally represent marl deposits and limestones, respectively.

A.4   References

Bertram, G. T., and Milton, N., 1989, Reconstructing basin evolution from sedimentary thickness; the importance of palaeobathymetric control, with reference to the North Sea: Basin Research, **1**, 247-257.

Glennie, K. W., 1990, Introduction to the petroleum geology of the North Sea: Blackwell Sci. Publ.

Isaksen D., and Tonstad, K., 1989, A revised Cretaceous and Tertiary lithostratigraphic nomenclature for the Norwegian North Sea: Norw. Petrolm. Direct. Bull., 5.

Appendix B

Physical models for high-porosity sandstones – Mathematical formulations

B.1 The contact-cement model

The contact-cement model (Dvorkin and Nur, 1996) assumes that porosity decreases from the initial critical porosity value due to the uniform deposition of cement layers on the surface of the grains. The diagenetic cement dramatically increases the stiffness of the sand by reinforcing the grain contacts (Figure B.1). The mathematical model is based on a rigorous contact-problem solution by Dvorkin et al. (1994).
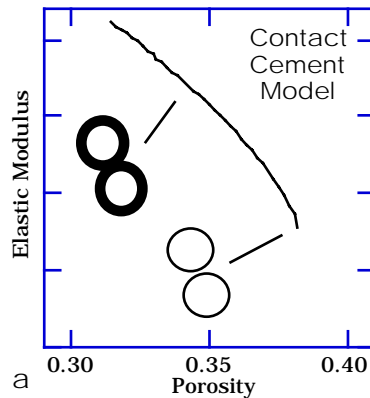

Figure B.1: Schematic depiction of the contact cement model and the corresponding diagenetic transformation (Courtesy of Jack Dvorkin).

In this model, the effective bulk (K_{dry}) and shear (G_{dry}) moduli of dry rock are:

$$K_{dry} = n(1 - \phi_c)M_cS_n \, / \, 6, \; G_{dry} = 3K_{dry} \, / \, 5 + 3n(1 - \phi_c)G_cS_\tau \, / \, 20, \tag{B-1}$$

where ϕ_c is critical porosity; K_s and G_s are the bulk and shear moduli of the grain material, respectively; K_c and G_c are the bulk and shear moduli of the cement material, respectively; $M_c = K_c + 4G_c/3$ is the compressional modulus of the cement; and n is the coordination number, defined as average number of contacts per grain (usually 8 or 9 for high porosity sands). S_n and S_τ are:

$$S_n = A_n(\Lambda_n)\alpha^2 + B_n(\Lambda_n)\alpha + C_n(\Lambda_n),\ A_n(\Lambda_n) = -0.024153 \cdot \Lambda_n^{-1.3646},$$

$$B_n(\Lambda_n) = 0.20405 \cdot \Lambda_n^{-0.89008},\ C_n(\Lambda_n) = 0.00024649 \cdot \Lambda_n^{-1.9864};$$

$$S_\tau = A_\tau(\Lambda_\tau, v_s)\alpha^2 + B_\tau(\Lambda_\tau, v_s)\alpha + C_\tau(\Lambda_\tau, v_s),$$

$$A_\tau(\Lambda_\tau, v_s) = -10^{-2} \cdot (2.26 v_s^2 + 2.07 v_s + 2.3) \cdot \Lambda_\tau^{0.079 v_s^2 + 0.1754 v_s - 1.342},$$

$$B_\tau(\Lambda_\tau, v_s) = (0.0573 v_s^2 + 0.0937 v_s + 0.202) \cdot \Lambda_\tau^{0.0274 v_s^2 + 0.0529 v_s - 0.8765},$$

$$C_\tau(\Lambda_\tau, v_s) = 10^{-4} \cdot (9.654 v_s^2 + 4.945 v_s + 3.1) \cdot \Lambda_\tau^{0.01867 v_s^2 + 0.4011 v_s - 1.8186};$$

$$\Lambda_n = 2G_c(1 - v_s)(1 - v_c)/[\pi G_s(1 - 2 v_c)],\ \Lambda_\tau = G_c/(\pi G_s);$$

$$\alpha = [(2/3)(\phi_c - \phi)/(1 - \phi_c)]^{0.5};$$

$$v_c = 0.5(K_c/G_c - 2/3)/(K_c/G_c + 1/3);$$

$$v_s = 0.5(K_s/G_s - 2/3)/(K_s/G_s + 1/3).$$

A detailed explanation of these equations and their derivation are given in Dvorkin and Nur (1996).

B.2   The friable sand model

The friable sand model (Dvorkin and Nur, 1996) assumes that porosity decreases from the initial critical porosity value due to the deposition of the solid matter away from the grain contacts. This non-contact additional solid matter weakly affects the stiffness of the rock (Figure B.2). The friable sand model allows one to accurately predict velocity in soft high-porosity sands
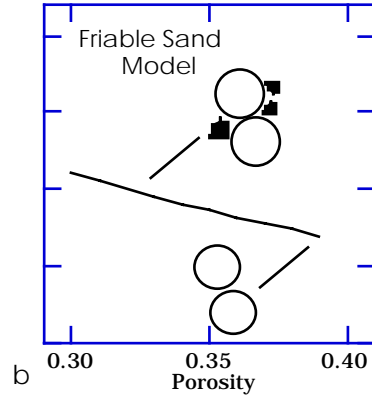
Figure B.2: Schematic depiction of the friable sand model and the corresponding sedimentologic variation (Courtesy of Jack Dvorkin).

The theoretical effective-medium model connects two end-points in the elastic-modulus-porosity plane. One end point is at critical porosity. The elastic moduli of the dry rock at that point are assumed to be the same as of an elastic sphere pack subject to confining pressure. These moduli are given by the Hertz-Mindlin (Mindlin, 1949) theory:

$$K_{HM} = [\frac{n^2(1-\phi_c)^2 G^2}{18\pi^2(1-\nu)^2} P]^{\frac{1}{3}}, \quad G_{HM} = \frac{5-4\nu}{5(2-\nu)}[\frac{3n^2(1-\phi_c)^2 G^2}{2\pi^2(1-\nu)^2} P]^{\frac{1}{3}}; \quad (B-2)$$

where K_{HM} and G_{HM} are the bulk and shear moduli at critical porosity ϕ_c, respectively; P is the differential pressure; K, G, and ν are the bulk and shear moduli of the solid phase, and its Poisson's ratio, respectively; and n is the coordination number.

The other end-point is at zero porosity and has the bulk (K) and shear (G) moduli of the pure solid phase. These two points in the porosity-moduli plane are connected with the curves that have the algebraic expressions of the lower Hashin-Shtrikman (1963) bound (bulk and shear moduli) for the mixture of two components: the pure solid phase and the phase that is the sphere pack. The reasoning is that in unconsolidated sediment, the softest component (the sphere pack) envelopes the stiffest component (the solid) in the Hashin-Shtrikman fashion (Figure 10).

At porosity ϕ the concentration of the pure solid phase (added to the sphere pack to decrease porosity) in the rock is $1 - \phi / \phi_c$ and that of the sphere-pack phase is ϕ / ϕ_c. Then the bulk (K_{Dry}) and shear (G_{Dry}) moduli of the dry frame are:

$$K_{Dry} = [\frac{\phi / \phi_c}{K_{HM} + \frac{4}{3}G_{HM}} + \frac{1 - \phi / \phi_c}{K + \frac{4}{3}G_{HM}}]^{-1} - \frac{4}{3}G_{HM},$$

$$G_{Dry} = [\frac{\phi / \phi_c}{G_{HM} + z} + \frac{1 - \phi / \phi_c}{G + z}]^{-1} - z, \ z = \frac{G_{HM}}{6}\left(\frac{9K_{HM} + 8G_{HM}}{K_{HM} + 2G_{HM}}\right).$$
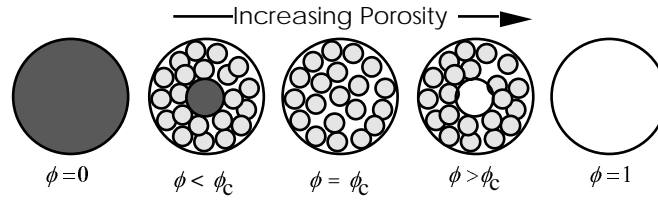
(B-3)

Figure B.3: Hashin-Shtrikman arrangements of sphere pack, solid, and void.

B.3   The constant cement model

We combine the two models above and obtain the <u>constant-cement model</u>. This model assumes that the initial porosity reduction from critical porosity is due to the contact cement deposition. At some high porosity, this diagenetic process stops and after that porosity reduces due to the deposition of the solid phase away from the grain contacts as in the friable sand model (Figure B.4). This model is mathematically analogous to the friable sand model except that the high-porosity end point bulk and shear moduli (K_b and G_b, respectively) are calculated at some "cemented" porosity ϕ_b from the contact-cement model. Then the dry-rock bulk and shear moduli are:

$$K_{dry} = \left(\frac{\phi / \phi_b}{K_b + 4G_b / 3} + \frac{1 - \phi / \phi_b}{K_s + 4G_b / 3}\right)^{-1} - 4G_b / 3,$$

$$G_{dry} = \left(\frac{\phi / \phi_b}{G_b + z} + \frac{1 - \phi / \phi_b}{G_s + z}\right)^{-1} - z, \quad z = \frac{G_b}{6} \frac{9K_b + 8G_b}{K_b + 2G_b}.$$
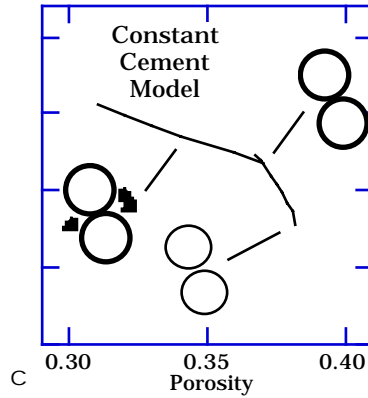
(B-4)

Figure B.4: Schematic depiction of the constant cement model and the corresponding sedimentologic and diagenetic change.

B.4   References

Dvorkin, J., Nur, A., and Yin, H., 1994, Effective Properties of Cemented Granular Materials, Mechanics of Materials, 18, 351-366.

Dvorkin, J., and Nur, A., 1996, Elasticity of High-Porosity Sandstones: Theory for Two North Sea Datasets, Geophysics, 61, 1363-1370.

Mindlin, R. D., 1949, Compliance of elastic bodies in contact, J. Appl. Mech., 16, 259-268.

Hashin, Z., and Shtrikman, S., 1963, A variational approach to the elastic behavior of multiphase materials: J. Mech. Phys. Solids, 11, 127-140.